

**Optimized, versatile
diamond-based sensors:
materials, fabrication and
novel applications**

Dissertation
zur Erlangung des Grades
des Doktors der Naturwissenschaften
der Naturwissenschaftlich-Technischen Fakultät
der Universität des Saarlandes

von
Richard Nelz

Saarbrücken
2019

Tag des Kolloquiums:	07.05.2020
Dekan:	Prof. Dr. Guido Kickelbick
Berichterstatter:	Dr. Elke Neu-Ruffing Prof. Dr. Uwe Hartmann
Vorsitz:	Prof. Dr. Rolf Pelster
Akad. Mitarbeiter:	Dr. Stephan Kucera

Abstract

Quantum sensing as one of the backbones of the second quantum revolution is about to enable a variety of novel applications requiring good spatial resolution and sensitivity. The atomic-sized, negatively charged nitrogen vacancy (NV) color center in single crystal diamond was found to enable magnetic field sensing at the nanoscale. Magnetic sensing using NV centers is enabled by bright photostable emission and optically addressable spin states. Due to its extraordinary coherence time, sensitivities of few $\text{nT}/\sqrt{\text{Hz}}$ can be achieved under ambient conditions. To enhance the spatial resolution of NV-based sensing, it is necessary to approach the NV center to a sample to investigate. Here, a challenging nanofabrication procedure is needed to sculpt the diamond into a photonic nanostructure usable as a scanning probe tip.

In this thesis, we report on the progress towards optimizing the applicability of NV centers as quantum sensors. We investigate novel material systems promising for upscaling nanofabrication. By introducing a novel approach to enhance the adhesion of etch masks and novel plasma treatments, we optimize the reliability of the nanofabrication procedure. In addition, we study a novel near-field interaction-based sensing resource. By investigating the interaction of shallow NV centers with a monolayer of WSe_2 , we were able to show simultaneous near-field and magnetic field sensing using the NV center.

Kurzzusammenfassung

Als eine der Säulen der zweiten Quanten-Revolution ermöglicht die Quantensensorik viele neue Anwendungen, die eine gute Ortsauflösung und Sensitivität benötigen. Das atomar kleine, negativ geladene Stickstoff-Fehlstellen (NV) Farbzentrum in einkristallinem Diamant ermöglicht das Detektieren von Magnetfeldern auf Nanomaßstäben. Magnetfelddetektion mittels NV Zentren wird durch helle, photostabile Emission und optisch adressierbare Spin-Zustände ermöglicht. Aufgrund seiner außergewöhnlichen Kohärenzzeit erreicht es Sensitivitäten von einigen $\text{nT}/\sqrt{\text{Hz}}$ unter Umgebungsbedingungen. Zur Verbesserung der Ortsauflösung NV-basierter Sensorik, muss das NV-Zentrum an die zu untersuchende Probe angenähert werden. Dies erfordert einen herausfordernden Nanofabrikationsprozess, um den Diamanten in eine photonische Struktur zu formen, die als Rastersonde nutzbar ist.

Diese Arbeit beschreibt Fortschritte zur Optimierung der Anwendbarkeit von NV-Zentren als Quantensensoren. Wir untersuchen neuartige Materialien, die vielversprechend für die Skalierbarkeit des Prozesses sind. Durch neue Ansätze zur Verbesserung der Adhäsion von Ätzmasken und neue Plasmabehandlungen optimieren wir die Zuverlässigkeit der Nanofabrikation. Zudem analysieren wir einen neuen, auf Nahfeldwechselwirkung beruhenden Sensorikansatz. Bei der Untersuchung der Wechselwirkung von oberflächennahen NV-Zentren mit monolagigem WSe_2 konnten wir das gleichzeitige Erfassen von Nah- und magnetischen Feldern mittels NV-Zentren zeigen.

Articles included in this thesis

The present thesis is a cumulative work including the six publications listed below. The sorting of the list represents the chapters of this thesis in which the respective publications occur. The contribution of the author of this thesis is stated on the first page of each chapter.

- Chap. 2 *Color center fluorescence and spin manipulation in single crystal, pyramidal diamond tips*
Richard Nelz, Philipp Fuchs, Oliver Opaluch, Selda Sonusen, Natalia Savenko, Vitali Podgursky, and Elke Neu
Applied Physics Letters **109**, 193105 (2016); doi: 10.1063/1.4967189
- Chap. 3 *Toward wafer-scale diamond nano- and quantum technologies*¹
Richard Nelz, Johannes Görlitz, Dennis Herrmann, Abdallah Slablab, Michel Chalker, Mariusz Radtke, Martin Fischer, Stefan Gsell, Matthias Schreck, Christoph Becher, and Elke Neu
APL Materials **7**, 011108 (2019); doi: 10.1063/1.5067267
- Chap. 4 *Reliable Nanofabrication of single-crystal diamond photonic nanostructures for nanoscale sensing*
Mariusz Radtke, Richard Nelz, Abdallah Slablab, and Elke Neu
Micromachines **10**, 718 (2019); doi: 10.3390/mi10110718
- Chap. 5 *Plasma treatments and photonic nanostructures for shallow nitrogen vacancy centers in diamond*
Mariusz Radtke, Lara Render, Richard Nelz, and Elke Neu
Opt. Mater. Express **9**, 4716-4733 (2019); doi: 10.1364/OME.9.004716
- Chap. 6 *Nanoscale sensing based on nitrogen vacancy centers in single crystal diamond and nanodiamonds: achievements and challenges*²
Mariusz Radtke, Ettore Bernardi, Abdallah Slablab, Richard Nelz, and Elke Neu
Nano Futures, in press (2019); doi: 10.1088/2399-1984/ab5f9b

¹This paper was selected as an Editor's Pick

²This paper is a topical review

Chap. 7 *Near-field energy transfer between a luminescent 2D material and color centers in diamond*

Richard Nelz, Mariusz Radtke, Abdallah Slablab, Zai-Quan Xu, Mehran Kianinia, Chi Li, Carlo Bradac, Igor Aharonovich, and Elke Neu
Adv. Quantum Technol. **1900088** (2019); doi: 10.1002/qute.201900088

Contents

1. Introduction	1
1.1. NV centers in diamond	5
1.2. Nanofabrication	11
1.3. Experimental setup and methods	12
2. Color center fluorescence and spin manipulation in single crystal, pyramidal diamond tips	17
3. Toward wafer-scale diamond nano- and quantum technologies	23
4. Reliable Nanofabrication of single-crystal diamond photonic nanostructures for nanoscale sensing	29
5. Plasma treatments and photonic nanostructures for shallow nitrogen vacancy centers in diamond	41
6. Nanoscale sensing based on nitrogen vacancy centers in single crystal diamond and nanodiamonds: achievements and challenges	61
7. Near-field energy transfer between a luminescent 2D material and color centers in diamond	93
8. Conclusion and Outlook	103
8.1. Materials for sensing applications	104
8.2. Optimized nanofabrication processes	106
8.3. Novel applications	108
8.4. Outlook	109
A. Supplementary informations	113
A.1. Chap. 2: Color center fluorescence and spin manipulation in single crystal, pyramidal diamond tips	113
A.2. Chap. 3: Toward wafer-scale diamond nano- and quantum technologies . .	118

1. Introduction

The breakthrough discoveries and theoretical descriptions of the photoelectric effect and the black-body radiation as well as the introduction of quanta started the first quantum revolution in the 20th century. This established new laws in form of quantum mechanics to describe the physical properties of atoms, solids and electro-magnetic fields. The understanding of the basic concepts of these new laws enabled the development of many technologies relevant for our modern society: For instance, the fundamental understanding of light matter interaction lead to the establishment of solar cells as well as to the development of lasers. But the first quantum revolution only enabled the understanding of quantum mechanics [1] while new developments in the 2000s allowed the active employment of quantum mechanics as a resource for novel applications. These findings initiated the second quantum revolution, where scientists found ways to actively create coherent superpositions or entanglement of quantum states.

The progress made in the last decades is pioneering the development of novel technologies like quantum computers [2–6], quantum cryptography [7–9] or quantum optics [10–13]. The later, for instance, lead to the disproof of Einstein’s view on quantum mechanics from 1935 [14, 15]. For most of these quantum-based applications, reliable sources of single photons are mandatory. In particular, the deterministic on-demand creation of photons is of major interest. Quantum photonics was used to optimize the properties of single photons and their collection efficiency [16–18]. To eventually design a quantum network comparable to the established internet, extensive quantum engineering is necessary [19]. While different quantum systems can act as e.g. memories like atomic ensembles [20, 21] or as repeaters [22], single photons are optimal to be used as qubits to entangle different nodes in the network [23, 24].

In general, single photons and quantum coherence represent the base onto which the backbones of the second quantum revolution are built. In addition to the above mentioned fields, quantum sensing and metrology is of major interest for a variety of novel applications leading to a better understanding of the microscopic properties of material systems, atoms and spins as well as processes in living cells. Most of these applications require extraordinary spatial resolutions and sensitivities. Especially color centers in diamond are promising quantum systems to fulfill these requirements while they are able to sense electric [25], magnetic [26] and optical near fields [27] as well as strain [28] and temperature [29]. In this thesis, we focus on the nitrogen vacancy (NV) center in diamond.

The NV center in diamond, which will be further introduced in Sec. 1.1, offers a remarkable applicability as a quantum sensor [26]. Here, we distinguish between ensemble and single center applications: First, we start with the NV ensemble which is extraordinary useful in wide-field applications like e.g. monitoring the activity of electrical and integrated

circuits [30, 31], imaging magnetic nanoparticles inside living cells [32] or characterizing fundamental material properties as crystal stress in diamond [33]. In addition, ensembles were used to study the fundamental properties of the NV centers' spin resonances. For instance, the influence of an external electric field onto the coherence properties of the spin resonances was used to confirm the lack of inversion symmetry of NV centers in diamond [34]. Due to the large number of involved NV centers with different orientations in the ensemble, it is possible to reach even sub-pT sensitivity [35], to extract the vectorial components of magnetic fields [36] and to use the NV ensemble as a radio frequency spectrum analyzer [37]. Here, often nanometer-thin layers of NV centers close to the surface of diamond are used to investigate the properties of a sample placed on top of the diamond with a good spatial resolution. However, this resolution is mainly limited by diffraction (i.e. the point spread function) of the used setup.

To overcome this limitation, it is necessary to use single NV centers in diamond. Due to the atomic size of a single center, the spatial resolution is only limited by the distance between the NV center and the sample under investigation. Using single NV centers in bulk single crystal diamond or nanocrystals opens up new possible applications like e.g. the usage of the NV center as a magnetic field probe to image and detect magnetic resonances (MRI and NMR) [38–40] and to measure magnetic fields on the nanoscale [41]. Further, it is possible to image the magnetic field of a single electron spin in ambient conditions [42]. Additionally, by bringing samples or particles close to a NV center embedded in bulk material, it is possible to image the magnetic resonances of the particles [43–46] and to study ballistic transport in metals [47] as well as spin waves [48]. In addition, using single NV centers as quantum sensors also draws interest of other communities like life sciences [49]. Here, especially the chemical inertness and non-toxicity of diamond is favorable for the insertion of NV centers into a living cell for e.g. bio-labeling [50], to remotely monitor chemical processes in the cells [51], for particle tracking [52] and in vivo temperature measurements [53].

In recent years, near-field interactions in form of an energy transfer between two close dipoles have become a commonly used tool to study processes in biological environments in life sciences [54–56]. This interaction is called Förster Resonance Energy Transfer (FRET). By bringing two dipoles in close proximity of a few nanometer, it is possible that a donor dipole transfers its energy non-radiatively to an acceptor dipole. The main requirement for an efficient transfer is a significant spectral overlap between the donor's emission and the acceptor's absorption bands. By exploiting the strong $1/\text{distance}^6$ -dependency of the interaction, it is possible to use FRET for superresolution imaging of dipoles. Despite the common usage of FRET in life science applications, the effect remains almost unexploited in the quantum sensing community. However, due to the broad emission spectrum of the NV center in diamond it is possible to find a variety of potential FRET partners rendering FRET a viable resource for sensing applications in general. At the beginning of this decade, there were some first experiments using FRET to establish an interaction between NV centers and molecules or graphene [27, 57]. These attempts used NV centers in nanocrystals attached to a scanning probe tip to study the interaction. While NV centers in nanocrystals might suffer from a bad surface of the nanocrystals and a limited quantum

efficiency, using NV centers in single crystal diamond should lead to stable NV centers with a potentially unity quantum efficiency and a reliable control of the NV-sample-distance. However, the usability of NV centers in single crystal diamond for FRET was not demonstrated yet.

One promising approach to harness the full potential of the NV center for sensing applications uses high-purity single crystal diamond while the NV center's surrounding is structured to form a photonic nanostructure in a complex top-down approach. These structures are usable as scanning probe tips [58] in an atomic-force microscope as proposed by Chernobrod and Berman in 2005 [59]: Here, especially the photonic enhancement of the photoluminescence as well as the good coherence properties due to the low density of impurities in the material aids to increase the achievable sensitivity [17, 60, 61]. Here, the tip-like geometry of the structure and the ability to approach a shallow NV center embedded in the structure to a sample surface enables high spatial resolution sensing in the sub-100 nm-regime [58]. This initiates completely novel applications for NV center-based sensing like, for example, imaging magnetic structures like vortices or domains and domain walls [62–68], characterizing magnetic properties of thin films [69–71] or by using a NV center at cryogenic temperatures to image superconductors and superconducting vortices [72–75]. Further, NV centers used as scanning probe tips were used to image currents [76] and magnetic resonances on the nanoscale [77].

While single crystal diamond scanning probes are highly promising for high-resolution and -sensitivity sensing, a persistent challenge in this approach is the complex, multistep process to fabricate such nanostructures (see Sec. 1.2). Here, especially the yield of the fabrication has to be optimized by using reliable processes and suitable diamond material. In this thesis, we will show routes to overcome these challenges. The progress we achieved is summarized in Fig. 1.1. First, we worked on the scalability of NV-based sensing by investigating novel material systems. We started by investigating commercially available single crystal diamond scanning probe tips with a pyramidal shape. Here, the tips were formed in a bottom-up approach by growing the diamond pyramids in a chemical vapor deposition process. This will be the topic of Chap. 2 published as Ref. [78]. Afterwards, we studied the properties of a wafer-sized single crystal diamond based on the successful scaling of heteroepitaxial nucleation during chemical vapor deposition. Here, we found single native NV centers which we exploited to characterize the material's suitability as a host for NV-based scanning probe devices (see Chap. 3 published as Ref. [79]).

As we found promising new material systems usable for sensing applications, we worked on the optimization of the nanofabrication procedure. Here, we mainly followed two approaches: First, we optimized the reliability of the fabrication. We used silicon as a thin adhesion layer for the etch mask and sophisticated plasma etching of the structures. This will be introduced in Chap. 4 published as Ref. [80]. Second, we studied the influence of the plasma treatment on shallow NV centers in the diamond. Here, we focused on the comparison of different plasma treatments to remove mechanical stress due to polishing the diamond surface. By implementing novel unbiased plasmas in our process, we found stable shallow NV centers in nanostructures promising for sensing applications (see Chap. 5 published as Ref. [81]).

Building a diamond sensor

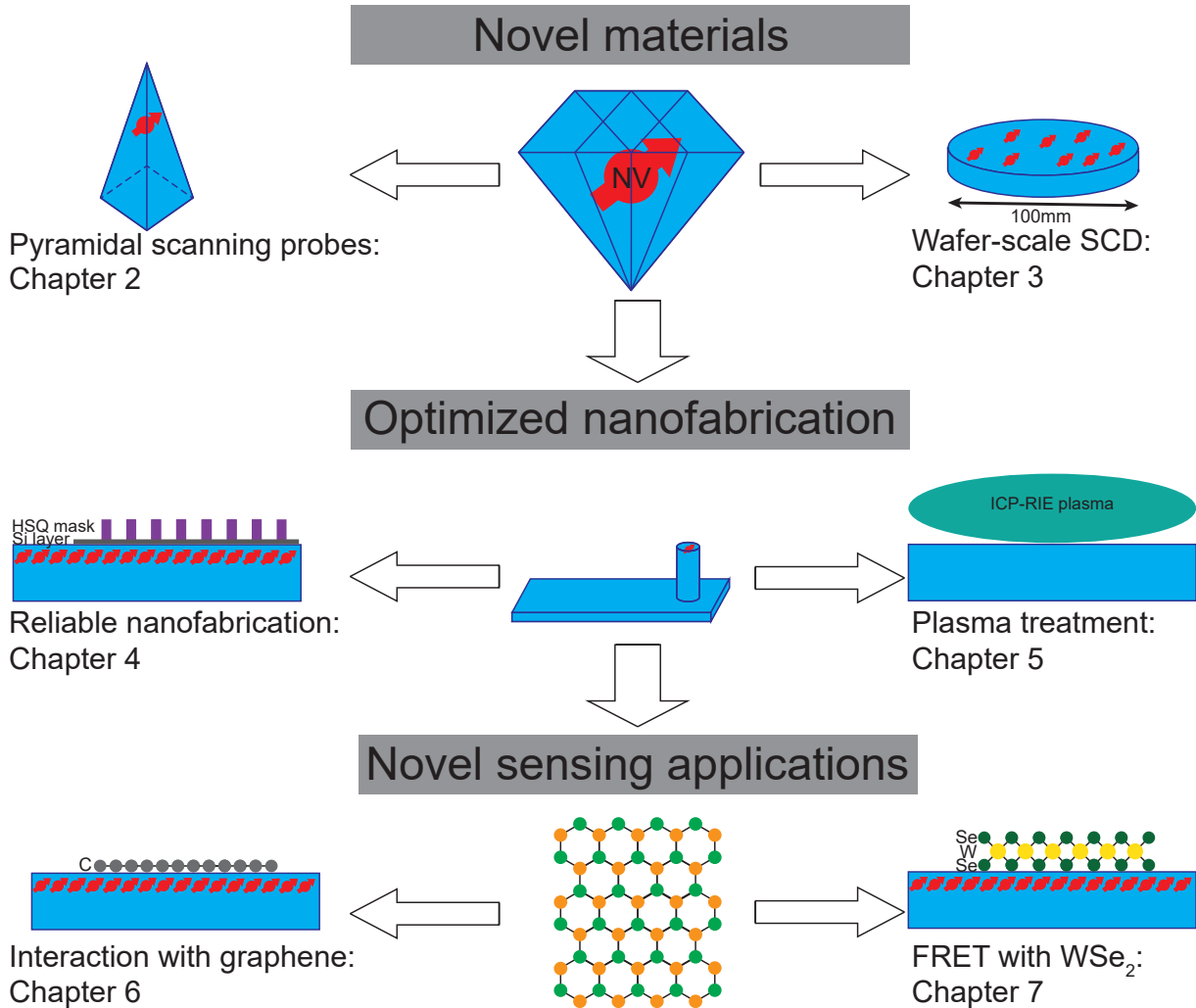


Figure 1.1.: Schematic representation of the topics with their respective occurrence in this thesis. We worked on all steps needed to improve the scalability and reliability of the nanofabrication process needed to build a NV-based diamond sensor. Further, we introduced a novel sensing resource for NV centers in single crystal diamond in form of near-field interaction, namely FRET, promising for a variety of applications.

Exploiting near-field interaction as a resource for sensing would enable a new functionality for NV centers in single crystal diamond. To investigate their usability for applications based on near-field interaction, we first performed a proof-of-principle experiment: By applying graphene on a diamond containing a shallow NV ensemble, we were able to study the quenching of the NV center's photoluminescence induced by the interaction. This will be part of the topical review in Chap. 6 published as Ref. [82]. After successfully demonstrat-

ing the suitability of NV centers as a donor for FRET processes via the interaction with graphene, we wanted to further evaluate the interaction. Here, we transferred a monolayer of a luminescent two-dimensional material, namely WSe₂, on the surface of a diamond containing shallowly implanted NV centers. By investigating the properties of the NV ensemble undergoing FRET with flakes of WSe₂, we found an outstanding novel feature of the NV center: as the NV center was able to retain its capability to sense magnetic fields while interacting with WSe₂, NV centers can be used as a multifunctional sensor. This will be described in Chap. 7 published as Ref. [83].

In Chap. 8, we shortly discuss and summarize the results of the publications included in this thesis. In addition, we will give a brief outlook on potential future applications of the NV center in single crystal diamond as a quantum sensor.

As some basic concepts as well as details of the experimental setup have been omitted for brevity in the manuscripts that form the main body of this thesis, we briefly summarize these in the following. We will give a short introduction to the NV center in diamond in Sec. 1.1. Afterwards, we will summarize the process needed to fabricate scanning probe devices in Sec. 1.2. Sec. 1.3 will introduce the experimental setups and methods in detail.

1.1. NV centers in diamond

The NV center is an optically active defect center consisting of a nitrogen atom and a neighboring vacancy within the diamond lattice. The NV center is oriented along one of the equivalent $\langle 111 \rangle$ crystal axes defining the quantization axis, and belongs to the C_{3v} symmetry group [84]. There are mainly two approaches to incorporate NV centers into the diamond. First, it is possible to incorporate nitrogen vacancies directly during the growth process of the diamond in a chemical vapor deposition (CVD) reactor or in a High Pressure High Temperature (HPHT) synthesis by creating substitutional nitrogen which can then be used to create NV centers. The main drawback hereby is to precisely control the lateral placement of the NV centers in the diamond itself. While most of these techniques suffer additionally from an insufficient control of the depth distribution of the NV centers, there are some promising approaches using complex δ -doping processes during the growth of the diamond [85]. However, implanting nitrogen into an ultra-pure diamond lead to a better positioning of the centers potentially down to nanometer resolution by using pierced AFM tips [86], nanomasks [87] or focused electron irradiation [88]. By subsequently annealing the diamond above 600 °C, the vacancies generated during the implantation can diffuse in the lattice towards substitutional nitrogen and then form the NV color center.

The nitrogen vacancy center in diamond can occur in different charge states: While the positively charged NV⁺ is non-fluorescent and is only accessible under enormous experimental effort [89], the neutral and negatively charged NV center offers radiative transitions between discrete energy levels in the large bandgap of diamond. It is possible to spectrally distinguish between both optical active charge states because of their different spectral po-

sitions. While the purely electronic transition from the excited to the ground state, termed zero-phonon line (ZPL), of the NV^0 lies at 575 nm, the ZPL of the NV^- lies at 637 nm. Both charge states have in common that they have a strong interaction with lattice vibrations leading to a broad phononic sideband with a width of more than 100 nm [see Fig. 1.2 a)].

Due to its extraordinary capabilities for sensing applications, we focus in the following on the negatively charged NV center which will be termed NV center in the following for simplicity. We will start by further discussing the electronic structure of the color center. To describe the NV center in diamond, it is necessary to consider six electrons: two from the nitrogen atom and three from each of the dangling bonds of the carbon atoms surrounding the vacancy. The sixth electron can be acquired from the vicinity of the NV center, most likely from nearby substitutional nitrogen. This results in an overall spin of 1. The electronic configuration, as depicted in Fig. 1.2 b), gives rise to two triplet states ($^3\text{A}_2$ for the ground state and ^3E for the excited states) with two singlet states (^1E for energetically lower state and $^1\text{A}_1$ for the higher state) in between. While the transition between the ground and excited state results in the ZPL at 637 nm, the radiative transition between the two singlet states give rise to the infrared ZPL at 1042 nm [90] [solid lines in Fig. 1.2 b)] which only offers a quite weak intensity compared to the optical transition due to strong competitive non-radiative decay channels [84] [dashed line between ^1A and ^1E in Fig. 1.2 b)].

The ground and excited state splits into two spin sub-levels $m_s = 0$ and $m_s = \pm 1$ separated by a zero field splitting of $D_{gs} = 2.87$ GHz and $D_{es} = 1.42$ GHz mainly due to spin-spin-interaction. By applying an external magnetic field, the degeneracy of the spin states $m_s = \pm 1$ is lifted by the Zeeman effect. The splitting of these two transitions is given by $2\gamma_{\text{NV}}B_{\text{NV}}$ where B_{NV} is the magnetic field projection onto the NV quantization axis and $\gamma_{\text{NV}} = 2.8$ MHz/G is the gyromagnetic ratio of the NV center.

The import role for sensing applications is given by the special dynamics of the NV center's excited state: While the transition from ground to excited state is highly spin preserving, the decay of the excited state is spin dependent: As represented by the dashed lines from the excited state to the singlet state system in Fig. 1.2 b), the $m_s = 0$ excited state has a high probability to decay back into the $m_s = 0$ ground state with a lifetime of 12 ns, whereas the $m_s = \pm 1$ excited state has a higher probability to decay non-radiatively into the single state system. This additional non-radiative decay channel results in a shorter lifetime of 7.8 ns [91]. The population of the singlet states decays (potentially emitting an infrared photon) to the lower singlet state with a lifetime of several hundreds of nanoseconds [92]. Here, the non-radiative transition from the lower singlet state to the ground state manifold is slightly preferential into the $m_s = 0$ spin state [84]. Because of the optical cycling of the $m_s = 0$ state and the dynamics of the $m_s = \pm 1$ excited state as well as the singlet state system, it is possible to polarize the NV center into its $m_s = 0$ ground state after a few optical cycles with a fidelity of up to 95% [93]. In addition, these different probabilities for the transition to the long lived singlet system in the excited state lead to a spin-dependent optical emission rate and thereby gives an opportunity to efficiently distinguish between $m_s = 0$ and $m_s = \pm 1$ by comparing the integrated fluorescence signal

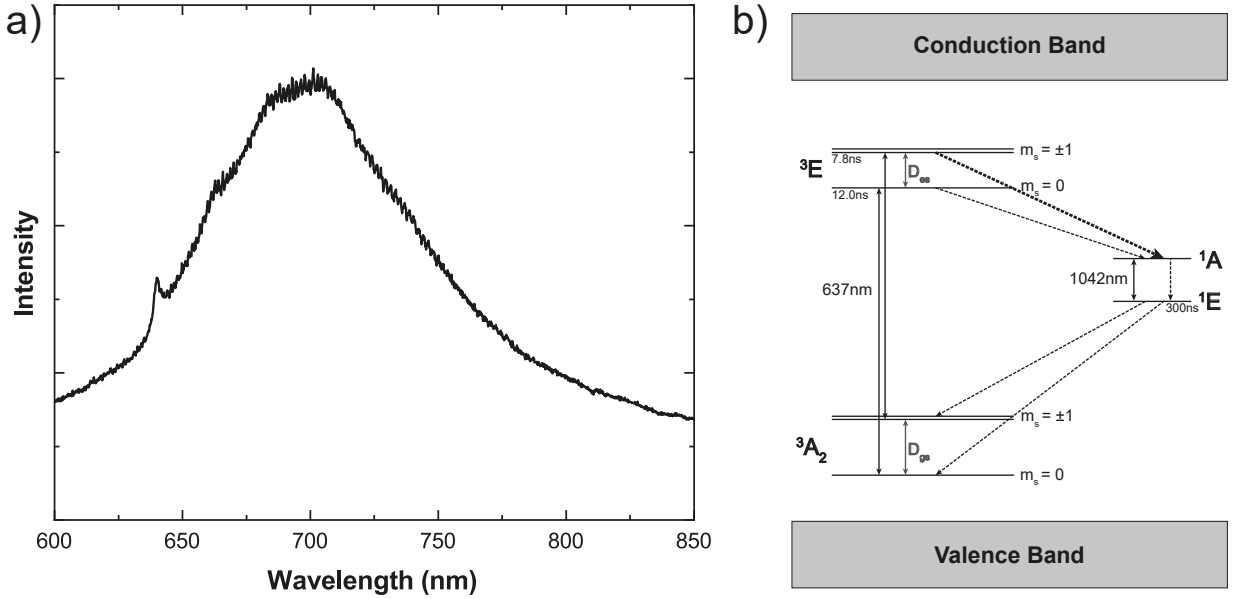


Figure 1.2.: a) Emission spectrum of the negatively charged NV center in diamond. A clear ZPL at 637 nm as well as the broad phononic sideband are visible. b) Electronic structure of the NV⁻ center in diamond. The zero field splitting of the spin-levels is $D_{gs} = 2.87$ GHz for the ground state and $D_{es} = 1.42$ GHz for the excited state, respectively. The solid lines indicate radiative transitions, while the dotted lines indicate non-radiative transitions. Here, the transition from the $m_s = \pm 1$ -excited state to the singlet states is stronger than from the $m_s = 0$ state leading to a spin-dependent fluorescence as described in the text.

upon optical excitation.

In addition, this readout can be used to measure the above mentioned splitting of the ground state spin states. By applying a magnetic field at a microwave frequency and sweeping its frequency, it is possible to induce spin flips when the microwave frequency matches the transition frequency between the $m_s = 0$ and the $m_s = \pm 1$ states. These spin flips lead to a reduction of the overall fluorescence rate when the NV is continuously excited. This is called optically detected magnetic resonance [ODMR, see Fig. 1.3 a)]. When a magnetic field is applied on axis and thereby the degeneracy between the $m_s = \pm 1$ states is lifted, two resonances can be detected when sweeping the microwave frequency. This can be used to evaluate an unknown magnetic field quantitatively.

The main measure for the performance of a sensor is its sensitivity η which describes the minimal magnetic field that can be detected in a time T . Thus η describes the smallest magnetic field strength which can be sensed in 1 s with a signal-to-noise ratio (SNR) of 1. In general, the intensity I of a NV center during an ODMR measurement can be described as

$$I(f) = I_0 \cdot \left[1 - C\mathcal{F} \left(\frac{f - f_{\text{NV}}}{\Delta f} \right) \right] \quad (1.1)$$

with the average intensity I_0 , the ODMR contrast C , the driving microwave frequency f , the resonance frequency f_{NV} and the full width at half maximum Δf of the NV center's spin resonance as well as the line shape profile \mathcal{F} of the resonance. As any fluctuation of the field strength leads to a shift of the resonance frequency the sensitivity depends on the minimum intensity difference depending on the resonance frequency $|\delta I/\delta f|$ which can be detected. This leads to a sensitivity

$$\eta = \frac{h}{g\mu_B} \frac{\sqrt{I_0}}{\max\left(\left|\frac{\delta I}{\delta f}\right|\right)} \approx \mathcal{P}_{\mathcal{F}} \frac{h}{g\mu_B} \frac{\Delta f}{C\sqrt{I_0}} \quad (1.2)$$

with the numerical parameter $\mathcal{P}_{\mathcal{F}}$ related to the specific lineshape \mathcal{F} of the resonance. Thus, the sensitivity mainly depends on the photon shot noise $\sqrt{I_0}$ as well as the contrast C and the linewidth Δf of the resonance. Hereby, the linewidth is fundamentally limited by the inhomogeneous dephasing rate $\Gamma_2^* = 1/T_2^*$ of the NV center's electron spin which is defined by the surrounding spin bath.

Under continuous excitation from the exciting laser and the microwave frequency, this fundamental limit can not be reached due to power broadening. In addition, the contrast C also depends on the laser as well as the microwave power impinging the NV center [94]. To describe the functional connection, we first need to introduce the saturation parameter $s = P_{\text{exc}}/P_{\text{sat}}$ given by the ratio between the excitation power and the saturation power which will be further introduced in Sec. 1.3 and the Rabi frequency $\Omega_R = g\mu_B B_{\text{MW}}/\hbar$ depending on the amplitude of the incoming microwave field B_{MW} . Therewith it is possible to calculate the ODMR contrast

$$C = \Theta \frac{\Omega_R^2}{\Omega_R^2 + \Gamma_p^\infty \Gamma_c^\infty \left(\frac{s}{1+s}\right)^2} \quad (1.3)$$

with a normalization factor Θ , the polarization rate Γ_p^∞ defined as the inverse combined lifetime of the singlet system and the optical cycling rate Γ_c^∞ defined by the inverse excited state lifetime [94]. As both rates Γ_p^∞ and Γ_c^∞ are constant for a given NV center, it is visible that for a fixed B_{MW} the contrast increases with decreasing optical power and for a fixed optical power the contrast increases with increasing microwave power. For strong microwave power the contrast saturates towards Θ . Under power broadening, the resonance has a Lorentzian profile with the linewidth Δf depending on the optical and microwave power [94]

$$\Delta f = \frac{\Gamma_c^\infty}{2\pi} \sqrt{\left(\frac{s}{1+s}\right)^2 + \frac{\Omega_R^2}{\Gamma_p^\infty \Gamma_c^\infty}} \quad (1.4)$$

With these expressions for the contrast and the linewidth, it is possible to find a Rabi frequency which optimizes the sensitivity η for continuously measured ODMR at a fixed excitation power [94]

$$\Omega_{R,opt} = \sqrt{2\Gamma_p^\infty \Gamma_c^\infty} \frac{s}{1+s} \quad (1.5)$$

To harness the full potential of the NV center in diamond in terms of sensitivity and therewith sensing capability, one approach can be to improve the photoluminescence (PL) rate and therewith the photon shot noise of the NV centers by embedding them into optimized photonic nanostructures (see Sec. 1.2) [64]. Additionally, it is possible to use more complex measurement schemes developed in nuclear magnetic resonance (NMR) to further optimize the coherence of the NV center. Hereby, a two level system is coherently manipulated while its states interact with a magnetic field. Here, different pulsed manipulation protocols have to be applied to increase the sensitivity.

The basic coherent spin manipulation is to drive Rabi oscillations, which is shown in Fig. 1.3 b). By applying a magnetic field, we are able to select one of the spin transitions.

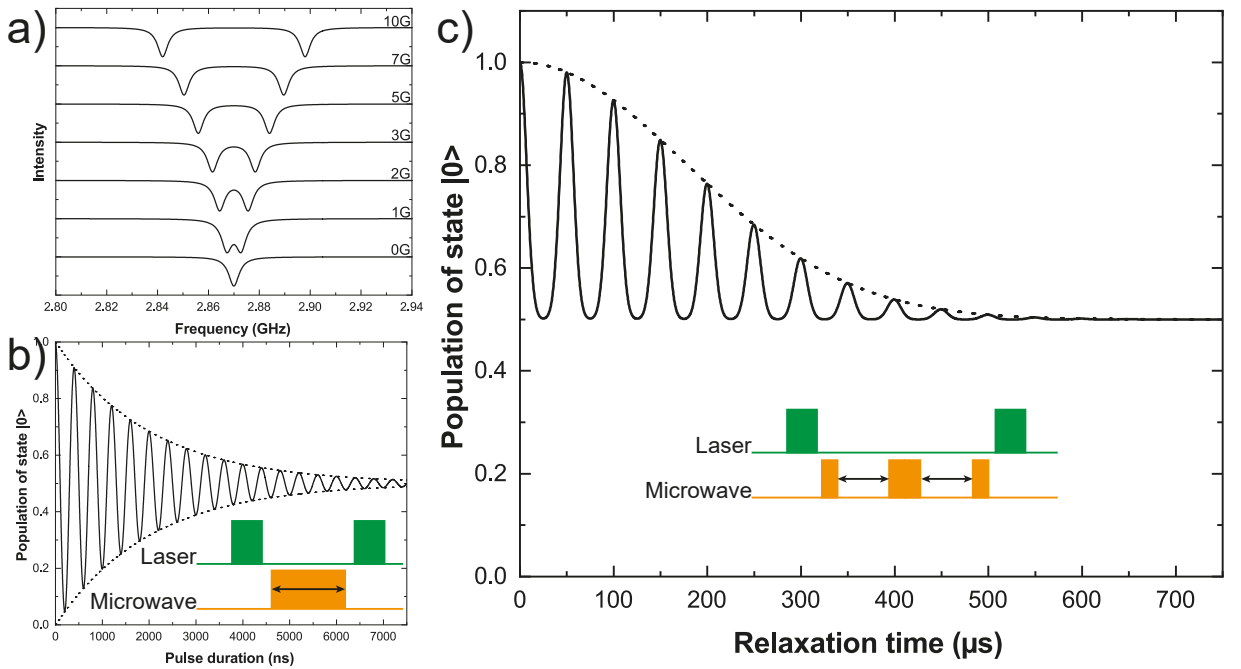


Figure 1.3.: a) Optically detected magnetic resonance for different applied magnetic fields. A clear splitting of the resonances is visible. b) Rabi oscillations on the transition $|0\rangle \rightarrow |1\rangle$. The oscillation is damped due to decoherence effects. The pulse sequence is shown as the inset. c) Spin-Echo measurement (see inset for the full pulse sequence) with spin revivals induced by the Larmor precession of near ^{13}C nuclear spin. The envelope of spin revivals yields the coherence time T_2 of the NV center.

Here, we use a magnetic field oscillating at the transition frequency between the $m_s = 0$ and $m_s = 1$ ground states with different pulse durations. This pulse changes then the amplitude of the spin states by coherently rotating the spin from $m_s = 0 \equiv |0\rangle$ towards $m_s = 1 \equiv |1\rangle$. By extending the pulse duration, the population oscillates following a cosine between both spin states. This oscillation is damped due to a complex dependency of different parameters like the coherence time of the NV center and the driving conditions of the oscillation. However, the important parameter of the Rabi oscillation is its frequency and especially the so-called π -pulse duration describing the pulse duration for which a full

spin flip occurs. This is important to further characterize the coherence time T_2 of the NV center via a Spin-Echo measurement [see Fig. 1.3 c)]. Here, we first bring the NV center's spin state in an equal superposition

$$\frac{1}{\sqrt{2}}(|0\rangle + |1\rangle) \quad . \quad (1.6)$$

We then allow the NV center to relax for a given time $\tau/2$ acquiring a phase caused by magnetic fields in the surrounding. Subsequently, applying a π -pulse lead to a swap of the phases of the eigenstates. Afterwards, a second relaxation time $\tau/2$ followed by a read-out pulse cancels the accumulated phase caused by slowly varying magnetic fields in the first relaxation time. This leads to a final superposition which is insensitive to static magnetic fields. The full pulse sequence is shown as an inset in Fig. 1.3 c). The read-out signal $I(\tau)$ can then be derived as [58,95]:

$$I(\tau) \propto \exp \left[- \left(\frac{\tau}{T_2} \right) \right]^n \sum_0^j \exp \left[- \left(\frac{\tau - j \cdot \tau_R}{T_{Dec}} \right)^2 \right] \quad (1.7)$$

Here, we use τ_R as the revival period of the Larmor precession of the ^{13}C nuclear spin near the NV centers and T_{Dec} as the correlation time of the ^{13}C nuclear spin bath. n is depending on the specific decoherence process. On the one hand, Spin-Echo measurements yield the T_2 coherence time of the NV centers but on the other hand they sense alternating magnetic fields. The sensitivity is hereby further depending on the contrast C , the mean intensity I_0 and the spin read-out time t_L [63]:

$$\eta_{AC} = \frac{\hbar}{g\mu_B} \frac{1}{C\sqrt{I_0 t_L}} \frac{1}{\sqrt{T_2}} \quad (1.8)$$

For shallow, single NV centers in nanofabricated structures as described in the following section, the sensitivity reaches the $\text{nT}/\sqrt{\text{Hz}}$ -regime [58].

While the above described sensing approaches are based on the spin properties of the NV center, we now want to describe attempts using the dipole of the NV center in other words the optical transitions for sensing applications. Here, we employ the near-field interaction of NV centers with other dipoles, namely Förster Resonance Energy Transfer (FRET). In general, FRET describes a process where a donor dipole transfers its energy non-radiatively to an acceptor dipole. The transfer efficiency E_{FRET} scales with the distance d between the dipoles as [27, 57, 83]

$$E_{FRET} = \left(\frac{R}{d} \right)^n \quad (1.9)$$

with the FRET radius R describing the distance where the FRET efficiency is 50% and the power n depending on the nature of the participating dipoles. For instance, two point-like dipoles like e.g. a NV-dye molecule pair lead to $n = 6$ while a point-like dipole and a two-dimensional dipole like e.g. a NV-WSe₂ or NV-graphene pair lead to $n = 4$ [27]. The main requirement for FRET is a spectral overlap between the donor's emission and the

acceptor's absorption band. In addition, the FRET radius depends on other parameters like the quantum efficiency of the donor and both dipole moments. FRET creates an additional non-radiative decay channel for the donor leading to a shorter effective excited state lifetime $\tau_{eff} = 1/\gamma_{eff}$ of the donor. Typically, the lifetime changes induced via efficient FRET are readily observable with our homebuilt confocal setup which will be described in Sec. 1.3:

$$\gamma_{eff} = \gamma_R + \gamma_{NR} = \gamma_R + \gamma_R \cdot \left(\frac{R}{d}\right)^n \quad (1.10)$$

with the decay rates γ_R and γ_{NR} for the radiative and non-radiative decay, respectively. Due to the strong distance-dependency, FRET is a viable novel approach for nanoscale imaging of e.g. molecules [57] or for the characterization of novel materials [83].

1.2. Nanofabrication

As introduced in Sec. 1.1, enhanced PL rates of NV centers optimize the sensitivity and therewith their usability in sensing applications. This can be achieved by sculpting the diamond into photonic structures. A promising approach is to structure cylindrical nanopillars as they potentially enhance the PL rate by a factor of > 5 [17, 61, 64]. Here, the nanopillar acts as a waveguide leading to a better collection of the emitted photons. To fabricate such structures, we start with a cleaned diamond substrate onto which a silicon adhesion layer is deposited (see Chap. 4). Afterwards, we spin-coat hydrogen silsesquioxane (HSQ) electron beam resist onto the diamond surface. By using electron beam lithography we form etch masks. Afterwards, the pillars are etched in an inductively coupled plasma reactive ion etch (ICP-RIE) process (see Chap. 4 and 5 for a detailed description of the process). Due to the anisotropic nature of the plasma, it is possible to etch close to cylindrical pillars with very steep sidewalls ($\leq 5^\circ$) [61].

To use the nanopillars for applications where a good spatial resolution is needed, it is necessary to approach the NV center in the pillar to a distance of several nanometer to the investigated sample. Here, using the pillar-structures as a scanning probe tip analogous to an atomic-force microscope (AFM) is of major interest [64]. The main challenge hereby is to integrate the pillar into the AFM. We address this challenge by first etching cantilever-like platforms into the diamond and then pillars onto the platforms. Afterwards, it is necessary to thin down the diamond until the platforms are free standing. This is achieved by etching the diamond from the backside. The freestanding devices are schematically depicted in Fig. 1.4. We glue the free-standing platform to quartz micro-capillaries [see Fig. 1.4 and 1.5 c)] which are then attached to the AFM head [64]. Using such approaches, it is possible to control the geometry of the diamond scanning probes. However, typical (high bias) ICP-RIE plasmas potentially damage the surface of the diamond [96]. Motivated by the potential damage, we study the influence of bias-free plasmas on the NV centers' stability and coherence (see Chap. 5).

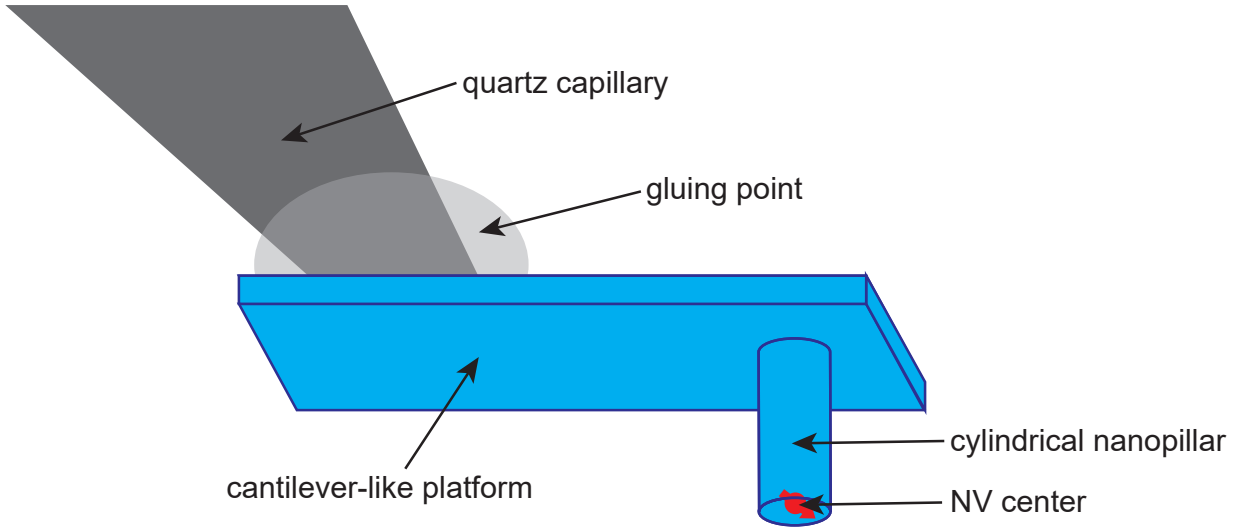


Figure 1.4.: Schematic image of the nanofabricated structure. Here, the shallow NV center is embedded in a cylindrical nanopillar usable as a scanning probe tip. To use these devices in an AFM, it is necessary to glue them to a quartz micro-capillary which is attached to an AFM head.

1.3. Experimental setup and methods

To harness the full potential of NV center sensing with good sensitivity and nanoscale spatial resolution, it is necessary to combine confocal microscopy and AFM [62]. While force feedback keeps the NV center close to the sample surface during scanning, we evaluate the NV center's spin dependent fluorescence to sense magnetic or electrical fields. To further study the near-field interaction of the NV centers with nearby dipoles, we implement pulsed excitation and time-resolved PL detection. To realize the above described techniques, two dedicated confocal PL microscopy setups, one combined with AFM functionality, have been designed and built during this thesis.

As the functionality of the two confocal microscopes employed to perform the measurements in the publications is mainly identical, we here summarize the features of the combined confocal microscope/AFM setup. The AFM setup, depicted in Fig. 1.5 a), contains two six-axes movement stages: one for positioning the diamond tip in the focus of the confocal microscope (NV-scanner) and one for positioning and scanning the sample (sample-scanner). The stages have three piezoelectric steppers (attocube, $2 \times$ ANPx101, $1 \times$ ANPz101, controlled by ANC350) for coarse positioning and a three-axes piezoelectric scanner (attocube, ANSxyz100, amplified by ANC250) for fine positioning in the nanometer-regime. While the NV-scanner and the x- and y-axis of the sample-scanner are controlled with an analog voltage of a data acquisition system (National Instruments, PXIe-1073 with modules: PXIe-6612 for timing, PXI-6733 for analog output channels, PXI-6220 for multifunctional acquisition), we use a scanning probe microscopy (SPM) controller (attocube, ASC500) to control the z-axis of the sample-scanner and therefore the distance between the diamond

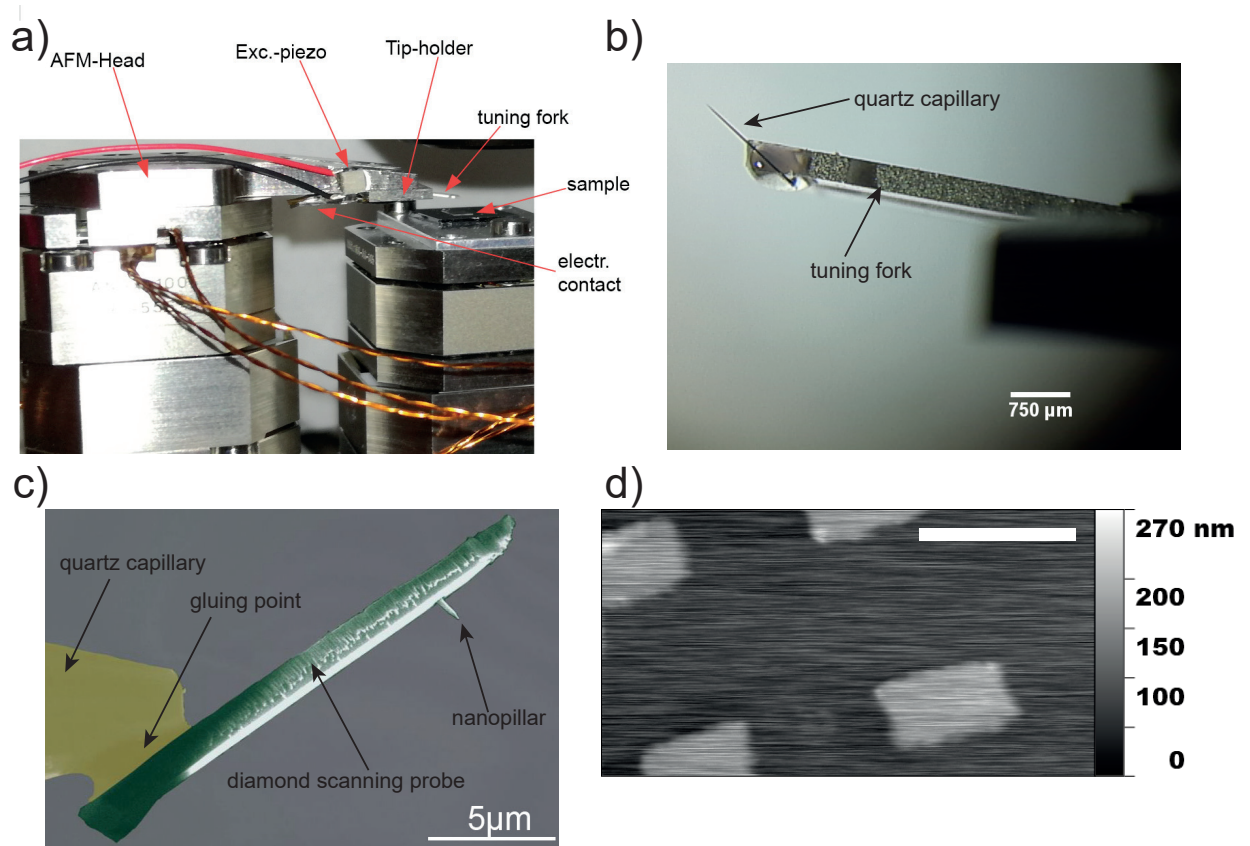


Figure 1.5.: AFM setup a) as described in the main text with zooms onto the tuning fork b) and a scanning electron image c) of the nanostructure attached to the quartz capillary. d) Exemplary measurement of an AFM test-sample in grid-geometry showing a nice depiction of the test structure. The white scale corresponds to $3\ \mu\text{m}$.

tip and the sample. Here, we establish force feedback by attaching the diamond pillar to a tuning fork [see Fig. 1.5b) and c)] where we use a dither-piezo at a defined frequency which excites oscillations of the tuning fork at its resonance. The tuning fork itself is made of quartz. To read out the response of the tuning fork, the piezoelectric effect is used. When the tuning fork oscillates, free charges are created which can be amplified and converted to a voltage signal (Femto, HQA-15M-10T, Amplification: $10\ \text{V/pC}$) measurable with the SPM controller. To control the distance between the diamond tip and the sample, we excite the tuning fork with a fixed amplitude and at a constant frequency. We chose a frequency in the slope of the resonance to optimize the gradient of the response of the tuning fork. While approaching the sample to the scanning probe tip, the resonance of the tuning fork shifts and therewith the voltage we read-out changes. While scanning, the AFM controller maintains a constant voltage signal (set point) from the tuning fork and thus keeps the distance between the diamond tip and the sample constant. Fig. 1.5d) shows an exemplary scan of an AFM test structure obtained with this setup. As described in Sec. 1.2, the diamond tips are attached to a quartz capillary [see Fig. 1.5 c)]. To perform

the measurements mentioned here, we glue the quartz capillary with the diamond tips to the tuning fork. Afterwards, we cut the capillary close to the gluing point to reduce the weight attached to the tuning fork. This is depicted in Fig. 1.5 b).

To detect the PL of NV centers, we bring them into the focus of our home-built confocal microscope (see Fig. 1.6). Here, we continuously excite the NV center with

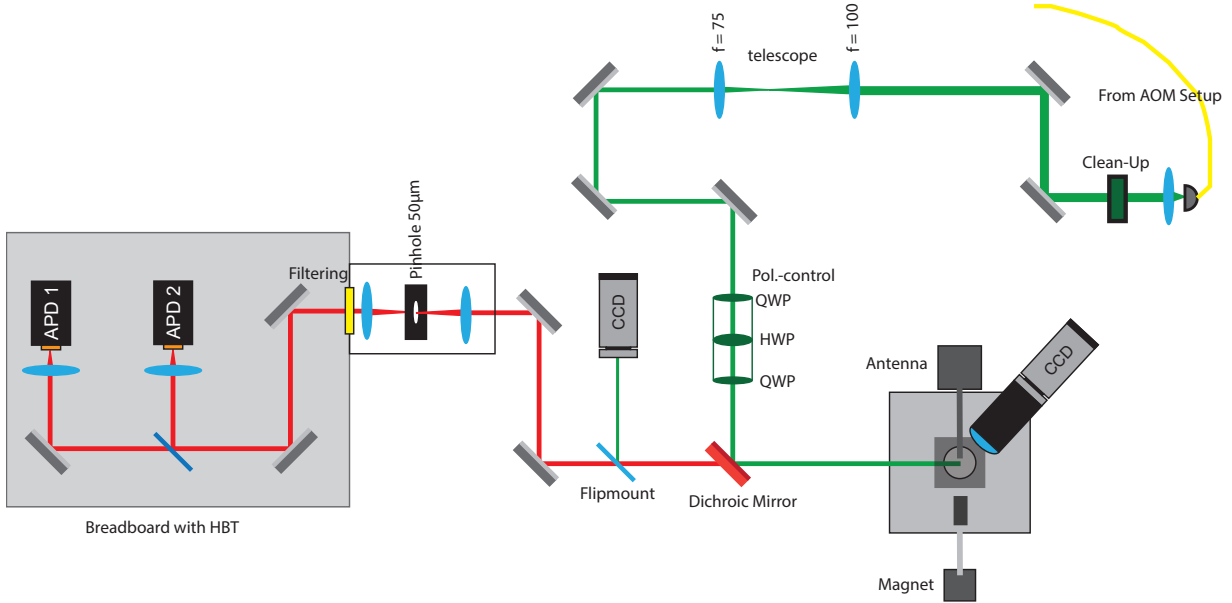


Figure 1.6.: Homebuilt confocal microscope to detect the photoluminescence of single NV centers in diamond. For details, see text.

a 532 nm diode-pumped solid-state (DPSS) laser (Laser Quantum, gem 532) or with a 594 nm DPSS laser (Cobolt, Mambo). The latter enables charge state detection of the NV center. To further realize pulsed excitation, we use an acousto-optic modulator (AOM; Crystal Technologies, 3200-146) with a rise-time of ≈ 13 ns in double-pass configuration for each laser system controlled by a TTL pulse generator (SpinCore, PulseBlasterESR-PRO). The excitation light is then focused onto the NV centers through a $100\times$ microscope objective (Olympus, LMPLFLN100X, numerical aperture: 0.8). We collect the PL of the NV centers focused on a $50\ \mu\text{m}$ pinhole to optimize the transmission of the setup. To separate the PL from the excitation light, we use a dichroic mirror (cut-in wavelength: 650 nm) and a 650 nm dielectric longpass filter. The collected PL is sent to either two highly-efficient photon counters (Excelitas SPCM-AQRH-14, quantum efficiency: $\approx 70\%$) in a Hanbury-Brown Twiss (HBT) interferometer setup or to a grating spectrometer (Princeton Instruments, Acton Spectra Pro 2500, Pixis 256OE CCD). To perform time-resolved PL analysis and lifetime measurements, we use a pulsed laser (NKT Photonics, EXW-12, pulse length: ≈ 50 ps) equipped with a dedicated filter system (NKT Photonics, SuperK Varia) tuneable from 450 nm to 850 nm as an excitation source and a single-photon counting time correlator (PicoQuant, PicoHarp 300). We model the instrument response function of the setup by a Gaussian function with a width of 326 ps. To perform ODMR measurements,

the setup is equipped with a microwave source (Stanford Research System, SG396) and a microwave amplifier (Mini Circuits, ZHL-42W+). The microwave is delivered through a movable near-field antenna [62] made out of a $25\ \mu\text{m}$ gold wire. The microwave circuit is also equipped with TTL-controlled switches (Mini Circuits, ZASWA-2-50DR+) enabling precise control of the microwave to coherently manipulate the NV center's ground state spin.

Next to standard confocal scanning, lifetime imaging and spin-manipulation of the NV centers, the setup is able to perform a variety of other measurements. First, an important characteristic of a NV center in a photonic structure is its PL saturation [see Fig. 1.7a)]. To investigate PL excitation, we measure the excitation power dependent PL rate of the NV center, which we model using:

$$I(P) = I_\infty \frac{P}{P + P_{sat}} + c_{BG}P \quad (1.11)$$

with the intensity I , the excitation power P , the saturation power P_{sat} and the maximum countrate of the NV center I_∞ . I_∞ indicates the performance of the photonic structure and $B = c_{BG}P$ estimates the background PL level of the NV center. Using equation 1.11, we optimize the signal S -to-background B ratio $s = S/(S + B)$, which is important for most measurements.

Another important characteristic of the NV centers is their photon statistics. This can

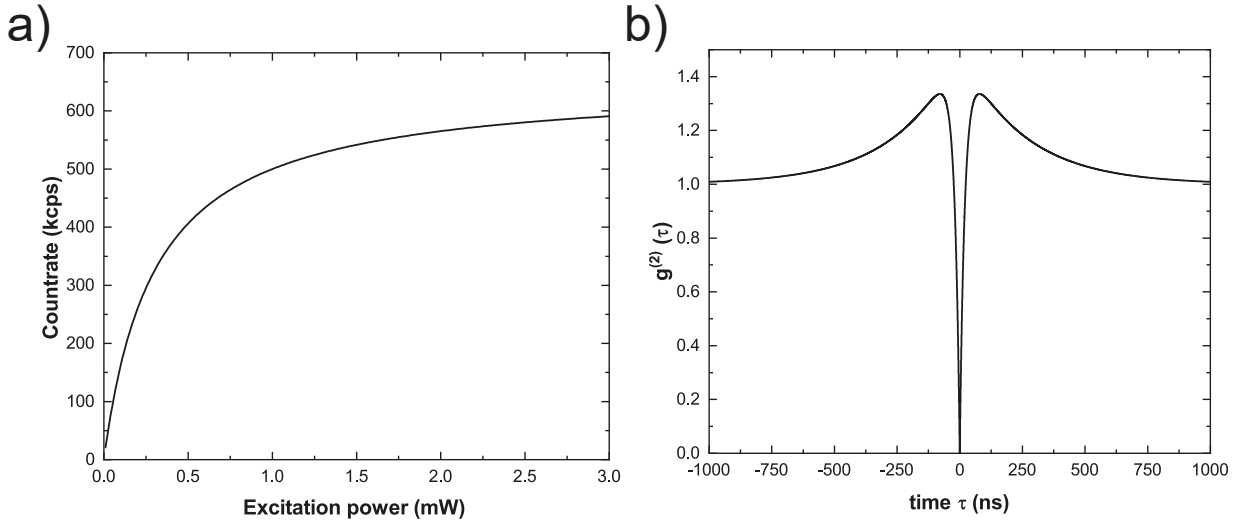


Figure 1.7.: a) Calculated saturation measurement for a single NV center in a photonic nanostructure. Here, $P_{sat} = 300\ \mu\text{W}$ and $I_\infty = 650\ \text{kcps}$ was used. b) Calculated $g^{(2)}$ -function for a single NV center with a strong influence of the third state but without any background fluorescence. Here, we used $a = 0.5$, $\tau_1 = 20\ \text{ns}$ and $\tau_2 = 250\ \text{ns}$.

be measured by time-correlating the collected photons in the HBT interferometer and calculating the second-order autocorrelation $g^{(2)}$ -function [see Fig. 1.7b)]. $g^{(2)}(\tau)$ is hereby

defined as

$$g^{(2)}(\tau) = \frac{\langle I(t)I(t+\tau) \rangle}{\langle I(t) \rangle^2} . \quad (1.12)$$

Here, $\langle \cdot \rangle$ indicates the time average of the intensity $I(t)$ at time t . By replacing intensities with number of photons $n(t)$, it is possible to rewrite $g^{(2)}(\tau)$:

$$g^{(2)}(\tau) = \frac{\langle n(t)n(t+\tau) \rangle}{\langle n(t) \rangle^2} \quad (1.13)$$

By introducing m as the number of single photon emitters, one can show

$$g^{(2)}(0) = 1 - \frac{1}{m} < 1 . \quad (1.14)$$

This reduction of correlation events for $\tau = 0$ is referred to antibunching. For a three level system with a shelving state in addition to the ground and excited state, which is the case for NV centers, $g^{(2)}(\tau)$ can be written as:

$$g^{(2)}(\tau) = 1 - (1 + a) \exp(-|\tau|/\tau_1) + a \exp(-|\tau|/\tau_2) \quad (1.15)$$

Hereby, the parameter τ_1 describes the anti-bunching timescale while τ_2 describes the bunching on intermediate time scales. a is given by the influence of the third state onto the population dynamics. It was shown experimentally that these parameters significantly depend on the excitation power compared to the saturation power [97–99]. By allowing a non-perfect signal-to-background ratio s , the measured $g^{(2)}$ -function $g_{meas}^{(2)}(\tau)$ is given by:

$$g_{meas}^{(2)}(\tau) = 1 + s^2 (g^{(2)}(\tau) - 1) \quad (1.16)$$

In particular, measuring $g^{(2)}(\tau)$ was important in Chap. 3 and 5. Here, we focus especially on measuring the properties of single NV centers rendering it necessary to characterize their photon statistics. Furthermore, we measured the PL saturation of NV centers in Chap. 2 and 5 to investigate the PL enhancement of the photonic structures used in the respective chapter.

Another important technique especially to study the near-field interaction of NV centers with a nearby dipole or to investigate the photonic environment is Fluorescent Lifetime Imaging (FLIM). Here, the lifetime of the NV center is measured on each position while scanning the sample. Here, we implemented advanced data evaluation techniques using dedicated Matlab codes to extract the lifetime. In the case of a spectral overlap of the emission of the NV center and the emission of the interacting dipole but distinguishable lifetimes, it is further possible to use pulsed excitation to increase the NV/dipole PL ratio by appropriate time-gating of the detection. This leads to a time-based filtering of the PL signal. Here, we typically use an integration time in the order of seconds to be able to clearly distinguish between both present lifetimes. However, it is possible to reduce the integration time to a few tens of millisecond in the case of pure NV center PL employing advanced approximation methods [100]. FLIM was used e.g. to evaluate changes in NV centers' lifetime caused by the photonic environment (see Chap. 2) and to characterize the interaction between a NV ensemble with other dipoles (see Chap. 6 and 7).

2. Color center fluorescence and spin manipulation in single crystal, pyramidal diamond tips

Richard Nelz, Philipp Fuchs, Oliver Opaluch, Selda Sonusen, Natalia Savenko, Vitali Podgursky, and Elke Neu

Applied Physics Letters **109**, 193105 (2016)
doi: 10.1063/1.4967189

The above stated manuscript discusses for the first time the usability of commercially available diamond scanning probe tips with a pyramidal shape for quantum sensing applications based on color centers in diamond.

Richard Nelz (R.N.) performed all measurements characterizing the nitrogen vacancy centers present in the material and evaluated all presented data. These measurements and their evaluation constitute the main body of the manuscript. Further, R.N. designed and realized the homebuilt confocal microscope that was used to characterize color centers in the material. The investigated diamond material was supplied by V. Podgursky, N. Savenko and the company Artech Carbon OÜ (Tallinn, Estonia). In addition, R.N. actively contributed to modeling the diamond tips via simulations to describe the photonic properties of the structures as well as verifying these simulations using appropriate measurements. To further study the interaction of the color centers in the material, R.N. developed a model estimating the density of color centers in different regions of the diamond tip. This model indicates the distance between centers explaining lifetime changes of nitrogen vacancy centers in the material. R.N. actively contributed to all discussions within the collaboration concerning conceiving and conducting experiments and evaluating data. Lastly, R.N. outlined and wrote the first draft of the manuscript as well as the supplementary material, designed all figures and actively contributed to all major revisions of the article.

Color center fluorescence and spin manipulation in single crystal, pyramidal diamond tips

Richard Nelz,¹ Philipp Fuchs,¹ Oliver Opaluch,¹ Selda Sonusen,¹ Natalia Savenko,² Vitali Podgursky,³ and Elke Neu^{1,a)}

¹Universität des Saarlandes, FR 7.2 Experimentalphysik, 66123 Saarbrücken, Germany

²Artech Carbon OÜ, Jõe 5, 10151 Tallinn, Estonia

³Tallinn University of Technology, Department of Materials Engineering, Ehitajate tee 5, 19086 Tallinn, Estonia

(Received 26 August 2016; accepted 24 October 2016; published online 7 November 2016)

We investigate bright fluorescence of nitrogen (NV)- and silicon-vacancy color centers in pyramidal, single crystal diamond tips, which are commercially available as atomic force microscope probes. We coherently manipulate NV electronic spin ensembles with $T_2 = 7.7(3) \mu\text{s}$. Color center lifetimes in different tip heights indicate effective refractive index effects and quenching. Using numerical simulations, we verify enhanced photon rates from emitters close to the pyramid apex rendering them promising as scanning probe sensors. © 2016 Author(s). All article content, except where otherwise noted, is licensed under a Creative Commons Attribution (CC BY) license (<http://creativecommons.org/licenses/by/4.0/>). [<http://dx.doi.org/10.1063/1.4967189>]

Sensitively measuring magnetic fields with high spatial resolution is of paramount importance for many applications in science and industry. Generally, sensing with nanometer resolution requires atomic sized sensors. Point defects in crystals (color centers) localize bound electrons on an atomic scale (<1 nm). Here, color centers in diamond, especially negatively charged nitrogen-vacancy centers (here termed NV centers), are very promising as they are photostable, show bright luminescence and highly coherent, controllable spins together with optically detected magnetic resonance (ODMR).¹ ODMR enables to read out spin states via luminescence, and thus even single centers can be used as low back action, quantum-enhanced sensors. Imaging magnetic fields using NV centers, e.g., contributed insights into superconductivity² or magnetic materials for spintronics.³ In life sciences, highly sensitive measurements of magnetic fields enable nuclear magnetic resonance detection even of single proteins.⁴

Employing scanning probe methods enables sensing with nanometer resolution (atomic force microscopy AFM).^{1–3,5} In essence, a nanostructure that reliably enables scanning embedded color centers in close proximity to a sample surface (tip-like geometry) is mandatory to fully harness the method's potential. Optimally, the structure also allows for efficient collection of the color center's fluorescence, consequently enhancing sensitivity. Top-down approaches sculpting scanning probe nanostructures from single crystal diamond⁵ produce stable probes with coherent spins and are thus preferred over approaches where nanodiamonds are attached to tips.³ However, such approaches require extensive efforts in nanofabrication.⁵ In contrast, bottom-up approaches form nanostructures during diamond growth that are often attached to the bulk diamond material and are not straightforwardly usable as scanning probes.⁶ An approach avoiding this problem is the growth of diamond pyramids detachable from the growth

substrate and transferable one-by-one to AFM cantilevers.⁷ AFM scanning probes using such pyramids are commercially available⁸ and might significantly broaden the application range of scanning probe imaging with color centers.

We here demonstrate the basic applicability of commercial single crystal, pyramidal AFM tips for magnetic sensing by showing coherent manipulation of *in-situ* created NV center spins in the devices. We investigate nature and origin of color centers in the tip and simulate how the pyramidal shape influences luminescence collection. Furthermore, we apply reactive ion etching to the tips, illustrating routes towards optimizing ready-to use devices for sensing via removal of diamond.

The single crystal diamond AFM tips from Artech Carbon are synthesized in a microwave plasma enhanced chemical vapor deposition (CVD) process based on a CH_4/H_2 gas mixture. Note that the same CVD technology is used for all tips from Artech Carbon. CVD is performed on silicon (Si) substrates pretreated with micron sized diamond powder to enhance the diamond nucleation density. Refs. 7 and 9 summarize details on fabrication of geometrically similar diamond tips using an alternative CVD technique. The parameters of our CVD process ensure that (100) facets grow slowest and thus with minimized defect density.⁷ In contrast, on lateral surfaces of crystals growing with (100) facets, highly defective, nano-crystalline diamond forms. As a consequence, pyramidal diamond micro-crystals with square, (100)-oriented basal planes evolve, which are embedded into the nano-crystalline material. Heat treatment in air entirely removes the latter and transferring the pyramids to AFM cantilevers becomes feasible.⁷ We note that the pyramids are mounted to the cantilevers using epoxy. The apex of the pyramid often has a radius of curvature of 2–20 nm, thus rendering these diamonds ideally suitable as ultra-hard AFM tips for high resolution topography imaging or nano-indentation measurements.

To investigate the topography of the pyramids, we record high resolution scanning electron microscopy (SEM)

^{a)}Electronic mail: elkneu@physik.uni-saarland.de

images, as displayed in Fig. 1(a). The rough, step-like surface of the pyramid does not straightforwardly reveal its single crystal nature. We prove single crystal nature using NV centers in the tip (see below), consistent with Raman microscopy characterization provided by the manufacturer.⁸ The pyramid in the SEM image has a basal plane of $3.5 \times 3.5 \mu\text{m}^2$ and a height of $10 \mu\text{m}$. The cone angle of the tip is as low as $\approx 10^\circ$ close to the apex (last $\approx 0.5 \mu\text{m}$) and $20\text{--}25^\circ$ closer to the base.

For sensing and quantum information, negatively charged nitrogen- and silicon-vacancy centers (here termed NV and SiV centers) are of major interest. We investigate the photoluminescence (PL) of both types of color centers in a home built confocal microscope (Numerical aperture NA 0.8, 532 nm laser excitation). Confocal filtering of PL is ensured using a single mode optical fiber. We record PL spectra using a grating spectrometer (Acton Spectra Pro 2500, Pixis 256OE CCD), whereas highly efficient photon counters (Quantum efficiency $\approx 70\%$, Excelitas SPCM-AQRH-14) enable quantifying PL intensity. To measure PL lifetimes of color centers, we employ pulsed laser excitation (NKT EXW-12, pulse length ≈ 50 ps, wavelength 527–537 nm) and time correlated photon counting (PicoQuant, PicoHarp 300).

In a first step, we investigate the diamond pyramids' PL under laser excitation in general. All 10 investigated pyramids show bright PL with detected photon rates easily exceeding 10^6 cps (Mcps) (wavelength range 680–720 nm) for moderate excitation power ($< 500 \mu\text{W}$) all over the tip. To further quantify the intensity of this PL, which is mainly due to NV centers, we investigate the PL saturation behavior focusing the laser onto the pyramid apex (see [supplementary material](#)). Estimated NV PL count rates into the first lens of our confocal microscope exceed 500 Mcps ($P_{\text{sat}} = 380 \mu\text{W}$) corresponding to an emitted power of ≈ 100 pW, which is accessible with common commercial photodiodes.

We now consider how the pyramids' PL varies with the spatial position of the laser focus. To this end, we record the PL in planes parallel to its basal plane (xy-planes) via scanning the pyramid through the laser focus. To enable 3-dimensional imaging, we change the position of the laser focus with respect to the height of the pyramid (z-position) and repeat the measurement. Focusing the laser close to the basal plane clearly reveals the square footprint of the pyramid as deduced from SEM images, while focusing the laser close to the pyramid's apex reveals PL stemming from a single point (data see [supplementary material](#)).

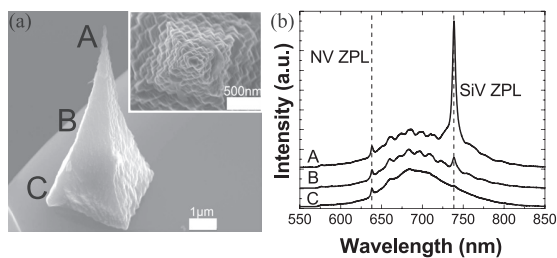


FIG. 1. (a) SEM image of a diamond pyramidal tip on a Si cantilever. Inset: View from the apex of the pyramid revealing the step-like surface (b) PL spectra recorded at apex (A), in the middle (B), and at the base of the pyramid (C). The SiV PL is rapidly decreasing compared to the NV PL. Note that all spectra are normalized to maximum of the NV PL. We note that we observe only minor broadband PL due to the epoxy at the pyramid base.

We now evaluate PL spectra recorded in different heights of the pyramid [see Fig. 1(b)]. For all heights, we clearly observe the characteristic spectrum of NV centers with a zero-phonon line (ZPL) at 638 nm [linewidth 4.1(2) nm] and broad phonon sidebands between 650 and 800 nm. When exciting PL closer to the pyramid apex, we furthermore observe the ZPL of SiV centers at 738 nm [linewidth 4.9(1) nm]. SiV PL is significantly more pronounced closer to the pyramid apex a spectrum is recorded. For spectra recorded at the apex, the SiV ZPL strongly dominates over the NV phonon sideband. PL spectra with the described features are consistently observed from all 10 investigated tips.

To interpret the PL spectra, it is useful to recall that the pyramid's apex is formed in the initial phase of CVD growth on a Si substrate: A CVD plasma etches Si substrates, consequently diamond films grown on Si contain up to 10^{19}cm^{-3} Si atoms.¹⁰ However, Si incorporation decreases significantly by more than one order of magnitude as soon as the growing diamond fully covers the substrate.¹⁰ Thus, we expect a higher concentration of Si impurities close to the apex formed in the starting phase of the growth. In contrast, nitrogen has been added to the gas mixture during the CVD process (0.1% volume fraction) and forms NV centers in all heights in the diamond pyramid. We investigate the brightness of NV and SiV PL in dependence of the z-position of the laser focus in more detail as shown in Fig. 2(a). Both PL signals decrease in brightness from apex to base; however, the SiV PL decreases faster, indicating a stronger confinement of the area with high SiV density close to the apex.

Despite a significantly reduced diamond volume exposed to the laser, NV and SiV PL are enhanced close to the apex, which we also attribute to photonic effects: we simulate the emission patterns of dipoles with horizontal and vertical alignment with respect to the pyramid base in the

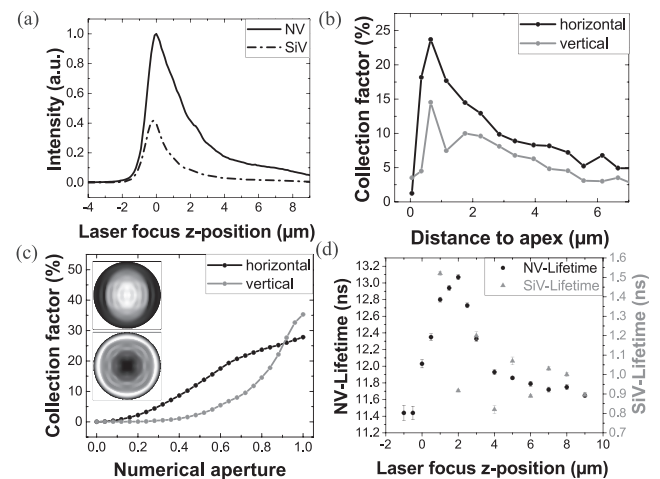


FIG. 2. (a) NV and SiV PL along the z-axis of the tip. (b) Simulated collection factor along the z-axis of the tip for horizontal and vertical dipoles. (c) Simulated collection factors for different NA and far field patterns as inset. For these simulations, we place the dipole at the location that maximizes the collection factor [see (b)]. (d) Measured excited state lifetimes along the z-axis of the pyramid; note the increase of the lifetime towards the apex as well as a decrease very close to the apex. The z-axis origin ($z = 0$) represents the tip apex in (a) and (d) determined as the z-position for which maximally spatially confined PL from the tip occurs (note the depth of focus of our confocal microscope of $\approx 0.9 \mu\text{m}$).

middle of the xy-plane for different z-positions. We use the Finite Difference Time Domain (FDTD) method implemented with a commercial software (Lumerical FDTD solutions). As sensing applications often demand to maximize the PL rate in the detection optics, we investigate the collection factor defined as the ratio of the power emitted into the NA to the emitted power in homogeneous diamond as a figure of merit, exemplarily for $\lambda = 700$ nm. The results of these simulations are displayed in Figs. 2(b) and 2(c) (details see [supplementary material](#)). The simulated data, which qualitatively agree with our measurements [Fig. 2(a)], show that the tip's shape leads to an enhanced photon rate in our NA for PL from color centers close to the apex. This situation is advantageous for scanning probe applications, as these centers are simultaneously in close proximity to the sample surface. Moreover, our simulations indicate that (for horizontal dipoles) even a moderate NA of ≈ 0.6 only reduces the collection factor by $\approx 25\%$.

To determine if the diamond tips are suitable for magnetometry applications, we perform ground state optically detected magnetic resonance (ODMR) of the NV centers. Applying a static magnetic field \vec{B} reveals four pairs of ODMR resonances, corresponding to the four equivalent $\langle 111 \rangle$ orientations of NV centers in the diamond lattice (data see [supplementary material](#)). The occurrence of four pairs of resonances witnesses the single crystal nature of the tip as any misoriented, polycrystalline grains would lead to additional resonances or blurring of the ODMR-spectrum. For the following measurements, we align \vec{B} onto one of the $\langle 111 \rangle$ axes and use the NV sub-ensemble to which \vec{B} is aligned. We verify coherent manipulation of NV electronic spins via Rabi oscillations [see Fig. 3(a)] and measure their coherence times T_2^* and T_2 .

Using a Spin echo-sequence, we measure T_2 [see Fig. 3(b)] at the base of 4 pyramids and find on average $T_2 = 7.7(3) \mu\text{s}$. We check T_2^* via a Ramsey-type experiment and find $T_2^* = 0.24(7) \mu\text{s}$ (data not shown). We verify $T_2 = 7.2(1) \mu\text{s}$ for NVs close to one pyramid's apex [Fig. 3(b)]. Thus, T_2 is preserved despite SiV incorporation and potentially lower crystal quality. T_2 and T_2^* are almost one order of magnitude higher than in high pressure high temperature diamond (typ. 100 ppm substitutional nitrogen $[\text{N}]^s$, $T_2 \approx 1 \mu\text{s}$ ¹), however, much lower than in high purity CVD diamond (1 ppb $[\text{N}]^s$, $T_2 \approx 300 \mu\text{s}$ ¹). Using T_2 and T_2^* as well as the PL count rate $I_0 = 162.7$ Mcps, the readout duration

$t_L = 350$ ns and the contrast of the ODMR $C = 7.4\%$, we calculate the DC and AC magnetic field sensitivities¹

$$\eta_{\text{DC}} \approx \frac{1}{\gamma_{\text{NV}}} \frac{1}{C \sqrt{I_0 t_L}} \times \frac{1}{\sqrt{T_2^*}} \approx 130.6 \text{ nT} / \sqrt{\text{Hz}}, \quad (1)$$

$$\eta_{\text{AC}} = \eta_{\text{DC}} \times \sqrt{\frac{T_2^*}{T_2}} \approx 22.9 \text{ nT} / \sqrt{\text{Hz}}. \quad (2)$$

Previous works report that lifetime changes of color centers evidence interaction with various defects^{12–14} as well as the photonic environment.¹⁵ To investigate lifetime changes in detail, we measure the excited state lifetime τ_{NV} (τ_{SiV}) of NV (SiV) centers along the z-axis of the pyramid [see Figs. 2(d) and [supplementary material](#)]. At the base ($z \approx 10 \mu\text{m}$), where we identified a reduced density of SiV centers, we find $\tau_{\text{NV}} = 11.79(3)$ ns, which well agrees with NV lifetimes in single crystal bulk diamonds [$\tau_{\text{NV, bulk}} = 12.9(1)$ ns]¹⁶ whereas $\tau_{\text{SiV}} = 0.89(1)$ ns, as previously observed in polycrystalline diamond.¹⁷ Approaching the pyramid apex ($z \approx 2–4 \mu\text{m}$), τ_{NV} [τ_{SiV}] increases to 13.07(3) ns [1.92(9) ns], potentially due to a decrease in the effective refractive index close to the nanoscale apex.¹⁵ In the region of increased SiV density very close to the apex ($z \approx 0–1 \mu\text{m}$), τ_{NV} drops to 11.44(8) ns. In the presence of graphitic or disordered carbon, τ_{NV} shortens.^{12,13} In this context, a high level of Si doping, here possibly induced by substrate etching,¹⁰ introduces structural defects.¹⁸ Thus, this shortening of τ_{NV} might be attributed to incorporated Si potentially lowering crystalline quality and inducing non-diamond phases. Moreover, $[\text{N}]^s$ can significantly quench NV PL via dipole-dipole interaction.¹⁴ Such energy transfer (Förster resonance energy transfer, FRET) requires an overlap of the quenched color center's (donor) emission band and the quenching defect's (acceptor) absorption band. Thus, also a high density of SiV centers potentially quenches NV PL: NV emission (≈ 650 to 750 nm) well overlaps with SiV absorption (540 to 740 nm¹⁹), especially with its dominant ZPL. FRET between NV and SiV centers has so far not been demonstrated; however, NV centers show efficient FRET transfer to dye molecules with absorption in a similar spectral range (50% efficiency at ≈ 6 nm distance).²⁰ We estimate the average distance between centers in the tip to be < 10 nm (see [supplementary material](#)); thus, FRET might be contributing to the quenching.

As a first step towards optimization of the tip for magnetometry, we etch it in an inductively coupled reactive ion etching plasma (Ar/O₂, 50 sccm each, 18.9 mTorr, 500 W ICP, 200 W RF power see also [supplementary material](#)) enabling highly anisotropic etching of diamond. We remove up to $\approx 1 \mu\text{m}$ of diamond, as measured from the pyramid height reduction, in several etch steps. We note that the pyramid still reveals a comparably defined apex of < 200 nm size and NV centers close to the apex retain coherence ($T_2^{\text{(base, unetched)}} = 9.4(2) \mu\text{s}$; $T_2^{\text{(apex, etched)}} = 8.9(2) \mu\text{s}$). Surface roughness remains mainly unchanged, while SiV PL significantly decreases, as we remove highly Si-doped diamond (details see [supplementary material](#)). We thus establish a procedure to tune the NV/SiV ratio even for readily mounted devices to tailor them for magnetometry.

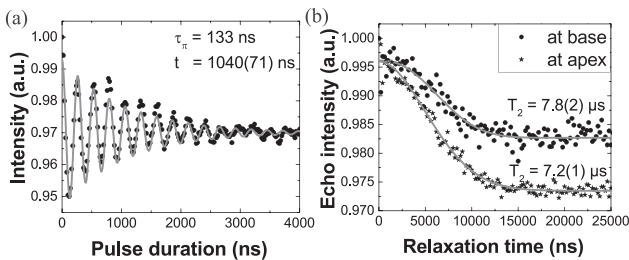


FIG. 3. (a) Measurement of a Rabi oscillations between the $m_s = 0$ and the $m_s = -1$ states of the Zeeman shifted sub-ensemble with a Rabi frequency of 3.76 MHz. (b) Spin echo measurement at apex and base, fitted employing the formalism derived in Ref. 11.

In conclusion, we show that single crystal diamond AFM tips from Artech Carbon show bright PL from *in-situ* created NV and SiV centers, easily measurable with standard photodiodes. In addition, we demonstrate their suitability for magnetometry ($T_2 = 7.7(3) \mu\text{s}$, $\eta_{\text{DC}} \approx 130.6 \text{ nT}/\sqrt{\text{Hz}}$, $\eta_{\text{AC}} \approx 22.9 \text{ nT}/\sqrt{\text{Hz}}$). FDTD simulations indicate high PL rates from centers close to the pyramid apex.

The outstanding advantage of the pyramidal tips is their commercial availability as well as a comparably low production cost per tip and high resolution topography imaging, compared to top-down approaches.⁵ The main drawback is a high color center density precluding to use single centers for imaging. Consequently, color centers in $\approx 1 \mu\text{m}$ tip height, limited by the confocal microscope, contribute to sensing and significantly limit spatial resolution. Nevertheless, the tips might, e.g., be utilized to monitor the activity of integrated circuits via magnetic measurements;²¹ here, nanoscale resolution is not mandatory and scanning devices avoid the necessity to place a diamond chip on the circuit under investigation. For single color center sensors, diamond purity has to be enhanced by reducing nitrogen in the process and the use of more etch resistant growth substrates (e.g., iridium). Creation of color centers might be feasible via recently developed nanoimplantation techniques,²² whereas mounting of the devices to transparent cantilevers, e.g., made from silicon nitride would allow optical access through the scanning device.

See [supplementary material](#) for additional information about our experimental setup, ODMR-spectra, technical details on the plasma treatment, the 3D fluorescence imaging, fluorescence saturation, and details on the numerical simulations.

This research has been funded via the NanoMatFutur program of the German Ministry of Education and Research (BMBF) under Grant No. FKZ13N13547 and Enterprise Estonia (EAS) Project No. Lep16012. We thank Jörg Schmauch for recording SEM images as well as Dr. Rene Hensel, Dr. Tobias Kraus, Dr. Daniel Brodoceanu, and Susanne Selzer (INM, Saarbrücken) for providing plasma etching tools and assistance.

- ¹L. Rondin, J.-P. Tetienne, T. Hingant, J.-F. Roch, P. Maletinsky, and V. Jacques, *Rep. Prog. Phys.* **77**, 056503 (2014).
- ²L. Thiel, D. Rohner, M. Ganzhorn, P. Appel, E. Neu, B. Müller, R. Kleiner, D. Koelle, and P. Maletinsky, *Nat. Nanotechnol.* **11**, 677 (2016).
- ³J. P. Tetienne, T. Hingant, L. J. Martínez, S. Rohart, A. Thiaville, L. H. Diez, K. Garcia, J. P. Adam, J. V. Kim, J. F. Roch, I. M. Miron, G. Gaudin, L. Vila, B. Ocker, D. Ravelosona, and V. Jacques, *Nat. Commun.* **6**, 6733 (2015).
- ⁴I. Lovchinsky, A. O. Sushkov, E. Urbach, N. P. de Leon, S. Choi, K. De Greve, R. Evans, R. Gertner, E. Bersin, C. Müller, L. McGuinness, F. Jelezko, R. L. Walsworth, H. Park, and M. D. Lukin, *Science* **351**, 836 (2016).
- ⁵P. Appel, E. Neu, M. Ganzhorn, A. Barfuss, M. Batzer, M. Gratz, A. Tschöpe, and P. Maletinsky, *Rev. Sci. Instrum.* **87**, 063703 (2016).
- ⁶I. Aharonovich, J. C. Lee, A. P. Magyar, D. O. Bracher, and E. L. Hu, *Laser Photonics Rev.* **7**, L61 (2013).
- ⁷A. N. Obraztsov, P. G. Kopylov, B. A. Loginov, M. A. Dolganov, R. R. Ismagilov, and N. V. Savenko, *Rev. Sci. Instrum.* **81**, 013703 (2010).
- ⁸See www.scdprobes.com for more information.
- ⁹A. Obraztsov and P. Kopylov, "Diamond nano-tip and method for production thereof," WO Patent Application No. PCT/EP2009/056,100 (2009).
- ¹⁰J. Barjon, E. Rzepka, F. Jomard, J.-M. Laroche, D. Ballutaud, T. Kociniowski, and J. Chevallier, *Phys. Status Solidi A* **202**, 2177 (2005).
- ¹¹L. Childress, M. V. Gurudev Dutt, J. M. Taylor, A. S. Zibrov, F. Jelezko, J. Wrachtrup, P. R. Hemmer, and M. D. Lukin, *Science* **314**, 281 (2006).
- ¹²B. R. Smith, D. Gruber, and T. Plakhotnik, *Diamond Relat. Mater.* **19**, 314 (2010).
- ¹³L.-H. Chen, T.-S. Lim, and H.-C. Chang, *J. Opt. Soc. Am. B* **29**, 2309 (2012).
- ¹⁴D. Gatto Monticone, F. Quercioli, R. Mercatelli, S. Soria, S. Borini, T. Poli, M. Vannoni, E. Vittone, and P. Olivero, *Phys. Rev. B* **88**, 155201 (2013).
- ¹⁵A. Beveratos, R. Brouri, T. Gacoin, J.-P. Poizat, and P. Grangier, *Phys. Rev. A* **64**, 061802 (2001).
- ¹⁶A. T. Collins, M. F. Thomaz, and M. I. B. Jorge, *J. Phys. C: Solid State Phys.* **16**, 2177 (1983).
- ¹⁷A. V. Turukhin, C.-H. Liu, A. A. Gorokhovskiy, R. R. Alfano, and W. Phillips, *Phys. Rev. B* **54**, 16448 (1996).
- ¹⁸A. Bolshakov, V. Ralchenko, V. Sedov, A. Khomich, I. Vlasov, A. Khomich, N. Trofimov, V. Krivobok, S. Nikolaev, R. Khmel'nitskii, and V. Saraykin, *Phys. Status Solidi A* **212**, 2525 (2015).
- ¹⁹L. J. Rogers, K. D. Jahnke, M. W. Doherty, A. Dietrich, L. P. McGuinness, C. Müller, T. Teraji, H. Sumiya, J. Isoya, N. B. Manson, and F. Jelezko, *Phys. Rev. B* **89**, 235101 (2014).
- ²⁰N. Mohan, Y.-K. Tzeng, L. Yang, Y.-Y. Chen, Y. Y. Hui, C.-Y. Fang, and H.-C. Chang, *Adv. Mater.* **22**, 843 (2010).
- ²¹L. Shao, R. Liu, M. Zhang, A. V. Shneidman, X. Audier, M. Markham, H. Dhillon, D. J. Twitchen, Y.-F. Xiao, and M. Lončar, *Adv. Opt. Mater.* **4**(7), 1075–1080 (2016).
- ²²J. Riedrich-Möller, S. Pezzagna, J. Meijer, C. Pauly, F. Mücklich, M. Markham, A. M. Edmonds, and C. Becher, *Appl. Phys. Lett.* **106**, 221103 (2015).

3. Toward wafer-scale diamond nano- and quantum technologies

Richard Nelz, Johannes Görlitz, Dennis Herrmann, Abdallah Slablab, Michel Challier, Mariusz Radtke, Martin Fischer, Stefan Gsell, Matthias Schreck, Christoph Becher, and Elke Neu

APL Materials **7**, 011108 (2019)
doi: 10.1063/1.5067267

This paper was selected as an Editor's Pick.

The above stated manuscript shows the potential of a novel diamond material to upscale diamond-based technologies.

Richard Nelz (R.N.) designed and realized the homebuilt confocal microscope that was used to characterize NV centers in the investigated novel, wafer-sized, heteroepitaxial single crystal diamond supplied by the company AuDiaTec (Augsburg Diamond Technology GmbH, Augsburg, Germany). R.N. performed all optical and spin measurements on NV centers presented in the manuscript. In addition, he evaluated the density of native NV centers and compared it to the density predicted by the gas composition during the growth of the material showing a good accordance. R.N. suggested using SiV centers in the material as a probe for internal strain. The corresponding measurements were performed by J. Görlitz and D. Herrmann. R.N. applied findings from previous work to proof the predicted relaxation of strain in the diamond. Following implantation of shallow NV centers, nanostructures were fabricated by M. Challier and M. Radtke. Subsequently, R.N. investigated the properties of the NV ensemble implanted into the top layer of the material and the NV centers in the fabricated nanostructures to further show the material's suitability for sensing applications. Lastly, R.N. outlined and wrote the first draft of the manuscript and the supplementary material. In addition, he designed all figures and actively contributed to all major revisions of the article and to all discussions throughout the collaboration on appropriate experiments and data evaluation.

Toward wafer-scale diamond nano- and quantum technologies

Cite as: APL Mater. 7, 011108 (2019); doi: 10.1063/1.5067267

Submitted: 16 October 2018 • Accepted: 2 January 2019 •

Published Online: 28 January 2019



Richard Nelz,¹  Johannes Görlitz,¹ Dennis Herrmann,¹ Abdallah Slablab,¹ Michel Challier,¹ Mariusz Radtke,¹ Martin Fischer,² Stefan Gsell,² Matthias Schreck,³  Christoph Becher,¹  and Elke Neu^{1,a)} 

AFFILIATIONS

¹Universität des Saarlandes, Fakultät NT, Physik, 66123 Saarbrücken, Germany

²Augsburg Diamond Technology GmbH, 86159 Augsburg, Germany

³Universität Augsburg, Institut für Physik, 86135 Augsburg, Germany

^{a)}Electronic mail: elkenu@physik.uni-saarland.de

ABSTRACT

We investigate native nitrogen vacancy (NV) and silicon vacancy (SiV) color centers in a commercially available, heteroepitaxial, wafer-sized, mm thick, single-crystal diamond. We observe single, native NV centers with a density of roughly 1 NV per μm^3 and moderate coherence time ($T_2 = 5 \mu\text{s}$) embedded in an ensemble of SiV centers. Using low temperature luminescence of SiV centers as a probe, we prove the high crystalline quality of the diamond especially close to the growth surface, consistent with a reduced dislocation density. Using ion implantation and plasma etching, we verify the possibility to fabricate nanostructures with shallow color centers rendering our material promising for fabrication of nanoscale sensing devices. As this diamond is available in wafer-sizes up to 100 mm, it offers the opportunity to up-scale diamond-based device fabrication.

© 2019 Author(s). All article content, except where otherwise noted, is licensed under a Creative Commons Attribution (CC BY) license (<http://creativecommons.org/licenses/by/4.0/>). <https://doi.org/10.1063/1.5067267>

Diamond nanostructures are of significant importance for various applications in science and industry including nanomechanical devices,¹ photonics² and sensing.³ A major challenge for most of these applications is the scalability of the fabrication process predominantly due to a lack of large area single-crystal diamonds (SCDs) with good crystalline quality and high purity. Manufacturing synthetic SCD on a wafer scale has been an active field of research^{4,5} leading to the commercial availability of SCD with a diameter of ≈ 100 mm recently. This progress opens the road toward up-scaling the fabrication of SCD nanostructures especially for diamond related sensing applications.⁶ Color centers in SCD, in particular, the negatively charged nitrogen vacancy (NV) center in nanostructures, have been extensively used to sensitively measure, e.g., magnetic fields in the last decade. Single color centers allow for sensing with high spatial resolution and offer bright, photostable photoluminescence (PL). In addition, NV centers provide highly coherent, controllable spin states³ and show optically detected magnetic resonance

(ODMR) enabling to read out their spin states via PL detection. As a consequence, even single NV centers can serve as quantum-enhanced sensors. Magnetic field imaging using NV centers has various applications ranging from material characterization in superconductors⁷ or magnetic materials for spintronics⁸ to life science applications where nuclear magnetic resonance detection of single proteins is of interest.⁹ Recently, silicon vacancy (SiV) centers emerged as alternative enabling all optical sensing of temperatures using their narrow electronic transitions.¹⁰

We here demonstrate the basic applicability of commercial, wafer-sized SCD for quantum technology applications. To this end, we demonstrate coherent manipulation of single native NV center spins in the SCD, while we use low-temperature spectroscopy of SiV center PL as a probe to prove the high crystalline quality of the material. In addition, we implant shallow NV centers (depth ≈ 10 nm), indispensable for nanoscale sensing, and investigate their suitability for quantum sensing applications.

Furthermore, we apply reactive ion etching to the material to illustrate routes toward up-scaling of diamond-related nanofabrication.

We use (100) oriented SCD from AuDiaTec (Augsburg Diamond Technology GmbH) synthesized in a microwave plasma enhanced chemical vapor deposition process based on a methane/hydrogen (CH_4/H_2) gas mixture at a temperature $>1000^\circ\text{C}$. H_2 was purified by passing it through a AgPd membrane, while the used CH_4 had a purity of 99.9995%. As a consequence, we estimate the nitrogen (N_2) concentration in the gas phase to be <0.5 ppm. The Ir/YSZ (yttria stabilized zirconia)/Si substrate was removed by chemical etching and grinding before the diamond wafer was cut into pieces of $3\text{ mm} \times 3\text{ mm}$ using a pulsed IR laser. The SCDs are 1.3 mm thick. For our experiments, we use the crystals with the as grown surface. SCD synthesis at AuDiaTec is based on the technology developed at the University of Augsburg. As described in Ref. 5, successful scaling of heteroepitaxial nucleation and growth to 100 mm wafer-size was achieved by the use of the multilayer substrate Ir/YSZ/Si. During heteroepitaxial growth of thick (mm) SCD, the dislocation density decreases proportional to the inverse of the SCD layer thickness indicating high crystalline quality for this material at the growth surface.⁵ Previous studies⁵ furthermore reveal a high homogeneity of the crystalline quality using Raman scattering and X-ray diffraction.

To investigate PL and perform spin manipulation of NV centers, we use a home-built confocal microscope (numerical aperture NA 0.8, 532 nm laser excitation) where confocal filtering of the PL is ensured by using a single mode optical fiber. To quantify the PL intensity, we use highly efficient photon counters (Excelitas SPCM-AQRH-14, quantum efficiency $\approx 70\%$). In addition, we use a grating spectrometer (Acton Spectra Pro 2500, Pixis 256OE CCD) to record the PL spectrum. To measure PL lifetimes, we employ time correlated photon counting (PicoQuant, PicoHarp 300) and pulsed laser excitation (NKT EXW-12, pulse length $\approx 50\text{ ps}$, wavelength 527–537 nm). The setup is equipped with a microwave source and an amplifier (Stanford Research Systems, SG384 and Mini Circuits, ZHL-42W+) for spin-manipulation of NV centers. To investigate SiV centers, we use a second confocal microscope (numerical aperture NA 0.9) embedded into a liquid helium flow cryostat employing a titanium-sapphire laser (Matisse, TX) at 690 nm as an excitation source. For confocal filtering, a single mode optical fiber is used. PL spectra of SiV centers are recorded using a grating spectrometer (Jobin Yvon, Horiba, Grating: 1800 g/mm).

We now discuss the PL results from our SCD under continuous laser excitation at 532 nm. Close ($<5\text{ }\mu\text{m}$) to the nucleation side, we observe very bright PL consisting of a broad background as well as distinctive NV and SiV PL. By contrast, PL maps recorded in a wavelength range from 680 nm to 720 nm from planes parallel and closer to the growth surface show bright, distinguishable spots [see Fig. 1(a)]. The spots clearly show PL spectra of NV centers [see Fig. 1(b)], constituting the first observation of individual native NV centers in heteroepitaxial SCD. Additionally, these PL spectra reveal the presence of homogeneously distributed SiV centers which,

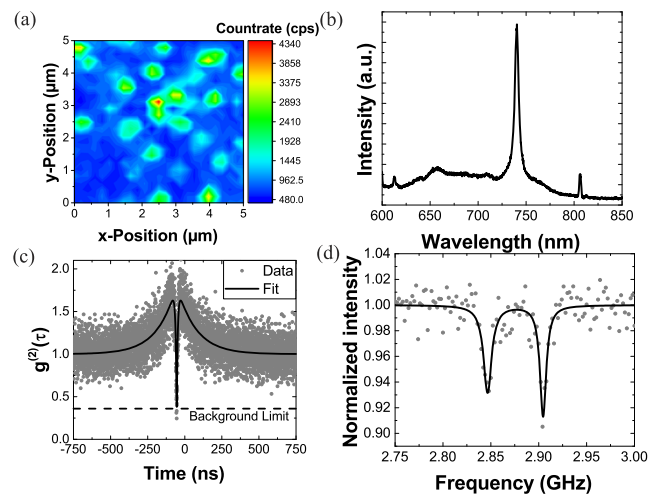


FIG. 1. (a) PL map of the SCD (detected wavelength range 680 nm–720 nm) showing ≈ 25 bright spots which all have NV PL. (b) Room temperature PL spectrum of one of these NVs. Bright SiV zero phonon line (ZPL) is visible leading to the background measured in the PL map in (a) despite spectral filtering. The narrow PL line observed at 805 nm is most probably connected to the SiV ensemble,^{14,15} while the peak at 610 nm corresponds to the second order Raman scattering of diamond. (c) $g^{(2)}$ -measurement of one of the NVs. A clear anti-bunching is visible. $g^{(2)}(0)$ is only limited by the background of the SiV ensemble (see the [supplementary material](#)). (d) ODMR measurement of single NV showing a background-corrected contrast C above 10% (external magnetic field approximately 11 G).

despite spectral filtering, influence observation of single NV centers as background.

To test the applicability of the material for NV-based quantum technologies, we investigate single, native NV centers in the highest-quality region, namely, the first micrometers below the growth surface. To prove the observation of single NV centers, we measure second order photon correlations $g^{(2)}$ [see Fig. 1(c)]. We achieve a signal-to-background ratio of less than 4, limited by SiV PL. Nevertheless, these measurements clearly show single photon emission of NV centers, while the SiV ensemble PL limits $g^{(2)}(0)$ (see the [supplementary material](#)). From PL maps recorded at different positions of the sample [see Fig. 1(a)], we determine a homogenous NV density of $\approx 1\text{ NV per }\mu\text{m}^3$ equivalent to a concentration of $\approx 0.005\text{ ppb}$. This value is in reasonable accordance with the density estimated from the nitrogen impurity concentration in the feed gases (for details, see the [supplementary material](#)). Subsequently, we perform photoluminescence lifetime imaging of individual NV centers (for data, see the [supplementary material](#)). The NV centers show on average a lifetime of 12.3(6) ns which agrees well with the lifetime in bulk SCD.¹¹ This finding rules out quenching, e.g., due to structural defects associated with the incorporation of silicon impurities¹² as well as quenching via potential near-field energy transfer between NV and SiV centers.¹³ Furthermore, we perform ground state ODMR measurements of single NVs. We obtain the ODMR-spectrum in Fig. 1(d) with narrow resonances (an external magnetic field of 11 G applied) and a contrast exceeding 10%. The zero-field-splitting of 2.876 GHz indicates low strain close

to the growth surface which would otherwise shift or split the resonance. Spin-Echo measurements of single NV centers at randomly chosen positions in the sample consistently show a coherence time of $T_2 = 5(1) \mu\text{s}$, proving homogenous properties of the NV centers in the SCD.

To further characterize the crystalline quality of the SCD, we study the SiV ensemble in detail. Hereby, we focus on the fine structure of the SiV zero phonon line (ZPL) which is a meaningful measure of the crystalline quality as strain shifts and broadens the fine structure components in the ensemble. Consequently, we measure the ZPL fine structure at 10 K in different depths along the growth direction (see Fig. 2). We observe a clear fine structure close to the growth surface, while ZPL broadening completely masks the fine structure deeper in the SCD toward the nucleation side where the growth started. We expect the ZPL to broaden linearly with dislocation density.¹⁶ To verify this fact, we fit the linewidth using a $1/\text{layer thickness}^n$ dependence. We obtain $n \approx 1$ which is in good agreement with the predicted dislocation density evolution during growth which should lead to an estimated density of dislocations of $\approx 10^7 \text{ cm}^{-2}$ close to the growth surface.⁵ In this area, we observe a fitted linewidth of 61.2(5) GHz (for details, see the [supplementary material](#)). Our observed linewidths are thus only roughly a factor of 6 higher than in high-quality, thin, homoepitaxial SCD films¹⁷ witnessing high crystalline quality.

Efficient nanoscale sensing using color centers in SCD typically requires shallow NV centers (<50 nm below the surface) incorporated into dedicated nanostructures, e.g., nanopillars.⁶ To test the usability of our novel SCD material, we shallowly implant nitrogen ions with an implantation energy of 6 keV and doses of 1.5 and $3 \times 10^{11} \text{ cm}^{-2}$ to form a NV layer 10 nm below the SCD surface. After annealing the sample, PL maps reveal homogenous creation of the NV layer across the sample for both doses. PL spectra from the implanted layer [see Fig. 3(a)] show strong NV PL, while weaker PL below 640 nm corresponds to phononic side bands originating from neutral NV centers; strong SiV PL is still visible. Due to the enhanced number of NVs, their PL is more pronounced, whereas the SiV PL remains mainly unchanged.

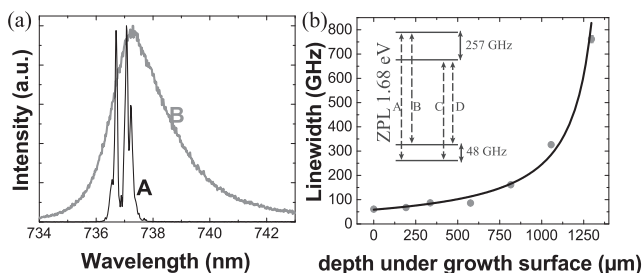


FIG. 2. Probing strain in the SCD material via SiV PL: (a) PL spectra of the SiV ensemble at 10 K. Close to the growth surface, a clear fine structure is visible (black curve A), while the ZPL continuously broadens along the growth direction. Closer to the substrate, broadening completely masks the fine structure components (gray curve B). (b) Linewidth of the transition C along the growth direction of the diamond. Inset: SiV level scheme according to Ref. 18.

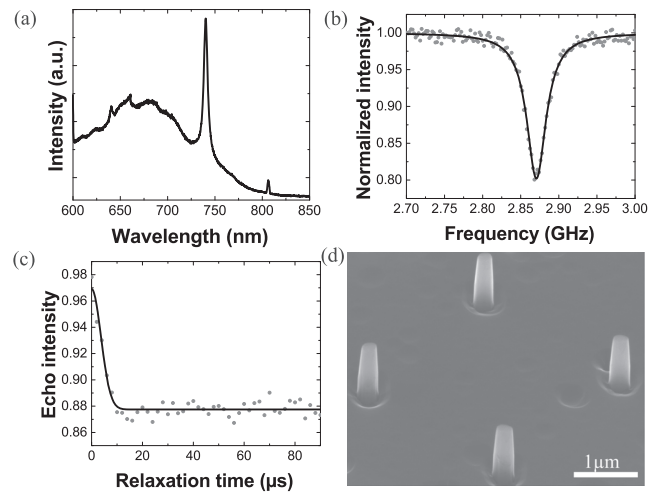


FIG. 3. (a) PL spectrum of the implanted NV ensemble. A clear NV^- as well as minor NV^0 spectrum is visible, while SiV PL remains unchanged. (b) ODMR spectrum without external magnetic field strongly broadened due to strong microwave pumping of the transition (unbroadened linewidth 10.67 MHz, $C = 20\%$). (c) Spin-echo-measurement of the implanted NV centers, fitted employing the formalism derived in Ref. 22. The coherence time is $T_2 = 5.2(3) \mu\text{s}$. (d) Scanning electron microscopy image of nanopillars etched into the growth surface of the SCD. The cylindrical pillars have a diameter of $\approx 200 \text{ nm}$ and a height of $\approx 1 \mu\text{m}$.

The PL lifetime of the implanted NV centers is longer than the native NV centers' lifetime due to their proximity to the surface. We find $\tau = 17 \text{ ns}$, typical for shallowly implanted NV centers.⁶ To demonstrate the usability of the NV center ensemble for magnetic sensing, we measure ODMR without applying an external magnetic field which shows a contrast of $C = 20\%$ [see Fig. 3(b)] at 2.871(2) GHz. Power broadening for the ODMR resonance occurs because of the strong microwave field necessary to saturate the ground state spin transition in the ensemble. To estimate the unbroadened linewidth, we follow Ref. 19 and obtain a linewidth of 10.67 MHz (see the [supplementary material](#)). Rabi oscillations of a sub-ensemble of the implanted NV centers using a bias magnetic field of 38 G confirm coherent manipulation of the spins. The spin coherence time $T_2 = 5.2(3) \mu\text{s}$ of the implanted NV centers is comparable to T_2 for the native NVs [see Fig. 3(c)] and consistent for positions several mm apart. Consequently, we assume that T_2 is limited by the properties of our SCD. Often, the concentration of substitutional nitrogen $[\text{N}]^s$ limits T_2 .³ However, as the estimated concentration of $[\text{N}]^s$ is in the ppb range for our SCD, we would expect T_2 to be at least an order of magnitude higher than observed. We also exclude minor concentrations of compensated boron acceptors as the source of decoherence. A possible spin bath reducing T_2 for the observed native NV centers might arise from various paramagnetic, silicon-containing defects in the material including neutral SiV centers and optically inactive silicon-hydrogen complexes.²⁰ Furthermore, vacancy complexes especially divacancies have been identified as a source of decoherence for implanted NV centers recently.²¹ We tentatively suggest that

vacancy complexes forming at dislocations might reduce T_2 in our material.

Another important test for the material is to manufacture well-defined and stable nanostructures by reactive ion etching like, e.g., nanopillars or scanning probes.⁶ Such photonic nanostructures significantly enhance photon rates from single color centers, consequently boosting sensor sensitivity.²³ We use the pristine growth surface (2.2 nm rms roughness, area $2\ \mu\text{m} \times 2\ \mu\text{m}$) to etch nanopillars in an inductively coupled reactive ion etching plasma (Ar/O₂, 50 sccm each, 18.9 mTorr, 500 W ICP, 200 W RF power) enabling highly anisotropic etching of SCD. The nanopillars have an almost cylindrical shape with a diameter of ≈ 200 nm and a height of $\approx 1\ \mu\text{m}$ [see Fig. 3(d)] closely resembling scanning probes optimized for high sensitivity magnetometry.²³ The surface roughness remains mainly unchanged (<4 nm rms roughness, area $2\ \mu\text{m} \times 2\ \mu\text{m}$) with no etchpits forming. We note that considering the estimated density of dislocations, the probability to find a dislocation within an individual pillar is only $\approx 1\%$ indicating the suitability of our high quality heteroepitaxial SCD for the production of quantum technology devices. Thus, our wafer-sized SCD opens up the way for up-scaling nanofabrication of NV center-related structures for various applications.

In conclusion, we show that our wafer-sized, heteroepitaxial SCD contains single, native NV centers with a homogeneous density of roughly 1 NV per μm^3 embedded in an ensemble of SiV centers. Native NVs show moderate coherence time of $T_2 = 5\ \mu\text{s}$ and are suitable for ODMR-related sensing applications. A clear fine structure of the SiV ZPL close to the growth surface witnesses low strain and high crystalline quality. Additionally, we shallowly implant NV centers as required for nanoscale sensing and demonstrate the fabrication of nanopillars into the pristine SCD growth surface.

The outstanding advantage of the present material system is its commercial availability and superior size, potentially enabling up-scaling of nanostructure fabrication for sensing and consequently reducing manufacturing cost for SCD-based devices. Due to wafer-scale growth, also the cost per carat can be reduced by potentially one order of magnitude compared to present high-purity SCD. Consequently, the material has the potential to eliminate a bottle neck in SCD-based technologies. Challenges arise from moderate NV coherence times in the material and the detrimental influence of the SiV PL on NV spin readout limiting the usability of NV centers for sensing. To reduce the incorporation of silicon, we envisage overgrowing millimeter-thick SCD wafers after removal of the Ir/YSZ/Si substrate since the Si-wafer is the main source of silicon in the process. For many applications, only thin active layers ($<10\ \mu\text{m}$) are required. As a consequence, a slow growth rate and process conditions for optimized crystal quality can be chosen. We anticipate that this approach will considerably improve NV coherence in the active zone. Nevertheless, the observed native NV centers are already useful for sensing using ODMR resonances shifts to detect magnetic fields with moderate strength, e.g., when performing failure analysis of electric circuits²⁴ or imaging of domain walls in thin ferromagnetic films applicable in

spintronics.⁸ Similarly, implanted ensembles of NV centers are suitable for wide-field imaging of magnetic particles in living cells.²⁵

See [supplementary material](#) for details about nitrogen incorporation, background determination of the $g^{(2)}$ -measurements, fitting of the SiV PL, PL lifetime maps, and estimation of the power broadening.

This research has been funded via the NanoMatFutur program of the German Ministry of Education and Research (BMBF) under Grant No. FKZ13N13547. We acknowledge funding via a PostDoc fellowship of the Daimler and Benz Foundation. We thank Jörg Schmauch for recording SEM images as well as Dr. Rene Hensel for the use of the ICP-RIE and assistance.

REFERENCES

- 1 J. Teissier, A. Barfuss, P. Appel, E. Neu, and P. Maletinsky, *Phys. Rev. Lett.* **113**, 020503 (2014).
- 2 I. Aharonovich and E. Neu, *Adv. Opt. Mater.* **2**, 911 (2014).
- 3 L. Rondin, J.-P. Tetienne, T. Hingant, J.-F. Roch, P. Maletinsky, and V. Jacques, *Rep. Prog. Phys.* **77**, 056503 (2014).
- 4 H. Yamada, A. Chayahara, Y. Mokuno, Y. Kato, and S. Shikata, *Appl. Phys. Lett.* **104**, 102110 (2014).
- 5 M. Schreck, S. Gsell, R. Brescia, and M. Fischer, *Sci. Rep.* **7**, 44462 (2017).
- 6 P. Appel, E. Neu, M. Ganzhorn, A. Barfuss, M. Batzer, M. Gratz, A. Tschöpe, and P. Maletinsky, *Rev. Sci. Instrum.* **87**, 063703 (2016).
- 7 L. Thiel, D. Rohner, M. Ganzhorn, P. Appel, E. Neu, B. Müller, R. Kleiner, D. Koelle, and P. Maletinsky, *Nat. Nano* **11**, 677 (2016).
- 8 J.-P. Tetienne, T. Hingant, J.-V. Kim, L. H. Diez, J.-P. Adam, K. Garcia, J.-F. Roch, S. Rohart, A. Thiaville, D. Ravelosona, and V. Jacques, *Science* **344**, 1366 (2014).
- 9 I. Lovchinsky, A. O. Sushkov, E. Urbach, N. P. de Leon, S. Choi, K. De Greve, R. Evans, R. Gertner, E. Bersin, C. Müller, L. McGuinness, F. Jelezko, R. L. Walsworth, H. Park, and M. D. Lukin, *Science* **351**, 836 (2016).
- 10 C. T. Nguyen, R. E. Evans, A. Sipahigil, M. K. Bhaskar, D. D. Sukachev, V. N. Agafonov, V. A. Davydov, L. F. Kulikova, F. Jelezko, and M. D. Lukin, *Appl. Phys. Lett.* **112**, 203102 (2018).
- 11 N. B. Manson, J. P. Harrison, and M. J. Sellars, *Phys. Rev. B* **74**, 104303 (2006).
- 12 A. Bolshakov, V. Ralchenko, V. Sedov, A. Khomich, I. Vlasov, A. Khomich, N. Trofimov, V. Krivobok, S. Nikolaev, R. Khmelnski, and V. Saraykin, *Phys. Status Solidi A* **212**, 2525 (2015).
- 13 D. Gatto Monticone, F. Quercioli, R. Mercatelli, S. Soria, S. Borini, T. Poli, M. Vannoni, E. Vittone, and P. Olivero, *Phys. Rev. B* **88**, 155201 (2013).
- 14 E. Neu, M. Fischer, S. Gsell, M. Schreck, and C. Becher, *Phys. Rev. B* **84**, 205211 (2011).
- 15 S. Lindner, A. Bommer, A. Muzha, A. Krueger, L. Gines, S. Mandal, O. Williams, E. Londero, A. Gali, and C. Becher, *New J. Phys.* **20**, 115002 (2018).
- 16 V. Hizhnyakov and P. Reineker, *J. Chem. Phys.* **111**, 8131 (1999).
- 17 E. Neu, C. Hepp, M. Hauschild, S. Gsell, M. Fischer, H. Sternschulte, D. Steinmüller-Nethl, M. Schreck, and C. Becher, *New J. Phys.* **15**, 043005 (2013).
- 18 C. Arend, J. N. Becker, H. Sternschulte, D. Steinmüller-Nethl, and C. Becher, *Phys. Rev. B* **94**, 045203 (2016).
- 19 A. Dréau, M. Lesik, L. Rondin, P. Spinicelli, O. Arcizet, J.-F. Roch, and V. Jacques, *Phys. Rev. B* **84**, 195204 (2011).
- 20 U. F. S. D'Haenens-Johansson, A. M. Edmonds, M. E. Newton, J. P. Goss, P. R. Briddon, J. M. Baker, P. M. Martineau, R. U. A. Khan, D. J. Twitchen, and S. D. Williams, *Phys. Rev. B* **82**, 155205 (2010).

²¹F. F. de Oliveira, D. Antonov, Y. Wang, P. Neumann, S. A. Momenzadeh, T. Häufsermann, A. Pasquarelli, A. Denisenko, and J. Wrachtrup, *Nat. Commun.* **8**, 15409 (2017).

²²L. Childress, M. V. Gurudev Dutt, J. M. Taylor, A. S. Zibrov, F. Jelezko, J. Wrachtrup, P. R. Hemmer, and M. D. Lukin, *Science* **314**, 281 (2006).

²³P. Fuchs, M. Challier, and E. Neu, *New J. Phys.* **20**, 125001 (2018).

²⁴A. Nowodzinski, M. Chipaux, L. Toraille, V. Jacques, J.-F. Roch, and T. Debuisschert, *Microelectron. Reliab.* **55**, 1549 (2015).

²⁵D. Le Sage, K. Arai, D. R. Glenn, S. J. DeVience, L. M. Pham, L. Rahn-Lee, M. D. Lukin, A. Yacoby, A. Komeili, and R. L. Walsworth, *Nature* **496**, 486 (2013).

4. Reliable Nanofabrication of single-crystal diamond photonic nanostructures for nanoscale sensing

Mariusz Radtke, Richard Nelz, Abdallah Slablab, and Elke Neu

Micromachines **10**, 718 (2019)
doi: 10.3390/mi10110718

The above mentioned manuscript details an optimized fabrication process for single crystal diamond scanning probes containing single NV centers. Richard Nelz (R.N.) monitored the NV centers' properties throughout the whole fabrication process including the performance of the final devices. To this end, a homebuilt confocal microscope was used which was designed and realized by R.N. The continuous monitoring of the NV center properties was highly important to the process development: one of the processing steps employed in the first version of the process was damaging the diamond surface rendering shallow NV centers unstable. Consequently, R.N. contributed to the optimization and reliability of the process via characterizing NV centers throughout the process. In addition, R.N. participated in all discussions during the project. He wrote the corresponding part of the manuscript and designed the appropriate figure. R.N. actively contributed to all major revisions of the article.

Article

Reliable Nanofabrication of Single-Crystal Diamond Photonic Nanostructures for Nanoscale Sensing

Mariusz Radtke [†], Richard Nelz , Abdallah Slablab  and Elke Neu ^{*}

Faculty of Natural Sciences and Technology, Saarland University, Physics, Campus E2.6,
66123 Saarbrücken, Germany

* Correspondence: elkeneu@physik.uni-saarland.de

† Current address: Department of Organic and Macromolecular Chemistry, Ghent University Krijgslaan 281,
building S4, 9000 Gent, Belgium.

Received: 26 September 2019; Accepted: 17 October 2019; Published: 24 October 2019



Abstract: In this manuscript, we outline a reliable procedure to manufacture photonic nanostructures from single-crystal diamond (SCD). Photonic nanostructures, in our case SCD nanopillars on thin (<1 μm) platforms, are highly relevant for nanoscale sensing. The presented top-down procedure includes electron beam lithography (EBL) as well as reactive ion etching (RIE). Our method introduces a novel type of inter-layer, namely silicon, that significantly enhances the adhesion of hydrogen silsesquioxane (HSQ) electron beam resist to SCD and avoids sample charging during EBL. In contrast to previously used adhesion layers, our silicon layer can be removed using a highly-selective RIE step, which is not damaging HSQ mask structures. We thus refine published nanofabrication processes to ease a higher process reliability especially in the light of the advancing commercialization of SCD sensor devices.

Keywords: top-down nanofabrication; single-crystal diamond; HSQ; electron beam lithography; inductively coupled-reactive ion etching (ICP-RIE)

1. Introduction

In recent decades, the use of optically active point defect, i.e., color centers, in single-crystal diamond (SCD) as atom-sized, solid-based quantum systems has emerged in various fields [1,2]. Applications span from quantum metrology (temperature [3], strain [4], electric [5] and magnetic fields [6]) to using color centers as spin qubits in quantum computing [7] and single photon sources for quantum communication [8,9]. The outstanding color center in diamond is the NV^- center due to its optically readable spin [10] and usage as sensor. For many of these applications, color centers will be incorporated into photonic nanostructures e.g., nanopillars [9] to ease fluorescence detection from the color centers and to enable, e.g., scanning a color center close to a sample surface [6].

SCD's wide indirect bandgap of ~ 5.45 eV makes undoped SCD a good insulator [11]. Moreover, SCD shows a high chemical inertness. Both properties render fabricating SCD nanostructures challenging: Top-down methods for nanofabrication will use lithography, typically electron beam lithography (EBL), as well as etching. As the high chemical inertness of SCD prevents wet etching, only plasma etching, typically inductively coupled reactive ion etching (ICP-RIE), is applicable. Moreover, the insulating nature of SCD renders EBL highly challenging due to uncontrolled sample charging and the resulting deflection of the electron beam. A peculiarity of SCD nanofabrication arises also from the fact that only certain materials can efficiently serve as an etch mask in the high-bias, high-density plasmas necessary for anisotropic SCD etching [12]. The now state-of-the-art masks for SCD nanostructuring are EBL written structures consisting of hydrogen silsesquioxane (HSQ). HSQ is stable in anisotropic etch plasmas used for SCD etching; it etches an order of

magnitude slower than SCD using typical etching recipes [12]. In general, HSQ enables creating very small mask structures down to 20 nm [13]. SCD structures etched using HSQ masks show smooth sidewalls [12]. Smooth sidewalls ensure low light scattering from photonic structures and defined waveguide properties. Consequently, HSQ masks enable etching almost cylindrical pillars with optimized shape and well-defined photonic properties [6,9,12,14,15]. On the other hand, we find that HSQ has a non-optimal adhesion to SCD. In previous work, this challenge has often been addressed using metallic inter-layers between HSQ and SCD, e.g., titanium [16]. However, even very thin (<1 nm) metallic residuals on SCD surfaces strongly disturb color centers placed shallowly below the surface [17]. Consequently, any metallic residues are detrimental for the process and a metal-free process is highly desirable. Often, removing the metallic layer also requires wet chemical removal [16] or the use of toxic etch gases such as chlorine [18]. The first can leave trace amounts of the etchant on the SCD surface and the second is technically demanding considering safety and reactor corrosion.

In this manuscript, we present a method to overcome two previously not satisfactorily addressed challenges in SCD nanofabrication, namely sample charging as well as non-optimal resist adhesion. We used the optimized process to fabricate SCD scanning probes, namely nanopillars on thin holding platforms [6,16]. We thus reliably fabricated SCD nanostructures easing, e.g., commercial fabrication of SCD scanning probes. Figure 1 depicts the steps of our nanofabrication process. We start with a clean SCD sample with a shallow NV⁻ layer (details on sample pre-treatment see Section 2) as mandatory for high resolution sensing. We use electron beam evaporation of silicon on SCD to form a de-charging and adhesive layer (Figure 1b, Section 3). This layer will enable highly reliable spin coating of HSQ (Figure 1c) as well as EBL (Figure 1d, Section 3). Subsequently, we remove the silicon adhesion layer selectively using ICP-RIE without damage to the HSQ mask (Figure 1e) and perform ICP-RIE of SCD to form the desired structures (Figure 1f, Section 4). Our method eases manufacturing complex structures, e.g., in our case, nanopillars (diameter 200 nm), on top of SCD platforms (size of the platform $\sim 3 \times 20 \mu\text{m}$): In the first structuring step, we form the platforms (Figure 1f). The silicon adhesion layer survives the subsequent wet-chemical removal of the HSQ mask (Figure 1g) and can be reused for a second round of processing (Figure 1h–l). In this second processing, we form the pillars. We note that, when etching the platforms, the HSQ mask protects NV centers in the whole area of the micrometer-sized platform. During pillar etching, only NVs protected by the pillar mask survive the process and will be used as nanoscale sensors. The method presented here has been filed for a patent (EP19198772.6).

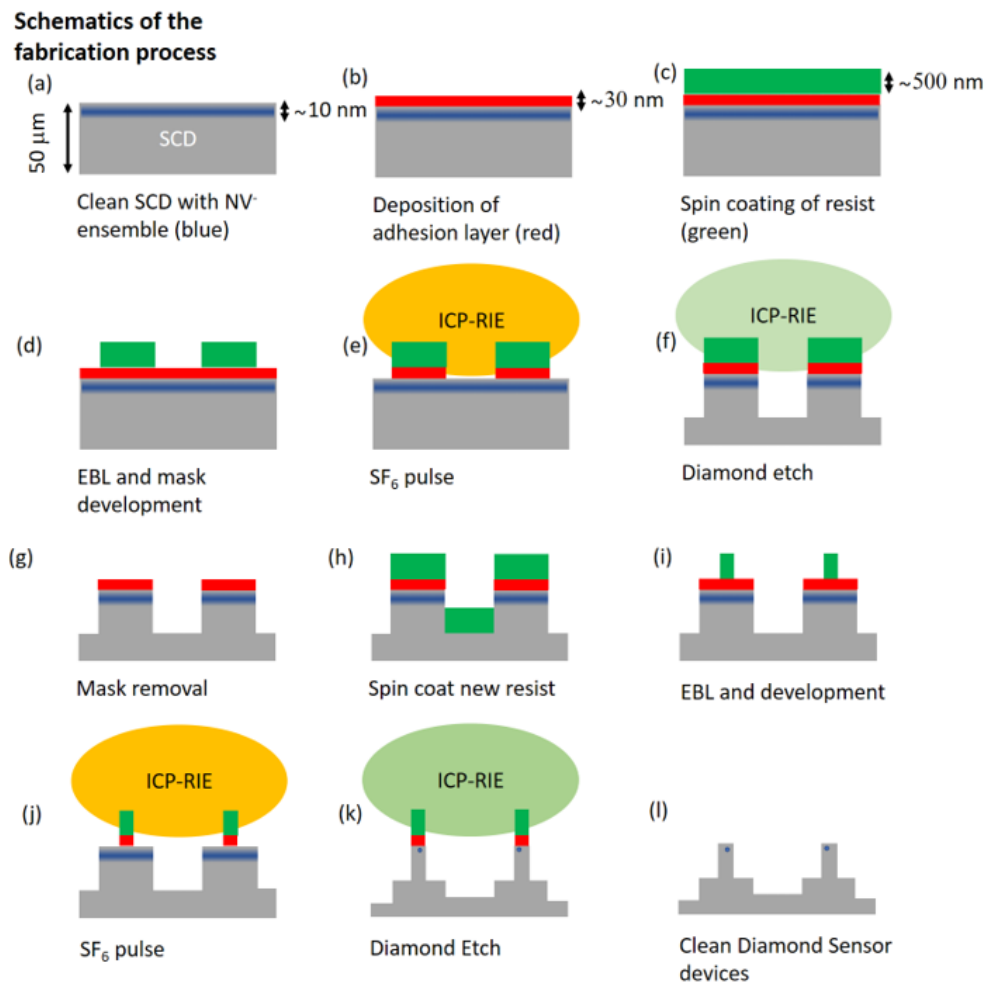


Figure 1. (a) The process starts with an SCD sample with a shallow layer of NV centers. Subsequently, we deposit (b) a silicon adhesion layer and (c) spin coat HSQ. (d) We use electron beam lithography (EBL) to structure the HSQ resist and obtain masks for the platforms. Using ICP-RIE, (e) we remove the silicon layer in-between the HSQ mask and (f) perform the structuring etch for SCD. (g) We finalize platform structuring via removing residual HSQ. We now (h) spin coat HSQ onto the remaining silicon layer and (i) perform EBL again. We repeat the ICP-RIE procedure, firstly (j) removing the silicon layer and then (k) etching the pillars into SCD. In a last step, (l) we remove residual HSQ as well as silicon to obtain clean SCD devices.

2. Sample Pre-Treatment

We purchased high-purity, (100)-oriented, chemical vapor deposited, SCD from Element Six (electronic grade quality, $[N]^s < 5$ ppb, $B < 1$ ppb). As we aimed for free standing SCD devices consisting of nanopillars on platforms, the SCD plates (size 2×4 mm²) were polished down to thickness of 50 μ m (Delaware Diamond Knives, Wilmington, DE, US). The SCD surface showed an initial roughness of $R_a < 3$ nm. As the mechanical polishing of the SCD can leave highly contaminated surfaces, we first wiped the sample surface using clean-room wipes and performed cleaning in an ultrasonic bath (solvents: isopropanol and acetone). We then cleaned the sample in boiling acids (1:1:1 mixture of sulfuric acid, perchloric acid and nitric acid, 5 mL each).

Mechanical polishing is suspected to introduce damage that potentially extends several micrometers deep into the SCD material [19,20]. To remove this potentially damaged and strained material, we applied ICP-RIE to our SCD samples. We avoided the use of toxic or corrosive gases in the process following our previously published routine [21]. We used a Plasmalab 100 ICP-RIE reactor (Oxford instruments, Abington, UK) and removed the topmost 3–5 μ m of SCD from each side. We

used a combination of SF₆, O₂, Ar biased plasmas with mixed RF and ICP discharges. Following recent approaches [22,23], we terminated the etching using low-damage, 0 V bias plasma with pure oxygen. The use of such soft etching was motivated by the potential close-to-surface damage due to highly biased ICP etching [24]. We typically obtain very smooth surfaces with an rms roughness of ~1 nm.

Using the above described procedure, we avoided creating NV centers in potentially damaged SCD. We formed a homogeneous layer of NV⁻ centers by implanting nitrogen ions with a density of 2×10^{11} ions/cm² and an energy of 6 keV. During the implantation, the sample was tilted by 7° with respect to the ion beam to avoid ion channeling. The SCD sample was then annealed in vacuum at 800 °C followed by an acid clean. This treatment will typically leave our sample with a mixed oxygen termination on the surface [25]. We found a contact angle for water of 67° [26], indicating a hydrophilic surface. As the electron beam resist we want to apply to the SCD was dissolved in methyl isobutyl ketone, a polar molecule, the resist's solvent had high affinity to hydrophilic surfaces. Despite the, in principle, fitting surface termination of the SCD sample, we observed non-reliable adhesion when applying HSQ to the SCD surface.

3. Deposition of Adhesion Layer and HSQ Mask Structuring

Motivated by the lack of reliable adhesion of HSQ to clean SCD surfaces, we explored silicon as an inter-layer. We expect this layer to foster adhesion between polysilicate HSQ resist and the native oxide (SiO₂) on the layer. To deposit the silicon adhesion layer, we used electron beam evaporation at a pressure of 10⁻⁶ Torr and 10 kV acceleration voltage with elliptical beam scanning mode in an electron beam evaporator "Pfeiffer Classic 500 L" machine. For the present work, we chose a thickness of the silicon layer of 25 nm. We note that we also found sputtered silicon layers to efficiently foster adhesion between SCD and HSQ. However, the SCD surface was attacked during the sputtering process. This in our case led to excess blinking and bleaching of NV⁻ centers in the final sensing devices and rules out this approach for our application. We also note that we tested spin coating Ti-prime as an adhesion promoter but did not obtain reliable results. We furthermore tested chromium layers as alternative to quickly oxidizing titanium layers [16]. Using this approach, we faced micromasking effects most probably arising from the incomplete, non-reliable wet-chemical removal of chromium layers. We note that our silicon layers still enable efficient HSQ adhesion weeks after deposition and storage under ambient conditions. We consequently conclude that the formation of a native oxide layer on the silicon, which will occur during storage at ambient conditions, is not detrimental. Thus, technically speaking, evaporation of silicon layers can be performed in batch processes for several SCD samples, which eases the fabrication workflow and reduces machine time. The evaporated silicon layers are very uniform and show a low roughness, as evidenced by AFM. We note that adhesion of the silicon layer to SCD was very reliable and we never observed any hints of cracking or peeling throughout the whole process, deduced from AFM and SEM microscopy. We have processed more than 10 samples using the here described method and no SEM images showed peeling or cracking of the silicon layer. To avoid any damage of the surface caused by contact with the tip (AFM) or amorphous carbon deposition (from SEM chamber), no routine checks were performed prior each fabrication step. We note we also observed the surface topography of samples covered with HSQ layers. In case of any silicon peeling, this would be evident by folding of spin-coated HSQ.

To manufacture etch masks based on HSQ, we used Fox 16 resist (Dow Corning, Midland, MI, USA), which we spin-coated onto the SCD plate. To ease handling of our small SCD plates, we glued them to silicon carrier chips using crystalbond adhesive. We note that the silicon carrier can be removed at the end of our nanofabrication process using acetone to dissolve crystalbond without damage to the SCD nanostructures. Prior to spin coating, we heated the SCD sample on the silicon carrier for 10 min at 120 °C to remove any moisture from the surface. We applied roughly 0.3 mL of Fox 16 solution to the SCD plate and spin-coated it at 1000 rpm for 10 s then increasing rotation speed to 3300 rpm for 60 s. Subsequently, we pre-baked the sample at 90 °C for 5 min. We note that great care has been taken to not exceed the shelf life of the Fox 16 resist. As a result of the small size of our samples as

well as the spin coating on already etched structures in the latter stages of our fabrication process, we can only estimate the thickness of the HSQ, which shows a significant variation from sample to sample. From SEM images of pillar masks on platforms, we estimate a HSQ layer thickness of $\sim 0.9 \mu\text{m}$. Consequently, considering a pillar diameter of $\sim 200 \text{ nm}$, we demonstrate reliable adhesion of HSQ masks with an aspect ratio of 4.5.

We inserted the SCD plate including the silicon carrier chip into our EBL machine (cold-cathode SEM, Hitachi S45000, Chiyoda, Japan, equipped with RAITH Elphy software). We note that EBL of the spin-coated HSQ layer has to be done directly after spin coating to avoid any reaction of HSQ with air. We performed EBL at 30 kV acceleration voltage and 20 μA extracting current. The working distance is kept at 15.3 mm for $400 \times 400 \mu\text{m}^2$ fields. During our device fabrication, larger structures, namely the rectangular holding platforms (size $\sim 3 \times 20 \mu\text{m}^2$) as well as masks for nanopillars (diameter 200 nm), were of interest. We wrote platforms using longitudinal writing mode and pillars using concentric writing modes. The doses for large structures were established to be optimal as 0.49 mC/cm^2 and for pillar structures, with a variation with thickness of the HSQ layer, between 2.24 (planar SCD) and 7 mC/cm^2 (pre-structured SCD with, e.g., platforms).

We developed the HSQ in 25% TMAH solution without swirling the solution. After 20 s, the SCD sample was placed in ultra-pure 18 MOhm cm MiliQ water and subsequently immersed several times in acetone and isopropanol. We note that the development has to take place directly after removing the SCD plate from the EBL vacuum chamber.

4. Selective ICP-RIE of Adhesion Layer and SCD Structuring

A dedicated ICP/RIE plasma sequence based on O_2 -based etching of SCD, preceded by a short pulse of SF_6 plasma, was designed. This sequence first selectively removes the silicon layer between the HSQ-based mask structures and subsequently enables highly anisotropic etching of SCD. The parameters of the plasmas are summarized in Table 1. In the final process, we ran the above mentioned sequence without removing the sample from the ICP-RIE reactor in-between the plasma steps to avoid any contamination.

Reliably removing the silicon layer without any residuals is vital to our process: We observed a partial etch stop as well as strong micromasking when applying the O_2 -based plasma without applying the SF_6 pulse (see Figure 2a). We deduced a complete and reliable removal of the silicon adhesion layer from two facts: First, in SEM images taken directly after the SF_6 pulse (see Figure 2b), a clear contrast between etched and non-etched areas is visible. We also investigated the SF_6 -based etching process by means of optical emission spectroscopy shown in Figure 2c. In the spectrum a series of emission lines corresponding to fluoride (F^-) was observed [27]. We attributed the etching of silicon to this F^- ions. Second, knowing that the O_2 plasma used to etch SCD was not etching the silicon layer, the absence of micromasking and very smooth surfaces in-between the etched structures (see Figure 3a) proved the complete removal of the silicon layer. We note that using pure SF_6 is vital to arrive at this result, as introduction of other gases (Argon or Oxygen) at this stage generated severe micromasking. Our SF_6 plasma removes the silicon layer while maintaining a 1:20 selectivity in favor of the HSQ mask. For our process, this means that, during removal of the 25 nm thick silicon adhesion layer, less than 2 nm of the HSQ mask, which in our case is several hundreds of nanometer thick, will be lost. This result corresponds well to similar plasmas obtained in different systems showing highly selective silicon etching while conserving SiO_2 (in our case HSQ) [28]. We furthermore observed no or minor etching of SCD during the SF_6 pulse and no roughening of the exposed SCD surface. We confirmed full etching of the silicon layer using Raman spectroscopy and XPS, whereas the latter only showed C1s and O1s peaks. Using EDX, we checked that there is no silicon contamination on the etched SCD after the O_2 -based plasma (see Figure 4).

Table 1. Etching plasma parameters. SF₆ pulse used to selectively remove the evaporated silicon layer (5 s including plasma ignition step). The O₂ plasma is subsequently used as an anisotropic etch for SCD to form the platforms as well as the pillars (10–15 min etching time).

Plasma	ICP Power W	RF Power W	Gas Flux sccm	Etch Rate nm/min	Pressure Pa
SF ₆ pulse	300	100	SF ₆ :25	Si: 1072 HSQ: 52	1.3
O ₂ plasma	500	200	O ₂ : 50	104	1.5

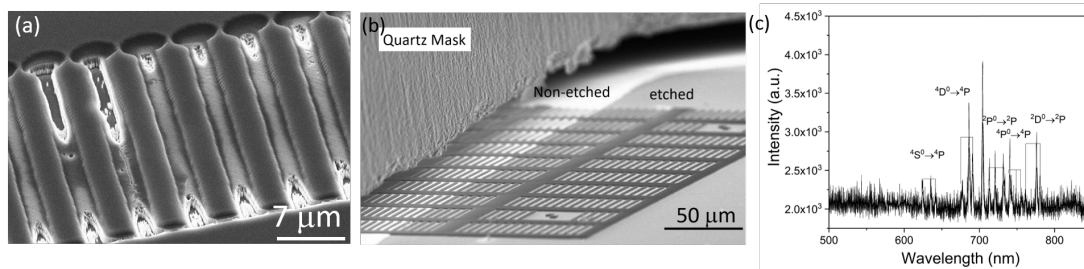


Figure 2. (a) Pattern of holding platforms etched with O₂ plasma without applying the SF₆ pulse plasma to remove the silicon layer, the SEM image shows the bare SCD structures. Strong micro-masking and corresponding roughening as well as a partial etch stop are visible (b) Scanning electron microscope (SEM) image of SCD surface with HSQ structures, here platforms, after SF₆ pulse. A part of the platforms is covered with a quartz plate (marked in the image) during the SF₆ pulse. The strongly reduced brightness of the etched surface in contrast to non-etched surface indicates the complete removal of the silicon adhesion layer. We furthermore observe no or minor etching of SCD during the SF₆ pulse and no roughening of the exposed SCD surface. (c) Optical emission spectrum of the SF₆ pulse plasma step indicating presence of fluoride (F⁻) species responsible for selective removal of silicon from the SCD surface.

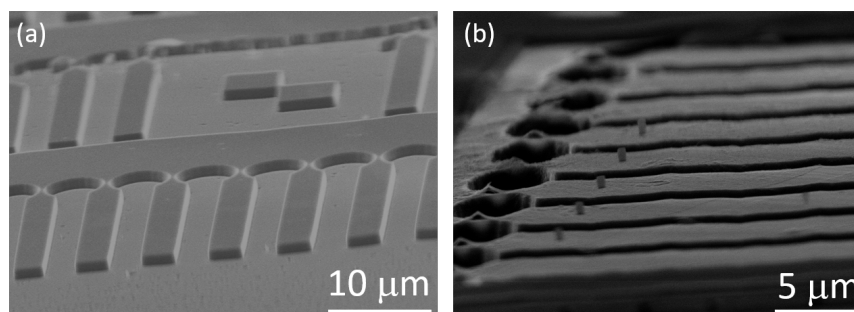


Figure 3. (a) Devices at intermediate stage of the process with etched-in platforms. Note that the SEM image shows the bare SCD structures that have been obtained via removing the adhesion layer using the SF₆ pulse followed by anisotropic O₂ RIE and subsequent cleaning. (b) HSQ masks for pillars etching written by EBL. The masks are residing on SCD platforms coated by a freshly evaporated silicon layer. Note that the silicon layer is not discernible in the SEM images.

After successfully structuring our SCD platforms, we removed HSQ residuals using HF-based buffered oxide etch by immersion of SCD for 20 min in the solution. Although this step removed the native oxide from our silicon adhesion layer, the layer itself survived the process, as clearly discernible from the EDX imaging in Figure 4b. Consequently, it can be re-used for consecutive steps. We then spin-coated HSQ again, which in our case formed a layer on top as well as in-between the platforms. We then re-employed EBL to create pillar masks on the platforms (see Figure 3b). We repeated the etching to transfer the pillar mask into the SCD platform creating almost cylindrical pillars.

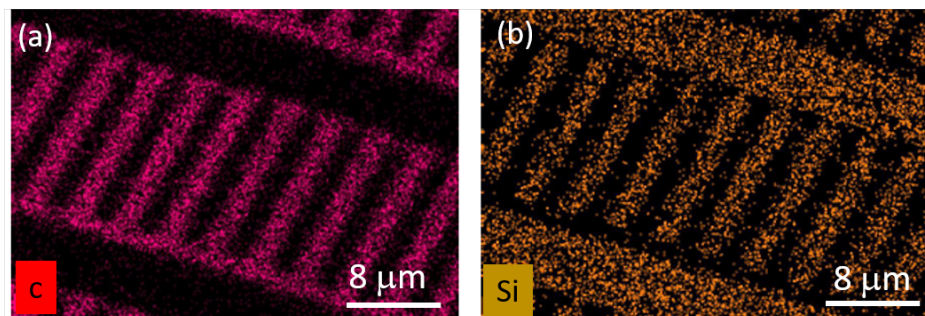


Figure 4. Energy dispersive X-ray (EDX) spectroscopy mapping of SCD cantilevers prepared by the presented method. The EDX mapping has been performed after the SF_6 plasma, the O_2 plasma etching the SCD structures (parameters see Table 1) and the wet chemical removal of residual HSQ: (a) carbon signal; and (b) silicon signal. The two maps show complementary images, clearly indicating that, in-between the platforms, we find bare SCD (carbon) with no silicon signal while on the platform, the silicon adhesion layer survived and is ready to be used in the next processing step.

5. Final Devices and Device Characterization

To obtain clean SCD devices, we removed all HSQ residuals using HF-based buffered oxide etch. We immersed the SCD into buffered oxide etch for 20 min which removes the HSQ as well as any native oxide on the silicon layer. Afterwards, we immersed the SCD sample in 3M potassium hydroxide at 80 °C for 30 min to remove the silicon adhesion layer and revealed the clean SCD structures. After this process, we repeated the three-acid cleaning described above before characterizing the photoluminescence (PL) of NV^- centers in the SCD nanostructures. Figure 5a displays devices obtained using this process. We note that, to obtain free standing devices, which we mounted to quartz capillaries as holders (see Figure 5b), the SCD plate has to be thinned from the non-structured side until the devices are fully released. For more details on the mounting, see Reference [16]. To this end, we employed previously published deep-etching routines [21] which are beyond the scope of this manuscript.

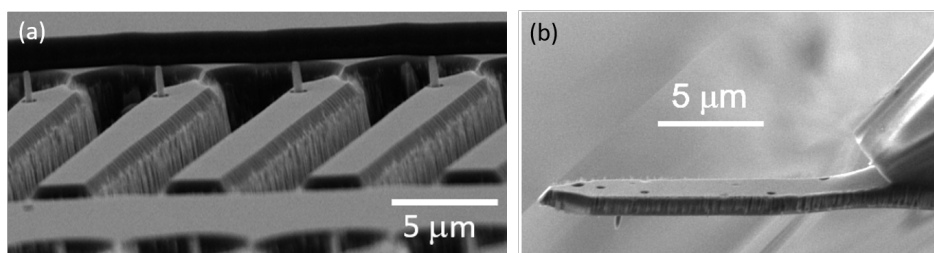


Figure 5. Scanning probe devices manufactured using the described nanofabrication process. (a) Pillars on platforms. The shown devices still need thinning of the SCD plate from the backside to release the devices. (b) Mounted SCD scanning probe. On the right hand side, a quartz capillary is visible that serves as a holder to mount the device to a scanning probe microscope.

To investigate the photonic properties of our SCD nanostructures, we used a custom-built confocal microscope (numerical aperture 0.8). Details of the setup are given in References [22,29–31].

We first measured confocal PL maps of the structures (see Figure 6a,b) excited at 532 nm with a power of 500 μW . We clearly observed intense PL (~ 100 kcps) originating from single NV^- centers in the pillars (see Figure 6a). We estimated the maximum achievable PL of the NV^- centers to be >300 kcps comparable to previous work [16]. In addition, we investigated the background PL from the etched surface (~ 1 kcps), which is negligible compared to the NV^- center PL from the pillar (see Figure 6b).

Keeping background PL from etched surfaces low is important as it limits the signal-to-background ratio and consequently the achievable magnetic field sensitivity [32]. Figure 6c shows an exemplary optically detected magnetic resonance (ODMR) measured on single NV^- centers in the structures. Here, we measured an ODMR contrast of $\sim 15\%$. By investigating the coherence of the NV^- centers in the nanostructures, we found a coherence time of $T_2 \leq 10 \mu s$. We attributed this to the NV^- centers' proximity to the surface which is in a good agreement with results from other groups measuring the coherence of shallow NV^- centers in three-acid-cleaned SCD [33]. Considering the already low T_2 , we cannot fully exclude a negative influence of the structuring on T_2 .

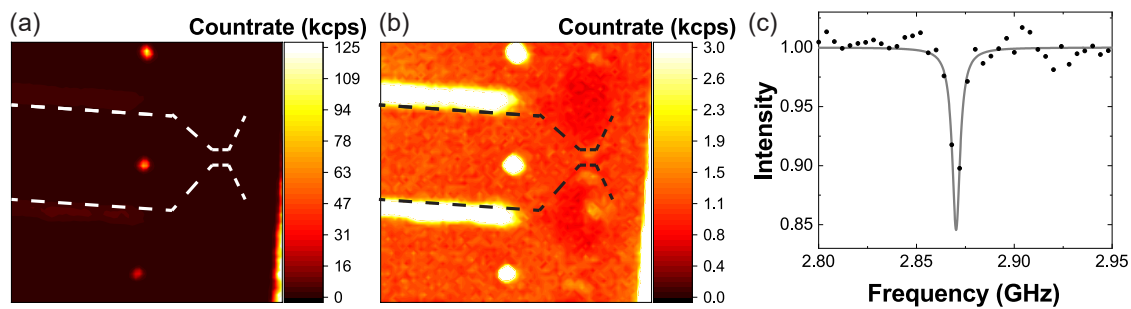


Figure 6. (a,b) PL map of SCD platforms with individual nanopillars fabricated with the process described in Section 4. The outer edge of the holding platform is indicated using a dashed line, while the pillars appear as bright spots. To enable comparing the background PL from the platforms with the PL of a few NV^- centers in the pillars, we show the same PL map with two different scaling: individual NV^- centers in the pillars show PL countrates above 125 kcps at an excitation power of $500 \mu W$ at 532 nm (a). (b) It is clearly discernible that the cantilevers show only a weak PL of $\sim 1 \text{ kcps}$. The enhanced background in-between the platform arises from a slight roughening between the structures. We detect NV^- PL in the wavelength range $>650 \text{ nm}$. (c) An exemplary optically detected magnetic resonance (ODMR) of one of the NV^- centers in the pillar. The resonance (without an external magnetic field) at 2.87 GHz is clearly visible and has a contrast of $\sim 15\%$.

6. Summary and Conclusions

In this paper, we present a reliable technology for nanofabrication of SCD structures. We used our method to manufacture SCD scanning probes with shallowly embedded negative nitrogen vacancies. The method introduces an evaporated silicon adhesion layer on the SCD surface to ease adhesion and EBL with spin-coated HSQ-based Fox 16 resist. We present a methodology for the selective removal of our silicon adhesive/decharging layer with SF_6 plasma. In areas protected by the HSQ mask, silicon layer survives etching as well as wet chemical removal of the residual HSQ mask and can be re-used for further nanofabrication, in our case for pillars on SCD platform. The shallowly implanted NV^- centers survived the nanofabrication process. We found this method to be reliable, which is a considerable advancement in SCD nanofabrication technology that can be expanded to various kinds of SCD structures including SCD cantilever or cavity structures (e.g., photonic crystals).

Author Contributions: Funding acquisition, E.N.; Investigation, M.R., R.N., A.S. and E.N.; Methodology, M.R., R.N., A.S. and E.N.; Supervision, E.N.; Writing—original draft, M.R., R.N. and E.N.; Writing—review and editing, M.R., R.N., A.S. and E.N.

Funding: This research was funded by NanoMatFutur grant of the German Ministry of Education and Research (FKZ13N13547).

Acknowledgments: We would like to acknowledge Sandra Wolff (TU Kaiserslautern, Germany) for help with electron beam evaporation, Jörg Schmauch (INM, Germany) for his help with acquiring high-quality SEM images and Rene Hensel (INM, Germany) for granting access to the ICP/RIE reactor. We acknowledge Michel Challier for his assistance and Andreas Ruh (Saarland University, Germany) for his help with EDX. We gratefully acknowledge cooperation and fruitful discussion with QNAMI (Basel), especially with Felipe Favaro De Oliveira and Patrick Maletinsky on the evaluation of our novel nanofab method. We note that the results presented in this study are filed for a patent, application number: EP19198772.6.

Conflicts of Interest: The authors declare no conflict of interest.

References

1. Atatüre, M.; Englund, D.; Vamivakas, N.; Lee, S.Y.; Wrachtrup, J. Material platforms for spin-based photonic quantum technologies. *Nat. Rev. Mater.* **2018**, *3*, 38. [[CrossRef](#)]
2. Casola, F.; van der Sar, T.; Yacoby, A. Probing condensed matter physics with magnetometry based on nitrogen-vacancy centres in diamond. *Nat. Rev. Mater.* **2018**, *3*, 17088. [[CrossRef](#)]
3. Kucsko, G.; Maurer, P.; Yao, N.; Kubo, M.; Noh, H.; Lo, P.; Park, H.; Lukin, M. Nanometre-scale thermometry in a living cell. *Nature* **2013**, *500*, 54–58. [[CrossRef](#)] [[PubMed](#)]
4. Teissier, J.; Barfuss, A.; Appel, P.; Neu, E.; Maletinsky, P. Strain coupling of a nitrogen-vacancy center spin to a diamond mechanical oscillator. *Phys. Rev. Lett.* **2014**, *113*, 020503. [[CrossRef](#)] [[PubMed](#)]
5. Dolde, F.; Doherty, M.W.; Michl, J.; Jakobi, I.; Naydenov, B.; Pezzagna, S.; Meijer, J.; Neumann, P.; Jelezko, F.; Manson, N.B.; et al. Nanoscale detection of a single fundamental charge in ambient conditions using the NV- center in diamond. *Phys. Rev. Lett.* **2014**, *112*, 097603. [[CrossRef](#)] [[PubMed](#)]
6. Maletinsky, P.; Hong, S.; Grinolds, M.; Hausmann, B.; Lukin, M.; Walsworth, R.; Loncar, M.; Yacoby, A. A robust scanning diamond sensor for nanoscale imaging with single nitrogen-vacancy centres. *Nat. Nanotechnol.* **2012**, *7*, 320–324. [[CrossRef](#)] [[PubMed](#)]
7. Neumann, P.; Kolesov, R.; Naydenov, B.; Beck, J.; Rempp, F.; Steiner, M.; Jacques, V.; Balasubramanian, G.; Markham, M.L.; Twitchen, D.J.; et al. Quantum register based on coupled electron spins in a room-temperature solid. *Nat. Phys.* **2010**, *6*, 249–253. [[CrossRef](#)]
8. Kurtsiefer, C.; Mayer, S.; Zarda, P.; Weinfurter, H. Stable solid-state source of single photons. *Phys. Rev. Lett.* **2000**, *85*, 290–293. [[CrossRef](#)]
9. Babinec, T.; Hausmann, B.; Khan, M.; Zhang, Y.; Maze, J.; Hemmer, P.; Loncar, M. A diamond nanowire single-photon source. *Nat. Nanotechnol.* **2010**, *5*, 195–199. [[CrossRef](#)]
10. Gruber, A.; Dräbenstedt, A.; Tietz, C.; Fleury, L.; Wrachtrup, J.; von Borczyskowski, C. Scanning confocal optical microscopy and magnetic resonance on single defect centers. *Science* **1997**, *276*, 2012–2014. [[CrossRef](#)]
11. Zaitsev, A. *Optical Properties of Diamond: A Data Handbook*; Springer: Berlin, Germany, 2001.
12. Hausmann, B.J.; Khan, M.; Zhang, Y.; Babinec, T.M.; Martinick, K.; McCutcheon, M.; Hemmer, P.R.; Loncar, M. Fabrication of diamond nanowires for quantum information processing applications. *Diam. Relat. Mater.* **2010**, *19*, 621–629. [[CrossRef](#)]
13. Grigorescu, A.; Hagen, C. Resists for sub-20-nm electron beam lithography with a focus on HSQ: State of the art. *Nanotechnology* **2009**, *20*, 292001. [[CrossRef](#)] [[PubMed](#)]
14. Neu, E.; Appel, P.; Ganzhorn, M.; Miguel-Sanchez, J.; Lesik, M.; Mille, V.; Jacques, V.; Tallaire, A.; Achard, J.; Maletinsky, P. Photonic nano-structures on (111)-oriented diamond. *Appl. Phys. Lett.* **2014**, *104*, 153108. [[CrossRef](#)]
15. Fuchs, P.; Challier, M.; Neu, E. Optimized single-crystal diamond scanning probes for high sensitivity magnetometry. *New J. Phys.* **2018**, *20*, 125001. [[CrossRef](#)]
16. Appel, P.; Neu, E.; Ganzhorn, M.; Barfuss, A.; Batzer, M.; Gratz, M.; Tschöpe, A.; Maletinsky, P. Fabrication of all diamond scanning probes for nanoscale magnetometry. *Rev. Sci. Instrum.* **2016**, *87*, 063703. [[CrossRef](#)]
17. Lillie, S.E.; Broadway, D.A.; Dontschuk, N.; Zavabeti, A.; Simpson, D.A.; Teraji, T.; Daeneke, T.; Hollenberg, L.C.; Tettegne, J.P. Magnetic noise from ultrathin abrasively deposited materials on diamond. *Phys. Rev. Mater.* **2018**, *2*, 116002. [[CrossRef](#)]
18. Xie, L.; Zhou, T.X.; Stöhr, R.J.; Yacoby, A. Crystallographic orientation dependent reactive ion etching in single crystal diamond. *Adv. Mater.* **2018**, *30*, 1705501. [[CrossRef](#)]
19. Volpe, P.N.; Muret, P.; Omnes, F.; Achard, J.; Silva, F.; Brinza, O.; Gicquel, A. Defect analysis and excitons diffusion in undoped homoepitaxial diamond films after polishing and oxygen plasma etching. *Diam. Relat. Mater.* **2009**, *18*, 1205–1210. [[CrossRef](#)]
20. Naamoun, M.; Tallaire, A.; Silva, F.; Achard, J.; Doppelt, P.; Gicquel, A. Etch-pit formation mechanism induced on HPHT and CVD diamond single crystals by H₂/O₂ plasma etching treatment. *Phys. Stat. Solidi* **2012**, *209*, 1715–1720. [[CrossRef](#)]

21. Challier, M.; Sonusen, S.; Barfuss, A.; Rohner, D.; Riedel, D.; Koelbl, J.; Ganzhorn, M.; Appel, P.; Maletinsky, P.; Neu, E. Advanced fabrication of single-crystal diamond membranes for quantum technologies. *Micromachines* **2018**, *9*, 148. [[CrossRef](#)]
22. Radtke, M.; Nelz, R.; Render, L.; Neu, E. Plasma treatments and photonic nanostructures for shallow nitrogen vacancy centers in diamond. *arXiv* **2019**, submitted.
23. De Oliveira, F.F.; Momenzadeh, S.A.; Wang, Y.; Konuma, M.; Markham, M.; Edmonds, A.M.; Denisenko, A.; Wrachtrup, J. Effect of low-damage inductively coupled plasma on shallow nitrogen-vacancy centers in diamond. *Appl. Phys. Lett.* **2015**, *107*, 073107. [[CrossRef](#)]
24. Kato, Y.; Kawashima, H.; Makino, T.; Ogura, M.; Traoré, A.; Ozawa, N.; Yamasaki, S. Estimation of inductively coupled plasma etching damage of boron-doped diamond using X-Ray photoelectron spectroscopy. *Phys. Status Solidi (A)* **2017**, *214*, 1700233. [[CrossRef](#)]
25. Krueger, A.; Lang, D. Functionality is key: Recent progress in the surface modification of nanodiamond. *Adv. Funct. Mater.* **2012**, *22*, 890–906. [[CrossRef](#)]
26. Challier, M.; Nelz, R.; Kiendl, B.; Slablab, A.; Radtke, M.; Mueller, F.; Krueger, A.; Neu, E. Wet Chemical Fluorine Treatment of Diamond: Towards Hydrophobic Diamond Nano-Devices for Single NV Sensing. Neu, E. Saarland University, Saarbrücken, Germany. Unpublished work, 2019.
27. d'Agostino, R.; Flamm, D.L. Plasma etching of Si and SiO₂ in SF₆ mixtures. *J. Appl. Phys.* **1981**, *52*, 162–167. [[CrossRef](#)]
28. Morshed, M.; Daniels, S. Electron density and optical emission measurements of SF₆ /O₂ plasmas for silicon etch processes. *Plasma Sci. Technol.* **2012**, *14*, 316–320. [[CrossRef](#)]
29. Nelz, R.; Fuchs, P.; Opaluch, O.; Sonusen, S.; Savenko, N.; Podgursky, V.; Neu, E. Color center fluorescence and spin manipulation in single crystal, pyramidal diamond tips. *Appl. Phys. Lett.* **2016**, *109*, 193105. [[CrossRef](#)]
30. Nelz, R.; Görlitz, J.; Herrmann, D.; Slablab, A.; Challier, M.; Radtke, M.; Fischer, M.; Gsell, S.; Schreck, M.; Becher, C.; et al. Toward wafer-scale diamond nano- and quantum technologies. *Appl. Mater.* **2019**, *7*, 011108. [[CrossRef](#)]
31. Nelz, R.; Radtke, M.; Slablab, A.; Kianinia, M.; Li, C.; Xu, Z.Q.; Bradac, C.; Aharonovich, I.; Neu, E. Near-field energy transfer between a luminescent 2D material and color centers in diamond. *arXiv* **2019**, *1907*, 12248.
32. Rondin, L.; Tetienne, J.P.; Hingant, T.; Roch, J.F.; Maletinsky, P.; Jacques, V. Magnetometry with nitrogen-vacancy defects in diamond. *Rep. Prog. Phys.* **2014**, *77*, 056503. [[CrossRef](#)] [[PubMed](#)]
33. Sangtawesin, S.; Dwyer, B.L.; Srinivasan, S.; Allred, J.J.; Rodgers, L.V.; De Greve, K.; Stacey, A.; Dontschuk, N.; O'Donnell, K.M.; Hu, D.; et al. Origins of diamond surface noise probed by correlating single spin measurements with surface spectroscopy. *Phys. Rev.* **2019**, *9*, 031052. [[CrossRef](#)]



5. Plasma treatments and photonic nanostructures for shallow nitrogen vacancy centers in diamond

Mariusz Radtke, Lara Render, Richard Nelz, and Elke Neu

Opt. Mater. Express **9**, 4716-4733 (2019)
doi: 10.1364/OME.9.004716

Plasma treatments are at the heart of single crystal diamond processing and nanofabrication: They thin and structure single crystal diamond but might also have detrimental effects like damaging the surface. The above stated manuscript evaluates in details different plasma treatments of single crystal diamond.

Richard Nelz (R.N.) investigated the material after the pre-treatment of the diamond to investigate background photoluminescence arising from different plasmas which is crucial for the investigation of single NV centers. Following NV center creation, R.N. investigated the NV ensemble's optical and spin properties in the different regions to identify the optimal plasma-treatment. Hereby, a homebuilt confocal microscope, designed and realized by R.N. was employed. After the fabrication of nanostructures in this area by M. Radtke and L. Render, R.N. selected the appropriate structures to characterize. He supervised L. Render, a bachelor student of the group, investigating the NV centers in the structures and helped to evaluate the data. Further, he wrote the corresponding parts of the manuscript and designed the corresponding figures. In addition, R.N. actively contributed to all discussions during the project and all major revisions of the manuscript.



Plasma treatments and photonic nanostructures for shallow nitrogen vacancy centers in diamond

MARIUSZ RADTKE, LARA RENDER, RICHARD NELZ, AND ELKE NEU* 

Saarland University, Department of Physics, Campus E2.6, 66123 Saarbrücken, Germany

*elkneu@physik.uni-saarland.de

Abstract: We investigate the influence of plasma treatments, especially a 0 V-bias, potentially low damage O₂ plasma as well as a biased Ar/SF₆/O₂ plasma on shallow, negative nitrogen vacancy (NV⁻) centers. We ignite and sustain our 0 V-bias plasma using purely inductive coupling. To this end, we pre-treat surfaces of high purity chemical vapor deposited single-crystal diamond (SCD). Subsequently, we create ~10 nm deep NV⁻ centers via implantation and annealing. Onto the annealed SCD surface, we fabricate nanopillar structures that efficiently waveguide the photoluminescence (PL) of shallow NV⁻. Characterizing single NV⁻ inside these nanopillars, we find that the Ar/SF₆/O₂ plasma treatment quenches NV⁻ PL even considering that the annealing and cleaning steps following ion implantation remove any surface termination. In contrast, for our 0 V-bias as well as biased O₂ plasma, we observe stable NV⁻ PL and low background fluorescence from the photonic nanostructures.

© 2019 Optical Society of America under the terms of the [OSA Open Access Publishing Agreement](#)

1. Introduction

Single-crystal diamond (SCD) with high purity, high crystalline quality and well-controlled surface properties is an enabling material for quantum technologies including quantum sensing [1,2]. SCD is transparent for visible light and supports light confinement and guiding in photonic nanostructures (refractive index 2.4 visible range, indirect electronic band gap 5.45 eV, [3]). SCD hosts more than 500 optically active point defects termed color centers [3]. Considering quantum technologies, the currently mostly investigated color center is the negative nitrogen vacancy complex (NV⁻). NV⁻ centers provide controllable, optically readable spins [4] and are stable electrical dipoles that emit single photons [5,6] or react to optical near-fields [7,8]. Their electronic spin degree of freedom renders them sensitive to magnetic fields [9], electric fields [10], temperature [11] and strain [12] in the diamond matrix. In this context, the key to sensitive measurements with simultaneously nanoscale spatial resolution is to employ individual NV⁻ centers placed shallowly (typically <10 nm) below SCD surfaces. To enable nanoscale imaging of various samples, it is mandatory to embed the sensing NV⁻ in a SCD scanning probe tip [9,13]. In addition to enable scanning of a sample, the SCD tip's photonic properties direct the NV⁻ photoluminescence (PL) to the collection optics and thus enhance sensitivity [9,14]. The most prominent candidates for SCD scanning probes are pyramidal tips [15,16] and cone-shaped or cylindrical pillars (on platforms) [9,13,14]. The latter require sophisticated top-down processes to sculpt the structures from SCD.

Top-down nanofabrication processes reliably create tailored sensing devices potentially enabling highly efficient sensing. However, these processes simultaneously endanger shallow NV⁻ centers: To ensure reliable processing, typically smooth (roughness several nanometers), mostly commercially available SCD plates are used. Mechanical polishing of ultra-hard SCD used to obtain these smooth surfaces, however, may create subsurface damage and stress extending several micrometers into SCD [17,18]. Consequently, SCD surfaces which are highly suited for nanofabrication might not be optimal to host shallow NV⁻. To circumvent this challenge, typically several micrometer of SCD are removed using inductively coupled plasma reactive ion

etching (ICP-RIE) [13]. Typical ICP-RIE plasmas, however, have been shown to damage the uppermost few nanometers of the etched SCD [19]. This damage will also potentially affect shallow NV^- created under this etched surfaces [20]. Moreover, e.g. chlorine gas in the etch plasma is very helpful to keep SCD surfaces smooth during etching [21,22] but might attach to the surfaces, potentially de-activating shallow NV^- [23]. Low damage plasmas in which the etching species are not accelerated towards the etched SCD (0 V-bias plasmas) have been investigated as a solution to the challenge of ICP-RIE induced damage [20]. Using ICP-RIE here is the method of choice as the density of activated species in the plasma and the acceleration towards the etched substrate can be controlled independently of each other by controlling the power inductively coupled to the plasma (ICP power) and the power coupled capacitively to the plasma (often termed radio frequency (RF) power or platen power) [24–26]. Previous work [20] employed the 0 V-bias plasma after creating shallow NV^- . Consequently, the plasma treatment removes SCD containing shallow NV^- centers and alters the NV^- density. Uncertainties in the etch rate of the 0 V-bias plasma thus transform into uncertainties in NV^- density rendering the reliable creation of individual NV^- in nanostructures challenging.

In this manuscript, we present a process to manufacture photonic nanostructures namely nanopillars with shallow, individual NV^- . We, for the first time, include a 0 V-bias O_2 plasma as pre-treatment for NV^- creation and SCD nanopillars fabrication thus avoiding changing the NV^- density by our plasma treatment. Figure 1 summarizes our nanofabrication process.

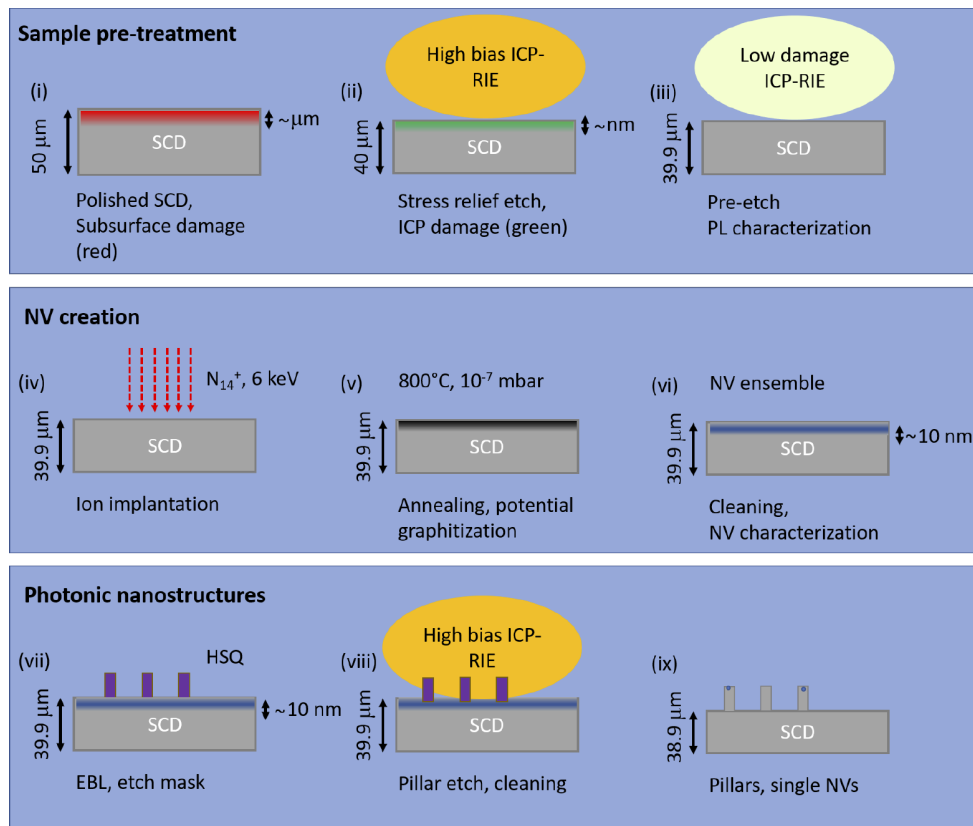


Fig. 1. Schematic of the employed nanofabrication process. The manuscript is structured into the sections according to these schematics.

Following our previous work [27], we restrict the used etch gases to non-corrosive, non-toxic gases namely Ar, SF₆ and O₂. Starting from polished, commercial SCD plates [Fig. 1(i)], we use high bias ICP-RIE to remove micrometer thick potentially damaged layers [**stress relief etch**, Fig. 1(ii)] while conserving smoothness. We finish this processing step with different plasma treatments, especially a potentially low damage O₂ plasma step [**pre-etch**, Fig. 1(iii)]. Following this sample pre-treatment, we use established techniques to create NV⁻ centers [Figs. 1(iv)–1(vi)]. We use an optimized process involving electron beam lithography (EBL) and ICP-RIE to structure nanopillars with single NV⁻ [Figs. 1(vii)–1(ix)]. We characterize single NV⁻ using PL spectroscopy, PL saturation, PL lifetime, photon correlation measurements as well as optically detected magnetic resonance (ODMR).

2. Experimental setup and methods

We use a custom-built confocal scanning microscope (numerical aperture 0.8) to characterize the NV centers' properties in the SCD where confocal filtering is ensured using a single mode fiber. To acquire confocal PL maps, we excite NV centers with a continuous diode-pumped solid-state (DPSS) laser with a wavelength of 532 nm. To investigate the charge state of NV centers, we use an additional DPSS laser with a wavelength of 594 nm. We detect the PL signal through a 650 nm longpass-filter and use highly-efficient photon counters (Excelitas SPCM-AQRH-14, quantum efficiency ~ 70 %) to quantify the PL intensity. In addition, we can send the light to a grating spectrometer (Acton Spectra Pro 2500, Pixis 2560E CCD). We use a tuneable (450-850 nm), pulsed laser (NKT EXW-12, pulse length ~ 50 ps) equipped with a filter system (NKT SuperK Varia) and correlation electronics (PicoQuant, PicoHarp 300) to perform time-resolved PL analysis for e.g. lifetime measurements. To perform spin manipulation on NV⁻ centers in the SCD, we equip the setup with a microwave source (Stanford Research Systems, SG 384) and an amplifier (Mini Circuits, ZHL-42W+) to deliver microwaves through a 20 μm thick gold wire. To perform ICP-RIE, we employ an Oxford Plasmalab 100 ICP RIE system. The plasma lab 100 uses a helical coil ICP configuration. We analyze the plasma composition by means of optical emission spectroscopy (Ocean Optics USB 2000+ coupled by fiber optics to the ICP-RIE system). We employ atomic force microscopy (AFM) measurements (Bruker Fastscan, tapping mode, silicon carbide cantilevers) to deduce the surface roughness of our etched surfaces. To create NV⁻ centers, ion implantation has been performed at Augsburg University (Ion-Implantation-System NV 3206, Axcelis Technologies). Samples were annealed at 800 °C under 1.5 × 10⁻⁷ mbar vacuum using a home-built annealing oven incorporating a heater plate (Tectra Boralectric). We employ a cold-cathode scanning electron microscope (SEM) (Hitachi S45000), equipped with RAITH Elphy software to perform electron beam-lithography (EBL).

3. Sample pre-treatment: stress relief- and pre-etch

In this study, we use commercially available SCD grown by chemical vapor deposition of electronic grade purity (nitrogen, [N_s⁰] <5 ppb and boron [B] <1 ppb, Element Six, UK). The SCD is polished to form plates with 50 μm thickness by Delaware Diamond Knives, US. Using such thin SCD plates is motivated by our goal to manufacture free-standing SCD scanning probe devices that require thinning the plate to a thickness <5 μm [13]. Here, a thickness of 50 μm is a good compromise between mechanical stability and process time for thinning. To ease handling during nanofabrication, we fix the SCD plate to a silicon carrier using small amounts of crystalbond adhesive. The plates have a roughness of R_a=3 nm according to manufacturer specifications and lateral dimensions of 2x4 mm. The received diamonds were cleaned by a boiling tri-acid mixture (1:1:1 v/v of H₂SO₄, HNO₃, HClO₄) and subsequent washing in acetone/isopropanol. We check surface cleanliness in a stereo microscope (50 x magnification) and find no visible residues over the entire SCD surface.

Subsequent to cleaning, we use an etching recipe published previously [27] to remove the topmost $2.3\ \mu\text{m}$ of our SCD plate. This stress relief etch [see also Fig. 1(ii)] is applied uniformly to the full surface of the SCD plate and uses an Ar/SF₆/O₂ plasma as final step (parameters see Table 1). This recipe avoids surface roughening, despite the fact that we are removing potentially damaged SCD material [27]. As indicated by previous work, adding a fluorine containing etch gas to the process aids in avoiding micromasking on the SCD arising from potential silicon contamination in typical ICP-RIE chambers [26].

Table 1. Plasma parameters for stress relief and pre-etch. The etch rate of the 0 V-bias O₂ plasma varied between 8 to 10 nm/min and was thus reasonably consistent.

Plasma	ICP Power (W)	RF Power (W)	DC Bias (V)	Gas Flux (sccm)	Etch Rate (nm/min)	Pressure (mTorr)	roughness (nm)
435 V O ₂	500	200	435	O ₂ : 50	98	11	0.7
Ar/SF ₆ /O ₂	700	100	150	O ₂ 22 SF ₆ :7 Ar:15	87	13	1
0 V O ₂	550	0	0	O ₂ : 50	8	12	0.7

While the stress relief etch procedure reliably removes even tens of micrometers of SCD keeping the surface smooth [27], highly energetic etch species in the plasma potentially damage the first nanometers of the SCD [19]. In this study, we thus systematically investigate the effect of additional plasma steps, termed pre-etch plasmas, which follow the stress relief etch and by which we terminate the removal of material [see Fig. 1(iii)]. We aim to compare different pre-etch treatments applied to the same SCD plate. We thus rule out that sample quality changes influence our findings. To this end, we protect not to be etched areas using a $100\ \mu\text{m}$ thin quartz plate and create three areas in the SCD plate [see Fig. 2(a)]. In two areas, we apply additional pre-etch plasmas (0 V-bias O₂ area I, 435 V-bias O₂ area III) prior to creating shallow NV⁻ centers (see Sec. 4). In contrast, area II is not treated by a pre-etch plasma and was consequently only etched by the Ar/SF₆/O₂ plasma of the stress relief etch.

Table 1 summarizes the parameters of the employed etch plasmas. We note that a larger variety of 0 V-bias plasmas has been tested but only the 0 V-bias O₂ plasma enabled etching without excess surface roughening (see Appendix 7.1). We also take great care to ignite the 0 V-bias plasma without bias building up in its starting phase by careful adjustments of capacitors in the reactor and without using capacitively coupled radio frequency power. As discernible from Table 1, the biased plasmas reach etch rates of almost 100 nm/min, while the 0 V-bias O₂ plasma's etch rate is an order of magnitude lower. As indicated above, $2.3\ \mu\text{m}$ of SCD were removed in the stress-relief etch (and consequently in area II). In area I, we additionally remove $\sim 200\ \text{nm}$ using the 0 V-bias O₂ plasma. In area III, we additionally remove $2\ \mu\text{m}$ using the 435 V-bias O₂ plasma.

After the pre-etches, we again clean the SCD sample as described above and measure the surface roughness in areas I, II and III using AFM. The results of these measurements are depicted in Figs. 2(b)–2(d) and summarized in Table 1. For all areas, we find an rms roughness below 1 nm, consequently all regions are usable for the fabrication of nanopillars with shallow NV⁻. Smooth surfaces are mandatory for high spatial resolution, scanning probe sensing using NV⁻ as any surface roughness will transform into uncontrolled stand-off distances between NV⁻ sensor and sample under investigation.

In the following, we discuss the etch mechanisms underlying the different plasma processes. While all surfaces show low roughness, remarkably the surface etched with the 0 V-bias O₂ plasma shows the lowest roughness. 0 V plasmas have been found to etch isotropically [28,29] via chemical etching effects. This situation might induce micromasking due to e.g. residual impurities/dust on the SCD surface that cannot be removed by this soft plasma or lead to preferential etching of

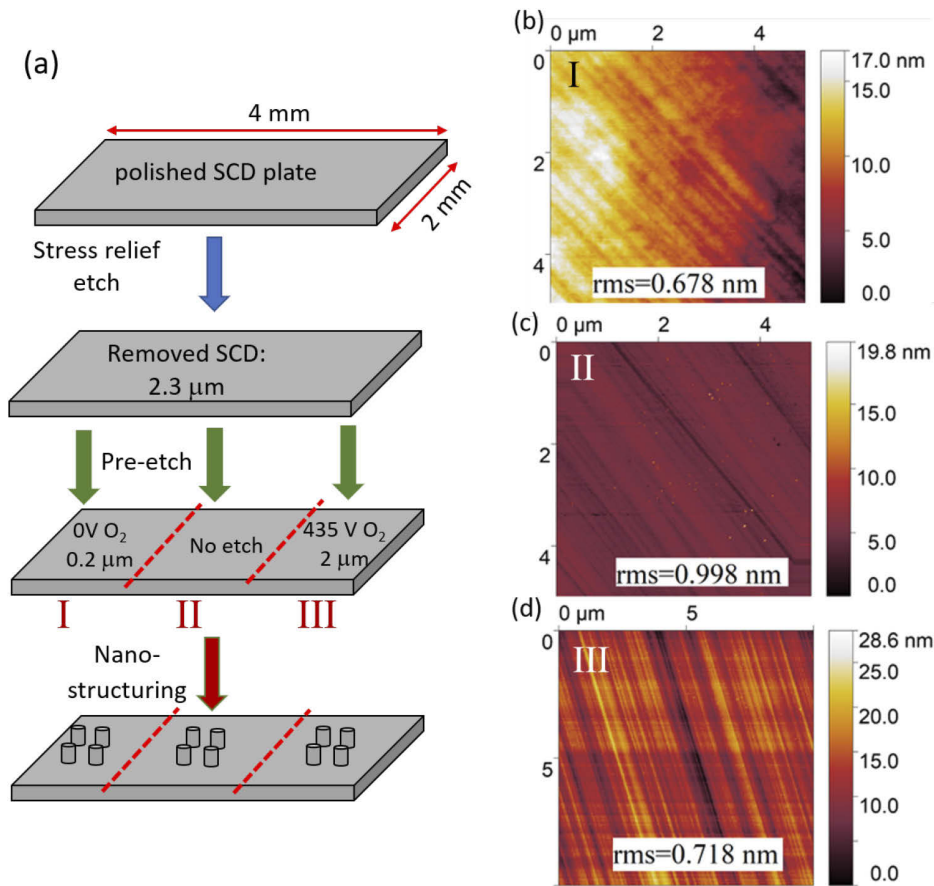


Fig. 2. (a) Sample layout for the characterization of different plasma treatments. The whole polished SCD plate first undergoes the stress relief etch. Subsequently, we apply different pre-etches to form three distinct areas (plasma type and depth of etch given in the sketch). The ordering of the plasma treatments for the pre-etch step is as follows: We cover areas II and III with a quartz plate (thickness $100\ \mu\text{m}$) and apply the $0\ \text{V}\ \text{O}_2$ plasma to area I. By moving the quartz plate and covering areas I and II, the $435\ \text{V}\ \text{O}_2$ plasma was applied to area III. Subsequently, we fabricate nanopillars in all areas. The pillars are not to scale and for illustration only. (b)-(d) AFM scans to determine the surface roughness in areas I, II and III. The given roughness is the rms value obtained from $5 \times 5\ \mu\text{m}^2$ tapping mode scans.

defective areas [26]. However, we do not observe pronounced micromasking in our work. We use optical emission spectroscopy to compare the composition of reactive species in our plasmas (see Fig. 3). Observing the molecular transitions depicted in the insets of Figs. 3(b) and 3(c), we analyze the concentration of ionized oxygen O_2^+ . In a biased O_2 plasma, O_2^+ is the main etching species as the charged ions are effectively accelerated towards the SCD sample and will induce physical etching [30,31]. We find a 50 times higher concentration of O_2^+ in the $435\ \text{V}$ -bias O_2 plasma compared to the $0\ \text{V}$ -bias O_2 plasma (see Fig. 3). In contrast, the etch rate of the $0\ \text{V}$ -bias O_2 plasma is only roughly one order of magnitude lower than for the $435\ \text{V}\ \text{O}_2$ plasma indicating an additional etching species in the $0\ \text{V}$ -bias plasma. We suggest this additional etching species to be (atomic) oxygen radicals. Observing the transitions $3s^5S^0 \rightarrow 3p^5P$ and $3s^5S^0 \rightarrow 3p^3P$ in the oxygen radical system, we find almost the same concentration of oxygen radicals in the

0 V-bias and 435 V-bias plasmas. For the 0 V-bias plasma, chemical etching based on the oxygen radicals is dominant which leads, as expected [32], to much lower etch rates (see Table 1). We expect chemical etching induced by non-accelerated radicals to introduce less damage to the SCD surface compared to the etching via ionized species accelerated under a DC bias. However, chemical etching is isotropic [28,29] and therefore not applicable for nanostructures that require steep sidewalls e.g. nanopillars.

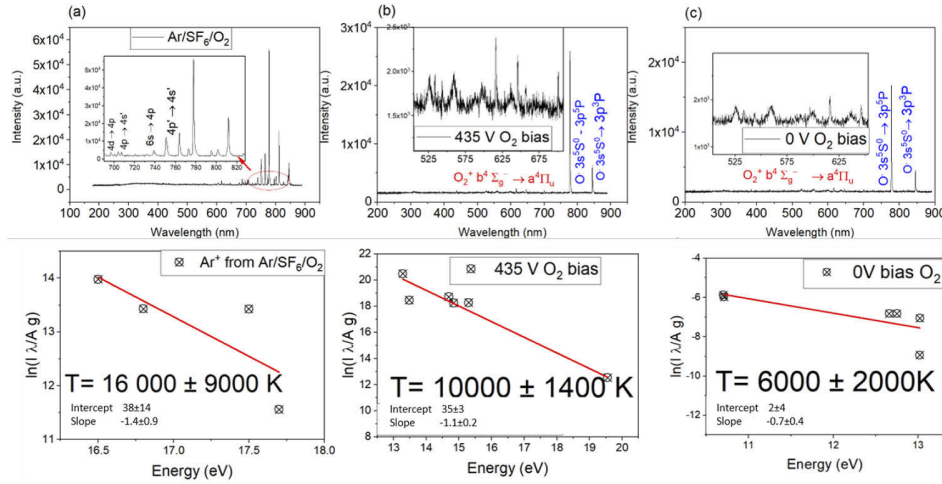


Fig. 3. Optical emission spectra of (a) Ar/SF₆/O₂, (b) O₂ 435 V and (c) O₂ 0 V (350 W ICP) plasmas with corresponding Boltzmann plots used to extract electron temperatures T_{el} .

To additionally characterize the employed O₂ plasmas, we investigate their electron temperature T_{el} . Electrons in the plasma will collide with the molecules/atoms of the etch gas exciting the gas. Consequently, higher electron densities transfer into a higher population of excited states in molecules/atoms. In the absence of a DC bias, the electron temperature can be an upper estimate for the thermal energy of the etching species in the plasma. It should be noted that the electrons might not fully transfer their thermal energy to the etching species but are still a clear indication of the plasma density [33]. In contrast in the case of a biased plasma, the energy of the etching species will be mainly governed by the DC bias [25]. We use the measured optical emission spectra of the plasmas to extract T_{el} . First, we consider that

$$\ln \frac{I\lambda}{g_k A} = -\frac{E_k}{kT_{el}} + C. \quad (1)$$

Here, λ is the wavelength and I the measured intensity of each transition. g_k is the statistical weight of the upper excited level, k the Boltzmann constant, E_k the energy of the excited upper level, A the Einstein coefficient for the respective transition and C is the constant of integration. We plot $\ln \frac{I\lambda}{g_k A}$ as a function of E_k and thus the slope measured is equal to $-\frac{1}{kT_{el}}$ and T_{el} can be extracted. The electronic transitions taken into account to determine T_{el} are marked in Fig. 3.

We find $T_{el}=6000 \pm 2000$ K for the 0 V O₂ plasma, $T_{el}=10000 \pm 1400$ K for the 435 V O₂ plasma and $T_{el}=16000 \pm 9000$ K for our Ar/SF₆/O₂ plasma. For the O₂ plasma especially the following transitions were chosen: $^5P_3 \rightarrow ^3S_2^0$ (544.04 nm), $^5P_1 \rightarrow ^3S_2^0$ (543.06 nm), $^3P_1 \rightarrow ^3S_2^0$ (646.18 nm), $^3D_2 \rightarrow ^3P_2^0$ (615.83 nm), $^3D_1 \rightarrow ^3D_0^0$ (599.45 nm), $^3D_1 \rightarrow ^3D_0^1$ (601.19 nm). These values clearly indicate the higher density of the biased plasmas.

After determining the surface roughness of our SCD samples, we also analyze the PL originating from the etched surfaces. Broadband PL from processed SCD surfaces is detrimental

in experiments with individual NV^- as it will lead to low signal-to-background ratios for single color center observation. Here, we find a spatially homogeneous background PL (detected at wavelengths > 650 nm, excited using 532 nm laser light) in the order of 30 kcps/mW for both O_2 -based pre-etches (areas I and III). The observed PL is stable under continuous laser illumination. In addition, we show that the background PL arises purely from the SCD surface as no PL is observed upon focusing the laser deeply ($> 5 \mu\text{m}$) into the SCD material. Thus, in contrast to previous work [20] that compared a biased Ar/ O_2 plasma with a 0 V- O_2 plasma, we do not find a reduction of PL background for the 0 V- O_2 plasma. We note that the observed background PL from these surfaces is in the same order of magnitude as the PL from single NV^- centers. We find similar background levels after creating shallow NV^- centers (see section 4). However, the fabrication of photonic nanostructures allows us to efficiently reduce the influence of background PL (see section 5).

In stark contrast, the SCD surface exposed to the Ar/ SF_6/O_2 plasma (area II) shows an intense, fast-bleaching background PL. The background that bleaches within ~ 100 ms is in the order of more than 7.5 Mcps/mW. For examples of the PL maps recorded on these surfaces, see Appendix Fig. 8. For diamond films, typically broadband PL in the red-spectral range is observed and attributed to highly defective material (sp^2 inclusions, disorder, amorphous carbon [34]). Significant broadband PL in the red spectral range thus indicates the presence of damaged material close to the surface which could not be removed using the acid clean. Interestingly, this background PL is removed after NV creation steps (see Sec. 4). We suspect that this is connected to the annealing process which in conjunction with acid cleaning aids in removing damaged layers at SCD surfaces [19].

4. Creation of NV centers

Subsequently, we implant the whole surface of our SCD plate using $^{14}N^+$ ions (Energy 6 keV, 2×10^{11} ions/cm²). We create NV^- centers via annealing at 800 °C for 4 hours. We note that directly after this procedure, we typically do not observe any NV^- PL and the emission spectrum of the SCD surface shows non-diamond Raman lines. Re-cleaning the sample in tri-acid mixture activates the NV^- PL which we attribute to the removal of non-diamond, graphitic phases from the SCD surface. We note that alternatively thin layers of NV^- centers can also be introduced using δ -doping, reducing crystal damage due to implantation [35].

We first characterize the influence of the plasma treatments on NV^- centers by investigating the implanted NV^- ensembles. To obtain illustrative results in the different areas, we investigate NV^- ensembles in micrometer-sized marker structures (crosses) that we obtained during nanofabrication (see Sec. 5). These structures do not significantly alter the collection efficiency for NV^- PL or the properties of NV^- ensembles due to their size in the micrometer range. However, they give us the possibility to clearly distinguish NV^- PL from background PL of the SCD surface as well as to clearly compare the different areas. First, we record PL maps of crosses and the corresponding PL spectra in areas I, II and III [see Figs. 4(a)–4(c)]. As clearly discernible from Fig. 4, in areas I and III, the NV^- ensemble has similar PL brightness and the recorded PL spectra clearly reveal the spectral features of NV^- PL. In contrast, in area II treated using the Ar/ SF_6/O_2 etch, we do not find any NV^- PL nor any evidence for neutral NV^0 centers. We note that we do not expect this effect to result from surface termination: First, fluorine terminated surfaces are supposed to stabilize NV^- [37]. Second, any surface termination would have most probably been removed during vacuum annealing and replaced by oxygen functional groups during the acid cleaning. The complete absence of an NV^- fingerprint supports the assumption of highly-damaged layers which prevented the creation of NV^- centers or strongly quench their PL.

In addition, we measure the excited state lifetime τ_{NV^-} [see Fig. 4(d)] of the NV^- ensemble in areas I and III. We obtain comparable results for both areas with $\tau_{NV^-} = 17(1)$ ns for area I and $\tau_{NV^-} = 16(1)$ ns for area III, respectively. Here, τ_{NV^-} is longer than the bulk lifetime (12 ns) due to

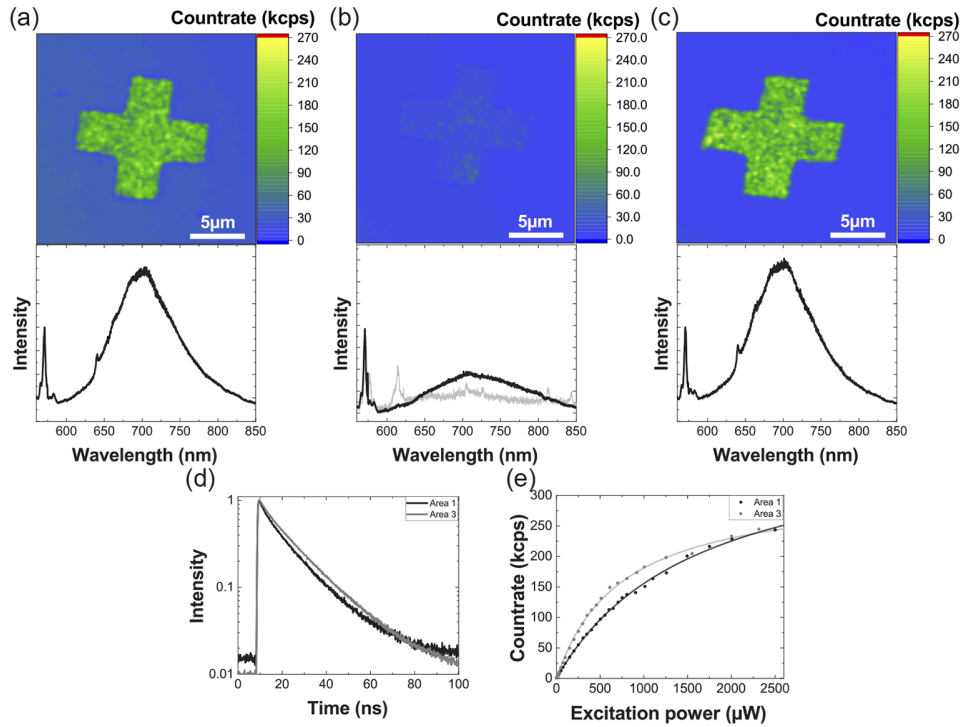


Fig. 4. NV^- center ensembles in areas exposed to different pre-etches: (a)-(c) show PL maps and the corresponding PL spectra. It is clearly visible that in the area exposed to the $\text{Ar}/\text{SF}_6/\text{O}_2$ stress-relief etch only [Area II, part (b)] we do not observe any NV^- PL. The measured spectrum only slightly differs from the background PL (light gray). Both areas treated with pure O_2 plasmas [Area I (unbiased):(a); Area III (biased):(c)] clearly show NV^- PL with a minor NV^0 signal. The peak at 574 nm is the first-order Raman line of SCD. Due to experimental constraints (laser linewidth, spectrometer resolution) the Raman line here does not allow to deduce the level of strain in the SCD material. (d) Excited state lifetime τ_{NV^-} of the NV^- ensemble as recorded in areas I and III. Both ensembles show similar average τ_{NV^-} 17(1) ns in area I and 16(1) ns in area III. τ_{NV^-} is thus prolonged compared to bulk SCD due to the NV^- 's proximity to the surface [36]. In addition, the measurements clearly show an absence of quenching. (e) Saturation behavior of the NV^- ensembles area I and III. Discussion see text.

the NV^- 's proximity to the surface [36]. However, we exclude quenching which would reduce τ_{NV^-} .

To further characterize the influence of the plasma-treatments onto the brightness of the NV^- ensemble, we measure PL saturation curves in areas I and III. Here, we note that we investigate a NV^- ensemble with a low density of ~ 7 NV^- centers statistically distributed in the laser focus of our confocal microscope (density estimate see Sec. 5). Consequently, the observed saturation behavior and the parameters extracted from it are only estimates as few NV^- centers experience different laser intensities as well as different collection efficiencies. We find saturation powers P_{sat} which are in the same order of magnitude (1.60(5) mW area I, 0.74(3) mW area III) as well as comparable background PL rates (~ 60 kcps/mW area I, ~ 40 kcps/mW area III) and count rates ($I_{\infty} = 407(7)$ kcps area I, $I_{\infty} = 315(5)$ kcps area III) in both O_2 -etched areas. We also note that the background PL level estimated here agrees with the level measured in area I and III before creating NV^- centers (see Sec. 3).

By applying microwave-driven spin manipulation to the NV ensembles in areas I and III, we are able to measure their coherence time $T_2 < 10 \mu\text{s}$ limited mainly by the proximity of the NV^- centers to the surface which agrees well with other measurements of shallow NV^- centers under tri-acid cleaned surfaces [38]. In contrast to previous work [20], we do not observe an enhancement of T_2 as a result of the 0 V-bias O_2 plasma treatment. We consequently conclude that T_2 for our NV^- centers is mainly governed by noise due to surface termination and we are not yet able to reveal positive effects of the 0 V-bias O_2 plasma treatment. As we do not observe significant strain-induced splittings of ODMR resonances, we conclude that our NV^- centers are not experiencing significant strain.

5. NV^- in photonic nanostructures

To assess the stability as well as brightness of individual NV^- centers created under the 0 V-bias O_2 plasma treated surface, we fabricate SCD nanopillars in the shape of truncated cones. We aim for diameters of the pillars' top facet that contains the NV^- center in the range of 200 nm. To this end, we use a refined process compared to previously published processes [6,13,39], details of the process are published elsewhere [40]. The steps in the process are:

- Deposition of a silicon adhesion layer onto SCD.
- Spin coating of hydrogen silsesquioxane (HSQ)-based negative tone EBL resist (Fox 16, Dow Corning).
- EBL to create pillar masks, development of resist.
- ICP-RIE removal of adhesion layer and subsequent etching of SCD to form pillars, details see Appendix 7.3 and Ref. [40]
- residual mask stripping in buffered oxide etch and sample cleaning (acid clean).

To demonstrate reliable nanofabrication on all plasma treated surfaces, we generate various patterns of nanopillars on the SCD sample. Using our optimized fabrication process, we reliably create large fields of pillars with high yield [see Fig. 5(a)]. Due to the novelty of our 0 V-bias O_2 plasma pre-treatment, we focus on area I. For consistency, we also check pillars with individual NV centers in area III, confirming stable, bright PL in accordance with previous work [13]. From various pillars fields written in area I using different EBL doses ($1.96\text{-}2.52 \text{ mC}/\text{cm}^2$) and etched using different plasmas (Ar, Ar/ O_2 pure O_2 , for details see Appendix 7.3), we focus on two fields in which we were straightforwardly able to identify single NV^- in the pillars. The tapered pillars written with an EBL dose of $2.2 \text{ mC}/\text{cm}^2$ show top diameters of 120 nm and 180 nm [see Figs. 5(b) and 5(c)].

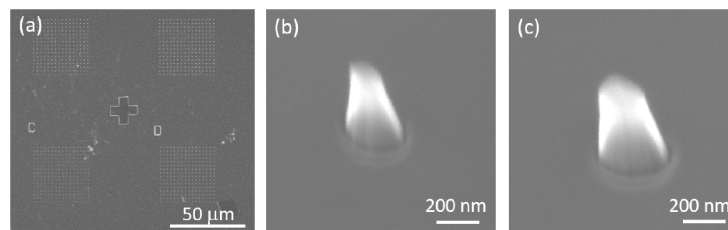


Fig. 5. Scanning electron microscope images of SCD nanopillars. (a) overview of large pillar field, (b) pillars with top diameter of 120 nm (c) pillars with top diameter of 180 nm Images recorded using a Jeol arm200 microscope at 20 kV acceleration voltage with no conductive layer applied.

The investigated pillars have been etched using a pure O₂ plasma (500 W ICP power, 50 W radio frequency (RF) power, 50 sccm O₂, pressure 1.5 Pa). We found O₂ plasmas to be most reliable for etching our SCD pillars and we obtain an etch rate of 65 nm/min. We observe smooth surfaces in-between the pillars without any indication of micromasking. In contrast to the O₂ plasma, mask erosion and micromasking was strong using a pure argon plasma due to excess sputtering of material. We note that the investigated pillars have a stronger taper angle than we typically aim for [14]. The novel fabrication process used here includes a SF₆-based plasma to remove the silicon adhesion layer which could potentially attack HSQ masks [40]. We however find that this plasma etches our thin (25 nm) silicon adhesion layer 20 times faster than the HSQ mask and should not cause mask erosion and strong tapering [40]. We consequently suspect

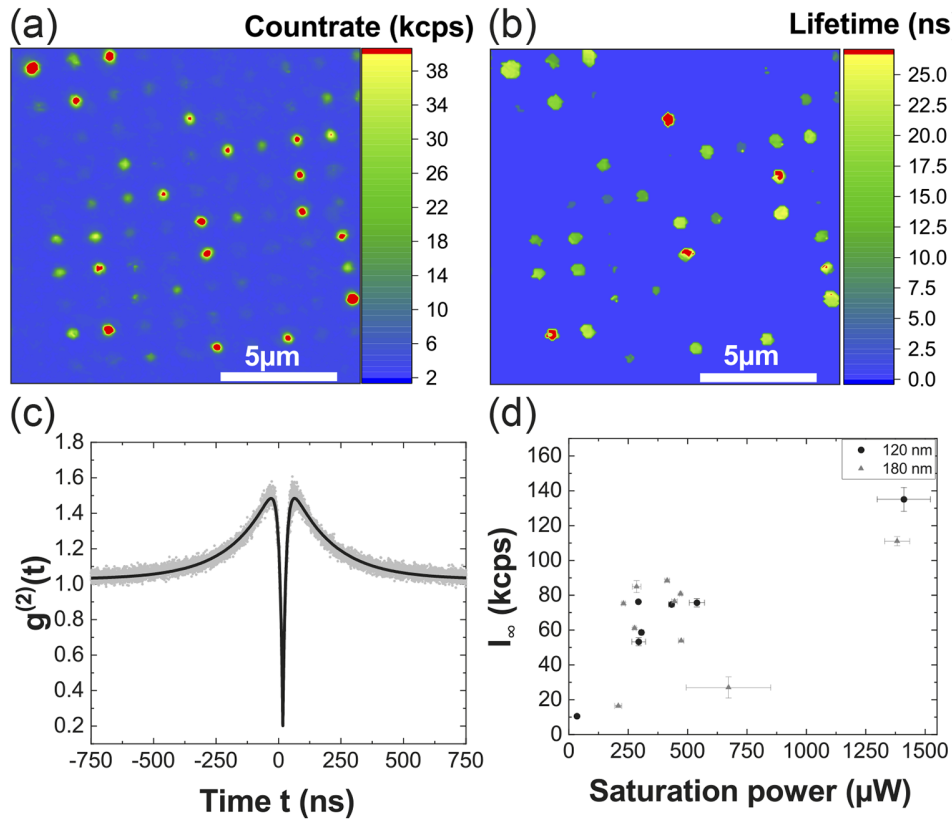


Fig. 6. (a) and (b) Fluorescence maps and lifetime τ_{NV^-} maps of a pillar field (top diameter: 180 nm, length: \sim 460 nm) in area I (0 V O₂ plasma). (a) shows the measured PL rate under pulsed excitation at 530-540 nm with a pulse energy of 15 nJ and a repetition rate of 8 MHz while (b) shows the corresponding lifetime map. It is nicely visible that bright pillars have a consistent lifetime corresponding to τ_{NV^-} measured for the ensemble in Sec. 4. (c) Exemplary second order correlation measurement $g^{(2)}$ of a NV⁻ center in the pillars clearly showing single-photon emission with a reasonable signal/background ratio. (d) Summary of PL saturation of several pillars containing single NV⁻ centers in the fields with top diameters of 120 nm and 180 nm. While most measured NV⁻ have comparable saturation powers, the 180 nm-pillars offer slightly higher countrates compared to the 120 nm-pillars as expected from their photonic properties [14]. However, these results indicate that even 120 nm-pillars act as waveguides, potentially improving AFM operation of NV⁻-based scanning probe devices.

an additional effect causing the tapering. One possibility might be a low thickness of the HSQ layer as the mask structures were not imaged using SEM prior to etching the pillars to avoid contamination. Also strong mask faceting might have occurred that is known to cause tapered sidewalls [41].

To characterize NV^- centers in our photonic nanostructures, we first measure PL and lifetime maps of the pillar fields [see Fig. 6(a) and 6(b)]. Here, we clearly observe a comparable lifetime for most of the pillars containing NV^- centers. In addition, the average lifetime of $\tau_{NV^-} = 17(2)$ ns agrees with τ_{NV^-} we find for the NV^- ensemble in Sec. 4. By measuring second order correlation functions $g^{(2)}$ [see Fig. 6(c)], we estimate a NV^- probability per pillar. We then use the pillars' top diameter from SEM images (Fig. 5) to calculate the NV^- density. Subsequently, we compare this with the implantation dose and extract an implantation yield of $0.01 NV^-/\text{implanted N}$ which is in good agreement with literature [13,42]. To estimate the PL enhancement in our nanostructures, we perform several PL saturation measurements on pillars containing single NV^- centers. These measurements are summarized in Fig. 6(d). Here, we compare NV^- centers in pillars with a length of ~ 460 nm and diameters of 120 nm and 180 nm, respectively. As discernible from Fig. 6(d), most measured NV^- centers show similar saturation power. The 180 nm-pillars offer slightly higher PL rates as the 120 nm-pillars. Simulations suggest a much stronger decrease in PL rate from pillars thinner than 180 nm [14]. However, the here observed brightness of single NV^- PL also indicates a sufficient usability of 120 nm-pillars for sensing applications. For most scanning probe based sensing applications, it would be advantageous to use pillars with a small top diameter, as a thinner scanning probe tip will be able to follow the topography of a sample more closely and keep the NV^- center closer to the surface under investigation e.g. when scanning over a step in the sample [13]. We note that we were not able to deduce NV^- and NV^0 probabilities for our NV centers [43–45] due to inconclusive results (see Appendix 7.4).

6. Conclusions

In the presented study, we investigate a chemically etching, pure ICP discharge, 0 V-bias O_2 plasma as a pre-etch for the fabrication of SCD photonic structures. We compare this treatment to a biased O_2 plasma as well as a $Ar/O_2/SF_6$ plasma. We analyze plasma compositions and etch rates. While the biased plasmas have etch rates exceeding 100 nm/min, the 0 V-bias plasma shows an order of magnitude lower etch rate. While etching in the biased O_2 plasma is dominated by oxygen ions, oxygen radicals dominate in the 0 V-bias case. Remarkably, we only succeed in creating shallow NV^- under the O_2 treated surfaces, while all NV^- centers are deactivated under the $Ar/O_2/SF_6$ treated surface. We investigate single NV^- centers in the nanopillars with 180 nm as well as 120 nm top diameter. We find stable, bright emission from single NV^- rendering our structures suitable for nanoscale sensing using single NV^- . We have shown that 0 V-bias plasmas can be integrated into the fabrication of SCD photonic nanostructures as a pre-treatment, opening the route towards low damage treatments of SCD surfaces within SCD nanodevice fabrication.

7. Appendix

7.1. Testing of 0 V plasmas and sample layout

To check the applicability of 0 V-bias plasmas to pre-etch our SCD surfaces, we run different plasmas. Figure 7 summarizes the tested 0 V plasmas. We select only the 0 V O_2 plasma for the main study due to the observed large surface roughening of 0 V Ar/SF_6 and Ar plasmas (rms ≥ 10 nm). We furthermore expect no significant etch rate in a 0 V SF_6 plasma and do thus also not use this plasma. Figure 7 shows the bias drop in time for each plasma after the ignition. This drop could be eliminated by optimizing the matching circuit parameter conditions- which required a run of pre-tests before actual etching prior to each process. The bias drop was found to be comparable in time for each plasma and was dependent on the chamber pressure and gas flux.

For the studies presented in the manuscript, we used the optimized parameters for the matching circuit and consequently avoid any buildup of bias.

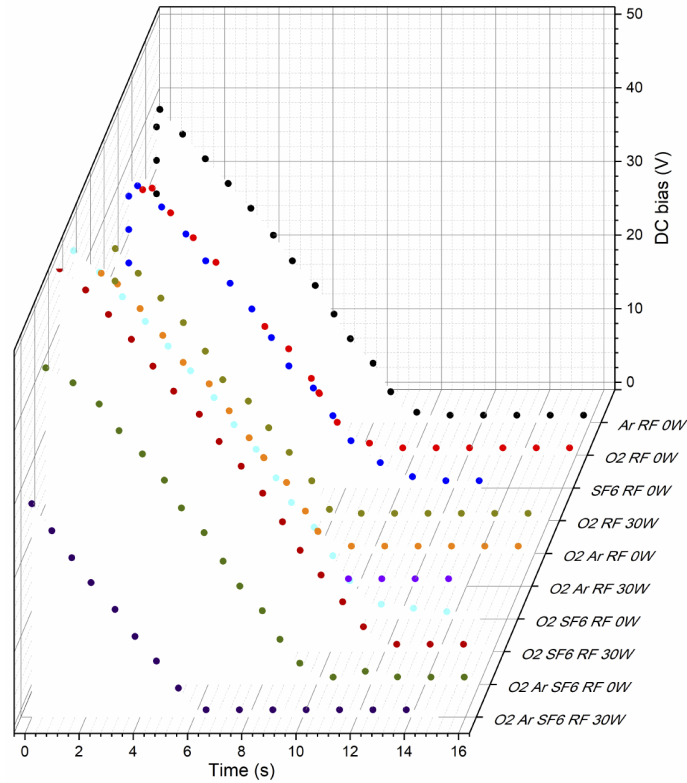


Fig. 7. Bias drop in time in generation of 0 V-bias plasmas using O₂, Ar, SF₆ and their mixtures.

7.2. Characterization of the pre-etched areas

As described in the main text, we characterize the three pre-etched areas after etching and cleaning before implanting nitrogen ions into the SCD.

Here, we see a similar behavior of the two oxygen etched areas leading to a spatially homogeneous background PL of 30 kcps/mW [see Figs. 8(a) and 8(c), area I and III]. In contrast, the Ar/SF₆/O₂-etched area II shows a different behavior: Here, we clearly see a high background PL in the order of 7.5 Mcps/mW which is rapidly bleaching within roughly 100 ms. This is clearly visible in Fig. 8(b). Here, we first measure a smaller PL map and afterwards a larger PL map around it. This second PL map clearly shows the bleached square of the first measurement. By further focusing the laser onto a single point (as can be seen in the lower left and upper right corner of the smaller square) we are able to further bleach the PL to PL rates comparable with the oxygen-etched areas. In addition, we scan the focus of our confocal laser microscope through the SCD surface (z-scans). Z-scans in all areas clearly show that the background PL originates only from the SCD surface. Note, that z-scans in area II [Fig. 8(b)] do not show a clear peak due to the bleaching behavior which is triggered by focusing onto the surface.

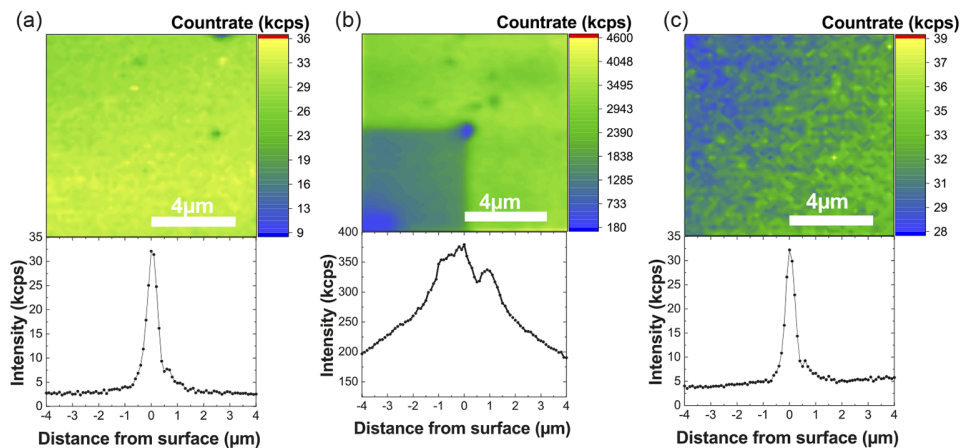


Fig. 8. Optical characterization of the three pre-etched areas: (a) unbiased O_2 , (b) $Ar/SF_6/O_2$, (c) biased O_2 . For further information, see text.

7.3. Details on pillar fabrication

7.3.1. Technical details on electron beam lithography

Diamond plates immobilized on a silicon chip and spin coated with negative tone, HSQ-based resist FOX-16 were inserted into cold-cathode SEM (Hitachi S45000), equipped with RAITH Elphy software. The electron beam is calibrated on a Si chip containing nanoparticles and the writing process is performed at 30 kV acceleration voltage and 20 μA extracting current. The beam current was measured always prior the lithography session and applied as correction for the writing dose in the software. The z-distance was kept constant at 15.3 nm for 400x400 μm fields. The writing process occurs at 100x magnification. The writing mode for long structures is kept longitudinal and for small structures concentric. The area dose is kept as 1400 $\mu As/cm^2$. The dose was established to be 2.24 mC/cm^2 for the pillar structures. Varying the dose in the electron beam lithography, influences the shape of the resulting nanopillars as well as their diameter.

7.3.2. Details on pillar etching

Areas I, II and III were divided into three sub-parts each. We fabricated various pillars masks using a variety of EBL parameters out of HSQ that were treated with various oxygen and argon plasmas to elucidate the effects of DC bias, RF/ICP power and gas flux on the geometry of the pillars.

In order to remove the adhesive layer used at the SCD/HSQ interface, a specialized SF_6 -based etching plasma was applied prior to etching the SCD pillars for 5 seconds. Figure 9 shows detailed scanning electron microscope images of etched SCD nanostructures. Figure 9(a) shows large pillar fields as an indication of the reliability of the employed nanofabrication process. Figure 9(b) gives examples of nanopillars written with different EBL doses and a nominal mask diameter of 180 nm. As clearly discernible from Fig. 10, increasing the dose increases the effective mask size and consequently the top diameter of the pillar. All SEM images were acquired at 20 kV acceleration voltage without the use of conductive layer. The mask erosion and resulting micromasking was especially visible with use of pure Ar plasma probably due to sputtering effects and we observed the generation of needles and damaged surface. This effect was lowered, while mixing argon with other gases (SF_6 , O_2) and totally removed by using only biased oxygen plasma for the etching. We achieved the best control over the pillar shape using a

O₂ plasma at 750 W ICP power and 50 W RF power, 90 ±5 nm etch rate, 2.2 mC/cm² writing dose for the FOX-16 mask (compare Table 2).

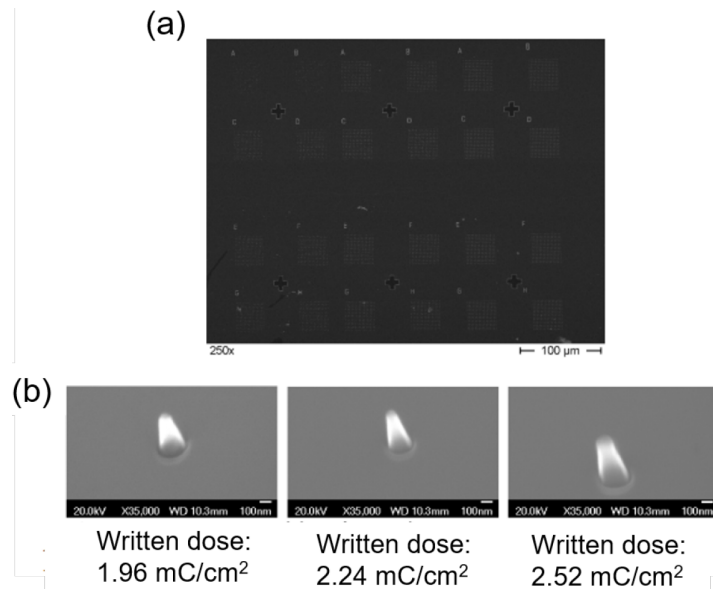


Fig. 9. SEM images of SCD nanopillars: (a) overview image of large pillar fields etched into the diamond by O₂ plasma (b) High magnification scanning electron microscope (Jeol arm200, 20 kV acceleration voltage, no conductive layer applied).

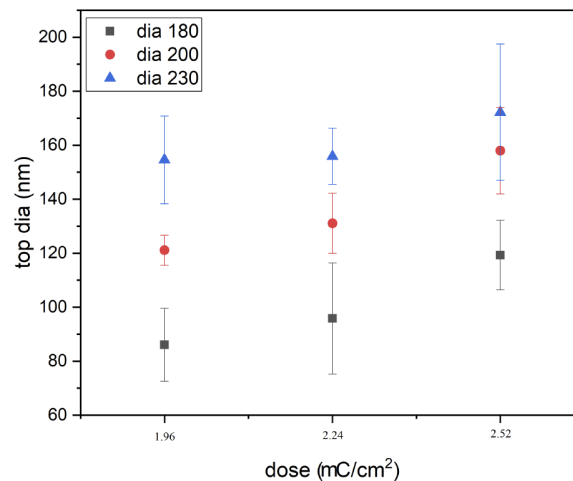


Fig. 10. Correlation between the EBL dose and the resulting top diameter of the nanopillars. The investigated pillars have been etched using a pure O₂ plasma with 500 W ICP power and 50 W RF power.

7.4. Charge state detection

To further study the influence of the different pre-etches on single NV⁻ centers, we investigate the switching between NV⁻ and NV⁰ for our centers according to [43–45]. Typically, this

Table 2. Parameters for different etch plasmas. Due to excess mask erosion etch rates of the pure Ar plasmas have to be considered coarse estimates.

Plasma	DC bias	RF power (W)	ICP Power (W)	etch rate (nm/min)
O ₂ /Ar	191	50	500	–
O ₂	170	50	500	65
Ar	149	50	500	20
O ₂ /Ar	157	50	750	65
O ₂	144	50	750	90
Ar	119	50	750	10

measurement shows two Poisson distributions whereas the distribution at low count rates corresponds to NV⁰ and the second one to NV⁻ PL. We here find one distribution broader than usual [see Fig. 11(a)]. This could be explained by the following: First, both distributions are joint hindering a clear distinction of both distributions [see Fig. 11(b)]. This could be mainly arising from enhanced background PL. This enhanced background might arise from residuals that were created during repeated cleaning of our sample before the charge state investigations. Second, these residuals could also cause a change of the electrical environment of the NV centers potentially increasing the charge state switching rates drastically. When this rate exceeds 1/read-out time, both distributions start to merge and eventually become one distribution centered around the mean PL of both charge states [see Fig. 11(c)]. Due to the limited amount of photons we detect under weak excitation with the 594 nm laser, we are not able to optimize our read-out time for fast charge state switching rates.

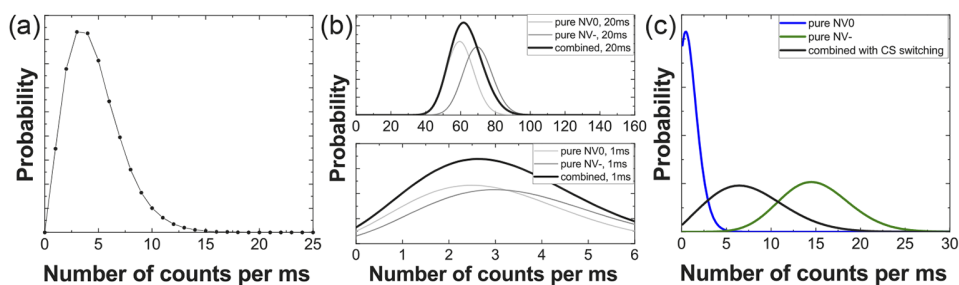


Fig. 11. (a) Exemplary measurement of the charge state distribution we obtain on the NV centers in the nanostructures. Here, we use the following parameters: 532 nm laser: 1 ms at 100 μ W, 594 nm-laser: 1 ms at 15 μ W, read-out time: 1 ms. While using excitation powers ranging from 1 μ W to 250 μ W for both lasers and integration times up to 25 ms, the mean values of the distributions are just shifting without a significant change of the distribution. (b-c) Calculated photon statistics for illustrating the behavior for special cases described in the text.

To further explain the behavior of the charge state detection measurement, we first have to briefly introduce the photon statistics model used to describe the process. Here, we follow the derivation of [44,45].

By allowing the charge state of the NV center to switch during the measurement, the resulting photon probability changes from two pure Poissonian distributions to a more complex distribution which involves a sum over an infinite number of Poisson distributions weighted by the probability for switching the charge state [44,45]. This leads to a complex behavior:

First, we describe the case of the Poissonian distributions lying closely together. This belongs to the case of a strong background PL or a weak NV⁻ PL as shown in Fig. 11(b). Both panels

in Fig. 11(b) show the same mean count-rate of the background and NV^- , respectively, with different read-out times (1 ms in the lower panel, 20 ms in the upper). Here, it is clearly visible that even by significantly increasing the read out time of the charge state detection it is not possible to distinguish two distributions when the difference of background PL and NV^- PL is too low. Note, we use a negligible charge state switching rate for this calculation.

Second, we describe the case of a fast switching between the charge states of the NV center compared to the read-out time. This is shown in Fig. 11(c). Here, we have two clearly distinguishable distributions for the pure NV charge states (blue for NV^0 and olive for NV^-). By calculating the complex photon statistics with ionization rates exceeding $1/\text{read-out time}$, we get the black curve. This shows that even distinguishable mean photon rates can result in an indistinguishable photon distribution in the case of fast charge state switching.

Funding

Bundesministerium für Bildung und Forschung (FKZ13N13547).

Acknowledgments

We would like to acknowledge Dr. Matthias Schreck and Wolfgang Brückner (Augsburg University, Germany) for performing nitrogen ion implantations, Dr. Ing. Sandra Wolff (TU Kaiserslautern, Germany) for help with electron beam evaporation, Jörg Schmauch (Saarland University, Germany) for his help with acquiring high-quality SEM images and Dr. Rene Hensel (INM, Germany) for granting access to the ICP RIE reactor. We acknowledge Michel Challier for his assistance.

Disclosures

We note that the nanofabrication method applied in this study is filed for a patent, application number: EP19198772.6. The authors declare no conflicts of interest.

References

1. M. Atatüre, D. Englund, N. Vamivakas, S.-Y. Lee, and J. Wrachtrup, "Material platforms for spin-based photonic quantum technologies," *Nat. Rev. Mater.* **3**(5), 38–51 (2018).
2. F. Casola, T. van der Sar, and A. Yacoby, "Probing condensed matter physics with magnetometry based on nitrogen-vacancy centres in diamond," *Nat. Rev. Mater.* **3**(1), 17088 (2018).
3. A. Zaitsev, *Optical Properties of Diamond: A Data Handbook* (Springer, 2001).
4. A. Gruber, A. Dräbenstedt, C. Tietz, L. Fleury, J. Wrachtrup, and C. von Borczyskowski, "Scanning confocal optical microscopy and magnetic resonance on single defect centers," *Science* **276**(5321), 2012–2014 (1997).
5. C. Kurtsiefer, S. Mayer, P. Zarda, and H. Weinfurter, "Stable solid-state source of single photons," *Phys. Rev. Lett.* **85**(2), 290–293 (2000).
6. T. Babinec, B. Hausmann, M. Khan, Y. Zhang, J. Maze, P. Hemmer, and M. Loncar, "A diamond nanowire single-photon source," *Nat. Nanotechnol.* **5**(3), 195–199 (2010).
7. J. Tisler, T. Oeckinghaus, R. J. Stöhr, R. Kolesov, R. Reuter, F. Reinhard, and J. Wrachtrup, "Single defect center scanning near-field optical microscopy on graphene," *Nano Lett.* **13**(7), 3152–3156 (2013).
8. R. Nelz, M. Radtke, A. Slablab, M. Kianinia, C. Li, Z.-Q. Xu, C. Bradac, I. Aharonovich, and E. Neu, "Near-field energy transfer between a luminescent 2d material and color centers in diamond," *Adv. Quantum Technol.* 1900088 (2019).
9. P. Maletinsky, S. Hong, M. Grinolds, B. Hausmann, M. Lukin, R. Walsworth, M. Loncar, and A. Yacoby, "A robust scanning diamond sensor for nanoscale imaging with single nitrogen-vacancy centres," *Nat. Nanotechnol.* **7**(5), 320–324 (2012).
10. F. Dolde, M. W. Doherty, J. Michl, I. Jakobi, B. Naydenov, S. Pezzagna, J. Meijer, P. Neumann, F. Jelezko, N. B. Manson, and J. Wrachtrup, "Nanoscale detection of a single fundamental charge in ambient conditions using the nv-center in diamond," *Phys. Rev. Lett.* **112**(9), 097603 (2014).
11. G. Kucsko, P. Maurer, N. Yao, M. Kubo, H. Noh, P. Lo, H. Park, and M. Lukin, "Nanometre-scale thermometry in a living cell," *Nature* **500**(7460), 54–58 (2013).
12. J. Teissier, A. Barfuss, P. Appel, E. Neu, and P. Maletinsky, "Strain coupling of a nitrogen-vacancy center spin to a diamond mechanical oscillator," *Phys. Rev. Lett.* **113**(2), 020503 (2014).

13. P. Appel, E. Neu, M. Ganzhorn, A. Barfuss, M. Batzer, M. Gratz, A. Tschöpe, and P. Maletinsky, "Fabrication of all diamond scanning probes for nanoscale magnetometry," *Rev. Sci. Instrum.* **87**(6), 063703 (2016).
14. P. Fuchs, M. Challier, and E. Neu, "Optimized single-crystal diamond scanning probes for high sensitivity magnetometry," *New J. Phys.* **20**(12), 125001 (2018).
15. R. Nelz, P. Fuchs, O. Opaluch, S. Sonusen, N. Savenko, V. Podgursky, and E. Neu, "Color center fluorescence and spin manipulation in single crystal, pyramidal diamond tips," *Appl. Phys. Lett.* **109**(19), 193105 (2016).
16. L. Nicolas, T. Delord, P. Huillery, E. Neu, and G. Hétet, "Diamond nano-pyramids with narrow linewidth s_{iv} centers for quantum technologies," *AIP Adv.* **8**(6), 065102 (2018).
17. P.-N. Volpe, P. Muret, F. Omnes, J. Achard, F. Silva, O. Brinza, and A. Gicquel, "Defect analysis and excitons diffusion in undoped homoepitaxial diamond films after polishing and oxygen plasma etching," *Diamond Relat. Mater.* **18**(10), 1205–1210 (2009).
18. M. Naamoun, A. Tallaire, F. Silva, J. Achard, P. Doppelt, and A. Gicquel, "Etch-pit formation mechanism induced on hpht and cvd diamond single crystals by h₂/o₂ plasma etching treatment," *Phys. Status Solidi A* **209**(9), 1715–1720 (2012).
19. Y. Kato, H. Kawashima, T. Makino, M. Ogura, A. Traoré, N. Ozawa, and S. Yamasaki, "Estimation of inductively coupled plasma etching damage of boron-doped diamond using x-ray photoelectron spectroscopy," *Phys. Status Solidi A* **214**(11), 1700233 (2017).
20. F. F. de Oliveira, S. A. Momenzadeh, Y. Wang, M. Konuma, M. Markham, A. M. Edmonds, A. Denisenko, and J. Wrachtrup, "Effect of low-damage inductively coupled plasma on shallow nitrogen-vacancy centers in diamond," *Appl. Phys. Lett.* **107**(7), 073107 (2015).
21. C. Lee, E. Gu, M. Dawson, I. Friel, and G. Scarsbrook, "Etching and micro-optics fabrication in diamond using chlorine-based inductively-coupled plasma," *Diamond Relat. Mater.* **17**(7-10), 1292–1296 (2008).
22. I. Friel, S. Clewes, H. Dhillon, N. Perkins, D. Twitchen, and G. Scarsbrook, "Control of surface and bulk crystalline quality in single crystal diamond grown by chemical vapour deposition," *Diamond Relat. Mater.* **18**(5-8), 808–815 (2009).
23. Y. Tao, J. Boss, B. Moores, and C. Degen, "Single-crystal diamond nanomechanical resonators with quality factors exceeding one million," *Nat. Commun.* **5**(1), 3638 (2014).
24. D. Hwang, T. Saito, and N. Fujimori, "New etching process for device fabrication using diamond; Proceedings of the 9th International Conference on New Diamond Science and Technology (ICNDST-9)," *Diamond Relat. Mater.* **13**(11-12), 2207–2210 (2004).
25. L. Xie, T. X. Zhou, R. J. Stöhr, and A. Yacoby, "Crystallographic orientation dependent reactive ion etching in single crystal diamond," *Adv. Mater.* **30**(11), 1705501 (2018).
26. M.-L. Hicks, A. C. Pakpour-Tabrizi, V. Zuerbig, L. Kirste, C. Nebel, and R. B. Jackman, "Optimizing reactive ion etching to remove sub-surface polishing damage on diamond," *J. Appl. Phys.* **125**(24), 244502 (2019).
27. M. Challier, S. Sonusen, A. Barfuss, D. Rohner, D. Riedel, J. Koelbl, M. Ganzhorn, P. Appel, P. Maletinsky, and E. Neu, "Advanced fabrication of single-crystal diamond membranes for quantum technologies," *Micromachines* **9**(4), 148 (2018).
28. B. Khanaliloo, M. Mitchell, A. C. Hryciw, and P. E. Barclay, "High-Q/V Monolithic Diamond Microdisks Fabricated with Quasi-isotropic Etching," *Nano Lett.* **15**(8), 5131–5136 (2015).
29. B. Khanaliloo, H. Jayakumar, A. C. Hryciw, D. P. Lake, H. Kaviani, and P. E. Barclay, "Single-crystal diamond nanobeam waveguide optomechanics," *Phys. Rev. X* **5**(4), 041051 (2015).
30. Y. Zhang, C. Charles, and R. Boswell, "Thermodynamic study on plasma expansion along a divergent magnetic field," *Phys. Rev. Lett.* **116**(2), 025001 (2016).
31. K. Bazaka, O. Baranov, U. Cvelbar, B. Podgornik, Y. Wang, S. Huang, L. Xu, J. W. M. Lim, I. Levchenko, and S. Xu, "Oxygen plasmas: a sharp chisel and handy trowel for nanofabrication," *Nanoscale* **10**(37), 17494–17511 (2018).
32. A. Sarangan, "5 - nanofabrication," in *Fundamentals and Applications of Nanophotonics*, J. W. Haus, ed. (Woodhead Publishing, 2016), pp. 149–184.
33. Y. Zhang, C. Charles, and R. Boswell, "Thermodynamic study on plasma expansion along a divergent magnetic field," *Phys. Rev. Lett.* **116**(2), 025001 (2016).
34. L. Bergman, M. McClure, J. Glass, and R. Nemanich, "The origin of the broadband luminescence and the effect of nitrogen doping on the optical properties of diamond films," *J. Appl. Phys.* **76**(5), 3020–3027 (1994).
35. F. F. de Oliveira, S. A. Momenzadeh, D. Antonov, J. Scharpf, C. Osterkamp, B. Naydenov, F. Jelezko, A. Denisenko, and J. Wrachtrup, "Toward Optimized Surface delta-Profiles of Nitrogen-Vacancy Centers Activated by Helium Irradiation in Diamond," *Nano Lett.* **16**(4), 2228–2233 (2016).
36. R. Nelz, J. Görlitz, D. Herrmann, A. Slablab, M. Challier, M. Radtke, M. Fischer, S. Gsell, M. Schreck, C. Becher, and E. Neu, "Toward wafer-scale diamond nano-and quantum technologies," *APL Mater.* **7**(1), 011108 (2019).
37. C. Osterkamp, J. Lang, J. Scharpf, C. Müller, L. P. McGuinness, T. Diemant, R. J. Behm, B. Naydenov, and F. Jelezko, "Stabilizing shallow color centers in diamond created by nitrogen delta-doping using sf₆ plasma treatment," *Appl. Phys. Lett.* **106**(11), 113109 (2015).
38. S. Sangtawesin, B. L. Dwyer, S. Srinivasan, J. J. Allred, L. V. Rodgers, K. De Greve, A. Stacey, N. Dontschuk, K. M. O'Donnell, D. Hu, and D.A. Evans, "Origins of diamond surface noise probed by correlating single spin measurements with surface spectroscopy," arXiv preprint arXiv:1811.00144 (2018).

39. E. Neu, P. Appel, M. Ganzhorn, J. Miguel-Sanchez, M. Lesik, V. Mille, V. Jacques, A. Tallaire, J. Achard, and P. Maletinsky, "Photonic nano-structures on (111)-oriented diamond," *Appl. Phys. Lett.* **104**(15), 153108 (2014).
40. M. Radtke, R. Nelz, L. Render, and E. Neu, "Reliable nanofabrication of single-crystal diamond photonic nanostructures for nanoscale sensing," *Micromachines* **10**(11), 718 (2019).
41. A. Toros, M. Kiss, T. Graziosi, H. Sattari, P. Gallo, and N. Quack, "Precision micro-mechanical components in single crystal diamond by deep reactive ion etching," *Microsyst. Nanoeng.* **4**(1), 12 (2018).
42. S. Pezzagna, B. Naydenov, F. Jelezko, J. Wrachtrup, and J. Meijer, "Creation efficiency of nitrogen-vacancy centres in diamond," *New J. Phys.* **12**(6), 065017 (2010).
43. N. Aslam, G. Waldherr, P. Neumann, F. Jelezko, and J. Wrachtrup, "Photo-induced ionization dynamics of the nitrogen vacancy defect in diamond investigated by single-shot charge state detection," *New J. Phys.* **15**(1), 013064 (2013).
44. D. Bluvstein, Z. Zhang, and A. C. B. Jayich, "Identifying and mitigating charge instabilities in shallow diamond nitrogen-vacancy centers," arXiv preprint arXiv:1810.02058 (2018).
45. B. J. Shields, Q. P. Unterreithmeier, N. P. de Leon, H. Park, and M. D. Lukin, "Efficient readout of a single spin state in diamond via spin-to-charge conversion," *Phys. Rev. Lett.* **114**(13), 136402 (2015).

6. Nanoscale sensing based on nitrogen vacancy centers in single crystal diamond and nanodiamonds: achievements and challenges

Mariusz Radtke, Ettore Bernardi, Abdallah Slablab, Richard Nelz, and Elke Neu

Nano Futures, in press (2019)
doi: 10.1088/2399-1984/ab5f9b

This article is a topical review.

The above mentioned manuscript is a review article summarizing the recent progress on manufacturing and structuring diamond as well as achievements and challenges in NV sensing. In addition, it gives an outlook on recently developed applications. In contrast to standard contributions to a review, Richard Nelz (R.N.) contributed the results of a proof-of-principle experiment which strongly support one novel approach to high-resolution imaging using color centers outlined in the review: R.N. investigated the interaction of NV centers with graphene flakes in their proximity to show the occurrence of FRET-like processes for NV centers in single crystal diamond. Furthermore, the experimental data strongly supports the applicability of NV centers as multifunctional sensors simultaneously undergoing FRET processes but retaining their spin-properties and magnetic sensing capabilities. In addition, R.N. contributed to the development of a model to describe the interaction of an ensemble of shallow NV centers with graphene. R.N. summarized all information necessary to integrate the experimental results in the manuscript and designed the corresponding figure. He actively contributed to all major discussions during writing and revising the review.

Nanoscale sensing based on nitrogen vacancy centers in single crystal diamond and nanodiamonds: achievements and challenges

M Radtke¹, E Bernardi¹‡, A Slablab¹, R Nelz¹, and E Neu¹

¹ Faculty for natural sciences and technology, Physics, Saarland University, 66123 Saarbrücken, Germany

Abstract. Powered by the mutual developments in instrumentation, materials and theoretical descriptions, sensing and imaging capabilities of quantum emitters in solids have significantly increased in the past two decades. Quantum emitters in solids, whose properties resemble those of atoms and ions, provide alternative ways to probing natural and artificial nanoscopic systems with minimum disturbance and ultimate spatial resolution. Among those emerging quantum emitters, the nitrogen-vacancy (NV) color center in diamond is an outstanding example due to its intrinsic properties at room temperature (highly-luminescent, photo-stable, biocompatible, highly-coherent spin states). This review article summarizes recent advances and achievements in using NV centers within nano- and single crystal diamonds in sensing and imaging. We also highlight prevalent challenges and material aspects for different types of diamond and outline the main parameters to consider when using color centers as sensors. As a novel sensing resource, we highlight the properties of NV centers as light emitting electrical dipoles and their coupling to other nanoscale dipoles e.g. graphene.

‡ Present address: Istituto Nazionale di Ricerca Metrologica, Strada delle cacce 91, 10137 Torino (To), Italy

1. Introduction

During the past two decades, color centers in diamond emerged as sensors for various relevant quantities like electric, magnetic and optical near fields as well as local temperature and strain [1–5]. As point defects with tightly-localized electrons, color centers in diamond resemble atomic-scale quantum systems. Thus, color centers open up routes towards nanoscale sensing technologies in which the spatial resolution is no longer limited by the sensor’s volume [6]. However, ultimate spatial resolution will only be attainable using individual defect centers. This approach simultaneously limits the intensity of the photoluminescence (PL) light which is mainly being used as the sensor read-out. Consequently, sacrificing ultimate spatial resolution, color center ensembles can provide enhanced sensitivity, speed up measurements and lower experimental complexity. In addition to being atomic-scale sensors, color centers are highly-sensitive, potentially quantum-enhanced sensors providing coherent superpositions of spin states as sensing resource. Diamond as a host material has a multitude of outstanding characteristics ranging from high optical transparency, to mechanical hardness and chemical inertness. Diamond also has the rare property that its crystal lattice is naturally almost free of nuclear spins as the most abundant carbon isotope (^{12}C , 98.9%, [7]) has nuclear spin zero. Consequently, the lattice has low magnetic noise (given that the concentration of paramagnetic impurities like e.g. nitrogen is low) and electronic spins of color centers can have long coherence times reaching the millisecond range even at room temperature. However, diamond’s high refractive index renders light extraction from color centers challenging and often demands structuring diamond to yield photonic structures or to use nanodiamonds (NDs). Due to this fact, the fields of diamond photonics and nanofabrication are strongly connected to sensing using color centers.

In 1997, the first observation of spin manipulation of an individual negatively-charged nitrogen vacancy (NV) center was reported [8]. In 2000, stable, room-temperature single photon emission from individual NVs added to their potential for quantum technologies [9]. The NV defect consists of a nitrogen atom replacing a carbon atom and a vacancy on a neighboring lattice site. For simplicity, NV center refers to the negatively-charged defect throughout this review. Since then, other defects have been characterized as single emitters. Among these novel defects there are several group IV-based centers namely silicon vacancy (SiV) [10], germanium vacancy (GeV) [11], tin vacancy (SnV) [12] and even lead-related defects [13]. In contrast to NV centers that show an almost 100 nm broad emission band, group IV-based defects concentrate almost all PL into their only a few nanometer wide zero phonon lines (ZPLs) even at room temperature. Temperature dependent shifts of these ZPLs have been exploited for all optical temperature sensing (see e.g. Refs. [14, 15]). Despite recent progress in sensing using group IV defects, negatively-charged NVs remain outstanding in the field of sensing. Their superior usability for sensing applications stems from the fact that the NV center’s electronic spins can be optically polarized using convenient, non-

resonant excitation at room temperature while they can be manipulated using microwave radiation in an easily accessible frequency band (2.88 GHz). Internal population dynamics of the NV center lead to different PL intensities for different spin states. Consequently, the spin state can be read out using this PL difference (optically-detected magnetic resonance, ODMR). However, sensing using NV centers is not limited to using the spin degree of freedom: Potential sensing resources include the NV's charge state, modulations of excited state lifetimes and absorption. The latter two exploiting the dipolar nature of the NV center's transitions.

In this paper, we will review recent advances in sensing with NV centers. We will summarize main breakthroughs and drawbacks in the field. The review is structured as follows: Section 2 presents basics of diamond material synthesis and structuring for sensing applications. Section 3 starts with a short introduction of NV properties and then details the main parameters characterizing NV sensors. In Section 4, we summarize the spatial resolution attainable with NV sensors in different sensing modes. Section 5 summarizes selected applications to illustrate recent progress using NV sensors.

2. Manufacturing and structuring of nano- and single crystal diamonds

2.1. Manufacturing of diamond

The major factors influencing diamond's properties and its potential applications are purity and crystallinity. The following retrospective summarizes recent developments within diamond growth and synthesis according to those parameters. In theory, diamond is a crystal consisting only of sp^3 hybridized covalently bound carbon atoms, which build a repetitive unit cell made of fused hexagonal chair cyclohexane conformations as depicted in Fig. 1 [16]. The Hermann Mauguin notation classifies diamond into the Fd3m-07h face centered cubic group. The unique arrangement of carbon atoms within diamond makes it not only the hardest material in Mohs scale, but also causes it to be inert towards chemical modifications without use of harsh conditions. Diamond's wide bandgap (indirect gap 5.45 eV) results in optical transparency for light up to ≈ 230 nm. The naturally almost spin free lattice of diamond (^{12}C , 98.9%, $I=0$, [7]) has been engineered by isotopically purifying diamond (residual ^{13}C , 0.3%) as presented in Ref. [7].

There are many types of diamonds and their classification is based on several factors. One classification system has its foundation in the origin of the diamonds: naturally occurring diamonds, diamond created via synthetic hydrothermal high-pressure high temperature (HPHT) protocols, shock wave synthesis (e.g. through detonation) and low pressure pyrolysis of hydrocarbon gases in chemical vapor deposition (CVD). The latter includes microwave assisted CVD (MWCVD) and hot filament CVD (HFCVD) deposition, whereas MWCVD is most suitable to grow high purity diamonds [19]. Fig. 2 summarizes this classification. For CVD diamond growth, the most common precursor gases are methane CH_4 and hydrogen H_2 . The detonation method only

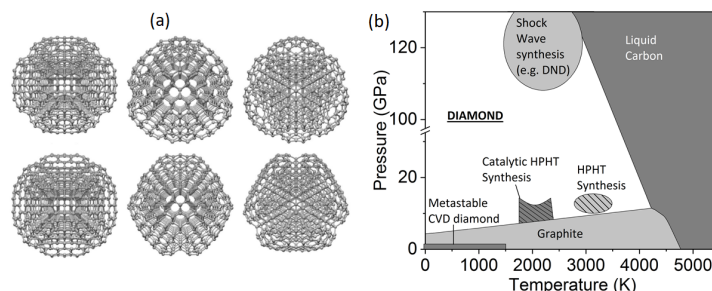


Figure 1. (a) Structures of nanodiamond supercells from various crystallographic axes. Reprinted with permission [17]. (b) Diamond phase diagram based on [18], Courtesy of AGU.

forms nanodiamonds (NDs) of about 5 nm size [20]. Figure 1 summarizes the temperature/pressure regimes for diamond synthesis through shock wave, metastable CVD diamond phase generation or HPHT protocols. In both HPHT and CVD synthesis, by tailoring the additives in the reaction chamber (e.g. insertion of N_2), diamonds with various color centers are obtained. For detonation diamonds (DNDs), creating luminescent NDs is challenging. However, recently density control of NV centers in 5 nm-sized DNDs was reported [21]. Usually DNDs require special post-treatment to remove graphitic sp^2 layers, e.g. through immersion in a boiling mixture of oxidizing mineral acids (HNO_3 , H_2SO_4 and $HClO_4$) and thermal annealing in vacuum or under oxygen for adequate stabilization of spectral properties [22]. Various synthesis methods generate diamond with tailored properties. For example DNDs are commonly used as abrasives in industry, while HPHT and CVD (especially single crystal) diamonds are often more suitable for quantum applications.

For HPHT and CVD methods, diamond growth is typically initiated on a substrate or seed. For CVD growth, this can be attained by directly growing on a diamond (homoepitaxy) or via using a non-diamond substrate (heteroepitaxy) which needs to be prepared suitably. Substrate pretreatments for CVD span from seeding with NDs to grow polycrystalline diamond to creation of nuclei using bombardment with carbon ions (bias enhanced nucleation for heteroepitaxy) [23]. Homoepitaxy limits the size of grown SCDs due to the size of available substrates. This can be overcome using heteroepitaxy [23].

The smallest possible seeds for diamond growth are so called diamondoids. Diamondoids mainly combine one or more adamantane molecules ($C_{10}H_{16}$), the smallest unit cage structure of the diamond crystal lattice. Using the smallest possible seed is among other reasons motivated by minimizing the influence of the seed on the resulting ND's properties. Refs. [16, 24] demonstrate the synthesis of nanoscale 'diamond molecules' (higher diamondoids, e.g. tetramantanes, less than 1 nm in size). Diamondoids were recently employed to enable the growth of high quality NDs in a HPHT process [25] and in a CVD process [26]. Ref. [27] reports that diamondoids serve as nuclei in CVD if they contain more than 26 carbon atoms. Another approach to

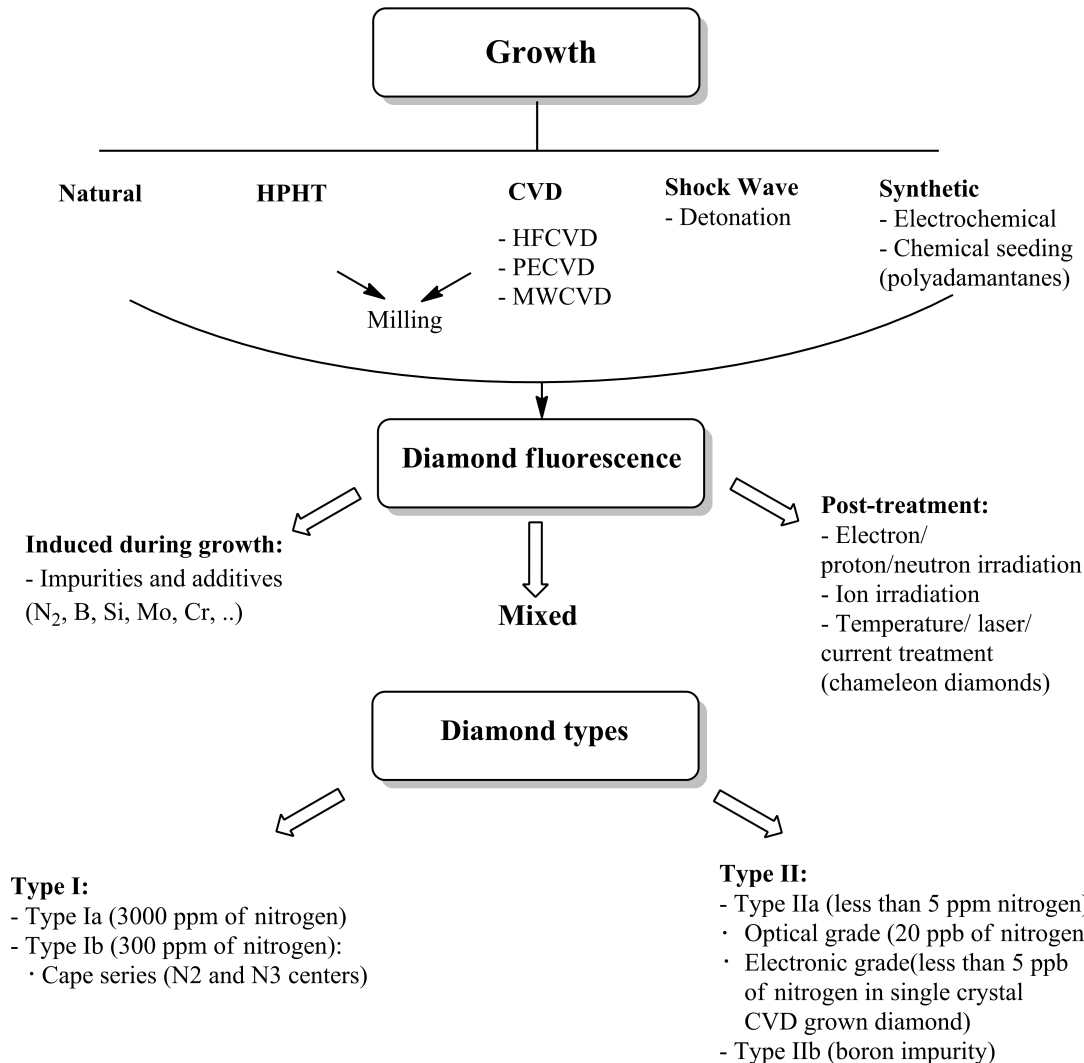


Figure 2. Classification of diamond, details see text.

molecular sized diamonds is the use of meteoritic diamonds [28]. For this material class, fluorescent SiV centers have been observed in NDs with only 1.6 nm size. However, this results has never been obtained using man-made NDs, thus significantly lowering applicability. A novel route to manufacturing an extreme diamond nanomaterial is the recently observed transformation of a bilayer of graphene into a single layer of (fluorine terminated) diamond [29].

The second system that classifies diamond, in addition to the origin of the diamond, is based on the crystallinity. Here diamonds are classified as single crystal (SCD), polycrystalline and (ultra-)nanocrystalline diamonds according to their crystallite size. For grain sizes below 10 nm the diamond is typically called ultrananocrystalline, between 10 nm and 50 nm nanocrystalline, and from 50 nm to 500 μm micro- or polycrystalline. If the crystallite size exceeds 500 μm , the diamond is termed single crystalline and a specified crystallographic growth plane can be assigned [30].

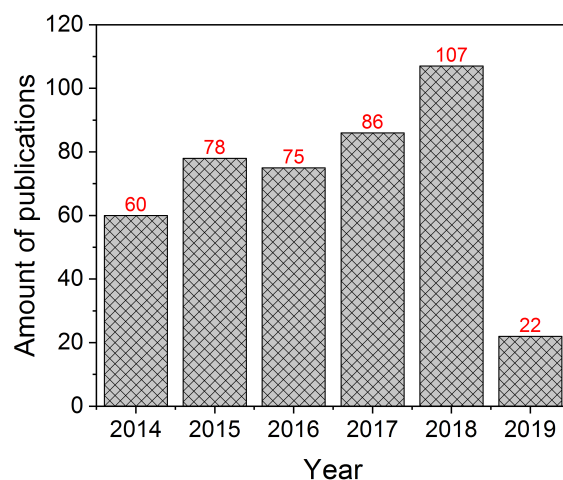


Figure 3. Timescale in period between 2013-2018 showing the evolution of the searching phrase "single crystal diamond growth", based on the database WorldCat.org.

The amount of publications detailing the phrase 'single crystal diamond growth' in WorldCat.org. in the time period between 2013-2018 yields 3.575 results (Fig. 3), illustrating the significance of the field.

Free standing wafer-sized polycrystalline diamond films are currently commercially available with diameter up to 140 mm (Element Six, UK). Recently, Ref. [23] presented a mm-thick SCD wafer with 98 mm diameter grown by heteroepitaxy. The basic usability of this material for sensing with NV centers has been demonstrated [31].

The most common growth direction in CVD is (100). However, for many applications it is advantageous to control the orientation of NV centers with respect to the SCD surface. Thus, alternative growth of (111) [32] diamond and (113) [33] has been realized that orients the dipoles of NV centers more optimal with respect to photonic structures manufactured into the SCD surface [34]. While single SCD allows for the highest purity material with the lowest background PL, poly- and nanocrystalline forms will always suffer from broadband PL occurring at grain boundaries [19].

The third classification has been historically established for natural diamonds and classifies them according to their optical absorption [35]. Figure 2 summarizes this classification. Type IIa diamonds were classified by a lack of optical absorption [35], so this were the purest diamonds in this classifications. The absorption of type I diamond is nowadays assigned to nitrogen [36]. Type Ia diamonds contain nitrogen in aggregated form; while in type Ib diamonds, it is present in its isolated form substituting single carbon atoms (substitutional nitrogen) [36]. Most CVD diamonds are of IIa type, while HPHT diamonds are often type Ib [37]. In contrast, type I diamonds are known to occur most commonly in nature. Type IIb contains boron in small quantities and has p-doped character. This historical classification doesn't sufficiently classify diamonds

typically used for sensing with color centers: These diamonds are mostly so pure that they are all class IIa but need further classification. So typically, the amount of substitutional nitrogen and boron is directly given. Pushing purity to the limit, electronic grade diamonds with less than 5 ppb nitrogen and less than 1 ppb boron are nowadays commercially available from ElementSix and are the basis for most sensing experiment especially using individual NV centers. In addition, ^{12}C isotopically-purified diamond has been demonstrated and termed quantum grade diamond [7].

When impurities in diamond are present in high concentration, they induce a coloration of diamonds. For sensing, typically low concentrations of defects are used, which does not necessarily lead to a coloration of diamond.

Color centers can be introduced into diamond using two approaches. The first approach creates color centers in the growing diamond via using selected precursors [38–40]. Often NV centers are also created due to background nitrogen in the process [34, 40–42]. However, for sensing applications it is important to carefully control color center density and depth below the diamond surface (see also Sec. 4). Creating thin layers containing NV centers has been attained in diamond CVD using δ -doping (e.g. Ref. [38, 43]): in a CVD process with low growth rate, nitrogen gas is introduced for a short time thus inducing an only 6 nm thick nitrogen-doped layer [38]. Moreover, nitrogen doped layers were obtained by overgrowing nitrogen-terminated diamond surfaces [44]. Using δ -doping, conversion of nitrogen impurities to NV centers is often fostered via irradiation e.g. using helium ions [45]. One advantage of forming color centers directly during diamond growth is that they can show preferential alignment: instead of aligning along all equivalent directions in the crystal, color centers only form with one orientation leading to a perfectly aligned ensemble of centers (see Refs. [39–41]). Moreover, NV centers created using conversion of grown-in nitrogen to NV centers have been found to have superior properties compared to centers arising due to implanted nitrogen [46, 47].

The second approach creates impurities after diamond manufacturing has finished. It utilizes irradiation (by electrons, neutrons or protons [46, 48]) and ion implantation [49–54]. It allows to control the fluence, which determines the density and the energy (ranging from keV to MeV) to set the implantation depth [55]. The creation of color centers can be also controlled in lateral dimension by implanting through a pierced AFM tip [56], using nanomasks [57] or focused ion beams [58]. Ion implantation in diamond requires post-treatment annealing (mostly at temperatures exceeding 600°C) in order to induce vacancy migration, repair implantation damage and form color center complexes like NV centers.

2.2. Nanostructuring of diamond

To efficiently extract color center PL from diamond, photonic structures e.g. nanopillar waveguides [34, 59], optical antennas [60], solid immersion lenses [61], bulls eye gratings [62] or pyramids [63–65] are highly-desirable (for reviews on diamond photonics, see

Refs. [66–69]). Figure 4 displays some examples of diamond nanostructures. Nanopillar waveguides channel the light into conveniently collectible emission angles ($\text{NA} < 0.95$) and circumvent total internal reflection [70]. Here, the high refractive index of diamond (2.4) aids in confining the light in the waveguide. In contrast, for unstructured diamond, it limits the collection efficiency to only a few percent [71]. While optical antennas, in principle, allow up to unity collection efficiency [60], tip-like structures as pillars or pyramids might simultaneously serve as a tip for a scanning probe microscope [72] thus enabling to scan a color center in close proximity to a sample under investigation. It is noteworthy that nanopillars have been produced incorporating not only NV centers [34, 70, 73] but also SiV centers [59] and lead-related defects [74]. Additionally, cavity structures like one or two-dimensional photonic crystals [56, 75] or microdisk (whispering gallery mode) resonators [76] allow the coupling of color centers to cavity modes with high Q-factor. Mostly, photonic structures are used to extract light from single color centers [59]. However, very recent studies also indicate the usefulness of pillar arrays for sensing with NV ensembles [73].

To harness the full potential of photonic structures, nanofabrication processes must be carefully controlled: First, the shape of the nanostructure will strongly influence its performance e.g. changing the taper angle of a nanopillar [see Fig. 4] changes the efficiency of light extraction [71, 77]. Second, nanofabrication, especially on example of plasma etching, might damage diamond surfaces [78]. This damage was estimated to reach several nanometers into the diamond and found to deteriorate the properties of shallow color centers [79]. Reduced damage and enhanced properties of NV centers have been reported by using plasmas with zero bias voltage and thus minimal acceleration of ions in the plasma [79] and with careful combinations of etching processes [46]. As diamond is highly chemically inert, wet chemical etching methods are not an alternative to plasma-based processing. Focused ion beam (FIB) milling leaves gallium impurities in the diamond that need to be removed using sophisticated post-processing [80]. So the most common processing techniques utilize standard nano-lithography techniques with electron beams, laser or 2-photon lithography (2PP) for mask generation and transfer the patterns into diamond using reactive ion etching (RIE), mostly in the form of inductively coupled reactive ion etching (ICP-RIE) [81, 82]. Plasma-etching of diamond requires special gases as well as resists for the masks (negative and positive tone). Most commonly oxygen/argon or chlorine-based mixtures are used. Masks are either based on PMMA with hard mask techniques (Al, Al_2O_3 , W) or directly on the negative tone resist hydrogensilsequioxane (HSQ) [34, 83].

Nanostructuring of diamond can be classified into traditional nanotechnology approaches: bottom up and top down approaches. For example nanodisc resonators with quality factor exceeding 300000 may be generated by top-down techniques involving electron-beam lithography, laser lithography and ICP-RIE [76].

In bottom-up approaches, nanostructures are directly formed during diamond growth thus potentially forming many structures at the same time and avoiding potential damage due to plasma-etching [64, 84]. However, top-down approaches have the

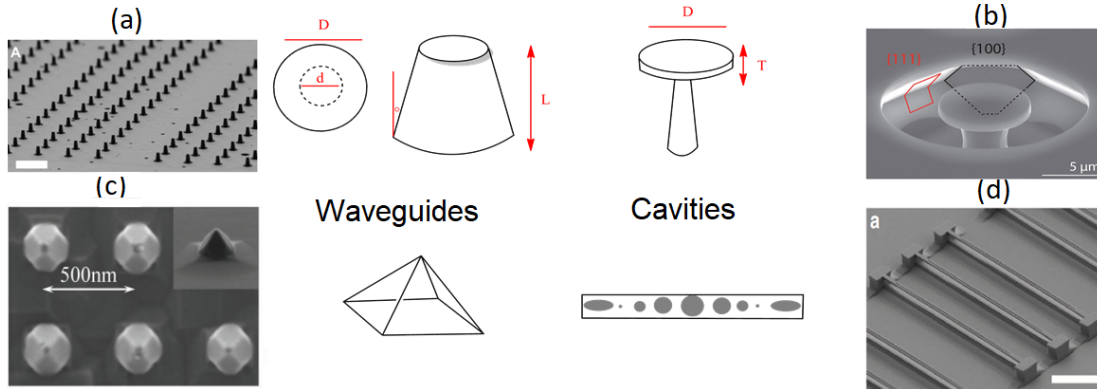


Figure 4. Current state of the art examples of successful nanofabrication performed on diamond. Fabricated structures include waveguides and cavities. As examples of nanowaveguides, part (a) shows nanopillars (reprinted with permission from Ref. [77]) and part (c) displays pyramids (reprinted with permission from Ref. [63]). As examples of nanocavities, part (b) shows a microdisk cavity (reprinted with permission from Ref. [76]), whereas part (d) shows nanobeams (reprinted with permission from Ref. [75]).

advantage, that color centers can be created while the diamond is still in its bulk form, which eases annealing and cleaning followed by fabrication of the nanostructures (e.g. Ref. [72]).

3. Achievements, improvements and challenges in NV sensing

The strengths of sensing using color centers in diamond are its spatial resolution and its sensitivity (for a tutorial on NV magnetometry see e.g. Ref. [85]). Moreover, depending on the application, it is important to consider in which modality the diamond sensor should be operated. This especially includes the host diamond's geometry (bulk, single-crystal diamond (SCD), nanostructures or nanodiamonds (NDs)) and how the color center is brought into interaction with the sample (e.g. NDs entering cells, SCD tip scanning over the sample, sample transferred to SCD surface). Moreover, a decision needs to be rendered if single color centers should be used or if ensembles are more suitable. Ensembles can provide better sensitivity whereas single centers, in combination with scanning probe operation, provide ultimate spatial resolution. In the following, we give a very short introduction to the physics of NV centers. We are not aiming for completeness nor we will describe any theoretical background here but just introduce the basic level scheme and effects needed to follow the discussed sensing topics. For details on the NV center see e.g. Ref. [86].

3.1. NV Basics

The NV center consists of a nitrogen atom that substitutes a carbon atom in the diamond lattice and a neighboring vacancy. Negatively-charged NV centers display a system of singlet and triplet levels. A strong optical transition (lifetime 12.9 ns, [87])

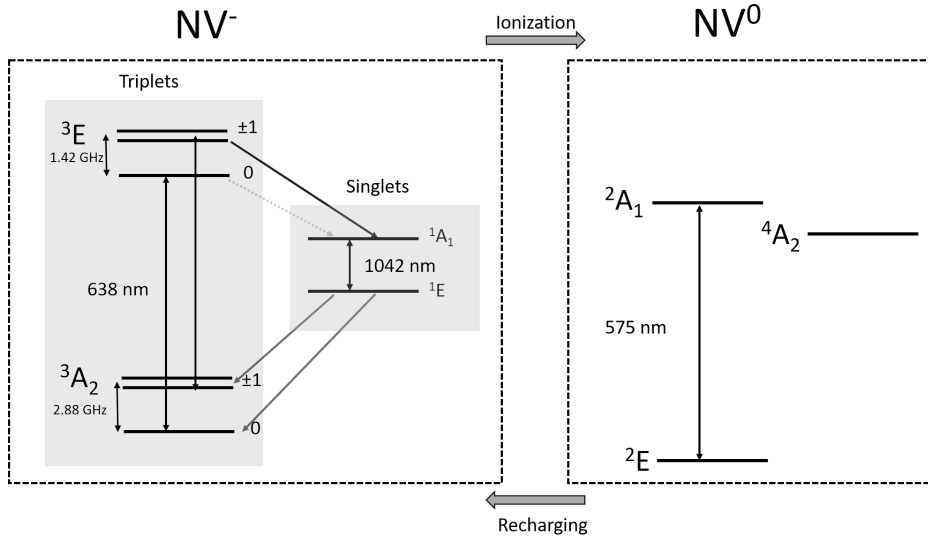


Figure 5. Basic level scheme of the negatively-charged and the neutral NV center. Explanation see text.

occurs between the 3A_2 ground state and the 3E excited state. This transition leads to the zero-phonon-line (ZPL) at 637 nm at room temperature. Due to phonon assisted transitions, the narrow ZPL is accompanied by a broad phonon sideband spanning almost 100 nm spectral width [88]. The $^3A_2 \rightarrow ^3E$ transition, which induces the visible photoluminescence (PL) of the NV center, is represented by two orthogonal transition dipoles. These dipoles are placed in the plane orthogonal to the NV's high-symmetry axis that connects the nitrogen and the adjacent vacancy. This axis is oriented along one of the equivalent [111]-directions of the diamond lattice [89,90].

In the triplet ground state of NV⁻, three spin states with $m_s = -1, 0$ and $+1$ are observed. Between the $m_s = 0$ level and the degenerate $m_s = -1, +1$ levels a zero-field splitting of 2.87 GHz occurs. These levels show spin-dependent PL: A NV center in the $m_s = 0$ cycles between 3A_2 and 3E and produces bright PL. In contrast, a NV center in the $m_s = -1$ or $+1$ state undergoes an intersystem crossing to the singlet states with higher probability. As the center will reside in these states for typically around 200 ns [91], the visible PL of the center is reduced. The PL difference between the two spin states under continuous, non-resonant laser excitation (e.g. using 532 nm laser light) can be up to 20% [2]. Simultaneously, non-resonant laser excitation polarizes the NV center into the $m_s = 0$ state. Following this initialization, transitions between the spin levels can be driven using microwaves.

Between their 1A_1 and 1E levels, NV centers display a transition in the infrared spectral range (1042 nm) [88]. As a result of non-radiative processes, the PL due to this transition is typically four orders of magnitude weaker than the visible PL [92]. Nevertheless, transitions in the singlet system are a valuable resource for sensing (see Sec. 3.2).

If one electron is removed from the NV^- center, it converts to a neutral NV^0 center. This occurs during optical excitation of NV^- when a NV^- center which resides in the excited state absorbs an additional photon. As a consequence, an electron is excited to the conduction band and via an Auger process, a free electron is created, while the center converts to NV^0 [93]. NV^0 centers display a ZPL at 575 nm, thus, light with wavelengths shorter than 575 nm is needed to excite NV^0 . As a consequence, light with wavelengths between 637 nm and 575 nm only excites NV^- but not NV^0 . This can be used to detect the charge state of NV centers [42, 94] even without changing the charge state: only if the center is NV^- , under excitation with e.g. 594 nm light PL occurs, while no PL is observed in the NV^0 case. To convert NV^0 back to NV^- it is necessary to excite NV^0 : If an electron from the lower orbitals of NV^0 is excited, an electron from deep lying orbitals in the valence band can be promoted to the NV^0 and re-charge the center to NV^- [93]. It should be noted that the NV charge state in an ensemble can strongly depend on previous laser excitation of the NVs [95].

3.2. Sensitivity

Sensing using NV centers can be classified into three broad categories, considering the physical quantity to be detected and the degree of freedom of the NV used:

- Detection of the (electronic) spin resonance frequencies (magnetometry, temperature sensing, conductivity measurement)
- Detection of NV PL intensity and excited state lifetime (near-field energy transfer, Förster-Resonance Energy Transfer (FRET) imaging, near field sensing)
- Detection of the charge state of NV centers (sensing of electrostatic environment)

Measurements based on the spin degrees of freedom are most mature, while near-field based sensing and using the NV charge state for sensing are rather novel. Regarding electronic spin-based sensing, we introduce the sensitivity η for DC magnetometry [2]:

$$\eta = \frac{h}{g\mu_B} \frac{\Delta\nu}{\sqrt{I_0 C}} \quad (1)$$

where I_0 is the NV PL rate, C is the ODMR contrast, $\Delta\nu$ the linewidth of the ODMR resonance, g the Landé factor and μ_B the Bohr magneton. Considering equation (1), improving sensitivity can be obtained by:

- Increasing I_0 via increasing the collected photon rates or the collection efficiency for NV PL [2, 34, 39, 40, 60, 62, 96–98]
- Decreasing $\Delta\nu$, which is connected to increasing the coherence time T_2^* [43, 44, 49–52, 79]
- Increasing the efficiency of the spin readout (in Eq. 1 represented via C) [50, 94, 99–105].

Equation (1) is valid for a single NV, if we use an ensemble including N NV centers, the sensitivity improves by a factor of \sqrt{N} . Indeed, to date, optimal sensitivities in the

pt/ $\sqrt{\text{Hz}}$ are reached using ensembles of $N \sim 10^{11}$ NVs [48]. For a recent review focusing on enhancing the sensitivity of NV ensemble-based sensors see Ref. [106].

For sensing schemes based on the NV charge state and FRET-based sensing and imaging, it is much more challenging to define a sensitivity. However, due to optical read-out, enhancing photon collection will enhance sensing capabilities. For FRET-based sensing, the quantum efficiency QE of the NV transitions, that is the probability for a radiative transition between excited and ground state, also plays a major role. Recent work indicates that the QE for shallow NVs, required for FRET-based sensing (4.5 nm below surface), amounts to 0.7 while defects deeper in the diamond reach QE of 0.86 [53].

In the following, we review the above mentioned methods and the main parameters influencing their sensitivity.

3.2.1. Collection efficiency As introduced in Section 3.1, the PL of NV centers originates in a semiclassical description from two emitting dipoles in the plane orthogonal to the NV axis. Two main factors limit the PL collection from NV centers in SCD:

- Refraction effects at the SCD-air interface. Due to the high refractive index of diamond (2.4), a significant fraction of the PL undergoes total internal reflection limiting the collected fraction of PL often to a few percent (see also Section 2.2).
- Dipole orientation and directionality of NV radiation: Optimal collection of PL is obtained for dipoles parallel to the SCD surface [34]. However, the most common CVD SCDs have (100) surfaces. Consequently, the NV axis lies under an oblique angle (54.7°) to the SCD surface, leaving the NV's dipoles in a non-optimal orientation. Consequently, a fraction of PL even if it escapes the SCD might not be collected because it is emitted into angles that exceed the numerical aperture of the collection optics.

Optimal orientation of NV dipoles can be obtained using SCD with (111)-oriented surfaces [34]. (111)-oriented CVD growth can even provide NV centers that all align along one [111] direction, namely the growth direction of the crystal [39–41]. No NVs in other equivalent directions are formed and a perfectly aligned ensemble can be created. As (111)-oriented CVD growth is technically very challenging, researchers also investigate similar growth directions like (113) that allow for an almost optimal orientation of NV centers [33].

Regarding refraction effects, PL collection can be improved further via shaping SCD into nanostructures as reviewed in Section 2.2.

3.2.2. Coherence time Shallow NVs typically used for sensing, present degraded coherence properties compared to NVs well below the surface [107,108]: Their coherence times T_2 and T_2^* reduce, leading, among other drawbacks, to an increased ODMR

linewidth $\Delta\nu$ and reduced sensitivity for DC magnetic fields (see Eq. 1). The main sources of noise leading to the reduced coherence are:

- Surface modified phononic-coupling [108]
- Surface electronic spin bath [108, 109]
- Paramagnetic defects due to implantation [51, 52]

Methods to improve coherence in shallow NVs are e.g. reviewed in Ref. [110].

As shallow NVs are often created using low energy (keV) ion implantation, noise due to the implantation process is crucial. Paramagnetic defects responsible for magnetic noise are vacancy clusters or chains created during post-implantation annealing of the diamond [49, 52]. Ref. [49] identifies the neutral di-vacancy complex V_2 as the main source of decoherence and avoids its formation via charging the vacancies in the space charge larger of a p-i-junction using boron-doped diamond [49]. Other work employs annealing at elevated temperatures to anneal out vacancy complexes [51, 52]. Alternatively, shallow NV centers can be produced using the δ -doping technique (see also Section 2.1). The subsequent creation of vacancies e.g. using a focused electron beam followed by annealing, introduces in general lower levels of magnetic noise and enhanced coherence times have been demonstrated [111].

The noise due to the surface of the diamond strongly depends on the pre-treatment of the surface as many functional groups can be present on the surface [20] as well as e.g. damage due to plasma treatment. Improvement of single NV coherence was observed after wet oxidizing chemistry and annealing in oxygen environment [50], however, other groups were not able to reproduce the enhancement for shallower NVs [112]. Considering plasma treatments, Ref. [79] shows increased coherence times for NVs below surfaces that have been treated using an oxygen plasma with low acceleration of ions towards the etched diamond (low-bias, soft plasma).

3.2.3. Readout and charge state For most sensing experiments, PL-based read-out of the NV electronic spin is performed (ODMR, see Section 3.1). Though being technically simple and versatile, this method has its limitations in the fact that the read-out laser re-polarizes the spin to the $m_s=0$ state and low collection efficiencies render single-shot read-out of the electronic spin impossible at room temperature.

Improving ODMR-based spin read-out is feasible using:

- Repetitive readout [50]
- Phase sensitive (lock-in) methods [104, 105]
- Noise reduction by mutual referencing of discrete readout windows [99]

For a repetitive read-out, the NV electronic spin state is transferred into the nuclear spin state of ^{14}N . In contrast to the electronic spin, the nuclear spin can be repeatedly probed via quantum non demolition measurements [113]. The advantage here is that the NV state is not reset to $m_s = 0$ during readout. Ref. [104] presents a technique modulating the microwave frequency used for spin manipulation or of the amplitude

of static magnetic fields; subsequently demodulating the PL response using lock-in amplification suppresses noise at low frequency (typically below 30 kHz). Another way to reduce noise due to uncertainties in microwave frequency or power is to subtract PL signals retrieved during subsequent pulse repetitions [99]. Using this approach, microwave noise with a correlation time exceeding the duration of a single pulse sequence is filtered out.

In recent years, novel approaches to read out NV electronic spins beyond ODMR arose, which we summarize here briefly. For a more detailed review see Ref. [114]. Novel read-out methods that partly bypass the challenge of low collection efficiency include:

- Absorption of infrared (IR) light due to transitions within the NV singlet system [101, 102]
- Laser threshold-related magnetometry [115, 116]
- Spin to charge conversion for more efficient spin-readout [94, 103]
- Readout based on the detection of photo-currents [117]

The absorption via the singlet transition ${}^1E \rightarrow {}^1A_1$ (level scheme see Section 3.1) depends on the population of the involved levels. As these levels are mainly populated from the $m_s = \pm 1$ states in the triplet (assuming the NV is pumped e.g. using green laser light), the IR absorption monitors the spin resonances in the triplet and consequently allows the measurement of magnetic fields [101, 102]. To measure the weak absorption on the ${}^1E \rightarrow {}^1A_1$ transition, it is advantageous to enclose the diamond in a cavity or at least to use a multipass configuration to enhance the signal. Using miniaturized Fabry Perot cavities sensitivities down to $28 \text{ pt}/\sqrt{\text{Hz}}$ have been shown [101].

Another approach to avoid the bottleneck of low PL detection is laser threshold magnetometry, which promises sensitivities down to the $\text{ft}/\sqrt{\text{Hz}}$ regime [115]. In this approach, NV centers serve as gain medium for a laser. A change in spin state and thus in PL intensity translates into switching on and off the laser, which operates very close to the laser threshold. However, this requires stimulated emission and population inversion in the NV triplet levels. Despite the fact that stimulated emission has been observed [118], ionization dynamics counteracting stimulated emission render this approach challenging. Combining the previously mentioned approaches, Ref. [116] presents a hybrid laser threshold magnetometer. The laser gain is supplied by an external laser material lasing at the ${}^1E \rightarrow {}^1A_1$ transitions wavelength. The diamond is inserted into the cavity of the external laser. Enhanced absorption on the IR transition increases the losses for the laser and stops laser emission.

In spin-to-charge conversion, the spin state of the NV center is mapped to a charge state (NV^- or NV^0) [94, 103]. In brief, the technique is based on the fact that NV^- centers are easily ionized from the triplet excited state 3E . In contrast, a transition to the singlet, which is more likely to occur if the center is in the $m_s = \pm 1$ state, protects the center from ionization. Consequently, $m_s = 0$ is mapped to NV^0 and $m_s = \pm 1$ is mapped to NV^- . Following the ionization, the charge state is read-out as described in

Section 3.1. Using this read-out method, enhanced sensing with a 25-fold increase in imaging speed has been demonstrated [103].

Each cycle of ionization and re-charging of a NV center under optical illumination creates an electron in the conduction band which can be detected in the form of a photocurrent if an electric field is applied using electrodes on the SCD surface. Photocurrents in the pA are observed for a single NV center and the contrast of the photoelectrical read-out is comparable to the ODMR based read-out [117].

3.2.4. Ensemble density and alignment of NVs for wide field imaging In wide field magnetic imaging, a thin layer of NV centers is used. To enable imaging a larger sample area, NV PL is collected using a camera. Typically, hundreds to 10000 of NV centers contribute to the signal in every pixel [119, 120]. In this way, every pixel encodes the properties of the local magnetic field.

Two properties of the NV layer determine the magnetic field sensitivity:

- The density of NVs
- The alignment of NVs

The most common way to increase the NV density is to increase the nitrogen implantation dose. This has two effects on sensitivity: On the one hand, it increases the PL rate and thus improves the sensitivity scaling with \sqrt{N} , where N is the number of NV defects. On the other hand, it increases the density of implantation-related defects (see also Section 3.2.2) and decreases the coherence [121]. These two counteracting effects have been found to result in a sensitivity which can be independent of the implantation dose [51]. The spin coherence time T_2 influences the range of AC frequencies to which the NV center is sensitive [122]. Consequently, the optimal NV density is determined by the specific needs of each sensing application. For a recent review focusing on the sensitivity using NV ensembles see Ref. [106]

For wide field imaging, also the orientation of NV centers has to be taken into account. NV centers oriented along different equivalent directions sense the projected field onto their high symmetry axis. Consequently, for an ensemble and an arbitrarily aligned magnetic field, 4 pairs of ODMR resonances are observed. Using these 4 ODMR resonance pairs, the magnetic field vector can be reconstructed. However, the ODMR contrast for each of the resonances is strongly reduced as only 25% of the NV centers contribute to each resonance line. For high-sensitivity experiments, consequently the use of an NV ensemble that is aligned along only one of the equivalent directions is advantageous. Using diamond oriented in [111] direction and creating NV centers during growth, perfectly aligned ensembles with high density ($d = 10^{19} \text{ cm}^{-3}$) and high ODMR contrast, comparable to the one reported for single NVs, have been demonstrated [39].

4. Spatial resolution in NV sensing

Using ensembles of NV centers often involves wide field imaging, where a larger diamond area is illuminated and NV PL is detected using a camera [123–127]. This technique typically leads to a spatial resolution on the order of $1\ \mu\text{m}$ [123–125, 127]. This spatial resolution allows e.g. to investigate microwave devices [127], integrated circuits [125] or magnetic features in cells [124]. In wide field imaging, the signal on each pixel of the camera involves hundreds to 10000 NV centers [119, 120]. DC magnetic field sensitivities in the order of $\mu\text{T}/\sqrt{\text{Hz}}$ have been quoted [120]. Enhancing the sensitivity can be obtained via increasing the number of NV centers participating in the signal creation. However, as discussed in Section 3.2.4, enhancing the volume density of NVs in SCD does not necessarily enhance the sensitivity. An alternative route enhances the number of NV centers via increasing the effective SCD volume contributing to the sensing signal: Ref. [96] employs light trapping in a SCD that forms a multi-pass waveguide (SCD dimensions $3\ \text{mm} \times 3\ \text{mm} \times 0.3\ \text{mm}$ to increase the number of interacting NV centers). Ref. [101] uses NV infrared absorption in a cavity realizing a probed volume of $390\ \mu\text{m} \times 4500\ \mu\text{m}^2$. Both approaches lead to sensitivities in the order of $10\ \text{pT}/\sqrt{\text{Hz}}$ range. Ref. [128] demonstrates $15\ \text{pT}/\sqrt{\text{Hz}}$ in a volume of $13\ \mu\text{m} \times 200\ \mu\text{m} \times 2000\ \mu\text{m}$, while Ref. [99] extends sensitivity even to the sub- $\text{pT}/\sqrt{\text{Hz}}$ using optimized diamond material and optimized pulse sequences.

Using a single NV center for sensing, the probed volume is in principle given by the spatial extent of the electronic wave-function of the NV center. Recent simulations show that the electrons bound to the NV defect are closely localized within a few lattice constants [129] rendering the NV center a truly atomic-scale sensor. However, the spatial resolution will be limited by the distance of the sensing NV center to the sample under investigation which is ultimately limited by the distance of the NV center to the diamond surface. NV centers have been observed to be stable 2 nm below a SCD surface [130]. In addition to this distance to the SCD surface, technical limitations of the scanning probe imaging have to be considered which lead to an additional stand-off distance: Using SCD scanning probes, NV-to-sample distances around 25 nm [131, 132] at ambient conditions and distances around 10 nm in vacuum at cryogenic temperature [133] have been demonstrated yielding spatial resolutions in the same order of magnitude [132]. Typically, scanning probe microscopy using single NV centers reaches $\mu\text{T}/\sqrt{\text{Hz}}$ sensitivity for DC magnetic fields, while sensitivities on the order of $\text{nT}/\sqrt{\text{Hz}}$ have been shown for AC magnetometry [131, 132]. While these sensitivities are significantly lower than obtained using ensemble magnetometry, one has to take into account that the color center is placed in the high field region of the sample. Considering that e.g. dipolar magnetic fields decay with the third inverse power of the distance to the sample [2], the lower sensitivity is at least partially compensated by the close proximity of single NVs to the sample in a scanning probe geometry.

5. Selected sensing/imaging applications for each type of diamond

Applications of color centers in diamond have been summarized in several recent reviews focusing on magnetometry [2, 110], NV sensing as a probe for solid state physics [134], single spin magnetic resonance [135] and the coupling of spins and mechanical oscillators [136]. In the following section, we select a few recent and novel applications using different diamond types to illustrate the points discussed above.

In addition to demonstrating novel applications, a trend has been arising to miniaturize NV-based sensing devices to enable mobile use and potential industrial applications [137]: via connecting the diamond to micro-optics (graded index lenses), integrating microwave driving on printed circuit boards and using an LED instead of a laser for excitation, the volume of a diamond sensing device has been reduced to less than 3 cm^3 . This small footprint in combination with a low power consumption of 1.5 W allows for highly-flexible field-use of the diamond device opening the route toward novel applications. Additionally, recent work presents the first integration of diamond sensors into complementary metal-oxide-semiconductor (CMOS) technology, paving the way toward chip-scale diamond quantum sensors [138].

5.1. Single-crystal, bulk diamond and Förster Resonance Energy Transfer (FRET): novel approaches to NV sensing to enhance versatility of NV sensors

While NVs in high-purity, single-crystal, bulk diamond (SCD) typically have superior properties compared to NVs in often less pure NDs, probing sample dynamics with high spatial resolution requires to transfer the sample under investigation onto the SCD surface and spatial resolution is typically limited by diffraction to around $0.5\ \mu\text{m}$. Nevertheless, shallow NVs in SCD have been used for various applications probing micron-scale dynamics especially in the context of novel materials and current imaging. The almost back-action-free detection of currents in graphene, where currents in the μAmpere regime are measured with a resolution of $0.5\ \mu\text{m}$ [139], and the usage of NV centers to investigate failure of integrated circuits [125] illustrate their potential to analyze currents on the micron scale. Very recently, NV centers measured the band bending inside a diode like device *in-situ* [54]. Whereas in Ref. [140] shallow NV centers are used as sensor to perform nuclear magnetic resonance spectroscopy of atomically-thin hexagonal boron nitride layers. Thus NV centers allow to bring the technology of magnetic resonance truly to the nanoscale. For probing liquid samples, Kehayias et al. structured SCD to form a microfluidic chip and flow the substance under investigation through the diamond device [141].

In contrast to the above mentioned applications which all rely on the spin-based sensing capability of NVs, sensing relying on the dipolar nature of the NV center is less advanced. There have been first demonstrations using nearfield-based energy transfer (Förster Resonance Energy Transfer, FRET) to detect dye molecules attached to the surface of NDs [142, 143]. Additionally, a scanning ND attached to an AFM tip has been used to image graphene flakes with nanoscale resolution [3]. Other authors reported non-

successful attempts to establish FRET using NDs potentially due to a lack of control over the surface properties of NDs [144]. Consequently, it would be highly-advantageous to broaden FRET-based sensing to shallow color centers in SCD. For sensing and imaging approaches using the dipolar nature of NV centers, it is significant to consider the role of the two electric transition dipoles, \vec{X} and \vec{Y} as we discuss in detail in section 7. As a first step toward FRET-based imaging using color centers in SCD, we here present quenching due to graphene deposited onto the SCD surface.

We use commercial, high-purity, chemical vapor deposited, electronic grade SCD from Element Six ($[N]^s < 5$ ppb, $B < 1$ ppb). To create shallow NVs, we implant the sample with $6 \times 10^{11} \text{ cm}^{-2}$ nitrogen ions (Innovion, USA). Via annealing to 800°C in vacuum and cleaning in boiling acids (nitric, sulfuric, perchloric acid, 1:1:1), we create a layer of NV centers on average 7 nm below the SCD surface. From this clean surface, we observe homogeneous NV PL. We estimate the number of NV centers in the laser focus of our confocal microscope to be on the order of < 10 . The NV ensemble shows a spatially consistent lifetime of 15.5 ± 1 ns, which is slightly higher than the bulk lifetime of 12.9 ± 0.1 ns [87] due to a decrease in effective refractive index close to the surface. We now apply graphene flakes from solution (pristine graphene monolayer flakes from graphene supermarket with an average flake size of 550 nm (150-3000 nm), dispersed in ethanol). We spin coat this solution as-received with 600 rpm onto the SCD surface. We observe a slight trend to agglomeration of graphene. While in principle not desired, these agglomerates enable to straightforwardly observe the interaction of the NV centers with the graphene: We identify agglomerates via white light illumination of the SCD surface as well as Raman spectroscopy revealing a G Band at 1586 cm^{-1} . At the position of graphene agglomerates, we observe a reduced PL intensity [see Fig. 6(a)] as well as a clearly decreased NV lifetime [see Fig. 6(b)]. We check our results on several positions on the sample and find typical results as shown in Fig. 6(a)-(c). From the decrease in lifetime and the graphene Förster radius of 15 nm [3], we estimate the average distance of the graphene to the NV centers to be 19 nm which is higher than the average depth of the NV centers of 7 nm. We attribute this finding to a strong quenching of NV centers very close to the surface. These centers consequently do not contribute significantly to the measured PL signal which is dominated by the NVs deeper inside the diamond. Using the distance to the graphene, we estimate a reduction to 75% of the non-quenched PL. We observe a stronger reduction to 50%. However, our simplified consideration does not take into account the unknown absorption of the excitation laser as well as the NV PL due to the graphene agglomerate. We now test if NV ensembles below graphene agglomerates still show the typical spin properties of NV centers. To this end, we record an ODMR of an NV ensemble [see Fig. 6(d)] below one of the agglomerates, which shows the characteristic ODMR resonance. This result thus strongly indicates that NV centers can serve as multifunctional sensors, which probe the presence of other dipoles as well as the magnetic environment simultaneously.

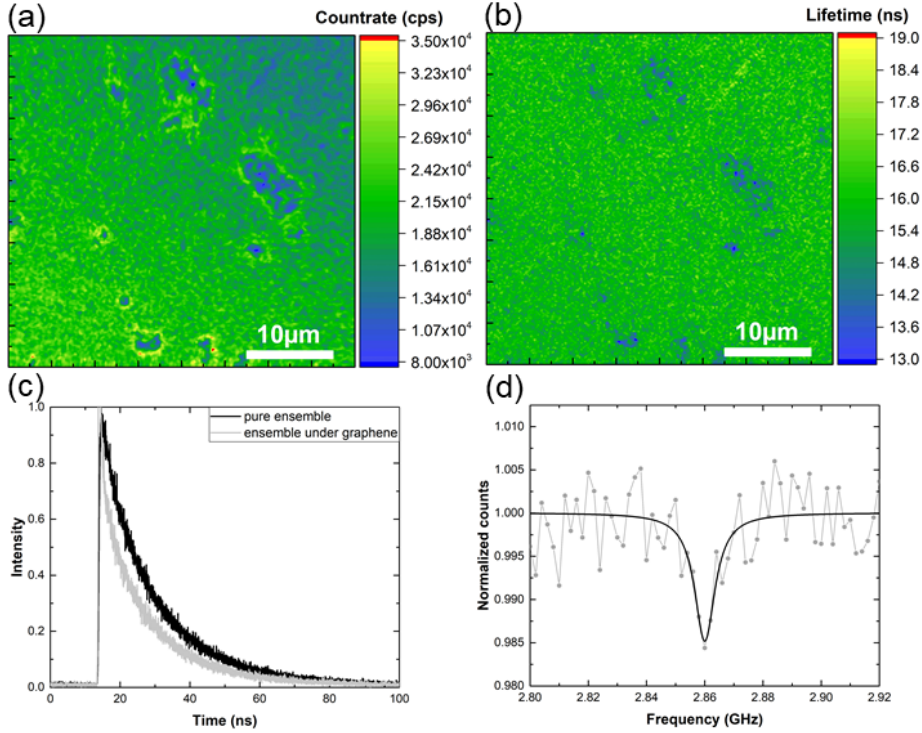


Figure 6. (a) PL map of the NV ensemble with graphene agglomerates (darker area) on the SCD surface (PL detected at wavelengths above 650 nm, excitation 0.7 mW at 532 nm). (b) Lifetime map of the same area like in (a). The excited state PL lifetime τ decreases up to 4 ns under the agglomerates. (c) NV ensemble lifetime measurement under the graphene (grey, $\tau=14.5$ ns) and next to a graphene agglomerate (black, $\tau=16.4$ ns). (d) ODMR measurement of the quenched NV centers under a graphene agglomerate.

5.2. Nanodiamonds for sensing and imaging

NDs are versatile tools in the life sciences as they can enter living cells and organisms. Their applications do not only cover sensing and imaging but also extend to drug delivery and tissue engineering. For recent reviews on these applications see Refs. [145–152]. Color centers in NDs first serve as non-bleaching fluorophores and additionally sense temperatures and magnetic fields inside cells. Moreover, novel approaches using the NV center’s charge state as a resource allow to sense the electrostatic environment of the NV center [153,154] and potential changes as small as 20 mV have been measured using this technique.

Considering electronic devices, NDs with NV ensembles enable the simultaneous measurement of local temperature and electric current distribution [155]. These quantities are relevant in the context of high electron mobility electronics, where local heating occurs and potentially induces device degradation [see Fig. 7(a)]. Both parameters can be measured in parallel as the local temperature affects the NV’s zero-field-splitting, while the local current density influences the splitting of the $m_s=-1$ and $m_s=1$ states as a result of the local magnetic field. Despite a certain scatter in the

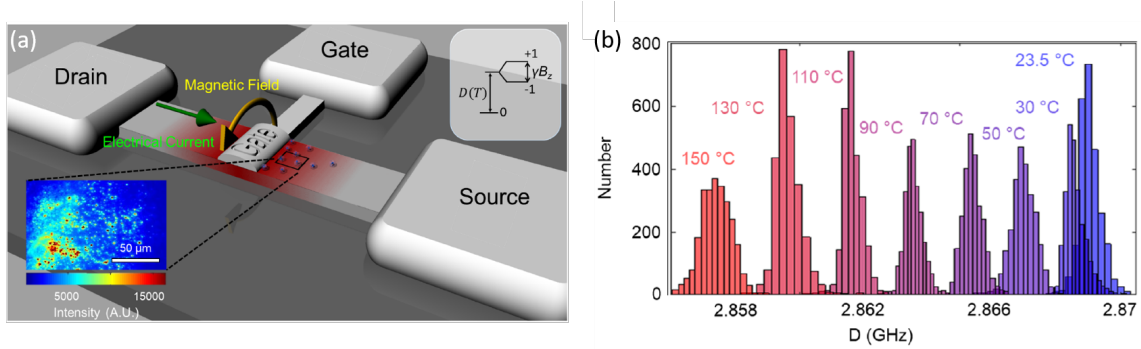


Figure 7. (a) Schematic of temperature and current (magnetic field) imaging using ND coated onto a transistor. (b) Zero-field-splitting statistics of NDs with NV ensembles. Reprinted from Ref. [155].

zero-field-splitting of individual NDs [see Fig. 7 (b)], the relevant temperature increases can be measured. For this applications, the ability to deposit NDs on almost all desired substrates and devices is highly advantageous.

5.3. Nanostructured diamond: pushing spatial resolution to the limit

Nanostructured SCD especially in the form of scanning diamond pillars has been used to image magnetic features with nanoscale resolution revealing magnetic features like superconducting vortices [133], skyrmions [156, 157] and magnetic properties in antiferromagnets [158]. Moreover, scanning NVs locally imaged the magnetic field arising due to microwave currents in a stripline [131]. As a novel field of application, NV centers in scanning tips have been used to probe the local conductivity of metallic structures [103] and have proven to be useful for the investigation of the magnetic field of a hard-disk write head [159]. To avoid the need for scanning pillars, also the sample under investigation e.g. a cell can be scanned over a stationary pillar. Using this approach, clusters of iron-storage molecules (Ferritin) have been imaged in a single cell [160].

Recently, the discovery of ferromagnetic behavior in two-dimensional van der Waals materials has triggered significant research interest. An example for such a material is CrI_3 . Using scanning NV magnetometry [see Fig. 8(a)], fundamental questions on the magnetism in CrI_3 have been addressed [161]: The measurements show that flakes with an even number of layers show no resulting magnetization in contrast to flakes with an odd number of layers [see Fig. 8(b)-(d)]. Due to the high spatial resolution and the low back-action in this sensing approach, it is possible to observe direct connections between structural and nanoscale magnetic properties of the material. Consequently, magnetic imaging using a scanning single NV center can help to understand magnetic two-dimensional materials which are candidates for future spintronic devices.

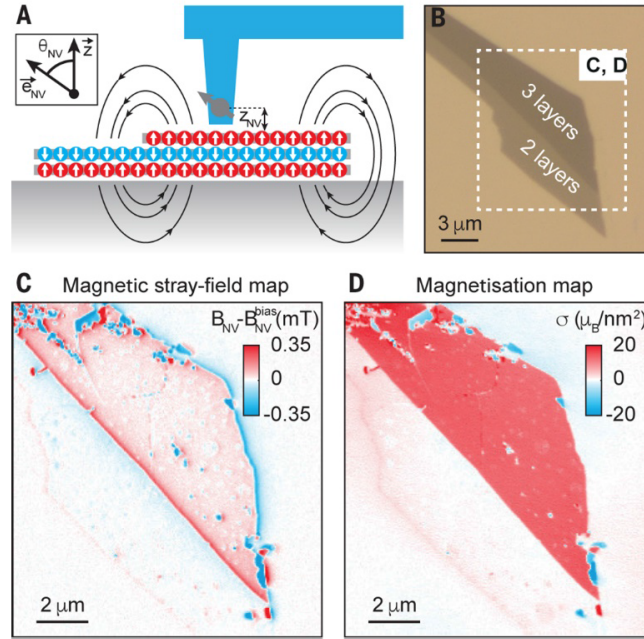


Figure 8. (a) Schematics of single NV scanning magnetometry (b) Optical micrograph of the CrI₃ flake with regions with 2 and 3 layers. (c) Magnetic stray field as imaged using a single NV center. (d) Calculated magnetization of the flake. Reprinted with permission from Ref. [161].

6. Conclusion and Outlook

In recent years, sensing using color centers has been applied to many novel fields of applications. Novel sensing and imaging modes are under development taking into account e.g. near-field interactions of color centers. Using such near field interactions, color centers will be efficient probes for the presence of other light emitting systems like e.g. quantum dots, molecules or two-dimensional materials [162]. Novel approaches to read-out the spin state of NV centers have made magnetic sensing faster and more efficient. Sensing capabilities of color centers have been extended not only to spin-based temperature sensing [4], but also to all optical temperature sensing [15]. The controlled coupling of color centers to strain and thus vibrational modes in nanoscale devices opens the route towards new control schemes in sensing and quantum information [163]. Moreover, the charge state of NV centers close to diamond surfaces has been found to depend strongly on the treatment of the surfaces [164]. Consequently, charge-state changes might be used as a future sensing resource. These ongoing developments will render color centers truly multi-functional sensors and the full potential of combining these recent results in sensing is still mainly un-explored.

Developments of new materials are ongoing and for example manufacturing of smaller and smaller nanodiamonds with active color centers will be pave the way towards enhanced usage of nanodiamonds inside cells [165]. Integrated sensors pave the way towards industrial applications and color center sensors have enabled new insights into

the nanoworld e.g. in the investigation of novel two-dimensional magnetic materials [161].

Challenges still arise from decoherence due to surfaces as well as implantation-related effects [47], and improvements and deeper understanding of the underlying effects could trigger a significant enhancement in NV sensor performance. A very recent example of novel approaches towards mitigating negative effects of nanofabrication is Ref. [46] in which a combination of electron-irradiation, high-temperature annealing and optimized etching lead to the creation of optically coherent NV centers. Similar approaches might be applied to sensing devices, enhancing their performance.

7. Appendix

7.0.1. Influence of the orientation of NV centers on near-field based sensing For sensing and imaging approaches using the dipolar nature of NV centers, it is significant to consider the role of the two electric transition dipoles, \vec{X} and \vec{Y} . The detection of near-field processes typically involves measuring the lifetime of the interacting systems. The following calculation illustrates how the observed lifetime is influenced by the existence of two dipoles \vec{X} and \vec{Y} .

\vec{X} and \vec{Y} are orthogonal to each other and located in the plane perpendicular to the NV axis (see Section 3.1, [89, 90]), while local strain determines the in plane orientation \vec{X} and \vec{Y} . Without local strain and the NV axis along [111], \vec{X} and \vec{Y} orient as $X \parallel [\bar{1}\bar{1}2]$ and $Y \parallel [1\bar{1}0]$ [90].

Following a semiclassical approximation, the radiative decay rate Γ^{rad} associated to a transition from an excited state to a ground state is given by [89]

$$\Gamma^{rad} = \frac{\mathcal{P}}{\hbar\omega}. \quad (2)$$

Here, \mathcal{P} is the power dissipated by the transition dipole $\vec{\mu}$. The lifetime τ for this transition is given as the inverse of the radiative decay rate Γ^{rad} (assuming a quantum efficiency of unity).

In a homogeneous medium with a dielectric constant ϵ_1 , we can write:

$$\Gamma_{hom}^{rad} = \frac{\mathcal{P}_{hom}}{\hbar\omega}, \quad \mathcal{P}_{hom}(\vec{\mu}^2) = \vec{\mu}^2 \sqrt{\epsilon_1} \omega^4 / 3c^3. \quad (3)$$

Assuming a homogenous dielectric is suitable for an NV center buried deeply in diamond. In this case, the observed decay rate (and hence the lifetime) will be given by the average of $\Gamma_{hom}^{\vec{X},rad}$ and $\Gamma_{hom}^{\vec{Y},rad}$:

$$\Gamma_{hom}^{rad} = \frac{1}{2}(\Gamma_{hom}^{\vec{X},rad} + \Gamma_{hom}^{\vec{Y},rad}). \quad (4)$$

To model a NV center close to the diamond surface, we have to use a layered system, with a NV center buried at a depth h . We decompose the power dissipated by the two dipoles $\mathcal{P}_{lay}^{\vec{X}}$, $\mathcal{P}_{lay}^{\vec{Y}}$ in components parallel and orthogonal to the surface:

$$\mathcal{P}_{lay}^{\vec{X}} = \frac{\vec{\mu}_{\perp,\vec{X}}^2}{\vec{\mu}_{\vec{X}}^2} \mathcal{P}_{lay,\perp} + \frac{\vec{\mu}_{\parallel,\vec{X}}^2}{\vec{\mu}_{\vec{X}}^2} \mathcal{P}_{lay,\parallel} \stackrel{!}{=} a_{\perp}^{\vec{X}^2} \mathcal{P}_{lay,\perp} + a_{\parallel}^{\vec{X}^2} \mathcal{P}_{lay,\parallel}, \quad (5)$$

$$\mathcal{P}_{lay}^{\vec{Y}} = \frac{\vec{\mu}_{\perp, \vec{Y}}^2}{\vec{\mu}_{\vec{Y}}^2} \mathcal{P}_{lay, \perp} + \frac{\vec{\mu}_{\parallel, \vec{Y}}^2}{\vec{\mu}_{\vec{Y}}^2} \mathcal{P}_{lay, \parallel} \stackrel{!}{=} a_{\perp}^{\vec{Y}^2} \mathcal{P}_{lay, \perp} + a_{\parallel}^{\vec{Y}^2} \mathcal{P}_{lay, \parallel}, \quad (6)$$

where $\mathcal{P}_{lay, \perp}$ ($\mathcal{P}_{lay, \parallel}$) is the power dissipated by the dipole component orthogonal (parallel) to the surface. We note that $\mathcal{P}_{lay, \perp}$ and $\mathcal{P}_{lay, \parallel}$ as well as all deduced quantities depend on the depth h of the NV center. Equations defining quantities and coefficient are highlighted using $\stackrel{!}{=}$.

Considering Eqns. 2, 3, Eq. 5, we find the decay rate $\Gamma_{lay}^{\vec{X}, rad}$ for \vec{X} :

$$\Gamma_{lay}^{\vec{X}, rad} = \frac{\mathcal{P}_{lay}^{\vec{X}}}{\hbar\omega} \stackrel{!}{=} F_{\vec{X}} \Gamma_{hom}^{rad} = (a_{\perp}^{\vec{X}^2} F_{\perp} + a_{\parallel}^{\vec{X}^2} F_{\parallel}) \Gamma_{hom}^{rad}, \quad (7)$$

with:

$$F_{\perp} \stackrel{!}{=} \frac{\mathcal{P}_{lay, \perp}}{\mathcal{P}_{hom}}, \quad F_{\parallel} \stackrel{!}{=} \frac{\mathcal{P}_{lay, \parallel}}{\mathcal{P}_{hom}}. \quad (8)$$

Similarly for \vec{Y}

$$\Gamma_{lay}^{\vec{Y}, rad} = \frac{\mathcal{P}_{lay}^{\vec{Y}}}{\hbar\omega} \stackrel{!}{=} F_{\vec{Y}} \Gamma_{hom}^{rad} = (a_{\perp}^{\vec{Y}^2} F_{\perp} + a_{\parallel}^{\vec{Y}^2} F_{\parallel}) \Gamma_{hom}^{rad}. \quad (9)$$

To obtain the total decay rate, we use Eq. 4:

$$\Gamma_{lay}^{rad} = \frac{1}{2} (\Gamma_{lay}^{\vec{X}, rad} + \Gamma_{lay}^{\vec{Y}, rad}). \quad (10)$$

Considering Eq. 7 and Eq. 9,

$$\Gamma_{lay}^{rad} = \frac{1}{2} \Gamma_{hom}^{rad} [F_{\perp} (a_{\perp}^{\vec{X}^2} + a_{\perp}^{\vec{Y}^2}) + F_{\parallel} (a_{\parallel}^{\vec{X}^2} + a_{\parallel}^{\vec{Y}^2})] = \Gamma_{hom}^{rad} [a_{\perp}^2 F_{\perp} + a_{\parallel}^2 F_{\parallel}] = \Gamma_{hom}^{rad} F_{lay}, \quad (11)$$

with:

$$F_{lay} \stackrel{!}{=} a_{\perp}^2 F_{\perp} + a_{\parallel}^2 F_{\parallel}, \quad (12)$$

and

$$a_{\perp}^2 \stackrel{!}{=} \frac{a_{\perp}^{\vec{X}^2} + a_{\perp}^{\vec{Y}^2}}{2}, \quad a_{\parallel}^2 \stackrel{!}{=} \frac{a_{\parallel}^{\vec{X}^2} + a_{\parallel}^{\vec{Y}^2}}{2}. \quad (13)$$

Considering in detail the possible orientations of \vec{X} and \vec{Y} in (100)-oriented SCD which is the most common SCD orientation, we find that that a_{\perp}^2 and a_{\parallel}^2 do not depend on the orientation of \vec{X} and \vec{Y} in the plane orthogonal to the NV axis, nor on which of the equivalent directions the NV occupies and $a_{\perp}^2 = \frac{1}{3}$ and $a_{\parallel}^2 = \frac{2}{3}$.

Consequently, Γ_{lay}^{rad} is the same for all equivalent orientations of NV axis and orientations of \vec{X} and \vec{Y} . Γ_{lay}^{rad} and the lifetime of the NV will depend only on the NV depth h . FRET will add a non-radiative channel to the system. In this case the total decay rate Γ_{lay}^{tot} for the layered system is:

$$\Gamma_{lay}^{tot} = \Gamma_{lay}^{rad} + \Gamma_{lay}^{nr} = \Gamma_{hom}^{rad} F_{lay} + \Gamma_{lay}^{nr}. \quad (14)$$

Consequently, we find a unique decay rate Γ_{lay}^{tot} for an ensemble of NV centers at the same depth h . Hence, the observed PL decay will be monoexponential characterized by a lifetime:

$$\tau = \frac{1}{\Gamma_{lay}^{tot}}. \quad (15)$$

Consequently, shallow NV centers in (100) oriented diamond may form highly-suitable sensors for FRET, despite their non-trivial transition dipoles.

References

- [1] Dolde F, Doherty M W, Michl J, Jakobi I, Naydenov B, Pezzagna S, Meijer J, Neumann P, Jelezko F, Manson N B and Wrachtrup J 2014 *Phys. Rev. Lett.* **112**(9) 097603 URL <http://link.aps.org/doi/10.1103/PhysRevLett.112.097603>
- [2] Rondin L, Tetienne J P, Hingant T, Roch J F, Maletinsky P and Jacques V 2014 *Rep. Prog. Phys.* **77** 056503 URL <http://stacks.iop.org/0034-4885/77/i=5/a=056503>
- [3] Tisler J, Oeckinghaus T, Stöhr R J, Kolesov R, Reuter R, Reinhard F and Wrachtrup J 2013 *Nano Lett.* **13** 3152–3156
- [4] Kucsko G, Maurer P, Yao N, Kubo M, Noh H, Lo P, Park H and Lukin M 2013 *Nature* **500** 54–58
- [5] Teissier J, Barfuss A, Appel P, Neu E and Maletinsky P 2014 *Phys. Rev. Lett.* **113**(2) 020503 URL <http://link.aps.org/doi/10.1103/PhysRevLett.113.020503>
- [6] Chernobrod B M and Berman G P 2005 *J. Appl. Phys.* **97** 014903 (pages 3) URL <http://link.aip.org/link/?JAP/97/014903/1>
- [7] Balasubramanian G, Neumann P, Twitchen D, Markham M, Kolesov R, Mizuochi N, Isoya J, Achard J, Beck J, Tissler J, Jacques V, Hemmer P, Jelezko F and Wrachtrup J 2009 *Nature Mater.* **8** 383–387
- [8] Gruber A, Dräbenstedt A, Tietz C, Fleury L, Wrachtrup J and von Borczyskowski C 1997 *Science* **276** 2012–2014 ISSN 0036-8075
- [9] Kurtsiefer C, Mayer S, Zarda P and Weinfurter H 2000 *Phys. Rev. Lett.* **85** 290–293
- [10] Becker J N and Becher C 2017 *physica status solidi (a)* **214** 1700586
- [11] Siyushev P, Metsch M H, Ijaz A, Binder J M, Bhaskar M K, Sukachev D D, Sipahigil A, Evans R E, Nguyen C T, Lukin M D *et al.* 2017 *Physical Review B* **96** 081201
- [12] Iwasaki T, Miyamoto Y, Taniguchi T, Siyushev P, Metsch M H, Jelezko F and Hatano M 2017 *Phys. Rev. Lett.* **119**(25) 253601 URL <https://link.aps.org/doi/10.1103/PhysRevLett.119.253601>
- [13] Ditalia Tchernij S, Lu?hmann T, Herzig T, Ku?pper J, Damin A, Santonocito S, Signorile M, Traina P, Moreva E, Celegato F *et al.* 2018 *ACS Photonics* **5** 4864–4871
- [14] Fan J W, Cojocar I, Becker J, Fedotov I V, Alkahtani M H A, Alajlan A, Blakley S, Rezaee M, Lyamkina A, Palyanov Y N, Borzdov Y M, Yang Y P, Zheltikov A, Hemmer P and Akimov A V 2018 *ACS Photonics* **5** 765–770 (*Preprint* <https://doi.org/10.1021/acsphotonics.7b01465>) URL <https://doi.org/10.1021/acsphotonics.7b01465>
- [15] Nguyen C T, Evans R E, Sipahigil A, Bhaskar M K, Sukachev D D, Agafonov V N, Davydov V A, Kulikova L F, Jelezko F and Lukin M D 2018 *Applied Physics Letters* **112** 203102
- [16] Dahl J E, Liu S G and Carlson R M K 2003 *Science* **299** 96–99 ISSN 0036-8075, 1095-9203 URL <http://science.sciencemag.org/content/299/5603/96>
- [17] Lai L and Barnard A S 2012 *Journal of Materials Chemistry* **22** 16774 ISSN 0959-9428, 1364-5501 URL <http://xlink.rsc.org/?DOI=c2jm32640j>
- [18] Bundy F P 1980 *Journal of Geophysical Research: Solid Earth* **85** 6930–6936 ISSN 2156-2202 URL <https://agupubs.onlinelibrary.wiley.com/doi/abs/10.1029/JB085iB12p06930>

- [19] Markham M, Dodson J, Scarsbrook G, Twitchen D, Balasubramanian G, Jelezko F and Wrachtrup J 2010 *Diam. Relat. Mater.* **20** 134–139
- [20] Krueger A, Ozawa M, Jarre G, Liang Y, Stegk J and Lu L 2007 *Phys. Status Solidi A* **204** 2881–2887 ISSN 0031-8965 12th Hasselt Diamond Workshop 2007 (SBDD XII), Belgium
- [21] Sotoma S, Terada D, Segawa T F, Igarashi R, Harada Y and Shirakawa M 2018 *Scientific Reports* **8** ISSN 2045-2322 URL <http://www.nature.com/articles/s41598-018-23635-5>
- [22] Fang C, Zhang Y, Zhang Z, Shan C, Shen W and Jia X 2018 *CrystEngComm* **20** 505–511 ISSN 1466-8033 URL <http://xlink.rsc.org/?DOI=C7CE02013A>
- [23] Schreck M, Gsell S, Brescia R and Fischer M 2017 *Scientific reports* **7** 44462
- [24] Balaban A T, Young D C, Plavec J, PeĀĀĀĀnik K, Pompe M, Dahl J E and Carlson R M K 2015 *Magnetic Resonance in Chemistry* **53** 1003–1018 ISSN 07491581 URL <http://doi.wiley.com/10.1002/mrc.4289>
- [25] Alkahtani M, Lang J, Naydenov B, Jelezko F and Hemmer P 2019 *ACS Photonics*
- [26] Tzeng Y K, Zhang J L, Lu H, Ishiwata H, Dahl J, Carlson R M, Yan H, Schreiner P R, Vuc?kovic? J, Shen Z X *et al.* 2017 *Nano letters* **17** 1489–1495
- [27] Gebbie M A, Ishiwata H, McQuade P J, Petrak V, Taylor A, Freiwald C, Dahl J E, Carlson R M K, Fokin A A, Schreiner P R, Shen Z X, Nesladek M and Melosh N A 2018 *Proceedings of the National Academy of Sciences* **115** 8284–8289 ISSN 0027-8424, 1091-6490 URL <http://www.pnas.org/lookup/doi/10.1073/pnas.1803654115>
- [28] Vlasov I I, Shiryaev A A, Rendler T, Steinert S, Lee S Y, Antonov D, V?r?r?s M, Jelezko F, Fisenko A V, Semjonova L F, Biskupek J, Kaiser U, Lebedev O I, Sildos I, Hemmer Philip Rand Konov V I, Gali A and Wrachtrup J 2014 *Nat. Nanotechnol.* **9** 54–58
- [29] Bakharev P V, Huang M, Saxena M, Lee S W, Joo S H, Park S O, Dong J, Camacho-Mojica D, Jin S, Kwon Y, Biswal M, Ding F, Kwak S K, Lee Z and Ruoff R S 2019 *arXiv:1901.02131 [cond-mat]* ArXiv: 1901.02131 URL <http://arxiv.org/abs/1901.02131>
- [30] May P W and Mankelevich Y A 2008 *The Journal of Physical Chemistry C* **112** 12432–12441 ISSN 1932-7447, 1932-7455 URL <https://pubs.acs.org/doi/10.1021/jp803735a>
- [31] Nelz R, G?rlitz J, Herrmann D, Slablab A, Challier M, Radtke M, Fischer M, Gsell S, Schreck M, Becher C *et al.* 2019 *APL Materials* **7** 011108
- [32] Tallaire A, Achard J, Boussadi A, Brinza O, Gicquel A, Kupriyanov I, Palyanov Y, Sakr G and Barjon J 2014 *Diamond Relat. Mater.* **41** 34 – 40 ISSN 0925-9635 URL <http://www.sciencedirect.com/science/article/pii/S0925963513002124>
- [33] Lesik M, Plays T, Tallaire A, Achard J, Brinza O, William L, Chipaux M, Toraille L, Debuisschert T, Gicquel A *et al.* 2015 *Diamond Relat. Mater.* **56** 47–53
- [34] Neu E, Appel P, Ganzhorn M, Miguel-Sanchez J, Lesik M, Mille V, Jacques V, Tallaire A, Achard J and Maletinsky P 2014 *Appl. Phys. Lett.* **104** 153108 URL <http://scitation.aip.org/content/aip/journal/apl/104/15/10.1063/1.4871580>
- [35] Robertson R, Fox J and Martin A 1934 *Philos. Trans. Roy. Soc. A* **232** 463–535
- [36] Walker J 1979 *Rep. Prog. Phys.* **42** 1605–1659
- [37] Balmer R S, Brandon J R, Clewes S L, Dhillon H K, Dodson J M, Friel I, Inglis P N, Madgwick T D, Markham M L, Mollart T P, Perkins N, Scarsbrook G A, Twitchen D J, Whitehead A J, Wilman J J and Woollard S M 2009 *J. Phys.: Condens. Matter* **21** 364221 ISSN 0953-8984
- [38] Ohno K, Joseph Heremans F, de las Casas C F, Myers B A, Aleman B J, Bleszynski Jayich A C and Awschalom D D 2014 *Appl. Phys. Lett.* **105** 052406 URL <http://scitation.aip.org/content/aip/journal/apl/105/5/10.1063/1.4890613>
- [39] Ishiwata H, Nakajima M, Tahara K, Ozawa H, Iwasaki T and Hatano M 2017 *Applied Physics Letters* **111** 043103
- [40] Michl J, Teraji T, Zaiser S, Jakobi I, Waldherr G, Dolde F, Neumann P, Doherty M W, Manson N B, Isoya J and Wrachtrup J 2014 *Appl. Phys. Lett.* **104** 102407 URL <http://scitation.aip.org/content/aip/journal/apl/104/10/10.1063/1.4868128>
- [41] Lesik M, Tetienne J P, Tallaire A, Achard J, Mille V, Gicquel A,

- Roch J F and Jacques V 2014 *Appl. Phys. Lett.* **104** 113107 URL <http://scitation.aip.org/content/aip/journal/apl/104/11/10.1063/1.4869103>
- [42] Doi Y, Fukui T, Kato H, Makino T, Yamasaki S, Tashima T, Morishita H, Miwa S, Jelezko F, Suzuki Y and Mizuochi N 2016 *Phys. Rev. B* **93**(8) 081203 URL <http://link.aps.org/doi/10.1103/PhysRevB.93.081203>
- [43] Ohno K, Joseph Heremans F, Bassett L C, Myers B A, Toyli D M, Bleszynski Jayich A C, Palmstrøm C J and Awschalom D D 2012 *Applied Physics Letters* **101** 082413
- [44] Chandran M, Michaelson S, Saguy C and Hoffman A 2016 *Applied Physics Letters* **109** 221602 (Preprint <http://dx.doi.org/10.1063/1.4971312>) URL <http://dx.doi.org/10.1063/1.4971312>
- [45] de Oliveira F F, Momenzadeh S A, Antonov D, Scharpf J, Osterkamp C, Naydenov B, Jelezko F, Denisenko A and Wrachtrup J 2016 *NANO LETTERS* **16** 2228–2233 ISSN 1530-6984
- [46] Ruf M, IJspeert M, van Dam S, de Jong N, van den Berg H, Evers G and Hanson R 2019 *Nano letters* **19** 3987
- [47] van Dam S B, Walsh M, Degen M J, Bersin E, Mouradian S L, Galiullin A, Ruf M, IJspeert M, Taminiau T H, Hanson R and Englund D R 2019 *Phys. Rev. B* **99**(16) 161203 URL <https://link.aps.org/doi/10.1103/PhysRevB.99.161203>
- [48] Wolf T, Neumann P, Nakamura K, Sumiya H, Ohshima T, Isoya J and Wrachtrup J 2015 *Physical Review X* **5** 041001
- [49] De Oliveira F F, Antonov D, Wang Y, Neumann P, Momenzadeh S A, Häußermann T, Pasquarelli A, Denisenko A and Wrachtrup J 2017 *Nature Communications* **8** 15409
- [50] Lovchinsky I, Sushkov A, Urbach E, de Leon N, Choi S, De Greve K, Evans R, Gertner R, Bersin E, Müller C *et al.* 2016 *Science* **351** 836–841
- [51] Tetienne J P, de Gille R, Broadway D, Teraji T, Lillie S, McCoey J, Dontschuk N, Hall L, Stacey A, Simpson D *et al.* 2018 *Physical Review B* **97** 085402
- [52] Yamamoto T, Umeda T, Watanabe K, Onoda S, Markham M, Twitchen D, Naydenov B, McGuinness L, Teraji T, Koizumi S *et al.* 2013 *Physical Review B* **88** 075206
- [53] Radko I P, Boll M, Israelsen N M, Raatz N, Meijer J, Jelezko F, Andersen U L and Huck A 2016 *Opt. Express* **24** 27715–27725 URL <http://www.opticsexpress.org/abstract.cfm?URI=oe-24-24-27715>
- [54] Broadway D, Dontschuk N, Tsai A, Lillie S, Lew C K, McCallum J, Johnson B, Doherty M, Stacey A, Hollenberg L *et al.* 2018 *Nature Electronics* **1** 502
- [55] Prins J F 2003 *Semiconductor Science and Technology* **18** S27–S33 ISSN 0268-1242 URL <http://stacks.iop.org/0268-1242/18/i=3/a=304?key=crossref.b7c783d110a65fb6a92f23e99a7be9eb>
- [56] Riedrich-Máčáüller J, Pezzagna S, Meijer J, Pauly C, Máčáijklich F, Markham M, Edmonds A M and Becher C 2015 *Applied Physics Letters* **106** 221103– URL <http://aip.scitation.org/doi/10.1063/1.4922117>
- [57] Jakobi I, Momenzadeh S A, de Oliveira F F, Michl J, Ziem F, Schreck M, Neumann P, Denisenko A and Wrachtrup J 2016 *Journal of Physics: Conference Series* **752** 012001 ISSN 1742-6588, 1742-6596 URL <http://stacks.iop.org/1742-6596/752/i=1/a=012001?key=crossref.9138b1526b5b6401c2226281e8cf6026>
- [58] Lesik M, Spinicelli P, Pezzagna S, Happel P, Jacques V, Salord O, Rasser B, Delobbe A, Sudraud Pierre ad Tallaire A, Meijer J and Roch J F 2013 *physica status solidi (a)* **210** 2055–2059
- [59] Marseglia L, Saha K, Ajoy A, Schröder T, Englund D, Jelezko F, Walsworth R, Pacheco J, Perry D, Bielejec E *et al.* 2018 *Optics express* **26** 80–89
- [60] Riedel D, Rohner D, Ganzhorn M, Kaldewey T, Appel P, Neu E, Warburton R J and Maletinsky P 2014 *Phys. Rev. Applied* **2**(6) 064011 URL <http://link.aps.org/doi/10.1103/PhysRevApplied.2.064011>
- [61] Wildanger D, Patton B R, Schill H, Marseglia L, Hadden J, Knauer S, Schönle A, Rarity J G, O'Brien J L, Hell S W and Smith J M 2012 *Adv. Mater.* **24** OP309–OP313
- [62] Li L, Chen E H, Zheng J, Mouradian S L, Dolde F, Schröder T, Karaveli S, Markham M L,

- Twitchen D J and Englund D 2015 *Nano letters* **15** 1493–1497
- [63] Jaffe T, Felgen N, Gal L, Kornblum L, Reithmaier J P, Popov C and Orenstein M 2019 *Advanced Optical Materials* **7** 1800715 ISSN 21951071 URL <http://doi.wiley.com/10.1002/adom.201800715>
- [64] Nelz R, Fuchs P, Opaluch O, Sonusen S, Savenko N, Podgursky V and Neu E 2016 *Applied Physics Letters* **109** 193105 URL <http://scitation.aip.org/content/aip/journal/apl/109/19/10.1063/1.4967189>
- [65] Choi S, Leong V, Alagappan G and Krivitsky L 2018 *ACS Photonics* **5** 4244–4248
- [66] Beha K, Fedder H, Wolfer M, Becker M C, Siyushev P, Jamali M, Batalov A, Hinz C, Hees J, Kirste L, Obloh H, Gheeraert E, Naydenov B, Jakobi I, Dolde F, Pezzagna S, Twittchen D, Markham M, Dregely D, Giessen H, Meijer J, Jelezko F, Nebel C E, Bratschitsch R, Leitenstorfer A and Wrachtrup J 2012 *BEILSTEIN JOURNAL OF NANOTECHNOLOGY* **3** 895–908 ISSN 2190-4286
- [67] Aharonovich I and Neu E 2014 *Adv. Opt. Mater.* **2** 911–928 ISSN 2195-1071 URL <http://dx.doi.org/10.1002/adom.201400189>
- [68] Schroder T, Mouradian S L, Zheng J, Trusheim M E, Walsh M, Chen E H, Li L, Bayn I and Englund D 2016 *JOURNAL OF THE OPTICAL SOCIETY OF AMERICA B-OPTICAL PHYSICS* **33** B65–B83 ISSN 0740-3224
- [69] Atatüre M, Englund D, Vamivakas N, Lee S Y and Wrachtrup J 2018 *Nature Reviews Materials* **3** 38
- [70] Babinec T, Hausmann B, Khan M, Zhang Y, Maze J, Hemmer P and Loncar M 2010 *Nature Nanotech.* **5** 195–199
- [71] Fuchs P, Challier M and Neu E 2018 *New Journal of Physics* **20** 125001
- [72] Appel P, Neu E, Ganzhorn M, Barfuss A, Batzer M, Gratz M, Tschöpe A and Maletinsky P 2016 *Review of Scientific Instruments* **87** 063703 URL <http://scitation.aip.org/content/aip/journal/rsi/87/6/10.1063/1.4952953>
- [73] McCloskey D, Dontschuk N, Broadway D, Nadarajah A, Stacey A, Tetienne J P, Hollenberg L, Prawer S and Simpson D 2019 *arXiv preprint arXiv:1902.02464*
- [74] Trusheim M E, Wan N H, Chen K C, Ciccarino C J, Flick J, Sundararaman R, Malladi G, Bersin E, Walsh M, Lienhard B *et al.* 2019 *Physical Review B* **99** 075430
- [75] Burek M J, Chu Y, Liddy M S Z, Patel P, Rochman J, Meesala S, Hong W, Quan Q, Lukin M D and Loncar M 2014 *Nature Communications* **5** ISSN 2041-1723 URL <http://www.nature.com/articles/ncomms6718>
- [76] Mitchell M, Lake D P and Barclay P E 2019 *APL Photonics* **4** 016101 ISSN 2378-0967 URL <http://aip.scitation.org/doi/10.1063/1.5053122>
- [77] Momenzadeh S A, Stănilău R J, de Oliveira F F, Brunner A, Denisenko A, Yang S, Reinhard F and Wrachtrup J 2015 *Nano Letters* **15** 165–169 ISSN 1530-6984, 1530-6992 URL <http://pubs.acs.org/doi/10.1021/nl503326t>
- [78] Kato Y, Kawashima H, Makino T, Ogura M, Traoré A, Ozawa N and Yamasaki S 2017 *physica status solidi (a)* **214** 1700233
- [79] de Oliveira F F, Momenzadeh S A, Wang Y, Konuma M, Markham M, Edmonds A M, Denisenko A and Wrachtrup J 2015 *APPLIED PHYSICS LETTERS* **107** 073107 ISSN 0003-6951
- [80] Riedrich-Möller J, Kipfstuhl L, Hepp C, Neu E, Pauly C, Mücklich F, Baur A, M Wandt M, Wolff S, Fischer M, Gsell S, Schreck M and Becher C 2012 *Nature Nanotech.* **7** 69
- [81] Ortiz-Huerta F, Chen L, Taverne M, Hadden J P, Johnson M, Ho Y L D and Rarity J G 2018 *Optics Express* **26** 33245 ISSN 1094-4087 URL <https://www.osapublishing.org/abstract.cfm?URI=oe-26-25-33245>
- [82] Sun P, Tang C, Xia X, Yao Z, Quan B, Yuan G, Gu C and Li J 2016 *Microelectronic Engineering* **155** 61–66 ISSN 01679317 URL <https://linkinghub.elsevier.com/retrieve/pii/S0167931716300739>
- [83] Tao Y, Boss J M, Moores B A and Degen C L 2014 *Nature Communications* **5** ISSN 2041-1723

- URL <http://www.nature.com/articles/ncomms4638>
- [84] Aharonovich I, Lee J C, Magyar A P, Bracher D O and Hu E L 2013 *Laser & Photonics Reviews* **7** L61–L65 ISSN 1863-8899 URL <http://dx.doi.org/10.1002/lpor.201300065>
- [85] Abe E and Sasaki K 2018 *Journal of Applied Physics* **123** 161101
- [86] Manson N B, Beha K, Batalov A, Rogers L J, Doherty M W, Bratschitsch R and Leitenstorfer A 2013 *Phys. Rev. B* **87**(15) 155209 URL <http://link.aps.org/doi/10.1103/PhysRevB.87.155209>
- [87] Collins A, Thomaz M and Jorge M 1983 *Journal of Physics C* **16** 2177–2181
- [88] Kehayias P, Doherty M W, English D, Fischer R, Jarmola A, Jensen K, Leefer N, Hemmer P, Manson N B and Budker D 2013 *Phys. Rev. B* **88**(16) 165202 URL <http://link.aps.org/doi/10.1103/PhysRevB.88.165202>
- [89] Davies G and Hamer M 1976 *Proc. R. Soc. Lond. A* **348** 285–298
- [90] Epstein R, Mendoza F, Kato Y and Awschalom D 2005 *Nature physics* **1** 94
- [91] Robledo L, Bernien H, van der Sar T and Hanson R 2011 *New J. Phys.* **13** 025013 URL <http://stacks.iop.org/1367-2630/13/i=2/a=025013>
- [92] Rogers L J, Armstrong S, Sellars M J and Manson N B 2008 *New J. Phys.* **10** 103024 ISSN 1367-2630
- [93] Siyushev P, Pinto H, Vörös M, Gali A, Jelezko F and Wrachtrup J 2013 *Phys. Rev. Lett.* **110**(16) 167402 URL <http://link.aps.org/doi/10.1103/PhysRevLett.110.167402>
- [94] Shields B J, Unterreithmeier Q P, de Leon N P, Park H and Lukin M D 2015 *Phys. Rev. Lett.* **114**(13) 136402 URL <http://link.aps.org/doi/10.1103/PhysRevLett.114.136402>
- [95] Dhomkar S, Jayakumar H, Zangara P R and Meriles C A 2018 *Nano Letters* **18** 4046–4052 pMID: 29733616 (*Preprint* <https://doi.org/10.1021/acs.nanolett.8b01739>) URL <https://doi.org/10.1021/acs.nanolett.8b01739>
- [96] Clevenson H, Trusheim M E, Teale C, Schroeder T, Braje D and Englund D 2015 *NATURE PHYSICS* **11** 393–397 ISSN 1745-2473
- [97] Lee K, Chen X, Eghlidi H, Kukura P, Lettow R, Renn A, Sandoghdar V and Göttinger S 2011 *Nature Photonics* **5** 166
- [98] Wan N H, Shields B J, Kim D, Mouradian S, Lienhard B, Walsh M, Bakhru H, Schröder T and Englund D 2018 *Nano letters* **18** 2787–2793
- [99] Wolf T, Neumann P, Nakamura K, Sumiya H, Ohshima T, Isoya J and Wrachtrup J 2015 *Phys. Rev. X* **5**(4) 041001 URL <http://link.aps.org/doi/10.1103/PhysRevX.5.041001>
- [100] Hrubesch F M, Braunbeck G, Stutzmann M, Reinhard F and Brandt M S 2017 *Physical review letters* **118** 037601
- [101] Chatzidrosos G, Wickenbrock A, Bougas L, Leefer N, Wu T, Jensen K, Dumeige Y and Budker D 2017 *Phys. Rev. Applied* **8**(4) 044019 URL <https://link.aps.org/doi/10.1103/PhysRevApplied.8.044019>
- [102] Jensen K, Leefer N, Jarmola A, Dumeige Y, Acosta V M, Kehayias P, Patton B and Budker D 2014 *Physical review letters* **112** 160802
- [103] Ariyaratne A, Bluvstein D, Myers B A and Jayich A C B 2018 *Nature communications* **9** 2406
- [104] El-Ella H A, Ahmadi S, Wojciechowski A M, Huck A and Andersen U L 2017 *Optics express* **25** 14809–14821
- [105] Shin C S, Avalos C E, Butler M C, Trease D R, Seltzer S J, Peter Mustonen J, Kennedy D J, Acosta V M, Budker D, Pines A *et al.* 2012 *Journal of Applied Physics* **112** 124519
- [106] Barry J F, Schloss J M, Bauch E, Turner M J, Hart C A, Pham L M and Walsworth R L 2019 *arXiv preprint arXiv:1903.08176*
- [107] Ofori-Okai B K, Pezzagna S, Chang K, Loretz M, Schirhagl R, Tao Y, Moores B A, Groot-Berning K, Meijer J and Degen C L 2012 *Phys. Rev. B* **86**(8) 081406 URL <http://link.aps.org/doi/10.1103/PhysRevB.86.081406>
- [108] Romach Y, Müller C, Unden T, Rogers L J, Isoda T, Itoh K M, Markham M, Stacey A, Meijer J, Pezzagna S, Naydenov B, McGuinness L P, Bar-Gill N and Jelezko F 2015 *Phys. Rev. Lett.*

- 114(1) 017601 URL <http://link.aps.org/doi/10.1103/PhysRevLett.114.017601>
- [109] Kim M, Mamin H, Sherwood M, Ohno K, Awschalom D and Rugar D 2015 *Physical review letters* **115** 087602
- [110] Bernardi E, Nelz R, Sonusen S and Neu E 2017 *Crystals* **7** 124
- [111] McLellan C A, Myers B A, Kraemer S, Ohno K, Awschalom D D and Bleszynski Jayich A C 2016 *Nano letters* **16** 2450–2454
- [112] Yamano H, Kawai S, Kato K, Kageura T, Inaba M, Okada T, Higashimata I, Haruyama M, Tanii T, Yamada K *et al.* 2017 *Japanese Journal of Applied Physics* **56** 04CK08
- [113] Neumann P, Beck J, Steiner M, Rempp F, Fedder H, Hemmer P R, Wrachtrup J and Jelezko F 2010 *Science* **329** 542–544
- [114] Hopper D A, Shulevitz H J and Bassett L C 2018 *Micromachines* **9** ISSN 2072-666X URL <http://www.mdpi.com/2072-666X/9/9/437>
- [115] Jeske J, Cole J H and Greentree A D 2016 *New Journal of Physics* **18** 013015
- [116] Dumeige Y, Roch J F, Bretenaker F, Debuisschert T, Acosta V, Becher C, Chatzidrosos G, Wickenbrock A, Bougas L, Wilzewski A *et al.* 2019 *Optics express* **27** 1706–1717
- [117] Siyushev P, Nesladek M, Bourgeois E, Gulka M, Hruby J, Yamamoto T, Trupke M, Teraji T, Isoya J and Jelezko F 2019 *Science* **363** 728–731
- [118] Jeske J, Lau D W M, Vidal X, McGuinness L P, Reineck P, Johnson B C, Doherty M W, McCallum J C, Onoda S, Jelezko F, Ohshima T, Volz T, Cole J H, Gibson B C and Greentree A D 2017 *Nature Communications* **8** ISSN 2041-1723
- [119] Steinert S, Dolde F, Neumann P, Aird A, Naydenov B, Balasubramanian G, Jelezko F and Wrachtrup J 2010 *Review of scientific instruments* **81** 043705
- [120] Chipaux M, Tallaire A, Achard J, Pezzagna S, Meijer J, Jacques V, Roch J F and Debuisschert T 2015 *EUROPEAN PHYSICAL JOURNAL D* **69** 166 ISSN 1434-6060
- [121] Pham L M, Le Sage D, Stanwix P L, Yeung T K, Glenn D, Trifonov A, Cappellaro P, Hemmer P, Lukin M D, Park H *et al.* 2011 *New Journal of Physics* **13** 045021
- [122] Taylor J, Cappellaro P, Childress L, Jiang L, Budker D, Hemmer P, Yacoby A, Walsworth R and Lukin M 2008 *Nature Physics* **4** 810
- [123] Shao L, Liu R, Zhang M, Shneidman A V, Audier X, Markham M, Dhillon H, Twitchen D J, Xiao Y F and Loncar M 2016 *Adv. Opt. Mater.* **10.1002/adom.201600039** ISSN 2195-1071 URL <http://dx.doi.org/10.1002/adom.201600039>
- [124] Le Sage D, Arai K, Glenn D, DeVience S, Pham L, Rahn-Lee L, Lukin M, Yacoby A, Komeili A and Walsworth R 2013 *Nature* **496** 486–489
- [125] Nowodzinski A, Chipaux M, Toraille L, Jacques V, Roch J F and Debuisschert T 2015 *Microelectronics Reliability* **55** 1549 ISSN 0026-2714 proceedings of the 26th European Symposium on Reliability of Electron Devices, Failure Physics and AnalysisSI:Proceedings of {ESREF} 2015 URL <http://www.sciencedirect.com/science/article/pii/S0026271415001614>
- [126] Schlüssel Y, Lenz T, Rohner D, Bar-Haim Y, Bougas L, Groswasser D, Kieschnick M, Rozenberg E, Thiel L, Waxman A, Meijer J, Maletinsky P, Budker D and Folman R 2018 *Phys. Rev. Applied* **10**(3) 034032 URL <https://link.aps.org/doi/10.1103/PhysRevApplied.10.034032>
- [127] Horsley A, Appel P, Wolters J, Achard J, Tallaire A, Maletinsky P and Treutlein P 2018 *Phys. Rev. Applied* **10**(4) 044039 URL <https://link.aps.org/doi/10.1103/PhysRevApplied.10.044039>
- [128] Barry J F, Turner M J, Schloss J M, Glenn D R, Song Y, Lukin M D, Park H and Walsworth R L 2016 *PROCEEDINGS OF THE NATIONAL ACADEMY OF SCIENCES OF THE UNITED STATES OF AMERICA* **113** 14133–14138 ISSN 0027-8424
- [129] Bockstedte M, SchÄÄijtz F, Garratt T, IvÄÄady V and Gali A 2018 *npj Quantum Materials* **3** ISSN 2397-4648 URL <http://www.nature.com/articles/s41535-018-0103-6>
- [130] Loretz M, Pezzagna S, Meijer J and Degen C L 2014 *Appl. Phys. Lett.* **104** 033102 URL <http://scitation.aip.org/content/aip/journal/apl/104/3/10.1063/1.4862749>
- [131] Appel P, Ganzhorn M, Neu E and Maletinsky P 2015 *New J. Phys.* **17** 112001 URL

- <http://stacks.iop.org/1367-2630/17/i=11/a=112001>
- [132] Maletinsky P, Hong S, Grinolds M, Hausmann B, Lukin M, Walsworth R, Loncar M and Yacoby A 2012 *Nat. Nanotechnol.* **7** 320–324
- [133] Thiel L, Rohner D, Ganzhorn M, Appel P, Neu E, Kleiner R, Koelle D and Maletinsky P 2016 *Nat. Nanotechnol.* **11** 677
- [134] Casola F, van der Sar T and Yacoby A 2018 *Nature Reviews Materials* **3** 17088
- [135] Wrachtrup J and Finkler A 2016 *Journal of Magnetic Resonance* **269** 225–236
- [136] Lee D, Lee K W, Cady J V, Ovartchaiyapong P and Jayich A C B 2017 *Journal of Optics* **19** 033001 ISSN 2040-8986
- [137] Stürner F M, Brenneis A, Kassel J, Wostradowski U, Rölver R, Fuchs T, Nakamura K, Sumiya H, Onoda S, Isoya J *et al.* 2019 *Diamond and Related Materials* **93** 59–65
- [138] Kim D, Ibrahim M I, Foy C, Trusheim M E, Han R and Englund D R 2018 *arXiv preprint arXiv:1810.01056*
- [139] Tetienne J P, Dontschuk N, Broadway D A, Stacey A, Simpson D A and Hollenberg L C 2017 *Science advances* **3** e1602429
- [140] Lovchinsky I, Sanchez-Yamagishi J, Urbach E, Choi S, Fang S, Andersen T, Watanabe K, Taniguchi T, Bylinskii A, Kaxiras E *et al.* 2017 *Science* **355** 503–507
- [141] Kehayias P, Jarmola A, Mosavian N, Fescenko I, Benito F M, Laraoui A, Smits J, Bougas L, Budker D, Neumann A *et al.* 2017 *Nature communications* **8** 188
- [142] Tisler J, Reuter R, Lämmle A, Jelezko F, Balasubramanian G, Hemmer P R, Reinhard F and Wrachtrup J 2011 *ACS Nano* **5** 7893–7898 URL <http://pubs.acs.org/doi/abs/10.1021/nn2021259>
- [143] Mohan N, Tzeng Y, Yang L, Chen Y, Hui Y, Fang C and Chang H 2010 *Adv. Mater.* **22** 843–847
- [144] Sekatskii S, Dukenbayev K, Mensi M, Mikhaylov A, Rostova E, Smirnov A, Suriyamurthy N and Dietler G 2015 *Faraday Discuss.* **184** 51–69
- [145] Claveau S, Bertrand J R and Treussart F 2018 *Micromachines* **9** ISSN 2072-666X URL <http://www.mdpi.com/2072-666X/9/5/247>
- [146] Schirhagl R, Chang K, Loretz M and Degen C L 2013 *Annu. Rev. Phys. Chem.*
- [147] Chipaux M, van der Laan K J, Hemelaar S R, Hasani M, Zheng T and Schirhagl R 2018 *Small* **14** 1704263
- [148] Chen X and Zhang W 2017 *Chemical Society Reviews* **46** 734–760
- [149] Prabhakar N and Rosenholm J M 2019 *Current Opinion in Colloid & Interface Science*
- [150] van der Laan K, Hasani M, Zheng T and Schirhagl R 2018 *Small* **14** 1703838
- [151] Wu Y, Jelezko F, Plenio M B and Weil T 2016 *Angewandte Chemie International Edition* **55** 6586–6598
- [152] Hsiao W W W, Hui Y Y, Tsai P C and Chang H C 2016 *Accounts of Chemical Research* **49** 400–407 pMID: 26882283 (Preprint <https://doi.org/10.1021/acs.accounts.5b00484>) URL <https://doi.org/10.1021/acs.accounts.5b00484>
- [153] Karaveli S, Gaathon O, Wolcott A, Sakakibara R, Shemesh O A, Peterka D S, Boyden E S, Owen J S, Yuste R and Englund D 2016 *Proceedings of the National Academy of Sciences* **113** 3938–3943
- [154] Petrakova V, Rehor I, Stursa J, Ledvina M, Nesladek M and Cigler P 2015 *NANOSCALE* **7** 12307–12311 ISSN 2040-3364
- [155] Foy C, Zhang L, Trusheim M E, Bagnall K R, Walsh M, Wang E N and Englund D R 2019 *arXiv preprint arXiv:1903.05717*
- [156] Jenkins A, Pelliccione M, Yu G, Ma X, Li X, Wang K L and Jayich A C B 2018 *arXiv preprint arXiv:1812.01764*
- [157] Gross I, Akhtar W, Hrabec A, Sampaio J, Martínez L, Chouaieb S, Shields B, Maletinsky P, Thiaville A, Rohart S *et al.* 2018 *Physical Review Materials* **2** 024406
- [158] Gross I, Akhtar W, Garcia V, Martínez L, Chouaieb S, Garcia K, Carrétéro C, Barthélémy A, Appel P, Maletinsky P *et al.* 2017 *Nature* **549** 252

- [159] Jakobi I, Neumann P, Wang Y, Dasari D B R, El Hallak F, Bashir M A, Markham M, Edmonds A, Twitchen D and Wrachtrup J 2017 *NATURE NANOTECHNOLOGY* **12** 67–72 ISSN 1748-3387
- [160] Wang P, Chen S, Guo M, Peng S, Wang M, Chen M, Ma W, Zhang R, Su J, Rong X *et al.* 2019 *Science advances* **5** eaau8038
- [161] Thiel L, Wang Z, Tschudin M A, Rohner D, Gutiérrez-Lezama I, Ubrig N, Gibertini M, Giannini E, Morpurgo A F and Maletinsky P 2019 *Science D*
- [162] Nelz R, Radtke M, Slablab A, Kianinia M, Li C, Xu Z Q, Bradac C, Aharonovich I and Neu E 2019 *arXiv preprint arXiv:1907.12248*
- [163] Barfuss A, Teissier J, Neu E, Nunnenkamp A and Maletinsky P 2015 *Nat. Phys.* **11** 820–825 ISSN 1745-2473
- [164] Rondin L, Dantelle G, Slablab A, Grosshans F, Treussart F, Bergonzo P, Perruchas S, Gacoin T, Chaigneau M, Chang H C, Jacques V and Roch J F 2010 *Phys. Rev. B* **82** 115449 ISSN 1098-0121
- [165] Bolshedvorskii S V, Zeleneev A I, Vorobyov V V, Soshenko V V, Rubinas O R, Zhulikov L A, Pivovarov P A, Sorokin V N, Smolyaninov A N, Kulikova L F *et al.* 2019 *ACS Applied Nano Materials*

7. Near-field energy transfer between a luminescent 2D material and color centers in diamond

Richard Nelz, Mariusz Radtke, Abdallah Slablab, Zai-Quan Xu, Mehran Kianinia, Chi Li, Carlo Bradac, Igor Aharonovich, and Elke Neu

Adv. Quantum Technol. **1900088** (2019)

doi: 10.1002/qute.201900088

The above detailed manuscript shows near-field transfer between two stable, luminescent solid state systems: NV centers in diamond and two-dimensional WSe₂.

Richard Nelz (R.N.) aided in pre-characterizing shallow NV ensembles in the single crystal diamond sample. The co-authors from University of Technology Sydney (Z.-Q. Xu, M. Kianinia, C. Li, C. Bradac and I. Aharonovich) used a process developed at their institution to transfer WSe₂ flakes to the diamond sample. Pre-characterization of the WSe₂ has been carried out at UTS. After the transfer, R.N. performed extensive photoluminescence mapping, lifetime imaging and spin measurements of the NV centers in proximity of WSe₂. These measurements constitute the main body of the manuscript. The employed confocal microscope was designed and realized by R.N. Evaluating the obtained data, R.N. found clear evidence for a resonant energy transfer, namely FRET, between the NV centers and the excitons in the WSe₂ flakes. R.N. developed a model which very well describes the interaction of the shallow NV ensemble with a monolayer WSe₂ flake. Applying this model, he estimated the FRET radius for the observed process. In addition, R.N. developed a measurement scheme to show the influence of the FRET process on the excitation of WSe₂ excitonic photoluminescence. By establishing lifetime-gated photoluminescence detection, R.N. showed that NV centers coupled to WSe₂ via FRET retain their magnetic sensing capabilities thus constituting multifunctional sensors. R.N. outlined and wrote the first draft of the manuscript including the design of all figures and was actively involved in all discussions during the collaboration. He actively contributed to all revisions of the manuscript.

Near-Field Energy Transfer between a Luminescent 2D Material and Color Centers in Diamond

Richard Nelz, Mariusz Radtke, Abdallah Slablab, Zai-Quan Xu, Mehran Kianinia, Chi Li, Carlo Bradac, Igor Aharonovich,* and Elke Neu*

Energy transfer between fluorescent probes lies at the heart of many applications ranging from bio-sensing and bio-imaging to enhanced photodetection and light harvesting. In this work, Förster resonance energy transfer (FRET) between shallow defects in diamond—nitrogen-vacancy (NV) centers—and atomically thin, 2D materials—tungsten diselenide (WSe₂)—is studied. By means of fluorescence lifetime imaging, the occurrence of FRET in the WSe₂/NV system is demonstrated. Further, it is shown that in the coupled system, NV centers provide an additional excitation pathway for WSe₂ photoluminescence. The results constitute the first step toward the realization of hybrid quantum systems involving single-crystal diamond and 2D materials that may lead to new strategies for studying and controlling spin transfer phenomena and spin valley physics.

1. Introduction

Förster resonance energy transfer (FRET) is the near-field transfer of energy due to the dipole–dipole interaction in a donor–acceptor pair system. FRET transfers energy from an excited donor to an acceptor which is initially in the ground state. The transfer does not involve the exchange of photons and occurs at a rate determined by the overlap integral, that is, the frequency-dependent oscillator strengths of the quantum spectroscopic (fluorescence/absorption) transition dipoles as well as their distance.^[1] For the donor, FRET provides a new decay channel and consequently reduces its excited state lifetime. In contrast, for the acceptor FRET constitutes a non-radiative


excitation pathway, thus not inducing life-time changes but potentially enhancing acceptor luminescence. Realized for a variety of heterogeneous donor–acceptor systems—quantum dots, molecules, chromophores, etc.^[2]—FRET constitutes the basis of a wide range of both fundamental effects and practical applications including single-molecule (bio)sensing and (bio)imaging, super-resolution fluorescence microscopy, as well as FRET-enhanced photodetection and light harvesting.

Evidently, the characteristics of the donor–acceptor systems are key to the practical realization of any FRET-based application. As fluorescent dye molecules

traditionally used in FRET may bleach, recent work has focused on exploring resonant energy transfer processes in luminescent solid-state systems. These show superior stability and much broader versatility for many of the proposed sensing, imaging, and optoelectronic applications. Luminescent point defects in diamond,^[3] including the well-studied nitrogen-vacancy (NV) center,^[4] are long-term stable, fluorescent probes with established nanoscale sensing capabilities for magnetic^[5] and electric fields,^[6] as well as temperature.^[7] Furthermore, FRET processes involving NV centers in nanodiamonds have already been demonstrated with organic molecules^[8,9] and graphene.^[10,11] Simultaneously, there is an entire family of fluorescent probes in atomically thin 2D transition metal dichalcogenide (TMDs) materials which exhibit ultra-bright luminescence. 2D-TMDs are leading candidates for emerging applications in optoelectronics, photodetection, and valleytronics^[12–14] rendering them significant for quantum technologies.^[15] So far, FRET involving luminescent 2D-TMDs has been demonstrated with organic dye molecules^[16] and colloidal quantum dots.^[17,18] Notably, electrical gating of 2D-TMDs enables control over the efficiency of the energy transfer process.^[19] It is noteworthy that FRET has been straightforwardly established between systems of different dimensionalities (e.g., 1D: molecules, quantum dots, color centers; 2D:TMDs) and involving dipole transitions of fundamentally different nature (atom-like transitions in color centers and molecules, excitons in quantum dots and TMDs).^[10,16–19] While the FRET mechanism itself is quite universal, the distance dependence of the process will reveal the nature of the participating dipoles. Conventionally, the rate of energy transfer between a pair of point dipoles such as molecules and chromophores scales with the distance z between the dipoles like $\frac{1}{z^6}$. In contrast, FRET between an

R. Nelz, Dr. M. Radtke, Dr. A. Slablab, Dr. E. Neu
Universität des Saarlandes
Fakultät NT, Physik, 66123 Saarbrücken, Germany
E-mail: elkeneu@physik.uni-saarland.de

Dr. Z.-Q. Xu, Dr. M. Kianinia, C. Li, Dr. C. Bradac, Prof. I. Aharonovich
School of Mathematical and Physical Sciences
Faculty of Science
University of Technology Sydney
Ultimo 2007, Australia
E-mail: Igor.Aharonovich@uts.edu.au

 The ORCID identification number(s) for the author(s) of this article can be found under <https://doi.org/10.1002/qute.201900088>

© 2019 The Authors. Published by WILEY-VCH Verlag GmbH & Co. KGaA, Weinheim. This is an open access article under the terms of the Creative Commons Attribution License, which permits use, distribution and reproduction in any medium, provided the original work is properly cited.

DOI: 10.1002/qute.201900088

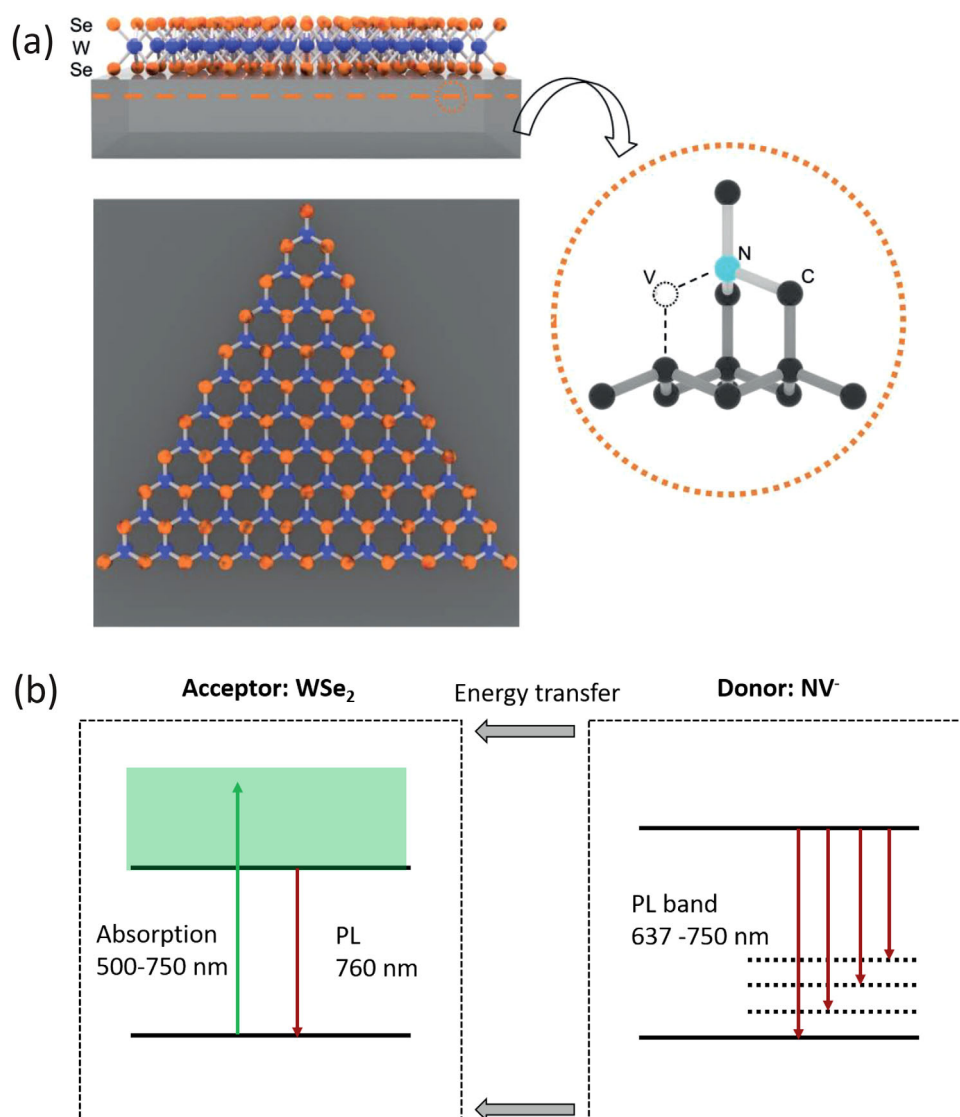


Figure 1. a) Schematics of the NV/WSe₂ hybrid system illustrating the crystal structure of WSe₂ as well as the structure of the NV color center. The transfer of WSe₂ flakes to the SCD surface is described in Section 2. b) Schematics of the FRET process investigated here: negative NV centers serve as donors, monolayer WSe₂ flakes as the acceptor in the FRET process. The strong overlap of the absorption band of the WSe₂ flakes with the emission band of the NV centers establishes the main pre-requisite for FRET.

exciton delocalized in 2D, as observed in graphene or in our case in WSe₂, and a quantum dot or an atomic-scale quantum system like a color center scales with $\frac{1}{d^4}$.^[10,20]

In this work, we report FRET between two solid-state, stable, luminescent quantum systems—an ensemble of shallowly implanted NV centers in single-crystal diamond (SCD) and a 2D WSe₂ monolayer. The investigated hybrid system is depicted in **Figure 1a**. Although the observation of FRET between NV centers and molecular donors or 2D materials like graphene has already been demonstrated for nanodiamonds,^[9,10] this is the first demonstration of FRET for shallowly implanted NV centers in SCD. In the process, NV centers act as donor dipoles which non-radiatively transfer their excitation energy to excitons in WSe₂. WSe₂ is an optimal FRET partner for NV centers, as its broad absorption band (500–750 nm)^[21,22] largely overlaps with the NV photoluminescence (PL) band between 640 and 750 nm. Fig-

ure 1b established the schematics of the donor–acceptor pair NV/WSe₂. We employ fluorescence lifetime imaging to measure lifetime changes due to FRET between WSe₂ flakes and NV centers. We also observe enhanced excitation of WSe₂ via FRET processes. We estimate the FRET radius for the NV/WSe₂ pair to be 13 nm, and we show that the spin-based magnetic sensing capabilities of NV centers are conserved when FRET takes place.

2. Experimental Section

High-purity, (100)-oriented, synthetic, SCD from Element Six (electronic grade quality, [N]⁻ < 5 ppb, B < 1 ppb) was used. The SCD sample (size 2 × 4 mm²) was polished to a roughness of R_a < 3 nm by Delaware Diamond Knives. Reactive ion etching^[23] was first employed to remove the top 15 μm of the SCD. Creating NV centers in the diamond top layers which are potentially

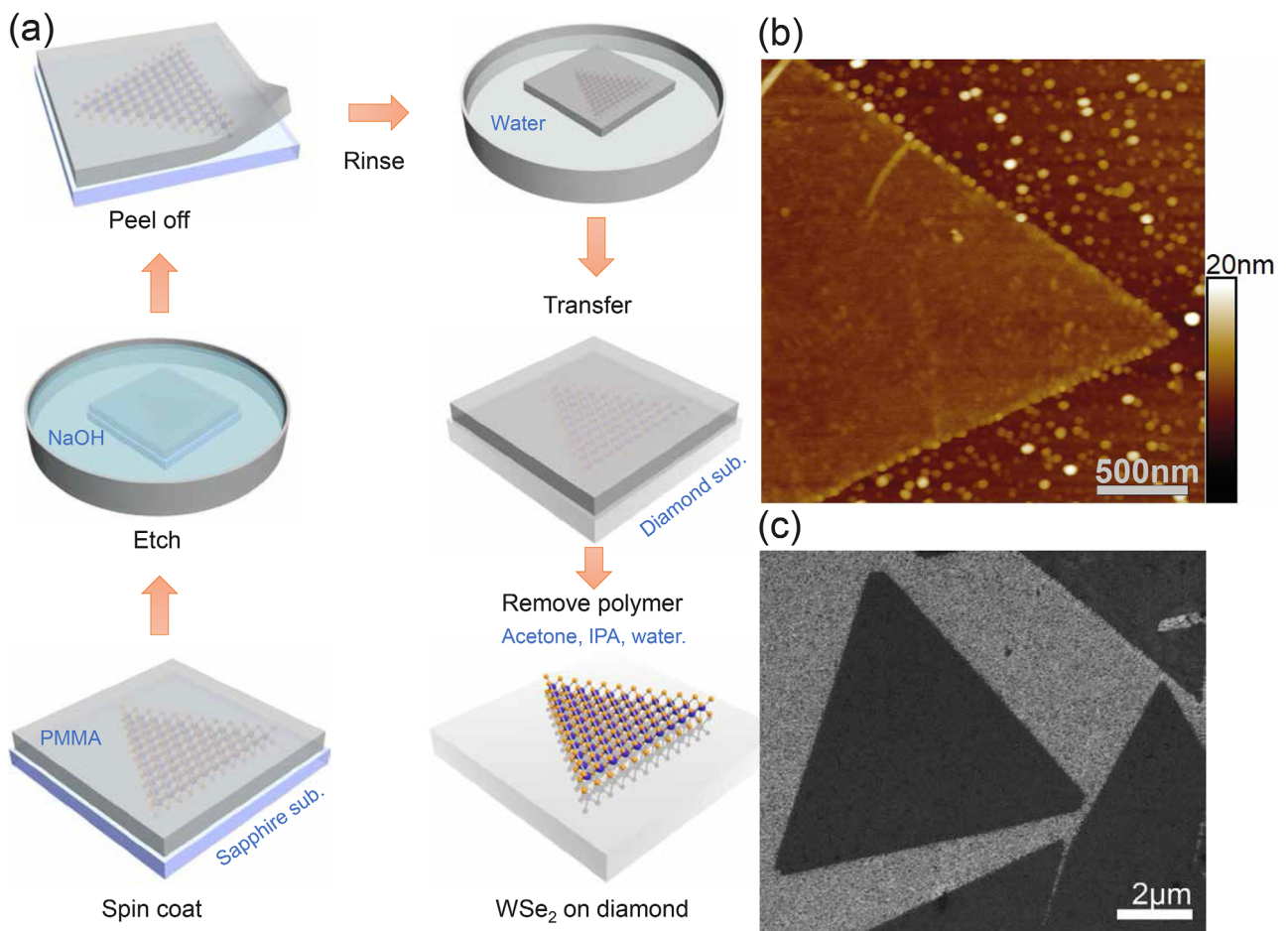


Figure 2. a) Transfer process of the WSe₂ flakes onto the SCD surface as described in the main text. b) Atomic force microscope image of a WSe₂ flake on top of a SiO₂ substrate. c) Scanning electron microscope image of WSe₂ flakes on an SCD surface.

damaged as a result of the mechanical polishing was thus avoided. A homogeneous layer of NV centers is then formed by shallowly implanting nitrogen ions with an implantation density of 4×10^{11} (nitrogen ions) cm^{-2} and an energy of 4 keV. During the implantation, the sample was tilted by 7° with respect to the ion beam to avoid ion channeling. The SCD sample was then annealed in vacuum at 800°C and cleaned in boiling acids (1:1:1 mixture of sulfuric acid, perchloric acid, and nitric acid). Using Monte Carlo simulations,^[24] a resulting depth of the NV centers of (6.5 ± 2.7) nm below the SCD surface was estimated. As the geometry of the implantation process avoided ion channeling, SRIM simulations were a valid approximation for the NV depth distribution in this case. Using PL measurements, the creation of a spatially homogeneous ensemble of NV centers was shown. Assuming typical creation yield in the order of 1%, the above given implantation density leads to a sparse NV ensemble with < 10 NV centers in the focus of the confocal microscope. Reactive ion etching onto a target area of the SCD to remove selectively all NV centers (area size $\approx 1 \times 0.4 \text{ mm}^2$) was also employed. Using this area, the properties of the WSe₂ flakes on SCD independently of interactions with NV centers were characterized.

WSe₂ monolayer flakes were synthesized on a sapphire (0001) substrate via chemical vapor deposition following Ref. [22].

The flakes were transferred onto our SCD sample using the method described below and depicted in **Figure 2a**. Poly(methyl methacrylate) (PMMA; Microchem, A4, MW 495K, solvent: anisole) was first spin coated at 3000 rpm for 1 min onto the sapphire substrate with the flakes. The sample was subsequently cured by heating it up on a hotplate at 180°C for 1 min. The PMMA-coated substrate was then immersed in 2 M NaOH solution at 80°C for 1 h to reduce the adhesion between the PMMA and the sapphire substrate. Subsequently, the PMMA layer was peeled off together with the WSe₂ flakes exploiting the surface tension between them. The PMMA/WSe₂ composite layer was rinsed three times in deionized (DI) water and placed onto the clean SCD surface (or onto a SiO₂ substrate for further characterization, see below). Heating on a hot plate for 20 min at 150°C enhanced the adhesion of the WSe₂ flakes to the new substrate. Finally, the SCD sample was immersed in hot acetone for 10 min followed by flush washing it in isopropanol (IPA) and DI water to remove the PMMA layer. The method had a high transfer yield over a millimeter-sized area, as confirmed by the density of WSe₂ flakes on the SCD being similar to that on the sapphire before transfer. The WSe₂ flakes mostly retained their triangular shape after transfer onto different substrates (see **Figure 2b,c**). Atomic force microscopy to measure the thickness of our WSe₂

Table 1. Experimental parameters at a glance.

	NV ⁻	WSe ₂
Absorption [nm]	460–630	500–750 ^[22]
Emitted PL [nm]	637–750	760 ± 20
Depth [nm]	6.5 ± 2.7	
Thickness [nm]		1.3 (4)
Detection [nm]	680–720	>650
Excitation [nm]	cw: 532 Pulsed: 460–600	cw: 532 Pulsed: 460–600

flakes was used. For a reference WSe₂ flake transferred onto a SiO₂ substrate, a thickness of 1.3 nm and a root mean square (rms) roughness of 0.4 nm was found. It was noted that this transferred flake was 0.6 nm thicker than our as-grown flakes. This observation was attributed to intercalated water in between the flake and SCD as well as potential residuals from the transfer on top of the WSe₂ flake. It was emphasized that the strong PL of the WSe₂ flakes at 760 nm presented in Section 3 together with the AFM-based thickness measurements clearly identified the flakes as monolayers.

A custom-built confocal scanning microscope (numerical aperture 0.8, pinhole size 50 μm) was used to investigate the interaction between the NV centers in the SCD and the WSe₂ monolayer. We used a tuneable (450–850 nm), pulsed laser (NKT EXW-12, pulse length ≈ 50 ps) equipped with a filter system (NKT SuperK Varia) as excitation source enabling pulsed PL and lifetime measurements. To acquire standard confocal microscopy PL maps, the sample was continuously excited with a diode-pumped solid-state laser at a wavelength of 532 nm while the collected PL was detected through a 650 nm longpass filter. The collected PL signal was either sent to highly efficient photon counters (Excelitas SPCM-AQRH-14, quantum efficiency ≈ 70 %) or to a grating spectrometer (Acton Spectra Pro 2500, Pixis 256OE CCD). A single-photon counting time correlator (PicoQuant, PicoHarp 300) was employed to perform time-resolved PL analysis. The measured instrument response function (IRF) of the setup was modelled by a Gaussian function with a full width at half maximum (FWHM) of 326 ps. When fitting PL decay curves, exponential decays convoluted with the IRF were used and consequently corrected the obtained PL lifetimes for the IRF. When performing PL lifetime imaging of NV centers, the PL in a spectral window of 680–720 nm was filtered. Consequently, the NV lifetime measurements did not reflect contributions from neutral NV centers but only from negative NV centers. The setup was equipped with a microwave source (Stanford Research Systems, SG384) and an amplifier (Mini Circuits, ZHL-42W+) which allowed for the delivery of microwaves through a 20 μm thick copper wire to enable electronic spin manipulation for NV centers. **Table 1** summarizes all important experimental parameters.

3. Photoluminescence and Lifetime Measurements

First, we characterize the hybrid NV/WSe₂ system depicted in Figure 1a under continuous excitation. The inset in **Figure 3b** shows a typical PL map of a triangular WSe₂ flake which we

localize due to its strong excitonic PL at 760 nm (see **Figure 3b**, gray curve). We find very similar PL spectra for our WSe₂ flakes transferred onto SiO₂ (see **Figure 3b**, red curve) and on the bare SCD (see **Figure 3b**, black curve). The observed PL is characteristic for WSe₂ monolayers as previously reported.^[22] Despite the dominant WSe₂ PL signal, we identify a zero-phonon line at 637 nm originating from NV centers located underneath the flakes (**Figure 3a**, gray curve). As expected, in between individual WSe₂ flakes, we only observe PL due to implanted NV centers. We note that for both cases, NV ensemble below WSe₂ flakes as well as bare NV ensemble, we do not observe any PL due to neutral NV centers. We consequently infer that the presence of WSe₂ does not significantly alter the NV charge state.

To further investigate the hybrid NV/WSe₂ system, we perform PL lifetime measurements. In the area in which all NV centers have been removed, we find a lifetime of the WSe₂ exciton recombination PL of $\tau_{WSe_2} = 0.41(5)$ ns. This is consistent with τ_{WSe_2} for pristine WSe₂ flakes before transfer. For our NV centers as donors, FRET will provide a new, additional decay channel. Consequently, their excited state lifetime (τ_{NV}) will reduce. In contrast, for the acceptor, FRET establishes a (non-radiative) excitation pathway. Thus FRET is not expected to change τ_{WSe_2} which is in accordance with our observations for pristine flakes, flakes on SCD not coupled to NV centers and flakes coupled to NV centers (see **Figure 4d** and the discussion below).

Figure 4b shows the PL decay recorded on a WSe₂ flake placed on the SCD surface with the shallowly implanted ensemble of NV centers. We fit two main components: a fast decay with a time constant of 0.42(3) ns and a slower decay with a time constant of 5.1(3) ns. While the fast decay clearly arises due to the WSe₂ PL (τ_{WSe_2}), we attribute the slower decay to the NV ensemble interacting with the WSe₂ flake (τ_{NV}). In contrast, in areas not covered by WSe₂ flakes we consistently measure a much longer NV lifetime with an average value of $\tau_{NV}^{bulk} \approx 12(1)$ ns (see **Figure 4c**), typical for NV centers in bulk diamond.^[25] For shallowly implanted NVs, slightly longer lifetimes of ≈ 16–17 ns have been previously reported.^[26] We point out that, in our experiment, residuals from the transfer process might slightly reduce the NV lifetime in between the flakes. Excitation with short (< ns) laser pulses potentially reveals internal spin dynamics of NV centers including spin-dependent lifetimes.^[27] The here observed value of $\tau_{NV}^{bulk} \approx 12(1)$ ns corresponds to the lifetime expected for the $m_s=0$ state.^[27] Indeed the high repetition rate (8 MHz) pulsed excitation that we use here will polarize the NV centers into $m_s=0$ as the time interval between subsequent pulses is several orders of magnitude shorter than typical NV T₁ times. For NV centers coupled to WSe₂ flakes, we find that τ_{NV} is halved compared to the non-coupled NVs in our sample. This finding proves the occurrence of non-radiative energy transfer—FRET—between NV centers in SCD and excitons in the WSe₂ flake. The WSe₂ flakes provides the NV centers with a non-radiative decay channel—mediated by dipole–dipole interaction—which reduces τ_{NV} .

To further investigate FRET between WSe₂ and NV centers, we perform PL lifetime imaging of different areas of the SCD sample (see **Figure 4a,c,d**). We fit a double exponential decay to the measured data and extract τ_{NV} and τ_{WSe_2} . We consistently observe $\tau_{NV} < 6$ ns in areas where the SCD surface is covered by a WSe₂ flake, as discernible from comparing the PL map in **Figure 4a** and the lifetime map in **Figure 4c**. In contrast, we find τ_{NV}^{bulk} on

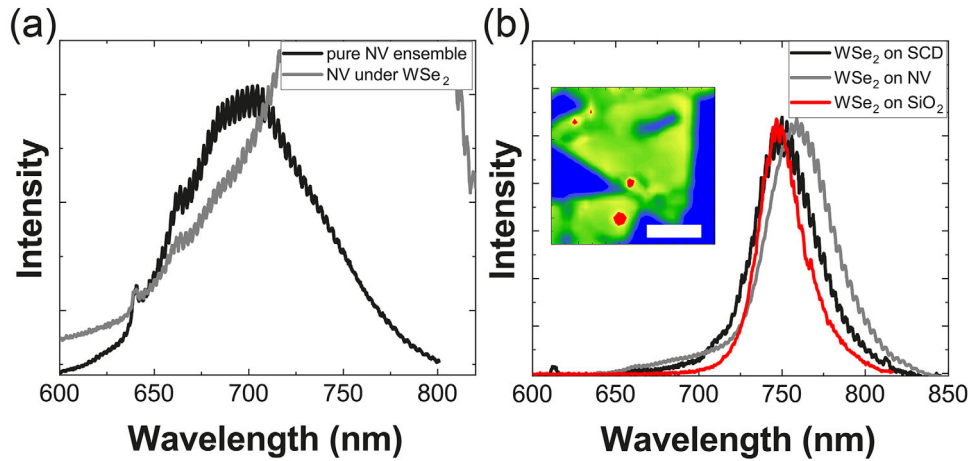


Figure 3. PL spectrum of the NV ensemble measured between WSe₂ flakes [black curve in (a)] showing the NV zero-phonon-line (at 637 nm) and phonon sideband. Gray curves in (a) and (b) show the PL spectrum of a WSe₂ flake with underlying NV ensemble. In (a) we normalize both spectra to the NV ZPL to facilitate comparison. In (b), we compare WSe₂ PL spectra on bare SCD (black) and SiO₂ (red) substrates as well as on the NV center ensemble in SCD (gray). All spectra have been normalized to their peak value. All spectra clearly reveal the characteristic PL of WSe₂ monolayers centered around ≈ 760 nm with maximum peak shifts of ≈ 10 nm. In contrast, the PL of a bilayer would occur centered around ≈ 815 nm.^[22] The inset shows a PL map (scale bar 2 μm) of a transferred WSe₂ flake (bright area) on top of the NV center ensemble (blue) recorded detecting wavelengths above 650 nm using continuous laser excitation at 532 nm (exc. power 700 μW).

all other positions. The pattern of the WSe₂ flakes is furthermore confirmed when plotting τ_{WSe_2} (see Figure 4d).

Below, we interpret these results in detail and highlight the peculiarities of the FRET process between an ensemble of NV centers and a WSe₂ flake. In our case, the FRET process is non-trivial as FRET strongly depends on the distance between the donor and the acceptor and our NV centers show a spread of depths z in the SCD. Assuming the flake is in direct contact with the SCD surface, each specific NV center of the ensemble lies at a different distance z from the WSe₂. We thus would expect a complicated multi-exponential PL decay corresponding to a spread of τ_{NV} . Experimentally, however, we find that the NV PL decay is very well described by a single exponential decay with time constant τ_{NV} . To simulate the PL decay expected from the NV ensemble coupled to the WSe₂ flake, we first calculate τ_{NV} as a function of z . To this end, we need to determine the non-radiative decay rate $\gamma_{\text{non-rad}}$ due to the FRET process. We assume that the exciton is fully delocalized in the WSe₂ flake and the flakes have infinite size compared to the atomic-sized NV centers; we find^[10]

$$\gamma_{\text{non-rad}}(z) = \gamma_{\text{rad}} \frac{R^4}{z^4} \quad (1)$$

where R is the Förster radius, that is, the distance at which the efficiency of the FRET mechanism is 50%. The quantity R depends on the quantum efficiency of the donor and on the spectral overlap between the donor's emission and the acceptor's absorption, as well as their dipole moments. We furthermore assume that the radiative decay rate γ_{rad} is constant for all NV centers and equal to the reference bulk value $(\tau_{\text{NV}}^{\text{bulk}})^{-1}$. For each NV center at a specific depth z , we should find a mono-exponential decay with $\tau_{\text{NV}}(z)$. Equation (1) shows that FRET is more efficient if z is smaller; consequently NV centers very close to the surface will

be strongly quenched and emit less photons. We calculate the PL intensity $I(z)$ of a NV center at a depth z as

$$I(z) = I_0 \frac{\gamma_{\text{rad}}}{\gamma_{\text{rad}} + \gamma_{\text{non-rad}}(z)} \quad (2)$$

where I_0 is the non-quenched PL intensity, and γ_{rad} and $\gamma_{\text{non-rad}}$ are the radiative and non-radiative decay rates, respectively.

To obtain the resulting PL decay of the ensemble, we weight each of the mono-exponential decay curves for each depth z with the intensity $I(z)$ (Equation (2)) and with the depth distribution $D(z)$ of NV centers resulting from the implantation process. We extract the depth distribution $D(z)$ using Monte Carlo Simulations (SRIM), which produce a depth profile of (6.5 ± 2.7) nm. As we observe all NV centers in the ensemble simultaneously, we integrate over the whole implantation profile to retrieve the observed PL decay.

Notably, the calculated PL decay of the NV ensemble indicates a decay which is well represented with a mono-exponential function with an effective $\tau_{\text{NV}}^{\text{eff}}$ (assuming $R > 5$ nm) in full agreement with our experimental observations. Figure 4e shows the expected value of $\tau_{\text{NV}}^{\text{eff}}$ for $5 \text{ nm} < R < 30 \text{ nm}$ —which we now use to estimate R for the NV/WSe₂ pair and find $R_{\text{NV/WSe}_2} = 13$ nm. To further confirm the agreement between the measured data and our model, we reduce the data to the time range in which the NV's mono-exponential decay is dominating. We do not include data from the first 3 ns—as this signal mainly represent PL from WSe₂—and we do not consider the long time tail—that is, all the data points with count rates below 1 % of the NV centers' peak value. This data treatment leads to the black line in Figure 4f which agrees very well with the calculated PL decay (red line), assuming $R_{\text{NV/WSe}_2} = 13$ nm, and resulting in $\tau_{\text{NV}}^{\text{eff}} = 5.2$ ns. We note that $\tau_{\text{NV}} = 5.2$ ns in this situation is expected for NV centers at a depth of ≈ 12 nm. Our value for $R_{\text{NV/WSe}_2}$ is comparable to that

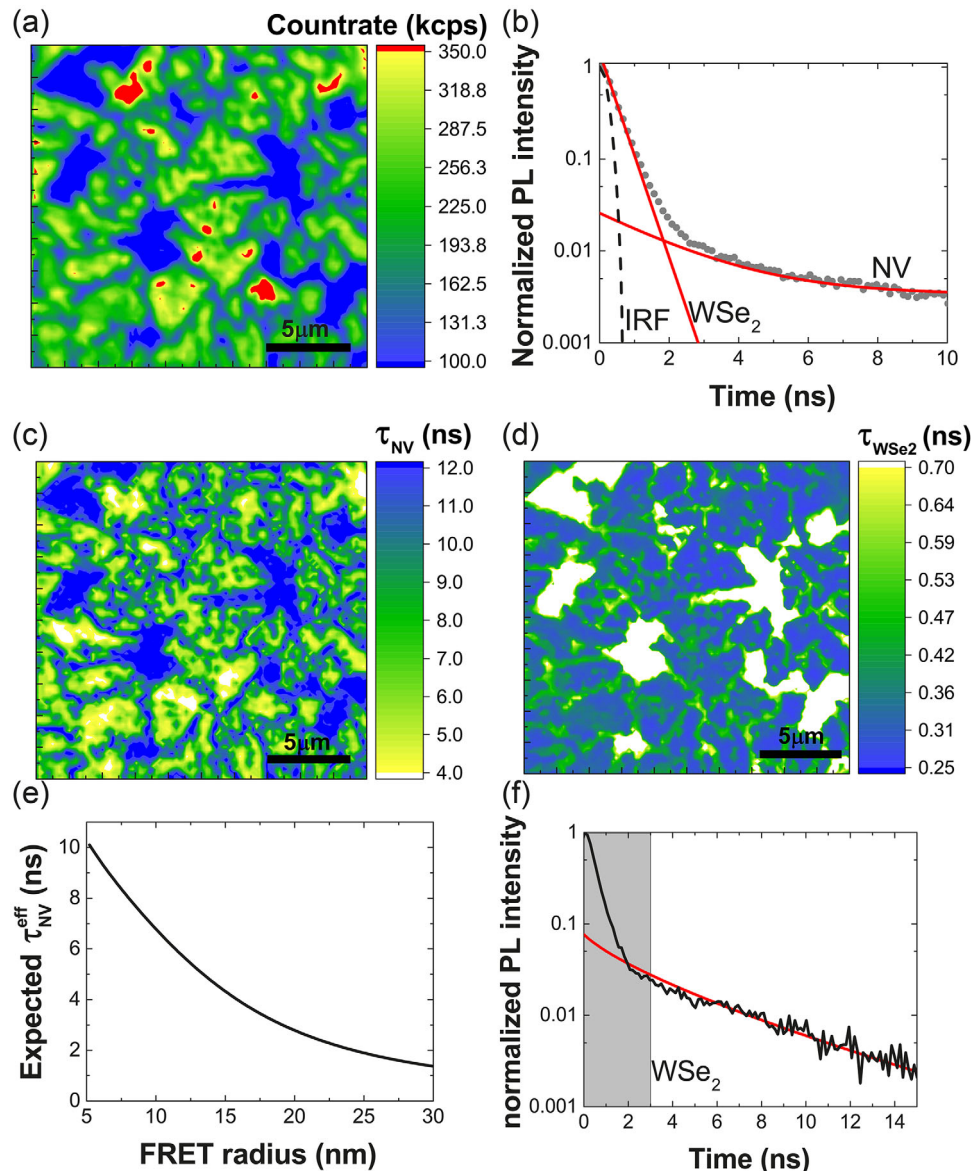


Figure 4. a) PL map of WSe₂ flakes on NV ensemble. Here we use pulsed excitation (≈ 9 ns), 8 MHz repetition rate, 2 s integration time per pixel, excitation bandwidth 530–534 nm. b) Exemplary lifetime measurement of the flakes and the underlying NV centers. The contributions of the instrument response (IRF), the WSe₂ PL, and the NV center PL are drawn separately. c,d) Lifetime maps using τ_{NV} and τ_{WSe_2} corresponding to the PL map in (a). We consistently observe quenching of NV centers underneath the WSe₂ flakes with $\tau_{\text{NV}} < 6$ ns. In contrast, between the flakes, we consistently find $\tau_{\text{NV}}^{\text{bulk}}$ and a lower overall PL level (blue areas in (a) and (c)). As we only detect NV center PL in these areas, we fit the corresponding data with a mono-exponential decay. Consequently, in these areas, no values for τ_{WSe_2} are obtained which we represent in (d) in white color. e) Observable NV ensemble lifetimes $\tau_{\text{NV}}^{\text{eff}}$ extracted from the simulation as a function of the FRET radius R . From our measurements, we extract a FRET radius of $R = 13$ nm. f) Simulated PL decay (red line) for the NV center ensemble using a Förster radius $R = 13$ nm in comparison to the observed PL decay (black line). Model and observed data agree very well.

reported for the NV/graphene system, $R_{\text{NV/graphene}}$ ^[10] strongly supporting the hereby observation of FRET between NV centers and WSe₂.

To further investigate the energy transfer mechanism between NV centers and WSe₂ flakes, we study how the WSe₂ PL intensity depends on the excitation wavelength λ_{exc} . Negatively charged NV centers act as donors for WSe₂. Consequently, FRET from excited NV centers constitutes an excitation path for WSe₂ PL which adds to laser excitation of WSe₂ PL. Especially when the

direct laser excitation of the acceptor is inefficient, FRET enhances the PL of the acceptor (and simultaneously reduces the PL of the donor). Recording PL spectra of ensembles of NVs at positions not covered by WSe₂ flakes, we clearly observe PL from negatively charged NV centers for $\lambda_{\text{exc}} > 465$ nm. We however note that we cannot infer a ratio of neutral and negative NV centers for excitation with blue laser light as the employed setup does not permit observing spectral features due to neutral NV centers (in contrast to the setup we used for $\lambda_{\text{exc}} = 532$ nm, see

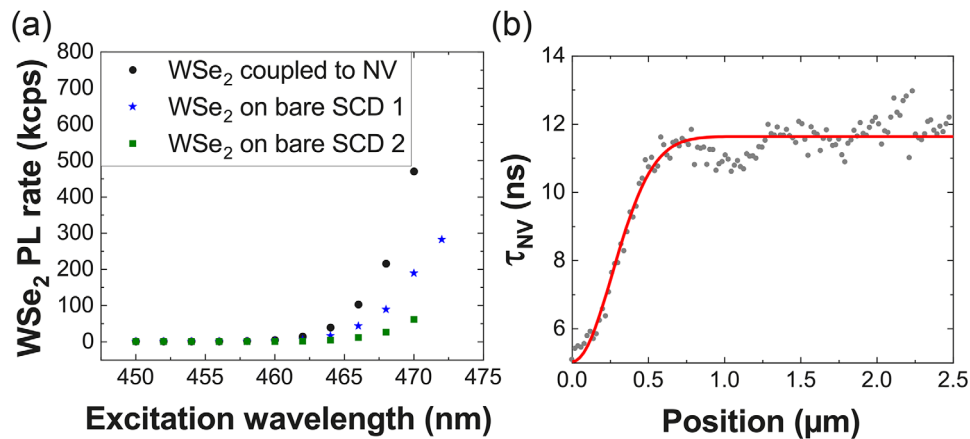


Figure 5. a) Median PL rate of the WSe₂ flakes for different excitation wavelengths λ_{exc} . Black dots: PL of WSe₂ coupled to NV centers. WSe₂ PL rates are corrected for background as well as for the PL of the underlying NV ensemble. Blue stars and green squares: PL of WSe₂ on bare SCD as recorded in two areas (1,2) separated by more than 0.5 mm. These measurements demonstrate that FRET from NV centers constitutes an additional excitation pathway for WSe₂ PL (for details see text). b) NV lifetime recorded along a line perpendicularly crossing the edge of a WSe₂ flake. We fit a Gaussian to the transition from bulk lifetime to the quenched lifetime (red curve). We obtain a FWHM of 620(30) nm which is comparable to the point spread function measured for our confocal setup.

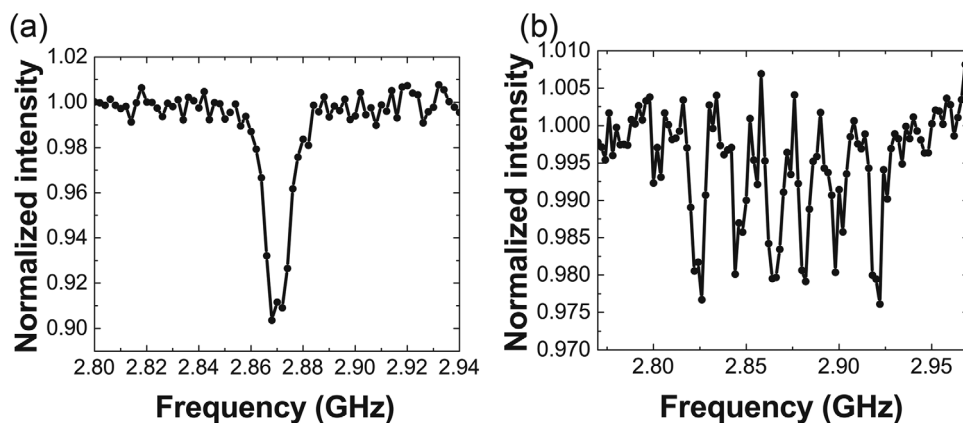


Figure 6. Optically detected magnetic resonance of the nitrogen vacancy centers ensemble a) without and b) with an external magnetic field of 25 G applied indicating the potential for NV centers as multi-functional sensors.

Figure 3). However, as we clearly observe negatively charged NV centers, they will contribute via FRET to the excitation of WSe₂ PL for $\lambda_{\text{exc}} > 465$ nm. We thus investigate this excitation wavelength range in detail. We investigate the PL rate of the WSe₂ flakes as a function of λ_{exc} (see Figure 5a) and aim to compare the situation where WSe₂ flakes are placed on the NV ensemble and the situation in which the WSe₂ flakes are placed on SCD regions where all NV centers have been removed via etching (see Section 2). To account for variations in the PL intensity for different flakes, we compare the median count rate of WSe₂ in areas of 20 by 20 μm^2 . To check for consistency, we furthermore investigate two areas without NV centers separated by more than 0.5 mm. We also correct the WSe₂ PL intensity for NV center and background PL. As we compare the WSe₂ PL intensity with and without NV centers, changes in the excitation laser power when changing λ_{exc} affect both measurements in the same way. Consequently, we did not correct for variations of the laser power as well as a potentially wavelength-dependent transmission of our

setup. We note that as a consequence of this, our measurements do not necessarily reveal the wavelength-dependent PL excitation probability of NV centers. Figure 5a displays a clear tendency of an enhanced excitation of WSe₂ PL for flakes coupled to the shallow NV ensemble. We note that the enhanced excitation cannot be due to the absorption of NV PL by the WSe₂ flakes as the PL is too weak to induce the observed enhancement. The observed excitation enhancement of WSe₂ in the presence of NV centers constitutes additional strong evidence for FRET between NV centers and WSe₂.

We now investigate the electronic spin properties for NV centers under the WSe₂ flakes. We use lifetime gating to separate NV PL and WSe₂ PL to enhance the measurement contrast when performing optically detected magnetic resonance (ODMR) measurements under pulsed laser excitation. Figures 6a,b show the ODMR of the NV ensemble underneath the WSe₂ flake in the absence and presence of an external magnetic field, respectively. We observe an ODMR contrast of 10 % without external field, which

is typical for shallow NV centers, and which proves clear separation of NV and WSe₂ PL. Observing ODMR with a magnetic-field-dependent splitting for NV centers undergoing FRET indicates that they can serve as multi-functional sensors: while using FRET processes to monitor the presence of other dipoles, NV centers can simultaneously sense magnetic fields. This observation renders NV centers promising as multi-functional sensors in biological systems or for the investigation of novel materials where they can operate as nanoscale probes for nuclear magnetic resonance spectroscopy^[28] that simultaneously couple to excitons via FRET.

We finally investigate how precisely we can localize the edge of a WSe₂ flake using the spatial variation of τ_{NV} . We measure τ_{NV} along a line perpendicularly crossing the edge of a WSe₂ flake (see Figure 5b). We fit τ_{NV} using a Gaussian function approximating the point spread function (PSF) of our setup. We find a FWHM of 620 nm which is closely matching the PSF of our setup which we estimated by imaging single color centers in nanodiamonds. Consequently, localizing the edge of a WSe₂ flake is limited by the setup's PSF only indicating the possibility for high-resolution imaging using the FRET process investigated here. We now address the imaging speed of the PL lifetime imaging. Typical detected PL rates of our NV ensemble amount to 70 kcps for a pulse energy of ≈ 10 nJ ($\lambda_{\text{exc}} = 530\text{--}534$ nm, repetition rate 8 MHz). Following ref. [29], we estimate the minimum number of photons needed to reliably determine τ_{NV} to be 1000. This leads to a minimum integration time per pixel of <15 ms.

4. Summary and Outlook

In conclusion, we have demonstrated FRET between shallow NV centers in SCD and WSe₂ flakes with an estimated Förster radius of 13 nm. The FRET process strongly reduces τ_{NV} to around 6 ns, whereas the coupling to the NV centers enhances the excitation of WSe₂ for λ_{exc} below 500 nm. We show that NVs undergoing FRET retain their ODMR and are applicable as multi-functional sensors.

In the future, we will investigate the transfer of WSe₂ flakes onto SCD photonic structures, for example, nanopillars with single NV centers. The first tests conducted during this work prove that typical SCD nanopillars are robust in the applied transfer process. Using such photonic structures will enhance the PL rates from single NV centers and will also allow for the modification of the excitonic properties of 2D materials via inducing local strain.^[30] While traditionally FRET pairs are formed by attaching FRET partners to larger molecules or nanoparticles^[8,31] or directly within a biological specimen,^[31] the extension to stable solid-state systems could enable the realization of scanning devices where FRET is established between a single quantum probe scanning the system under investigation. Consequently, the distance between sample and probe can be varied continuously, which allows for in-depth characterization of the FRET process and imaging the sample on the nanoscale. Such techniques termed FRET-Scanning near-field optical microscopy (FRET-SNOM)^[32] will highly profit from stable probes like NV centers in SCD. The first demonstration of FRET-SNOM enabled nanoscale imaging of graphene flakes using a scanning NV center in a nanodiamond.^[10] Moreover, hybrid systems involving NV centers

and 2D materials are potential candidates for spin transfer and spin valley physics. The latter has triggered intense research in TMDs and has potential for quantum information and sensing applications.^[33] The FRET process investigated here can potentially aid to determine the depth of shallow color centers in SCD given the FRET radius of the WSe₂/NV pair is precisely known. One advantage of this approach would be its applicability to color centers that do not possess an electronic spin.

Acknowledgements

This research has been funded via the NanoMatFutur program of the German Ministry of Education and Research (BMBF) under grant number FKZ13N13547. The Australian research council (via DP180100077, DP190101058 and DE180100810), the Asian Office of Aerospace Research and Development Grant FA2386-17-1-4064, and the Office of Naval Research Global under Grant N62909-18-1-2025 are gratefully acknowledged. The authors acknowledge funding via a PostDoc fellowship of the Daimler and Benz foundation. The authors also thank Jörg Schmauch for recording SEM images as well as Dr. Rene Hensel for use of the ICP-RIE and Michel Challier for help with the RIE etching of the sample.

Conflict of Interest

The authors declare no conflict of interest.

Keywords

diamond, Förster resonance energy transfer, nitrogen vacancy centers, two dimensional materials

Received: July 28, 2019

Revised: October 22, 2019

Published online:

- [1] R. M. Clegg, in *The History of Fret* (Eds: C. D. Geddes, J. R. Lakowicz), Springer US, Boston, MA **2006**, pp. 1–45.
- [2] S. Kim, D. H. Shin, J. Kim, C. W. Jang, S. S. Kang, J. M. Kim, J. H. Kim, D. H. Lee, J. H. Kim, S.-H. Choi, S. W. Hwang, *Sci. Rep.* **2016**, *6*, 27145.
- [3] I. Aharonovich, E. Neu, *Adv. Opt. Mater.* **2014**, *2*, 911.
- [4] M. W. Doherty, N. B. Manson, P. Delaney, F. Jelezko, J. Wrachtrup, L. C. L. Hollenberg, *Phys. Rep.* **2013**, *528*, 1.
- [5] L. Rondin, J.-P. Tetienne, T. Hingant, J.-F. Roch, P. Maletinsky, V. Jacques, *Rep. Prog. Phys.* **2014**, *77*, 056503.
- [6] F. Dolde, M. W. Doherty, J. Michl, I. Jakobi, B. Naydenov, S. Pezzagna, J. Meijer, P. Neumann, F. Jelezko, N. B. Manson, J. Wrachtrup, *Phys. Rev. Lett.* **2014**, *112*, 097603.
- [7] P. Neumann, I. Jakobi, F. Dolde, C. Burk, R. Reuter, G. Waldherr, J. Honert, T. Wolf, A. Brunner, J. H. Shim, D. Suter, H. Sumiya, J. Isoya, J. Wrachtrup, *Nano Lett.* **2013**, *13*, 2738.
- [8] N. Mohan, Y. Tzeng, L. Yang, Y. Chen, Y. Hui, C. Fang, H. Chang, *Adv. Mater.* **2010**, *22*, 843.
- [9] J. Tisler, R. Reuter, A. Lämmle, F. Jelezko, G. Balasubramanian, P. R. Hemmer, F. Reinhard, J. Wrachtrup, *ACS Nano* **2011**, *5*, 7893.
- [10] J. Tisler, T. Oeckinghaus, R. J. Stöhr, R. Kolesov, R. Reuter, F. Reinhard, J. Wrachtrup, *Nano Lett.* **2013**, *13*, 3152.

- [11] A. Brenneis, L. Gaudreau, M. Seifert, H. Karl, M. S. Brandt, H. Huebl, J. A. Garrido, F. H. Koppens, A. W. Holleitner, *Nat. Nanotechnol.* **2015**, *10*, 135.
- [12] J. R. Schaibley, H. Yu, G. Clark, P. Rivera, J. S. Ross, K. L. Seyler, W. Yao, X. Xu, *Nat. Rev. Mater.* **2016**, *1*, 16055.
- [13] K. F. Mak, J. Shan, *Nat. Photonics* **2016**, *10*, 216.
- [14] B. Peng, P. K. Ang, K. P. Loh, *Nano Today* **2015**, *10*, 128.
- [15] M. Toth, I. Aharonovich, *Annu. Rev. Phys. Chem.* **2019**, *70*, 123.
- [16] H. Zhou, C. Qin, R. Chen, W. Zhou, G. Zhang, Y. Gao, L. Xiao, S. Jia, *J. Phys. Chem. Lett.* **2019**, *10*, 2849.
- [17] H. Zang, P. K. Routh, Y. Huang, J.-S. Chen, E. Sutter, P. Sutter, M. Cotlet, *ACS Nano* **2016**, *10*, 4790.
- [18] F. Prins, A. J. Goodman, W. A. Tisdale, *Nano Lett.* **2014**, *14*, 6087.
- [19] D. Prasai, A. R. Klots, A. Newaz, J. S. Niezgodna, N. J. Orfield, C. A. Escobar, A. Wynn, A. Efimov, G. K. Jennings, S. J. Rosenthal, K. I. Bolotin, *Nano Lett.* **2015**, *15*, 4374.
- [20] K. M. Goodfellow, C. Chakraborty, K. Sowers, P. Waduge, M. Wanunu, T. Krauss, K. Driscoll, A. N. Vamivakas, *Appl. Phys. Lett.* **2016**, *108*, 021101.
- [21] Y. Niu, S. Gonzalez-Abad, R. Frisenda, P. Maruhn, M. Drüppel, P. Gant, R. Schmidt, N. Taghavi, D. Barcons, A. Molina-Mendoza, S. M. De Vasconcellos, R. Bratschitsch, D. P. De Lara, M. Rohfing, A. Castellanos-Gomez, *Nanomaterials* **2018**, *8*, 725.
- [22] J.-K. Huang, J. Pu, C.-L. Hsu, M.-H. Chiu, Z.-Y. Juang, Y.-H. Chang, W.-H. Chang, Y. Iwasa, T. Takenobu, L.-J. Li, *ACS Nano* **2013**, *8*, 923.
- [23] M. Challier, S. Sonusen, A. Barfuss, D. Rohner, D. Riedel, J. Koelbl, M. Ganzhorn, P. Appel, P. Maletinsky, E. Neu, *Micromachines* **2018**, *9*, 148.
- [24] Estimated using the software SRIM-The stopping range of ions in matter, <http://www.srim.org/> (accessed: October 2019).
- [25] N. B. Manson, J. P. Harrison, M. J. Sellars, *Phys. Rev. B* **2006**, *74*, 104303.
- [26] R. Nelz, J. Görlitz, D. Herrmann, A. Slablab, M. Challier, M. Radtke, M. Fischer, S. Gsell, M. Schreck, C. Becher, E. Neu, *APL Mater.* **2019**, *7*, 011108.
- [27] L. Robledo, H. Bernien, T. van der Sar, R. Hanson, *New J. Phys.* **2011**, *13*, 025013.
- [28] I. Lovchinsky, J. Sanchez-Yamagishi, E. Urbach, S. Choi, S. Fang, T. Andersen, K. Watanabe, T. Taniguchi, A. Bylinskii, E. Kaxiras, P. Kim, H. Park, M. D. Lukin, *Science* **2017**, *355*, 503.
- [29] E. Gratton, S. Breusegem, J. D. B. Sutin, Q. Ruan, N. P. Barry, *J. Biomed. Opt.* **2003**, *8*, 381–390.
- [30] C. Palacios-Berraquero, D. M. Kara, A. R.-P. Montblanch, M. Barbone, P. Latawiec, D. Yoon, A. K. Ott, M. Loncar, A. C. Ferrari, M. Atatüre, *Nat. Commun.* **2017**, *8*, 15093.
- [31] L. M. Loura, M. Prieto, *Front. Physiol.* **2011**, *2*, 82.
- [32] S. Sekatskii, G. Dietler, V. Letokhov, *Chem. Phys. Lett.* **2008**, *452*, 220.
- [33] X. Lu, X. Chen, S. Dubey, Q. Yao, W. Li, X. Wang, Q. Xiong, A. Srivastava, *Nat. Nanotechnol.* **2019**, *14*, 426.

8. Conclusion and Outlook

In this thesis, we optimized nanoscale sensing based on NV centers in single crystal diamond (SCD). We address the whole process of building optimized SCD sensors, including novel materials, optimized nanofabrication and novel sensing schemes (see Fig. 8.1).

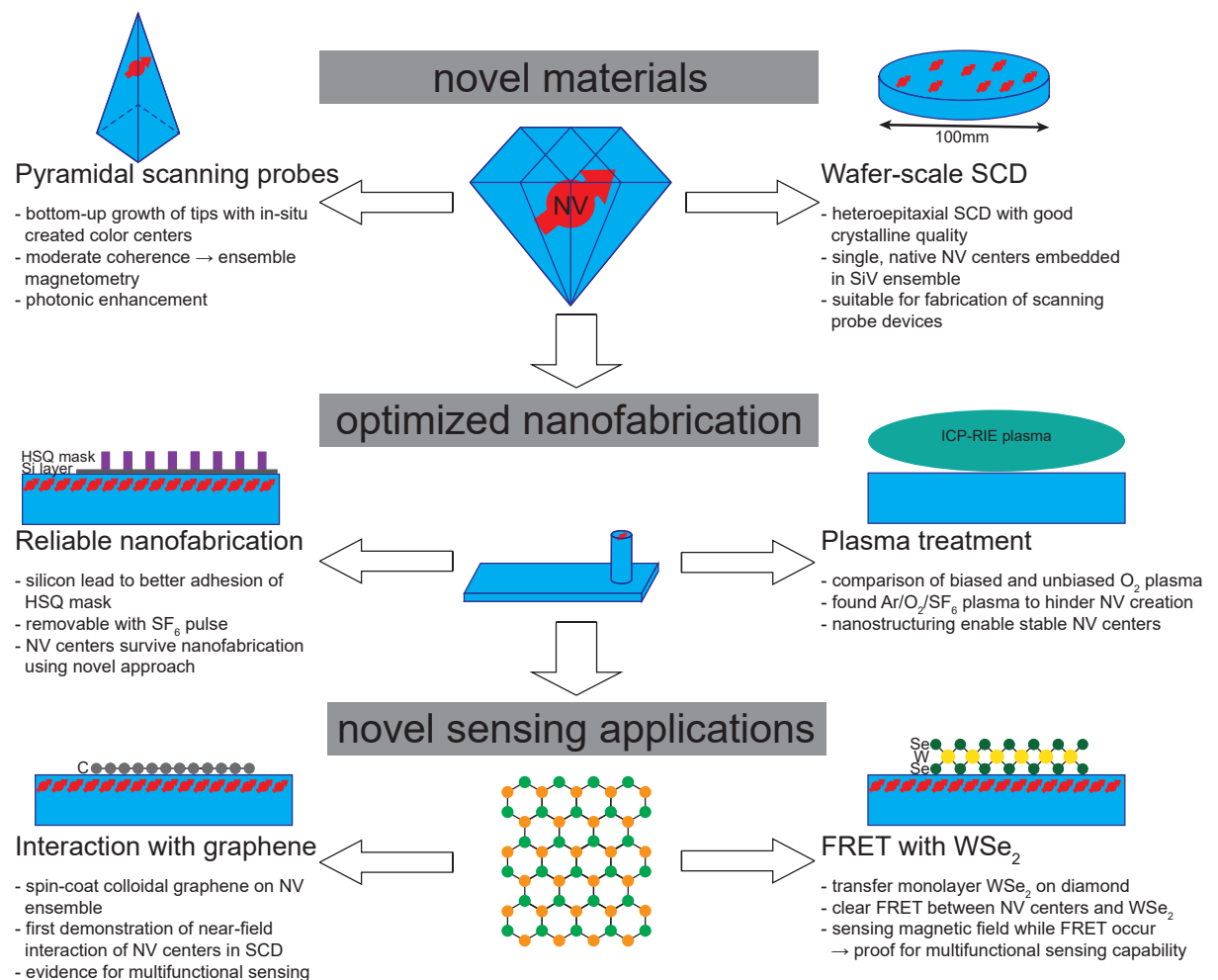


Figure 8.1.: Scheme of the progress made in this thesis with a summary of all main findings of the publications.

Due to the very complex and time consuming fabrication procedure for appropriate SCD nanostructures usable for sensing applications (see Sec. 1.2), we investigated novel material systems potentially enable upscaling of sensor manufacturing. Here, we compared

a bottom-up approach where the structure is already formed during SCD growth with conventional top-down approaches fabricating devices after the growth. Further, we characterized wafer-sized SCD material and tested its applicability for manufacturing sensors on the wafer-scale. This would overcome one significant limitation for fabricating nanostructures in large quantities as so far, high purity SCD is only available in limited sizes in the order of few millimeters. The outstanding advantage of bottom-up and top-down approaches on the wafer-scale are their potential to provide NV-based scanning probe tips in large quantities.

Afterwards, we optimized the nanofabrication process itself by introducing new steps to improve its reliability and reproducibility. Here, a new approach using silicon as a thin adhesion layer for the HSQ etch mask significantly enhanced the fabrication yield. Novel plasma treatments were investigated to improve the quality of SCDs' surface as well as of shallow NV centers. Here, we characterized the photoluminescence (PL) of single NV centers in photonic nanostructures as well as their spin properties to identify the effect of the optimization.

Lastly, we studied novel concepts for NV-based sensing: We investigated near-field interaction in form of Förster Resonance Energy Transfer (FRET) as a source for sensing and imaging applications. We studied the near-field interaction of a NV ensemble shallowly implanted into SCD with two-dimensional materials applied to the surface. Here, especially the work on the interaction with a luminescent monolayer of WSe₂ enabled deep insights of the NV center's usability as a donor for FRET-based applications. During this, we also found the NV center in SCD to be an extraordinary candidate for multifunctional sensing. While we can use FRET-based approaches for detecting nearby dipoles, we can use the retaining spin properties of the NV center to sense a variety of physical quantities like e.g. local magnetic fields.

In the following, we discuss and summarize all publications included in this thesis whose main findings are summarized in Fig. 8.1 followed by an outlook on how NV centers in SCD can be employed in the future.

8.1. Materials for sensing applications

In Chap. 2 and 3, we investigated novel material systems applicable for NV-based sensing. Here, especially approaches allowing to upscale nanostructure fabrication are of major interest to efficiently use complex and time consuming fabrication routines.

In the publication of Chap. 2, we focused on a bottom-up approach used to create SCD tips with a pyramidal shape which are commercially available. While our conventional top-down process is only able to fabricate a few hundred tips in parallel, the main advantage of this bottom-up approach is the large amount of tips ($> 10^5$) producible in a single growth process. Here, a complex chemical vapor deposition (CVD) process is used to selectively grow in (100) direction while other crystal facets grow highly defective. This leads to an evolving micro-pyramid with a square (100)-oriented basal plane surrounded by nano-crystalline material removable by air annealing. After the growth, the structures are

attached to cantilevers using epoxy and offer a good usability as ultra-hard AFM tips due to their small radius of curvature of 2-20 nm. To investigate the usability of these structures for sensing applications, we characterized native NV and SiV color centers created during the growth process by using our homebuilt confocal microscope. Characterizing several diamond pyramids, we found that they consistently show intense NV center PL in the order of 500 Mcps at a reasonable excitation power of $P < 400 \mu\text{W}$. This PL rate corresponds to an emitted power of $\sim 100 \text{ pW}$ easily measurable with common photodiodes. By investigating the PL originating from various planes parallel to the basal plane, we found that SiV centers are only present close to the apex of the pyramid. We were able to explain this by the growth process itself: The plasma involved in the CVD process etches the silicon substrate used to grow the diamond film on. The etched silicon is then incorporated into the growing diamond and forms SiV centers. As soon as the substrate is fully covered with diamond, the incorporation of silicon rapidly decreases leading to an occurrence of SiV centers only at the apex of the diamond pyramid. In addition, we found an increased PL of NV centers close to the apex despite constant incorporation of nitrogen during the growth. Simulating the photonic properties, we estimate PL intensity that agree very well with the measured one. Here, we were able to identify a clear photonic enhancement of detected PL from color centers close to the apex. However, by characterizing the color centers' lifetime along the growth direction, we found a quenching of NV centers close to the apex. Hereby, quenching describes a process decreasing the PL intensity as well as excited state lifetime due to opening an additional non-radiative decay channel. This can be caused by e.g. the near-field interaction with nearby dipoles or other structural defects. To explain this quenching, we first established a model estimating the mean distance between SiV and NV centers and found a mean distance between a NV center and the closest SiV center of $< 10 \text{ nm}$. Thus, dipole-dipole interaction in form of energy transfer from the NV centers to the SiV centers is feasible. In addition, the quenching of NV centers might be explainable by a lower quality at the apex. Further, we characterized the spin properties of the NV centers present at the pyramid apex and compared them to the NV centers in the bulk-like SCD close to the basal plane of the pyramid. Using Spin-Echo measurements, we found moderate coherence times of $T_2 = 7.2(1) \mu\text{s}$ for NV centers at the apex and $T_2 = 7.8(2) \mu\text{s}$ close to the basal plane. Despite the strong doping with silicon and nitrogen during the growth, T_2 is almost an order of magnitude better than in typical industrial diamonds (HPHT). However, they are much lower than in high purity CVD diamonds conventionally used for NV-based sensing approaches. We found good sensitivities η for DC and AC magnetic fields of up to $\eta_{DC} \approx 131 \text{ nT}/\sqrt{\text{Hz}}$ and $\eta_{AC} \approx 23 \text{ nT}/\sqrt{\text{Hz}}$. The present pyramidal tips offer a comparable low spatial resolution for sensing approaches due to the spatially spread NV ensemble. To overcome this, it would be necessary to drastically reduce the nitrogen and silicon incorporation. However, the present pyramidal tips are applicable for applications where scanning the sensor over the sample is mandatory and spatial resolution in the micrometer-range are sufficient.

Since the doping of the investigated diamond pyramids was too strong to identify single color centers, we also followed another approach to upscale the fabrication process: In Chap. 3 we investigated commercial SCD material available up to 100 mm wafer-size and

its suitability for quantum technologies. The material is grown in a microwave-enhanced CVD process at high temperatures based on the successful scaling of heteroepitaxial nucleation resulting in a 100 mm wafer-size [101]. First, we characterized color centers close to the growth surface using a homebuilt confocal microscope and observed for the first time individual native NV centers in a heteroepitaxial SCD. However, we found these NV centers embedded in an ensemble of native SiV centers incorporated during the growth process. As the dislocation density reduces during growth [101], we expected the highest material quality close to the growth surface of thick samples. To confirm this, we used the SiV center ensemble as a strain sensor. We exploited the fine structure of the SiV zero phonon line as strain caused by dislocations would lead to a shift and broadening of the fine structure components. By measuring the linewidth of the SiV centers' fine structure along the growth direction, we were able to confirm the expected reduction of dislocation density. Consequently, we investigated the native NV centers' properties in this region. Here, we found single NV centers with a density of ≈ 1 NV per μm^3 (≈ 0.005 ppb) which is in accordance with the nitrogen concentration in the feed gases of the CVD reactor. By measuring NV center excited state lifetimes, we found an average lifetime of 12.3(6) ns agreeing well with reported bulk lifetimes of NV centers [84]. In addition, this finding also excludes any possible quenching of the NV centers due to structural defects or near-field interaction with the SiV centers in the surrounding in contrast to the bottom-up approach in Chap. 2. To investigate the NV centers' spin properties, we performed Spin-Echo measurements finding a coherence time of $T_2 = 5(1) \mu\text{s}$. By shallowly implanting NV centers into the growth surface, we found spin properties comparable to the native NV centers mainly limited by the material potentially caused by surrounding silicon-containing defects. In addition, we showed that the fabrication of nanopillars is analogous to the commonly used SCD rendering the material applicable for scanning probe devices. However, the main challenge of using the present material for high-sensitivity sensing applications emerges from the limited coherence times of the NV centers. To overcome this limitation, it might be necessary to tweak the growth to drastically reduce silicon incorporation. This could be achieved by overgrowing the SCD wafers in a silicon-free CVD process. Here, already thin layers of overgrown material will be sufficient for most applications.

In general, the publications addressed here show a vast potential to upscale the fabrication of NV-based sensors. This would lead to a strong reduction of the cost per device. As there are already a few existing start-up companies, this upscaling might help to open novel fields of application. However, for both material systems reducing the defect concentration is mandatory to be able to sense fields with a good spatial resolution and sensitivity.

8.2. Optimized nanofabrication processes

In the publications of Chap. 4 and 5, we optimized a procedure to fabricate nanostructures usable in scanning probe based applications. Here, our main goal was to establish a reliable and most important a reproducible process. Further, we studied the influence of reactive ion etching on shallow NV centers in SCD.

In the publication in Chap. 4, we improved the reliability of a top-down nanofabrication process. Here, the most important step enhancing the reliability was to use a silicon layer to improve the adhesion of the HSQ etch mask and to find the critical parameters used in the plasma etching. We used our homebuilt confocal microscope to characterize the PL of NV centers in structures fabricated with the newly implemented method. Here, we observed an intense PL of the NV centers as well as a low background photoluminescence from the etched surfaces. We found that the background intensity (< 1 kcps) is negligible compared to the NV center intensity (~ 100 kcps) which is important as the signal-to-background ratio fundamentally limits the achievable sensitivity to detect magnetic fields using NV centers. Further, we were able to show a good contrast ($C \sim 15\%$) in ODMR comparable to other shallow NV centers [58]. We also found a quite short coherence time $T_2 \leq 10 \mu\text{s}$ mainly limited by the NV center's proximity to the three acid cleaned surface matching observations in the literature [102]. As we found stable NV centers in the fabricated structures, we exclude any negative effect of silicon on the NV centers. In addition, we showed that the usage of a silicon adhesion layer for HSQ improves the reliability of the fabrication significantly rendering it advantageous for nanofabrication-based technology. The publication in Chap. 5 contains a study of the influence of novel plasma treatments on shallow NV centers. Here, we compared three different plasmas: a 435 V O_2 plasma, a 0 V O_2 plasma and an $\text{Ar}/\text{SF}_6/\text{O}_2$ plasma. The bias voltage is hereby a parameter defined by the applied RF power of the reactive ion etching controlling the anisotropy of the plasma. We studied the influence of each plasma as the final step of the process needed to remove mechanical stress induced by polishing. By shallowly implanting NV centers in each etched area, we characterized the influence of the plasma on the NV centers. While both O_2 plasmas lead to similar results in terms of emission spectra, coherence and intensity of the NV centers, the $\text{Ar}/\text{SF}_6/\text{O}_2$ plasma influenced the SCD negatively such that we do not find any signature of NV centers present in this area. We exclude any effect of surface termination by the plasma as fluorine should stabilize the negative charge state of the NV center and vacuum annealing after implantation most probably removes any surface termination. Due to the complete absence of any NV centers, we suspect the $\text{Ar}/\text{SF}_6/\text{O}_2$ to strongly damage the surface preventing NV centers creation. Although the bias-free O_2 plasma should prevent subsurface damage compared to the biased O_2 plasma [96], we were so far not able to reveal any positive effect of the unbiased plasma on the NV centers. To further study the intensity and stability of NV centers under a bias-free etched surface, we fabricated nanopillars with a variety of diameters. First, we map the NV center lifetime in various pillar fields as a damaged surface would quench NV centers and consequently shorten the lifetime. We observed a consistent lifetime in all pillars as well as the ensemble before pillar fabrication. By comparing single NV centers in pillars with a top-diameter of 120 nm and 180 nm, we found that the 180 nm-pillars offer slightly higher photoluminescence rates than the 120 nm-pillars as expected from simulations [61]. In contrast to the simulations, we found a significant photonic enhancement for NV centers' photoluminescence in the 120 nm-pillars. This would be advantageous for scanning probe based applications as thinner scanning probe tips would be able to keep the NV center closer to the surface under investigation because the tip follows the sample topography more closely.

In conclusion, the publications discussed here constitute important steps towards the optimization of the nanofabrication procedure used to sculpt scanning probe devices with NV centers embedded as a sensor.

8.3. Novel applications

In the publications of Chap. 6 and 7, we investigated novel concepts to sensing using NV centers in SCD based on the near-field interaction with nearby dipoles. In parallel, we investigate the spin properties of shallow NV centers undergoing a near-field interaction. Here, different material systems have been employed: while graphene mainly quenches the NV centers' emission without producing any luminescence by itself, we also used a luminescent two-dimensional material WSe₂ which offers promising applications in quantum technologies [103].

In Chap. 6, we studied the influence of graphene on NV centers in SCD. Based on literature [27], it was known that near-field interaction with graphene significantly quenches NV centers. However, this observation was so far restricted to NV centers in nanodiamonds. To demonstrate this interaction also for NV centers in SCD, we spin coated colloidal graphene onto the surface of a shallow NV ensemble in SCD. Hereby, the flakes formed agglomerates on the SCD surface easily visible by light microscopy in our homebuilt confocal microscope. To study the influence of the graphene agglomerates on the NV centers, we measured their excited state lifetime and photoluminescence and identify a strong quenching in presence of the graphene. We clearly showed near-field interaction of color centers in SCD and their basic applicability for imaging applications based on this process. We, for the first time, present evidence that the NV center offers multifunctional sensing capabilities by investigating the preservation of the spin resonance while interacting with graphene.

In the publication of Chap. 7, we investigated the interaction of a NV ensemble with a monolayer of two-dimensional WSe₂. Here, we first prepared a SCD by creating shallow NV centers. Collaborators from University of Technology Sydney then transferred monolayer WSe₂ flakes on this SCD. We identified the strongly fluorescent WSe₂ flakes based on confocal PL mapping. Afterwards, we studied the interaction between the NV ensemble and the WSe₂. We clearly showed that FRET opens an additional non-radiative decay channel for the NV centers as their lifetime drastically reduced in the proximity of WSe₂ to 5.1 ns instead of the bulk lifetime of 12(1) ns. By exciting the FRET pair at a wavelength at the edge of the absorption of WSe₂ and by investigating the WSe₂ photoluminescence, we showed that FRET opens an additional excitation path for the excitons in WSe₂. These findings constituted a clear proof for the occurrence of FRET between NV centers and monolayer WSe₂. Combining the estimated depth profile of our implanted NV centers with the distance-dependency of FRET, we identified a FRET radius of 13 nm. This is comparable to the results reported for a FRET process between NV and graphene [27]. Using the calculated FRET radius, we calculated the expected PL decay for the NV ensemble which agrees very well with our measurements. To estimate the potential speed of FRET-based imaging, we have to determine the minimal integration time needed to

measure the lifetime of the NV centers. By using a previously reported model [100], we found an integration time of 15 ms rendering the NV center promising to use FRET as a tracking tool for moving particles. To proof the multifunctional sensing capabilities of the NV center, we measure an external applied magnetic field while the NV centers undergo FRET with the WSe₂ flakes. Since the emission of the WSe₂ excitons is more intense than the NV centers' emission, we implemented an advanced detection scheme. Here, we synchronized the detection with the pulsed excitation of the system. By an appropriate choice of the detection time, we separated the WSe₂ and NV photoluminescence and sensed the external magnetic field with a good signal-to-background ratio rendering the NV center in SCD applicable in multifunctional sensing schemes.

By investigating FRET, we introduced a novel sensing resource usable with NV centers in SCD. With this publications, we open routes towards novel possible sensing schemes based on near-field interaction and to use NV centers in SCD for nanoscale imaging of dipoles in e.g. molecules or solids.

In conclusion, the publications contained in this thesis represent important steps for NV-based sensing in general by addressing some of the major challenges related to fabrication of nanostructures based on SCD. We were able to show the potential for upscaling the processes by using wafer-scale SCD and by developing novel procedures rendering nanofabrication more reliable. Further, we showed a potential new sensing resource for NV centers in SCD in form of FRET. In particular, the multifunctional sensing capability by combining FRET with spin-based sensing approaches has to be highlighted. This might lead to new applications for NV-based sensors in the future.

8.4. Outlook

Recently, we started to optimize NV-based sensing schemes by exploiting the charge state properties of the NV center in SCD. During a bachelor project [104], we built a setup usable to detect the charge state of the NV center. Here, we employed a complex pulse sequence containing green (532 nm) and yellow (594 nm) laser pulses. As the yellow laser pulse excites only the negative charged NV center, it is possible to distinguish both charge states by photon counting [105]. This can be used to investigate e.g. the influence of different surface treatments on shallow NV centers. In addition, by including charge state detection in other pulsed schemes like Rabi measurements, it is possible to increase the contrast between the different spin states of the NV center's ground state. Here, the charge state is checked prior to the spin manipulation to exclude an insufficient NV⁻ initialization caused by a charge conversion to NV⁰ [106]. The charge state properties can be further used to optimize the efficiency to readout the spin state of the NV center [107,108]. During the time in which the $m_s = \pm 1$ state undergo the transition to the singlet state system and is kept there, it is possible to ionize the $m_s = 0$ state by an intense red laser pulse (637 nm). This then leads to a conversion of the spin state into a charge state which can

be detected by a yellow laser pulse. Here, detecting NV^0 corresponds to the $m_s = 0$ state while the detection of NV^- corresponds to the $m_s = \pm 1$ state. This approach potentially reduces the time needed to e.g. measure the T_1 time of NV centers by a factor of 25 due to an increased signal-to-noise ratio [109].

In the future, NV centers in nanostructured SCD used as a scanning probe or in bulk SCD will enable completely new applications in other scientific fields. For instance, NV-based magnetometers have become a common tool called *quantum diamond microscope* for analyzing the magnetic properties of geological samples [110]. However, further optimizing the nanofabrication seems mandatory. Based on our experiments on wafer-scale SCD, it is potentially possible to overgrow the wafer-sized SCD with a silicon-free high purity diamond layer using a homoepitaxial CVD process. This would allow to grow high quality SCD comparable with the commercially available electronic-grade standard. This would enable upscaling nanofabrication to the wafer-scale potentially reducing the fabrication cost per device by an order of magnitude. This will attract more scientist from other research areas to employ NV centers to their applications.

In addition, it will be necessary to further optimize the properties of shallow NV centers in SCD. This could be reached by appropriate surface treatment of the devices. Here, first promising results have been achieved in our group by wet-chemically terminating the SCD surface using fluorine [111]. A stabilized negative charge state of the NV center could be advantageous for sensing applications due to an enhanced signal-to-background ratio. This enhancement is caused by reducing the amount of measurements not containing any sensing informations as the NV center converted to its neutral charge state during the measurement. In addition, the results of our studies show a hydrophilic instead of a hydrophobic surface normally created by acid-cleaning the SCD [111]. This could lead to a better implementation into biological relevant conditions and will enable novel applications studying the magnetic fluctuations and currents in cells and tissues.

Due to the NV centers' potential for bio-applications, we also started a collaboration with the group of Marc Schneider at Saarland University. Here, we want to use our NV-scanning probes to investigate the properties of magnetic nanoparticles used for magnetic heating in cells. Hereby a clear characterization of the magnetic field of the particle is necessary to be able to efficiently design particles for in-vivo use them inside human tissue.

By employing scanning-FRET, it will be possible to study the interaction of NV centers with different kinds of acceptor systems in detail. Here, concerning life science applications, especially the interaction with a variety of luminescent particles and dye molecules used as bio-markers is of major interest. By employing the multifunctional sensing capabilities of NV centers, it enables a spatially resolved in-depth look on processes usually occurring in cells. However, scanning-FRET also allows the development of a novel technique to determine the depth of NV centers under the SCD surface. By approaching a FRET-partner with a known FRET radius to a shallow NV center, it is possible to use the distance-dependency of the interaction to precisely extract the depth of the NV center: By attaching a dye molecule to the scanning probe tip of our AFM setup and approaching it to a shallow NV center in bulk SCD as well as by approaching a NV center in a scanning probe device to a FRET partner placed in the AFM, it is possible to precisely determine

the depth of NV centers in scanning probe devices as well as in bulk SCD. In contrast to the conventional approach of bringing a spin ensemble in form of an immersion oil onto the surface and using NMR techniques [112], using scanning-FRET to determine the depth is additionally applicable using color centers without a spin.

In addition, the NV center in SCD is a viable research tool for nanomaterials. For instance, the magnetic field sensing capabilities of the NV center might lead to new approaches to characterize magnetic nanoparticles. In particular, characterizing magnetic nanoparticles with a fluorescent shell might benefit from the good spatial resolution achievable by combining magnetic field sensing and scanning-FRET using a NV center as a scanning probe. Furthermore, the possibility to detect small magnetic fields present on the surface of thin-films will enable to study e.g. the evolution of nanoscale antiferromagnetic domains and the transition between paramagnetic and antiferromagnetic phases [71] or to study the coupling between single antiferromagnetic layers [74]. Additionally, using NV-based magnetometry aid to enable studies on Skyrmions in ultrathin magnetic films [69, 113].

In particular, the NV center's potential to sense physical quantities with an extraordinary sensitivity combined with an exceptional spatial resolution under ambient conditions will potentially revolutionize many applications. Here, we mention for example a project under the coordination of Prof. Jörg Wrachtrup called *BrainQSens* [114]. The aim of this project is to use the NV center in SCD to sense neuronal magnetic fields. The signatures of these fields are supposed to be used as an interface between humans and machines potentially enabling a better control of e.g. the movement of prostheses.

By establishing appropriate surface treatments ensuring bio-compatibility and combining scanning-FRET with techniques enabling to sense temperatures and magnetic fields or currents simultaneously [115], the potential of NV-based sensing will lead to a completely new insight of mechanisms and their occurrence in biological systems. This could lead to a better understanding of biological processes in general.

A. Supplementary informations

In the following sections, we will provide the supplementary informations for the publications in Chap. 2 and Chap. 3.

A.1. Chap. 2: Color center fluorescence and spin manipulation in single crystal, pyramidal diamond tips

Chapter 2: *Color center fluorescence and spin manipulation in single crystal, pyramidal diamond tips*

Richard Nelz, Philipp Fuchs, Oliver Opaluch, Selda Sonusen, Natalia Savenko, Vitali Podgursky, and Elke Neu

Applied Physics Letters **109**, 193105 (2016); doi: 10.1063/1.4967189

Supplementary information for manuscript: Color center fluorescence and spin manipulation in single crystal, pyramidal diamond tips

Richard Nelz,¹ Philipp Fuchs,¹ Oliver Opaluch,¹ Selda Sonusen,¹ Natalia Savenko,² Vitali Podgursky,³ and Elke Neu^{1, a)}

¹⁾ *Universität des Saarlandes, FR 7.2 Experimentalphysik, 66123 Saarbrücken, Germany*

²⁾ *Artech Carbon OÜ, Jõe 5, 10151 Tallinn, Estonia*

³⁾ *Tallinn University of Technology, Department of Materials Engineering, Ehitajate tee 5, 19086, Tallinn, Estonia*

(Dated: 6 October 2016)

This supplementary material summarizes technical details on the experimental setup. We also present additional photoluminescence (PL) spectra and 3-dimensional PL maps of the diamond tips together with further information on the numerical simulation of photonic properties. The supplementary material also gives further details on the measurement and evaluation of optically detected magnetic resonance (ODMR) spectra and color center lifetimes. Finally, we here summarize details on the plasma treatments as well as the respective electron microscopy images and PL spectra.

I. EXPERIMENTAL SETUP

We analyze the photoluminescence (PL) of the diamond tips by mounting them onto a three-axes piezoelectric scanner (Attocube ANS xyz100) in our home built confocal microscope. We use a 532 nm DPSS laser (Integrated Optics, Matchbox 532L-21B) and an acousto-optic modulator (AOM, Crystal Technologies, 3200-146, 11 ns rise-time) to realize pulsed and continuous excitation of our samples. A 100× microscope objective (Olympus, LMPLFLN100X) with a numerical aperture (NA) of 0.8 focuses the excitation light onto the sample and collects the PL. Two dichroic mirrors (cut in wavelength: 560 nm) and a dielectric longpass filter (cut in wavelength: 650 nm) separate the excitation light from the emitted PL photons. We subsequently couple the PL to a single mode fiber (Thorlabs SM600, MFD 3.6 - 5.3 μm, NA 0.1 - 0.14) which serves as a pinhole.

The single mode fiber directs the PL of the sample to our detection setup. This detection setup contains a Hanbury-Brown Twiss interferometer (HBT) consisting of two avalanche photodiodes (APD, Excelitas SPCM-AQRH-14) to obtain the time resolved PL rate of the defects and a grating spectrometer from Princeton Instruments (Acton SpectraPro SP-2500 with Pixis 256OE CCD) to measure the spectral properties of the PL. Using microwave electronics (SpinCore PulseBlaserESR-PRO, Stanford Research Systems SG384, MiniCircuits ZASWA-2-50DR+) together with a moveable nearfield antenna,¹ we are able to perform optically detected magnetic resonance (ODMR) measurements of nitrogen-vacancy (NV) centers as well as coherent manipulation of NV electronic spins.

To quantify the color centers' excited state lifetime, we perform pulsed excitation using a supercontinuum laser

(NKT Photonics, EXW-12, pulse length \approx 50 ps) with a filter system (Varia) to select a defined wavelength range. Together with a time tagging module (PicoQuant, PicoHarp 300), this allows for time correlated (single) photon counting with high temporal resolution.

II. 3-DIMENSIONAL PL MAPPING AND SPECTRA

Figure S1 summarizes 3-dimensional PL mapping of the tips and is obtained via the following method: First, we measure the PL on each point in the xy-plane. Subsequently, we change the focus to a different z-position of the pyramid and repeat the measurement. Thus, we construct a 3-dimensional PL map. Together with the PL spectra at each z-position, we deduce information about the density of color centers at the respective positions in the pyramid. For the interpretation of the spectra, see the main manuscript.

In the lower row of Fig. S1, a bright background emission is visible in a distance of about 2 μm to the pyramid base. This background probably results from a contamination on the Si cantilever and is thus not related to the diamond device itself. The epoxy used for gluing the tips to the cantilever only produces minor, broadband PL observed when focusing the laser to the base of the diamond pyramid.

III. PL SIMULATIONS

To simulate the color centers' emission characteristics inside the pyramidal tip, we use a commercial Finite Difference Time Domain (FDTD) software (Lumerical FDTD Solutions). The software allows for broadband simulations, nevertheless we restrict our analysis to a single wavelength of 700 nm, which corresponds to the center of the used filter window for NV sideband detection. The pyramidal tip is abstracted as a frustum with a square

^{a)} Electronic mail: elkeneu@physik.uni-saarland.de

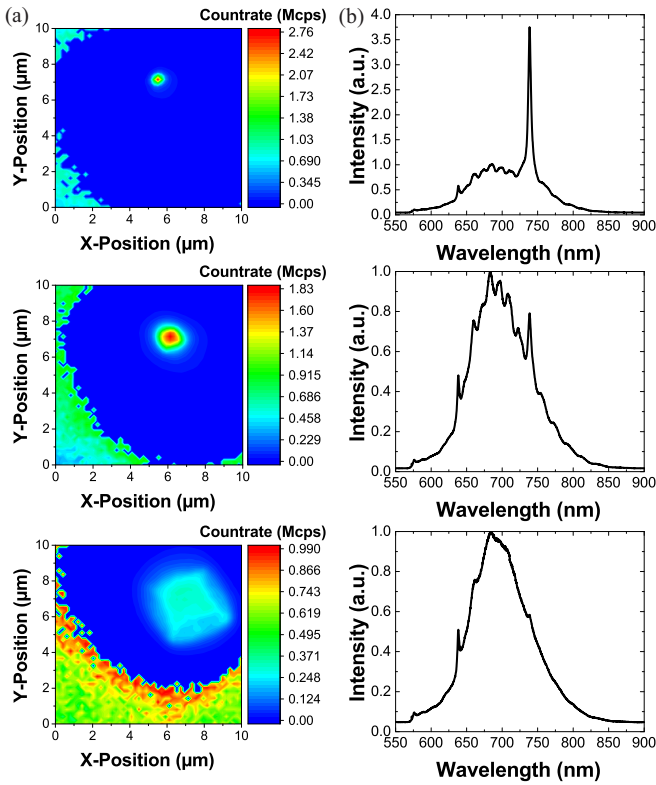


FIG. S1. Mapping of NV fluorescence (680-720 nm) (a) and PL spectra (b) at the bottom (lower), the middle (middle) and the apex (upper) of the tip. The SiV PL is rapidly decreasing compared to the NV PL. Note that the count rates are measured through an OD1 neutral density filter. The spectra are normalized on the maximum in NV PL.

base of $5 \times 5 \mu\text{m}^2$ that narrows to $20 \times 20 \text{nm}^2$ at the top, a height of $10 \mu\text{m}$ and a refractive index of $n = 2.4$. An electric point dipole, placed in the horizontal center of the pyramid, represents the color center. Its vertical position is varied over the height of the pyramid, corresponding to an experimental excitation in different focal planes (z -positions). The whole simulation area is surrounded by perfectly matched layers and is meshed with $15 \times 15 \times 15 \text{nm}^3$ Yee cells. A monitor, placed 100nm above the pyramid's top, records the fields emitted towards the upper half-space. This allows us to calculate the far field and thereby the power radiated into a specific NA.

As sensing applications often demand to maximize the photon flux into the detection optics, our figure of merit is the ratio of the radiated power into a specific NA to the radiated power in homogeneous diamond, here called collection factor ξ .

$$\xi = \frac{P_{\text{NA}}}{P_{\text{hom}}} \quad (\text{S1})$$

Note that the denominator $P_{\text{hom}} = n \times P_0$, with P_0 the total time-average power radiated by an electric dipole in vacuum, is independent from the dipole's position inside

the diamond. The refractive index $n = 2.4$ is determined by the host material. Thus, the collection factor quantifies the power or the photon flux, respectively, into the NA in a more handy and comparable way than absolute powers do. Note that a high collection efficiency, usually defined with the denominator being the total time-average power radiated by the dipole in the specific dielectric environment, does not necessarily indicate a high photon flux.

IV. SATURATION

Figure S2 shows the saturation measurement done at the apex of the pyramid detecting PL in the wavelength range from 680 to 720 nm. This detection window has been chosen to separate the NV PL from the SiV PL. We find a saturation power $P_{\text{sat}} = 377(6) \mu\text{W}$ and a maximal count rate $I_{\infty} = 5.52(3) \text{Mcps}$. The data are fitted with

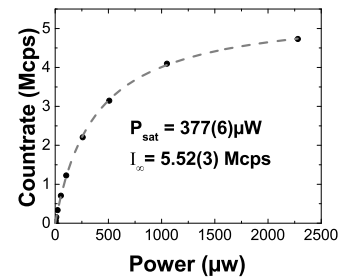


FIG. S2. Saturation measurement at the apex fitted with Eq. S2.

the following function of the excitation power P including a linearly increasing background PL B :

$$I(P) = I_{\infty} \times \frac{P}{P + P_{\text{Sat}}} + B \times P \quad (\text{S2})$$

With this, we calculate an estimation of the PL count rate emitted into the first lens of our confocal microscope. First, we estimate the fraction of the whole NV spectral intensity we detect to be roughly one third of the full intensity. Knowing the transmission of our confocal setup ($T = 44\%$) and the detection efficiency of our avalanche photodiodes (70%) as well as the transmission of the OD1 filter, we estimate the count rate emitted into the first lens to be 500Mcps . This is easily measurable with a common commercial photodiode as this corresponds to PL in the 100pW regime.

V. LIFETIME MEASUREMENTS

We measure the excited state lifetimes of NV τ_{NV} and SiV (silicon-vacancy) τ_{SiV} along the z -axis of the pyramid. By choosing suitable filters (680 - 720 nm for NV and 735 - 745 nm for SiV), we aim at separating the PL of NV and SiV centers. Fitting the NV PL decay with a

single exponential decay yields very good agreement with the measured data [see Fig. S3(a)] and we extract τ_{NV} on every z -position. For τ_{SiV} , fitting the measured data with a double exponential decay is necessary [see Fig. S3(b)] because of the NV sideband PL which also partly falls in the wavelength range 735 - 745 nm. The double exponential fit reveals τ_{SiV} and τ_{NV} , where the latter is consistent with the independent determination of τ_{NV} in the wavelength range 680 - 720 nm.

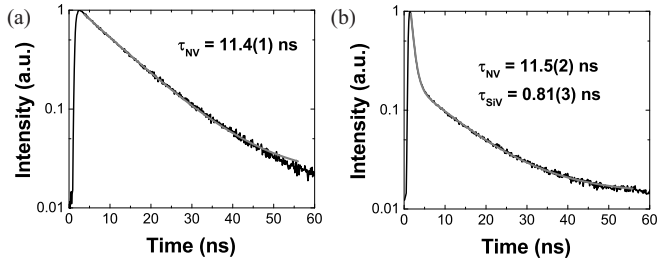


FIG. S3. Excited state lifetime measurements plotted using logarithmic scaling for the intensity for NV (a) fitted with a single exponential decay and SiV PL (b) fitted with a double exponential decay.

VI. ODMR-SPECTRA

To determine the suitability of the tips as magnetic sensors and to prove that the tips are single crystals, we first measure ground state ODMR spectra of the embedded NV centers in a PL detection window between 680 and 720 nm. Applying a randomly-oriented magnetic field \vec{B} gives us ODMR-spectra with eight dips, comparable to the measurement shown in Fig. S4. These eight dips corresponds to the four equivalent NV $\langle 111 \rangle$ orientations in the diamond lattice. The occurrence of four pairs of resonances witnesses the single crystal nature of the tip as any misoriented, polycrystalline grains would lead to additional resonances or blurring of the ODMR-spectrum. For spin manipulations, it is helpful to align the mag-

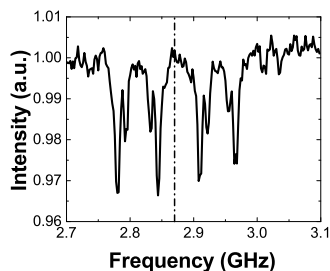


FIG. S4. Full ODMR-spectrum of the tip with randomly aligned \vec{B} .

netic field \vec{B} onto one of these NV axes and to use the sub-ensemble onto which \vec{B} is aligned. This is shown in Fig. S5(a). The obtained ODMR-spectrum reveals a

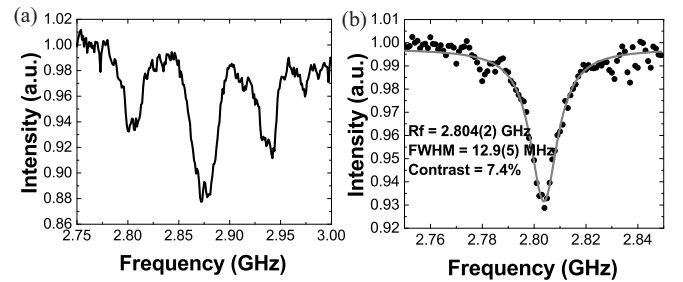


FIG. S5. (a) Full ODMR-spectrum of a tip with \vec{B} aligned onto one of the NV axes. (b) Zoom onto the $m_s = 0 \rightarrow -1$ transition at a frequency of 2.8 GHz; we find a linewidth of 12.9(5) MHz. The contrast is $C = 7.4\%$.

contrast of $C = 7.4\%$ [see Fig. S5(b)]. The linewidth of the dip is 12.9(5) MHz at a central frequency of 2.8 GHz. Assuming a T_2^* limited linewidth, this would indicate $T_2^* \approx 13$ ns. However, Ramsey type measurement reveal $T_2^* = 0.24(7) \mu\text{s}$, indicating significant power broadening in the ODMR spectra.

As visible in Fig. S5, there is still a splitting in the central dip of 8 MHz despite the alignment onto one of the NV axes. This splitting could occur due to non-perfect alignment of the external magnetic field \vec{B} , because we use a permanent magnet mounted in a rotation stage on a three-axes linear translation stage. However, this splitting is also measurable when no external magnetic field is applied. Therefore, we suspect strain in the diamond itself causing this splitting.² However, we can not fully rule out that this splitting results from residual magnetic fields due to magnetized components in our setup which is still present after removing the magnet.

VII. PLASMA TREATMENTS OF DIAMOND TIPS

As a first step towards optimization of the tips for magnetometry, we tested cleaning of the diamond tip using a plasma cleaning device (Diener Femto, 0.3 mbar, 4 min O_2 plasma with 80 W RF power at 13.56 MHz). We intended to remove possible surface contamination or highly defective regions at the tip surface. This treatment was not successful, but rather introduced additional broadband luminescence (possible due to residual contamination in the cleaning plasma), so this approach was not further investigated.

In a next step, we use an Ar/O_2 plasma for etching the diamond in accordance with previous approaches.^{3,4} Similar plasma recipes have been found to provide highly-anisotropic etching of diamond as well as an etch rate almost independent of crystal orientation. Such a plasma can also smoothly etch polycrystalline diamond and does not selectively attack grain boundaries and defects (see Ref. 4 and the corresponding supplementary material). We use Ar/O_2 gases, 50 sccm each, 18.9 mTorr, 500 W ICP, 200 W RF power in an

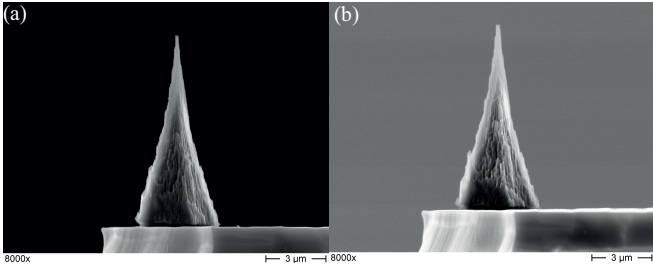


FIG. S6. 90° SEM picture of the tip after the second (a) and third (b) etch step.

Oxford Plasmalab inductively coupled reactive ion etcher (ICP-RIE), while the wafer is cooled to 20 °C. From etching of diamond pillars in (100) diamond using Fox16 (Dow corning) electron beam resist as mask, we determine an etch rate of ≈ 110 nm/min and verify anisotropic etching. Whereas ICP-RIE processes allow for smooth, high-rate etching of diamond and other inert materials, they simultaneously bear the risk of sample heating in the plasma. The epoxy used to mount the tip is stable up to 200 °C (information from supplier). To not exceed this temperature range, we restrict the maximum duration of the plasma steps (see below). The tip has been subjected to the following etch steps:

1. 90 s etching
2. 4 cycles of 60 s etching, 300 s cooling under Ar after each etch step
3. 3 cycles of 60 s etching, 300 s cooling under Ar after each etch step

From SEM images taken under an angle of 90° [see Fig. S6], we estimate the rate, with which the height of the pyramid is reduced during the etching to be 120 nm/min. We note that despite significant removal of diamond the surface roughness is still comparable and the pyramid still shows a sharp apex. The PL measurements reveal that we are able to significantly reduce the SiV density at the apex of the pyramid. This is shown in Fig. S7. In Fig. S7, a clear change in the spectra is visible. The SiV PL is drastically decreasing while the NV PL is nearly unchanged (compared by 3-dimensional PL maps). Thus, we are able to change the color center composition at the apex by our established plasma treatment. Please note that all these etch steps are realized while the pyramid is glued to its cantilever. Thus, we implemented a tool to tailor ready made devices.

VIII. DISTANCE BETWEEN COLOR CENTERS

From previous work, we estimate 60 ppm silicon⁵, while our measurement tentatively suggest ≈ 10 ppm nitrogen.

The yield to form color centers (0.1 % for N \rightarrow NV⁶ and

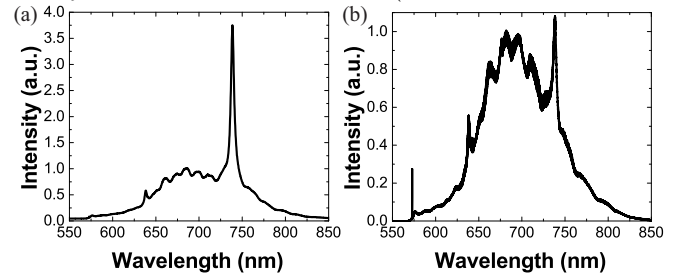


FIG. S7. PL spectra recorded at the pyramid apex before (a) and after (b) all etch steps. A significant change in SiV density is visible. This means, that we are able to actively change the color center composition at the apex of the tip. Note that the spectrum in (b) has been measured using a higher dispersion grating.

15 % for Si \rightarrow SiV⁷) indicates the parameters from Tab. SI. This means that in average one out of 232 unit cells con-

TABLE SI. Parameters for the estimation of the mean distance between the color centers.

	NV	SiV
Density (cm ⁻³ /ppm)	$1.8 \times 10^{18}/10$	$10^{19}/57$
Conversion to color center	0.001	0.15
Color center dens. (ppm)	0.01	≈ 8
number of unit cells (1D)	232	28
Distance between two (nm)	83	10

tains a NV center and one out of 28 unit cells a SiV center. This gives an approximate mean distance between centers < 10 nm at the apex. Thus, FRET between NV and SiV centers might be feasible.

¹P. Maletinsky, S. Hong, M. S. Grinolds, B. Hausmann, M. D. Lukin, R. L. Walsworth, M. Loncar, and A. Yacoby, *Nat. Nanotechnol.* **7**, 320 (2012).

²J. Teissier, A. Barfuss, P. Appel, E. Neu, and P. Maletinsky, *Phys. Rev. Lett.* **113**, 020503 (2014).

³P. Appel, E. Neu, M. Ganzhorn, A. Barfuss, M. Batzer, M. Gratz, A. Tschöpe, and P. Maletinsky, *Rev. Sci. Instrum.* **87**, 063703 (2016).

⁴E. Neu, P. Appel, M. Ganzhorn, J. Miguel-Sánchez, M. Lesik, V. Mille, V. Jacques, A. Tallaire, J. Achard, and P. Maletinsky, *Appl. Phys. Lett.* **104**, 153108 (2014), <http://dx.doi.org/10.1063/1.4871580>.

⁵J. Barjon, E. Rzepka, F. Jomard, J.-M. Laroche, D. Ballutaud, T. Kociniowski, and J. Chevallier, *physica status solidi (a)* **202**, 2177 (2005).

⁶J. R. Rabeau, A. Stacey, A. Rabeau, S. Praver, F. Jelezko, I. Mirza, and J. Wrachtrup, *Nano Lett.* **7**, 3433 (2007).

⁷A. Bolshakov, V. Ralchenko, V. Sedov, A. Khomich, I. Vlasov, A. Khomich, N. Trofimov, V. Krivobok, S. Nikolaev, R. Khmel'nitskii, and V. Saraykin, *physica status solidi (a)* **212**, 2525 (2015).

A.2. Chap. 3: Toward wafer-scale diamond nano- and quantum technologies

Chapter 3: *Toward wafer-scale diamond nano- and quantum technologies*

Richard Nelz, Johannes Görlitz, Dennis Herrmann, Abdallah Slablab, Michel Challier, Mariusz Radtke, Martin Fischer, Stefan Gsell, Matthias Schreck, Christoph Becher, and Elke Neu

APL Materials **7**, 011108 (2019); doi: 10.1063/1.5067267

Supplementary information for manuscript: Towards wafer-scale diamond nano- and quantum technologies

Richard Nelz,¹ Johannes Görlitz,¹ Dennis Herrmann,¹ Abdallah Slablab,¹ Michel Challier,¹ Mariusz Radtke,¹ Martin Fischer,² Stefan Gsell,² Matthias Schreck,³ Christoph Becher,¹ and Elke Neu^{1, a)}

¹⁾ *Universität des Saarlandes, Fakultät NT, Physik, 66123 Saarbrücken, Germany*

²⁾ *Augsburg Diamond Technology GmbH, 86159 Augsburg, Germany*

³⁾ *Universität Augsburg, Institut für Physik, 86135 Augsburg, Germany*

(Dated: 7 December 2018)

This supplementary material summarizes details on the estimation of the NV concentration in the diamond. In addition, we estimate the power broadening of the NV optically-detected magnetic resonance and present further data on NV spin manipulation and the fitting of SiV PL lines.

I. ESTIMATION OF NV DENSITY AND CONCENTRATION OF SUBSTITUTIONAL NITROGEN

To estimate the expected number of NV centers, we use the nitrogen concentration in the gas phase of ≈ 0.5 ppm N_2 . Ref. 1 finds for a concentration of 10 ppm N_2 in the gas phase a concentration of substitutional nitrogen of ≈ 55 ppb and a concentration of negatively-charged NV centers of ≈ 0.2 ppb. Assuming similar incorporation and conversion efficiencies in our case, we expect a substitutional nitrogen concentration of ≈ 2.75 ppb and a concentration of negatively-charged NV centers of ≈ 0.01 ppb. Now, we compare this value with the number of NVs we observe in the diamond material.

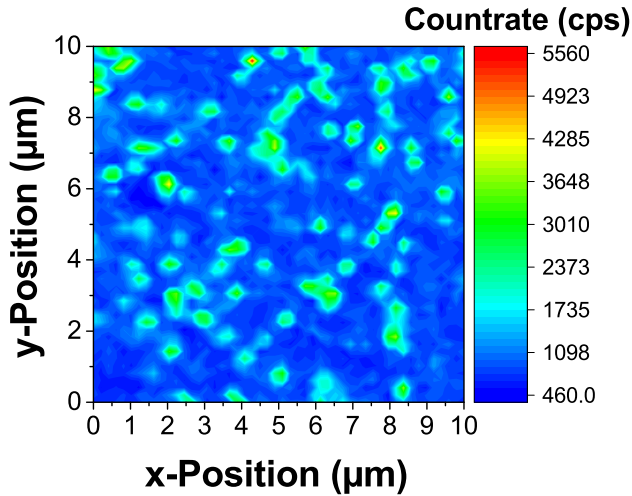


FIG. S1. xy-scan of a $10 \times 10 \mu\text{m}^2$ -sized area of the diamond. With a depth-to-focus of about $1 \mu\text{m}$, we can estimate the density of NVs to $1 \text{ NV}/\mu\text{m}^3$.

We estimate the density of NV centers from the PL map visible in Fig. S1. Hereby, we obtain ≈ 100 NV centers in an area of $10 \times 10 \mu\text{m}^2$. By taking into account the depth-of-focus of the used confocal microscope ($\approx 1 \mu\text{m}$),

we find an observed NV density of $1 \text{ NV per } \mu\text{m}^3$. By comparing this to the number of unit cells in this volume and the number of carbon atoms per unit cell, we can calculate the measured NV center concentration to

$$[\text{NV}^-]_{\text{measured}} \approx 0.005 \text{ ppb}$$

Thus, the observed density of NV centers agrees well with the expected density.

II. PL LIFETIME IMAGING

To characterize the lifetime of the native NV centers in the diamond, we measure lifetime maps of different areas of the diamond. In Fig. S2, we show an exemplary measurement of the lifetime in a $10 \times 10 \mu\text{m}^2$ large area of the sample. On average, we obtain a lifetime of $12.3(6)$ ns of the NV centers.

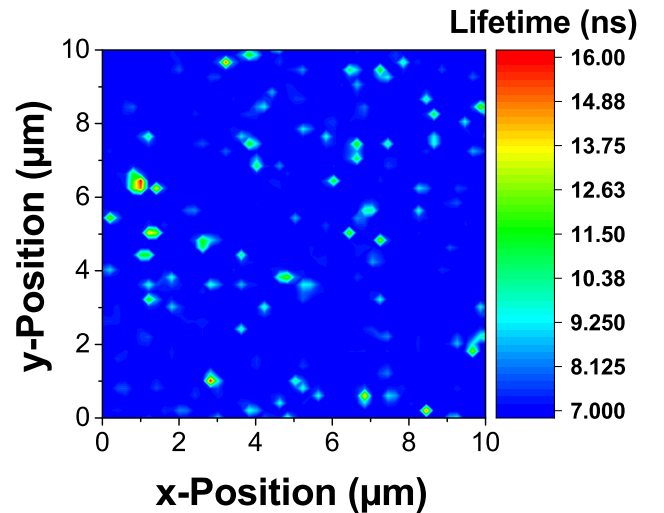


FIG. S2. PL lifetime image of individual NV centers in our diamond. From the fitted data, we obtain a lifetime of $12.3(6)$ ns of the NVs.

^{a)} Electronic mail: elkeneu@physik.uni-saarland.de

III. ION IMPLANTATION OF SHALLOW NV CENTERS

For several sensing-related applications and fabrication procedures, it is important to form NV centers close to the surface of the diamond.² To obtain individual NV centers in nanostructures, typical NV densities in the order of 10^9 cm^{-2} are necessary.² Therefore, we use ion implantation to create such shallow NV centers. Here, we use an implantation energy of 6 keV and doses of 1.5 and $3 \times 10^{11} \text{ cm}^{-2}$ which leads to a formation of NV centers on average 10 nm below the surface. After annealing, we first move the implanted layer along the optical axis (z -axis) through the laser focus of our confocal microscope, while recording the PL intensity. The recorded PL trace is visible in Fig. S3. A clear PL peak coinciding with the diamond surface is visible. The width of the peak is given by the optics of our confocal microscope. The slight asymmetry of the PL trace arises due to the PL of the SiV center ensemble in the diamond material which, despite careful spectral filtering, is still discernible when observing NV PL in our diamond material.

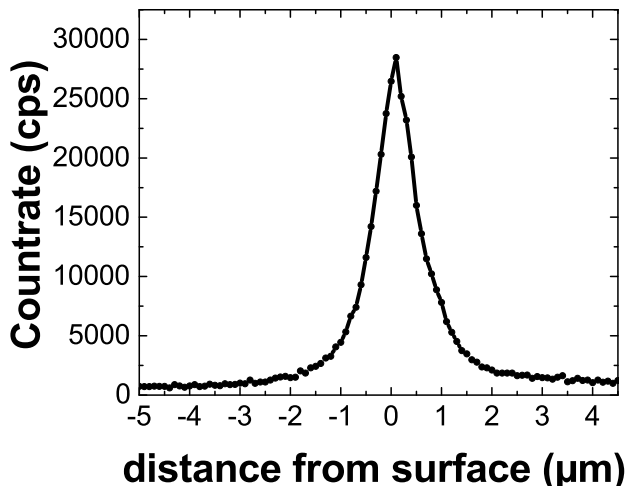


FIG. S3. PL trace of the implanted layer of NV centers. A clear PL peak is visible at the surface.

IV. MEASUREMENT OF INTENSITY AUTOCORRELATION OF NATIVE NV CENTERS

To prove observation of single NV centers, we measure second order correlation functions $g^{(2)}(\tau)$. In general, $g^{(2)}$ is defined as

$$g^{(2)}(\tau) = \frac{\langle I(t)I(t+\tau) \rangle}{\langle I(t) \rangle^2}$$

with the intensity $I(t)$ and $\langle \cdot \rangle$ indicates the time average. By using a 3-level model to describe the NV center, the measured $g^{(2)}$ function can be fitted by:³

$$g^{(2)}(\tau) = 1 - (1 + a) \exp(-|\tau|/\tau_1) + a \exp(-|\tau|/\tau_2)$$

with τ_1 and τ_2 describing the anti-bunching and bunching time constants; a is a measure for the impact of the shelving state.

We now take background contributions into account by defining $p_f = s/(s+b)$ with the signal- s and background-count rate b , leading to:

$$g_{\text{det}}^{(2)}(\tau) = 1 + p_f^2 \{ - (1 + a) \exp(-|\tau - \tau_0|/\tau_1) + a \exp(-|\tau - \tau_0|/\tau_2) \}$$

This means, that the minimum achievable $g^{(2)}(0)$ is determined by

$$g^{(2)}(0) \geq 1 - p_f^2 = 1 - \frac{s^2}{(s+b)^2}$$

In the main text, we show a $g^{(2)}$ measurement of a single NV center in the presented diamond material. The investigated NV center has a photon count rate of $s = 2870$ cps while the background is $b = 719$ cps determined from the PL map depicted in the main text. This leads to a minimum $g_{\text{min}}^{(2)}(0) = 0.36$, assuming that the background consists of fully uncorrelated emission. The observed background is attributed to PL from the SiV ensemble. Despite spectral filtering, minor parts of the SiV PL overlap with our window for NV observation 680 – 720 nm.

V. SPIN MANIPULATION OF IMPLANTED NV ENSEMBLE

To show the basic usability of the implanted NV ensemble layer for quantum technologies, we first measure an Optically Detected Magnetic Resonance (ODMR). To further show the usability for more complex sensing schemes, we coherently manipulate the spin states of the NVs. This, we show by performing Rabi oscillations of a subensemble of the NV centers as depicted in Fig. S4.

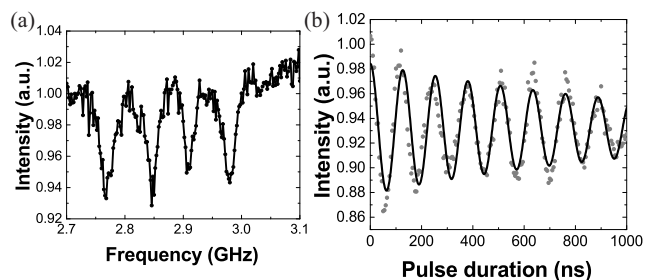


FIG. S4. (a) ODMR measurement of the NV ensemble. The different resonances belong to the different equivalent orientations of the NV center. (b) Coherent spin manipulation of the NV subensemble resonant to 2.768 GHz, clear Rabi oscillations are discernible.

VI. ESTIMATION OF POWER BROADENING OF ODMR LINewidth

Fig. S5 shows the ODMR measurements obtained from a single, native NV and an ensemble of shallowly-implanted NVs. To calculate the linewidth of the ODMR resonances

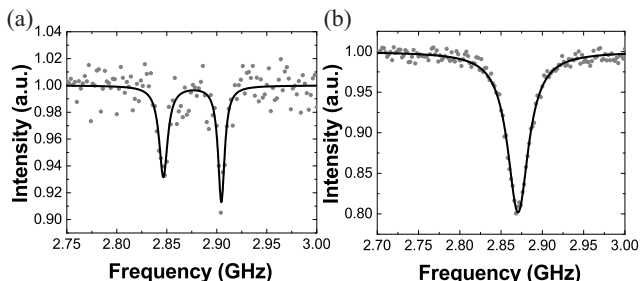


FIG. S5. ODMR measurements of a (a) single NV center and (b) of an ensemble of NV centers in the diamond. Both lines have a comparably broad linewidth due to power broadening. In the text, we estimate the unbroadened linewidth.

$\Delta\nu$ we use the formula developed in Ref. 4

$$\Delta\nu = \frac{\Gamma_c^\infty}{2\pi} \sqrt{\left(\frac{s}{1+s}\right)^2 + \frac{\Omega_R^2}{\Gamma_p^\infty \Gamma_c^\infty}}$$

with the Rabi frequency Ω_R , the rate of optical cycles at saturation Γ_c^∞ which is given by the inverse excited state lifetime, the polarization rate Γ_p^∞ which is given by the inverse lifetime of the metastable singlet state (in the order of 200 ns at room temperature) and the ratio between the optical pumping power and the saturation power of the transition s . Table S1 summarizes the estimated data. To further narrow the ODMR linewidth,

TABLE S1. Parameters for the estimation of unbroadened ODMR linewidth.

	single NV	Ensemble
measured linewidth (MHz)	7.9	15.46
Γ_c^∞ (10^7 1/s)	8.6	5.81
$s = P_{\text{opt}}/P_{\text{sat}}$	0.8	0.8
Rabi frequency (10^6 1/s)	1.9	7.94
calc. unbroadened linewidth (MHz)	7.7	10.67

it would be possible to decrease the excitation power to around $s = 0.2$. This would lead to a reduction of the linewidths by a factor of ≈ 2.6 . On the other hand, this would also decrease the obtainable contrast of the resonance.

VII. FITTING OF SiV PL LINES

To determine the linewidth of the SiV ZPL components, we fit Voigt profiles to the measured PL lines. To account for the instrument response function of the spectrometer, we used a fixed Gaussian width of $w_G = 0.0452$ nm. The Lorentzian width of the line is determined using a least chi-square fitting algorithm implemented in Origin (Origin Lab Corporation).

¹A. Tallaire, A. Collins, D. Charles, J. Achard, R. Sussmann, A. Gicquel, M. Newton, A. Edmonds, and R. Cruddace, *Diamond and Related Materials* **15**, 1700 (2006).

²P. Appel, E. Neu, M. Ganzhorn, A. Barfuss, M. Batzer, M. Gratz, A. Tschöpe, and P. Maletinsky, *Review of Scientific Instruments* **87**, 063703 (2016).

³C. Kurtsiefer, S. Mayer, P. Zarda, and H. Weinfurter, *Phys. Rev. Lett.* **85**, 290 (2000).

⁴A. Dréau, M. Lesik, L. Rondin, P. Spinicelli, O. Arcizet, J.-F. Roch, and V. Jacques, *Phys. Rev. B* **84**, 195204 (2011).

Bibliography

- [1] A. G. J. MacFarlane, J. P. Dowling, and G. J. Milburn, “Quantum technology: the second quantum revolution,” *Philosophical Transactions of the Royal Society of London. Series A: Mathematical, Physical and Engineering Sciences* **361**, 1655–1674 (2003).
- [2] R. P. Feynman, “Simulating physics with computers,” *International journal of theoretical physics* **21**, 467–488 (1982).
- [3] F. Arute, K. Arya, R. Babbush, D. Bacon, J. C. Bardin, R. Barends, R. Biswas, S. Boixo, F. G. Brandao, D. A. Buell *et al.*, “Quantum supremacy using a programmable superconducting processor,” *Nature* **574**, 505–510 (2019).
- [4] A. Wallraff, D. I. Schuster, A. Blais, L. Frunzio, R.-S. Huang, J. Majer, S. Kumar, S. M. Girvin, and R. J. Schoelkopf, “Strong coupling of a single photon to a superconducting qubit using circuit quantum electrodynamics,” *Nature* **431**, 162 (2004).
- [5] J. You and F. Nori, “Atomic physics and quantum optics using superconducting circuits,” *Nature* **474**, 589 (2011).
- [6] J. Koch, M. Y. Terri, J. Gambetta, A. A. Houck, D. Schuster, J. Majer, A. Blais, M. H. Devoret, S. M. Girvin, and R. J. Schoelkopf, “Charge-insensitive qubit design derived from the Cooper pair box,” *Physical Review A* **76**, 042319 (2007).
- [7] N. Gisin, G. Ribordy, W. Tittel, and H. Zbinden, “Quantum cryptography,” *Rev. Mod. Phys.* **74**, 145–195 (2002).
- [8] V. Scarani, H. Bechmann-Pasquinucci, N. J. Cerf, M. Dušek, N. Lütkenhaus, and M. Peev, “The security of practical quantum key distribution,” *Rev. Mod. Phys.* **81**, 1301–1350 (2009).
- [9] E. Diamanti, H.-K. Lo, B. Qi, and Z. Yuan, “Practical challenges in quantum key distribution,” *npj Quantum Information* **2**, 16025 (2016).
- [10] H. J. Kimble, M. Dagenais, and L. Mandel, “Photon Antibunching in Resonance Fluorescence,” *Phys. Rev. Lett.* **39**, 691–695 (1977).
- [11] T. Basché, W. E. Moerner, M. Orrit, and H. Talon, “Photon antibunching in the fluorescence of a single dye molecule trapped in a solid,” *Phys. Rev. Lett.* **69**, 1516–1519 (1992).

-
- [12] C. Kurtsiefer, S. Mayer, P. Zarda, and H. Weinfurter, “Stable Solid-State Source of Single Photons,” *Phys. Rev. Lett.* **85**, 290–293 (2000).
- [13] P. Michler, A. Kiraz, C. Becher, W. V. Schoenfeld, P. M. Petroff, L. Zhang, E. Hu, and A. Imamoglu, “A Quantum Dot Single-Photon Turnstile Device,” *Science* **290**, 2282–2285 (2000).
- [14] B. Hensen, H. Bernien, A. E. Dréau, A. Reiserer, N. Kalb, M. S. Blok, J. Ruitenbergh, R. F. Vermeulen, R. N. Schouten, C. Abellán *et al.*, “Loophole-free Bell inequality violation using electron spins separated by 1.3 kilometres,” *Nature* **526**, 682 (2015).
- [15] A. Einstein, B. Podolsky, and N. Rosen, “Can Quantum-Mechanical Description of Physical Reality Be Considered Complete?” *Phys. Rev.* **47**, 777–780 (1935).
- [16] J. Riedrich-Möller, L. Kipfstuhl, C. Hepp, E. Neu, C. Pauly, F. Mücklich, A. Baur, M. Wandt, S. Wolff, M. Fischer *et al.*, “One- and two-dimensional photonic crystal microcavities in single crystal diamond,” *Nature nanotechnology* **7**, 69 (2012).
- [17] E. Neu, P. Appel, M. Ganzhorn, J. Miguel-Sánchez, M. Lesik, V. Mille, V. Jacques, A. Tallaire, J. Achard, and P. Maletinsky, “Photonic nano-structures on (111)-oriented diamond,” *Applied Physics Letters* **104**, 153108 (2014).
- [18] R. Albrecht, A. Bommer, C. Deutsch, J. Reichel, and C. Becher, “Coupling of a Single Nitrogen-Vacancy Center in Diamond to a Fiber-Based Microcavity,” *Physical Review Letters* **110**, 243602 (2013).
- [19] H. J. Kimble, “The quantum internet,” *Nature* **453**, 1023 (2008).
- [20] L.-M. Duan, M. Lukin, J. I. Cirac, and P. Zoller, “Long-distance quantum communication with atomic ensembles and linear optics,” *Nature* **414**, 413 (2001).
- [21] A. I. Lvovsky, B. C. Sanders, and W. Tittel, “Optical quantum memory,” *Nature photonics* **3**, 706 (2009).
- [22] H.-J. Briegel, W. Dür, J. I. Cirac, and P. Zoller, “Quantum Repeaters: The Role of Imperfect Local Operations in Quantum Communication,” *Phys. Rev. Lett.* **81**, 5932–5935 (1998).
- [23] L. Childress and R. Hanson, “Diamond NV centers for quantum computing and quantum networks,” *MRS Bulletin* **38**, 134–138 (2013).
- [24] T. Northup and R. Blatt, “Quantum information transfer using photons,” *Nature photonics* **8**, 356 (2014).
- [25] F. Dolde, M. W. Doherty, J. Michl, I. Jakobi, B. Naydenov, S. Pezzagna, J. Meijer, P. Neumann, F. Jelezko, N. B. Manson, and J. Wrachtrup, “Nanoscale Detection of a Single Fundamental Charge in Ambient Conditions Using the NV⁻ Center in Diamond,” *Phys. Rev. Lett.* **112**, 097603 (2014).

- [26] L. Rondin, J.-P. Tetienne, T. Hingant, J.-F. Roch, P. Maletinsky, and V. Jacques, “Magnetometry with nitrogen-vacancy defects in diamond,” *Reports on progress in physics. Physical Society (Great Britain)* **77**, 056503 (2014).
- [27] J. Tisler, T. Oeckinghaus, R. J. Stöhr, R. Kolesov, R. Reuter, F. Reinhard, and J. Wrachtrup, “Single defect center scanning near-field optical microscopy on graphene,” *Nano Letters* **13**, 3152–3156 (2013).
- [28] J. Teissier, A. Barfuss, P. Appel, E. Neu, and P. Maletinsky, “Strain Coupling of a Nitrogen-Vacancy Center Spin to a Diamond Mechanical Oscillator,” *Phys. Rev. Lett.* **113**, 020503 (2014).
- [29] P. Neumann, I. Jakobi, F. Dolde, C. Burk, R. Reuter, G. Waldherr, J. Honert, T. Wolf, A. Brunner, J. H. Shim, D. Suter, H. Sumiya, J. Isoya, and J. Wrachtrup, “High-Precision Nanoscale Temperature Sensing Using Single Defects in Diamond,” *Nano Letters* **13**, 2738–2742 (2013). PMID: 23721106.
- [30] S. Steinert, F. Dolde, P. Neumann, A. Aird, B. Naydenov, G. Balasubramanian, F. Jelezko, and J. Wrachtrup, “High sensitivity magnetic imaging using an array of spins in diamond,” *Review of Scientific Instruments* **81**, 043705 (2010).
- [31] L. Shao, R. Liu, M. Zhang, A. V. Shneidman, X. Audier, M. Markham, H. Dhillon, D. J. Twitchen, Y.-F. Xiao, and M. Lončar, “Wide-Field Optical Microscopy of Microwave Fields Using Nitrogen-Vacancy Centers in Diamonds,” *Advanced Optical Materials* **4**, 1075–1080 (2016).
- [32] D. Le Sage, K. Arai, D. R. Glenn, S. J. DeVience, L. M. Pham, L. Rahn-Lee, M. D. Lukin, A. Yacoby, A. Komeli, and R. L. Walsworth, “Optical magnetic imaging of living cells,” *Nature* **496**, 486 (2013).
- [33] P. Kehayias, M. J. Turner, R. Trubko, J. M. Schloss, C. A. Hart, M. Wesson, D. R. Glenn, and R. L. Walsworth, “Imaging crystal stress in diamond using ensembles of nitrogen-vacancy centers,” *Phys. Rev. B* **100**, 174103 (2019).
- [34] E. V. Oort and M. Glasbeek, “Electric-field-induced modulation of spin echoes of N-V centers in diamond,” *Chemical Physics Letters* **168**, 529 – 532 (1990).
- [35] T. Wolf, P. Neumann, K. Nakamura, H. Sumiya, T. Ohshima, J. Isoya, and J. Wrachtrup, “Subpicotesla Diamond Magnetometry,” *Phys. Rev. X* **5**, 041001 (2015).
- [36] H. Clevenson, L. M. Pham, C. Teale, K. Johnson, D. Englund, and D. Braje, “Robust high-dynamic-range vector magnetometry with nitrogen-vacancy centers in diamond,” *Applied Physics Letters* **112**, 252406 (2018).

-
- [37] M. Chipaux, L. Toraille, C. Larat, L. Morvan, S. Pezzagna, J. Meijer, and T. Debuisschert, “Wide bandwidth instantaneous radio frequency spectrum analyzer based on nitrogen vacancy centers in diamond,” *Applied Physics Letters* **107**, 233502 (2015).
- [38] G. Balasubramanian, I. Chan, R. Kolesov, M. Al-Hmoud, J. Tisler, C. Shin, C. Kim, A. Wojcik, P. R. Hemmer, A. Krueger *et al.*, “Nanoscale imaging magnetometry with diamond spins under ambient conditions,” *Nature* **455**, 648 (2008).
- [39] H. J. Mamin, M. Kim, M. H. Sherwood, C. T. Rettner, K. Ohno, D. D. Awschalom, and D. Rugar, “Nanoscale Nuclear Magnetic Resonance with a Nitrogen-Vacancy Spin Sensor,” *Science* **339**, 557–560 (2013).
- [40] T. Staudacher, F. Shi, S. Pezzagna, J. Meijer, J. Du, C. A. Meriles, F. Reinhard, and J. Wrachtrup, “Nuclear Magnetic Resonance Spectroscopy on a (5-Nanometer)³ Sample Volume,” *Science* **339**, 561–563 (2013).
- [41] J. Maze, P. Stanwix, J. Hodges, S. Hong, J. Taylor, P. Cappellaro, L. Jiang, M. G. Dutt, E. Togan, A. Zibrov *et al.*, “Nanoscale magnetic sensing with an individual electronic spin in diamond,” *Nature* **455**, 644 (2008).
- [42] M. S. Grinolds, S. Hong, P. Maletinsky, L. Luan, M. D. Lukin, R. L. Walsworth, and A. Yacoby, “Nanoscale magnetic imaging of a single electron spin under ambient conditions,” *Nature Physics* **9**, 215 (2013).
- [43] M. Pelliccione, B. A. Myers, L. M. A. Pascal, A. Das, and A. C. Bleszynski Jayich, “Two-Dimensional Nanoscale Imaging of Gadolinium Spins via Scanning Probe Relaxometry with a Single Spin in Diamond,” *Phys. Rev. Applied* **2**, 054014 (2014).
- [44] T. Häberle, D. Schmid-Lorch, F. Reinhard, and J. Wrachtrup, “Nanoscale nuclear magnetic imaging with chemical contrast,” *Nature nanotechnology* **10**, 125 (2015).
- [45] D. Schmid-Lorch, T. Häberle, F. Reinhard, A. Zappe, M. Slota, L. Bogani, A. Finkler, and J. Wrachtrup, “Relaxometry and Dephasing Imaging of Superparamagnetic Magnetite Nanoparticles Using a Single Qubit,” *Nano Letters* **15**, 4942–4947 (2015). PMID: 26218205.
- [46] D. Rugar, H. Mamin, M. Sherwood, M. Kim, C. Rettner, K. Ohno, and D. Awschalom, “Proton magnetic resonance imaging using a nitrogen–vacancy spin sensor,” *Nature nanotechnology* **10**, 120 (2015).
- [47] S. Kolkowitz, A. Safira, A. A. High, R. C. Devlin, S. Choi, Q. P. Unterreithmeier, D. Patterson, A. S. Zibrov, V. E. Manucharyan, H. Park, and M. D. Lukin, “Probing Johnson noise and ballistic transport in normal metals with a single-spin qubit,” *Science* **347**, 1129–1132 (2015).
- [48] T. Van der Sar, F. Casola, R. Walsworth, and A. Yacoby, “Nanometre-scale probing of spin waves using single electron spins,” *Nature communications* **6**, 7886 (2015).

- [49] R. Schirhagl, K. Chang, M. Loretz, and C. L. Degen, “Nitrogen-Vacancy Centers in Diamond: Nanoscale Sensors for Physics and Biology,” *Annual Review of Physical Chemistry* **65**, 83–105 (2014). PMID: 24274702.
- [50] C.-C. Fu, H.-Y. Lee, K. Chen, T.-S. Lim, H.-Y. Wu, P.-K. Lin, P.-K. Wei, P.-H. Tsao, H.-C. Chang, and W. Fann, “Characterization and application of single fluorescent nanodiamonds as cellular biomarkers,” *Proceedings of the National Academy of Sciences* **104**, 727–732 (2007).
- [51] V. Petráková, A. Taylor, I. Kratochvílová, F. Fendrych, J. Vacík, J. Kučka, J. Štursa, P. Cígler, M. Ledvina, A. Fišerová, P. Kneppo, and M. Nesládek, “Luminescence of Nanodiamond Driven by Atomic Functionalization: Towards Novel Detection Principles,” *Advanced Functional Materials* **22**, 812–819 (2012).
- [52] L. P. McGuinness, Y. Yan, A. Stacey, D. A. Simpson, L. T. Hall, D. Maclaurin, S. Praver, P. Mulvaney, J. Wrachtrup, F. Caruso *et al.*, “Quantum measurement and orientation tracking of fluorescent nanodiamonds inside living cells,” *Nature nanotechnology* **6**, 358 (2011).
- [53] G. Kucsko, P. C. Maurer, N. Y. Yao, M. Kubo, H. J. Noh, P. K. Lo, H. Park, and M. D. Lukin, “Nanometre-scale thermometry in a living cell,” *Nature* **500**, 54 (2013).
- [54] Y. Chen, J. D. Mills, and A. Periasamy, “Protein localization in living cells and tissues using FRET and FLIM,” *Differentiation* **71**, 528 – 541 (2003).
- [55] R. Roy, S. Hohng, and T. Ha, “A practical guide to single-molecule FRET,” *Nature methods* **5**, 507 (2008).
- [56] H. Uhm, W. Kang, K. S. Ha, C. Kang, and S. Hohng, “Single-molecule FRET studies on the cotranscriptional folding of a thiamine pyrophosphate riboswitch,” *Proceedings of the National Academy of Sciences* **115**, 331–336 (2018).
- [57] J. Tisler, R. Reuter, A. Lämmle, F. Jelezko, G. Balasubramanian, P. R. Hemmer, F. Reinhard, and J. Wrachtrup, “Highly efficient FRET from a single nitrogen-vacancy center in nanodiamonds to a single organic molecule,” *ACS Nano* **5**, 7893–7898 (2011).
- [58] P. Appel, E. Neu, M. Ganzhorn, A. Barfuss, M. Batzer, M. Gratz, A. Tschöpe, and P. Maletinsky, “Fabrication of all diamond scanning probes for nanoscale magnetometry,” *Review of Scientific Instruments* **87**, 063703 (2016).
- [59] B. M. Chernobrod and G. P. Berman, “Spin microscope based on optically detected magnetic resonance,” *Journal of Applied Physics* **97**, 014903 (2005).
- [60] D. Riedel, D. Rohner, M. Ganzhorn, T. Kaldewey, P. Appel, E. Neu, R. J. Warburton, and P. Maletinsky, “Low-Loss Broadband Antenna for Efficient Photon Collection from a Coherent Spin in Diamond,” *Phys. Rev. Applied* **2**, 064011 (2014).

- [61] P. Fuchs, M. Challier, and E. Neu, “Optimized single-crystal diamond scanning probes for high sensitivity magnetometry,” *New Journal of Physics* **20**, 125001 (2018).
- [62] P. Maletinsky, S. Hong, M. S. Grinolds, B. Hausmann, M. D. Lukin, R. L. Walsworth, M. Loncar, and A. Yacoby, “A robust scanning diamond sensor for nanoscale imaging with single nitrogen-vacancy centres,” *Nature Nanotechnology* **7**, 320–324 (2012).
- [63] L. Rondin, J.-P. Tetienne, P. Spinicelli, C. Dal Savio, K. Karrai, G. Dantelle, A. Thiaville, S. Rohart, J.-F. Roch, and V. Jacques, “Nanoscale magnetic field mapping with a single spin scanning probe magnetometer,” *Applied Physics Letters* **100**, 153118 (2012).
- [64] P. Appel, M. Ganzhorn, E. Neu, and P. Maletinsky, “Nanoscale microwave imaging with a single electron spin in diamond,” *New Journal of Physics* **17**, 112001 (2015).
- [65] L. Rondin, J.-P. Tetienne, S. Rohart, A. Thiaville, T. Hingant, P. Spinicelli, J.-F. Roch, and V. Jacques, “Stray-field imaging of magnetic vortices with a single diamond spin,” *Nature communications* **4**, 2279 (2013).
- [66] J.-P. Tetienne, T. Hingant, J.-V. Kim, L. H. Diez, J.-P. Adam, K. Garcia, J.-F. Roch, S. Rohart, A. Thiaville, D. Ravelosona, and V. Jacques, “Nanoscale imaging and control of domain-wall hopping with a nitrogen-vacancy center microscope,” *Science* **344**, 1366–1369 (2014).
- [67] J.-P. Tetienne, T. Hingant, L. Martínez, S. Rohart, A. Thiaville, L. H. Diez, K. Garcia, J.-P. Adam, J.-V. Kim, J.-F. Roch *et al.*, “The nature of domain walls in ultrathin ferromagnets revealed by scanning nanomagnetometry,” *Nature communications* **6**, 6733 (2015).
- [68] I. Gross, W. Akhtar, V. Garcia, L. Martínez, S. Chouaieb, K. Garcia, C. Carrétéro, A. Barthélémy, P. Appel, P. Maletinsky *et al.*, “Real-space imaging of non-collinear antiferromagnetic order with a single-spin magnetometer,” *Nature* **549**, 252 (2017).
- [69] I. Gross, W. Akhtar, A. Hrabec, J. Sampaio, L. J. Martínez, S. Chouaieb, B. J. Shields, P. Maletinsky, A. Thiaville, S. Rohart, and V. Jacques, “Skyrmion morphology in ultrathin magnetic films,” *Phys. Rev. Materials* **2**, 024406 (2018).
- [70] D. Rohner, J. Happacher, P. Reiser, M. A. Tschudin, A. Tallaire, J. Achard, B. J. Shields, and P. Maletinsky, “(111)-oriented, single crystal diamond tips for nanoscale scanning probe imaging of out-of-plane magnetic fields,” *Applied Physics Letters* **115**, 192401 (2019).
- [71] P. Appel, B. J. Shields, T. Kosub, N. Hedrich, R. Hübner, J. Faßbender, D. Makarov, and P. Maletinsky, “Nanomagnetism of Magnetoelectric Granular Thin-Film Antiferromagnets,” *Nano Letters* **19**, 1682–1687 (2019). PMID: 30702895.

-
- [72] L. Thiel, D. Rohner, M. Ganzhorn, P. Appel, E. Neu, B. Müller, R. Kleiner, D. Koelle, and P. Maletinsky, “Quantitative nanoscale vortex imaging using a cryogenic quantum magnetometer,” *Nature nanotechnology* **11**, 677 (2016).
- [73] D. Rohner, L. Thiel, B. Müller, M. Kasperczyk, R. Kleiner, D. Koelle, and P. Maletinsky, “Real-Space Probing of the Local Magnetic Response of Thin-Film Superconductors Using Single Spin Magnetometry,” *Sensors* **18** (2018).
- [74] L. Thiel, Z. Wang, M. A. Tschudin, D. Rohner, I. Gutiérrez-Lezama, N. Ubrig, M. Gibertini, E. Giannini, A. F. Morpurgo, and P. Maletinsky, “Probing magnetism in 2D materials at the nanoscale with single-spin microscopy,” *Science* **364**, 973–976 (2019).
- [75] V. M. Acosta, L. S. Bouchard, D. Budker, R. Folman, T. Lenz, P. Maletinsky, D. Rohner, Y. Schlüssel, and L. Thiel, “Color Centers in Diamond as Novel Probes of Superconductivity,” *Journal of Superconductivity and Novel Magnetism* **32**, 85–95 (2019).
- [76] K. Chang, A. Eichler, J. Rhensius, L. Lorenzelli, and C. L. Degen, “Nanoscale Imaging of Current Density with a Single-Spin Magnetometer,” *Nano Letters* **17**, 2367–2373 (2017). PMID: 28329445.
- [77] L. Luan, M. S. Grinolds, S. Hong, P. Maletinsky, R. L. Walsworth, and A. Yacoby, “Decoherence imaging of spin ensembles using a scanning single-electron spin in diamond,” *Scientific reports* **5**, 8119 (2015).
- [78] R. Nelz, P. Fuchs, O. Opaluch, S. Sonusen, N. Savenko, V. Podgursky, and E. Neu, “Color center fluorescence and spin manipulation in single crystal, pyramidal diamond tips,” *Applied Physics Letters* **109**, 193105 (2016).
- [79] R. Nelz, J. Görlitz, D. Herrmann, A. Slablab, M. Challier, M. Radtke, M. Fischer, S. Gsell, M. Schreck, C. Becher, and E. Neu, “Toward wafer-scale diamond nano- and quantum technologies,” *APL Materials* **7**, 011108 (2019).
- [80] M. Radtke, R. Nelz, A. Slablab, and E. Neu, “Reliable Nanofabrication of Single-Crystal Diamond Photonic Nanostructures for Nanoscale Sensing,” *Micromachines* **10** (2019).
- [81] M. Radtke, L. Render, R. Nelz, and E. Neu, “Plasma treatments and photonic nanostructures for shallow nitrogen vacancy centers in diamond,” *Opt. Mater. Express* **9**, 4716–4733 (2019).
- [82] M. Radtke, A. SLABLAB, E. Bernardi, R. Nelz, and E. Neu, “Nanoscale sensing based on nitrogen vacancy centers in single crystal diamond and nanodiamonds: achievements and challenges,” *Nano Futures* (2019).

- [83] R. Nelz, M. Radtke, A. Slablab, Z.-Q. Xu, M. Kianinia, C. Li, C. Bradac, I. Aharonovich, and E. Neu, “Near-Field Energy Transfer between a Luminescent 2D Material and Color Centers in Diamond,” *Advanced Quantum Technologies* **n/a**, 1900088 (2019).
- [84] M. W. Doherty, N. B. Manson, P. Delaney, F. Jelezko, J. Wrachtrup, and L. C. Hollenberg, “The nitrogen-vacancy colour centre in diamond,” *Physics Reports* **528**, 1–45 (2013).
- [85] K. Ohno, F. Joseph Heremans, L. C. Bassett, B. A. Myers, D. M. Toyli, A. C. Bleszynski Jayich, C. J. Palmstrøm, and D. D. Awschalom, “Engineering shallow spins in diamond with nitrogen delta-doping,” *Applied Physics Letters* **101**, 082413 (2012).
- [86] J. Riedrich-Möller, S. Pezzagna, J. Meijer, C. Pauly, F. Mücklich, M. Markham, A. M. Edmonds, and C. Becher, “Nanoimplantation and Purcell enhancement of single nitrogen-vacancy centers in photonic crystal cavities in diamond,” *Applied Physics Letters* **106**, 221103 (2015).
- [87] I. Jakobi, S. A. Momenzadeh, F. F. de Oliveira, J. Michl, F. Ziem, M. Schreck, P. Neumann, A. Denisenko, and J. Wrachtrup, “Efficient creation of dipolar coupled nitrogen-vacancy spin qubits in diamond,” *Journal of Physics: Conference Series* **752**, 012001 (2016).
- [88] C. A. McLellan, B. A. Myers, S. Kraemer, K. Ohno, D. D. Awschalom, and A. C. Bleszynski Jayich, “Patterned Formation of Highly Coherent Nitrogen-Vacancy Centers Using a Focused Electron Irradiation Technique,” *Nano Letters* **16**, 2450–2454 (2016). PMID: 27010642.
- [89] B. Grotz, M. V. Hauf, M. Dankerl, B. Naydenov, S. Pezzagna, J. Meijer, F. Jelezko, J. Wrachtrup, M. Stutzmann, F. Reinhard, and J. A. Garrido, “Charge state manipulation of qubits in diamond,” *Nature Communications* **3**, 729– (2012).
- [90] L. J. Rogers, S. Armstrong, M. J. Sellars, and N. B. Manson, “Infrared emission of the NV centre in diamond: Zeeman and uniaxial stress studies,” *New Journal of Physics* **10**, 103024 (2008).
- [91] A. Batalov, C. Zierl, T. Gaebel, P. Neumann, I.-Y. Chan, G. Balasubramanian, P. R. Hemmer, F. Jelezko, and J. Wrachtrup, “Temporal Coherence of Photons Emitted by Single Nitrogen-Vacancy Defect Centers in Diamond Using Optical Rabi-Oscillations,” *Phys. Rev. Lett.* **100**, 077401 (2008).
- [92] V. M. Acosta, A. Jarmola, E. Bauch, and D. Budker, “Optical properties of the nitrogen-vacancy singlet levels in diamond,” *Phys. Rev. B* **82**, 201202 (2010).

-
- [93] J. Wrachtrup and F. Jelezko, “Processing quantum information in diamond,” *Journal of Physics: Condensed Matter* **18**, S807–S824 (2006).
- [94] A. Dréau, M. Lesik, L. Rondin, P. Spinicelli, O. Arcizet, J.-F. Roch, and V. Jacques, “Avoiding power broadening in optically detected magnetic resonance of single NV defects for enhanced dc magnetic field sensitivity,” *Phys. Rev. B* **84**, 195204 (2011).
- [95] L. Childress, M. V. Gurudev Dutt, J. M. Taylor, A. S. Zibrov, F. Jelezko, J. Wrachtrup, P. R. Hemmer, and M. D. Lukin, “Coherent Dynamics of Coupled Electron and Nuclear Spin Qubits in Diamond,” *Science* **314**, 281–285 (2006).
- [96] Y. Kato, H. Kawashima, T. Makino, M. Ogura, A. Traoré, N. Ozawa, and S. Yamasaki, “Estimation of Inductively Coupled Plasma Etching Damage of Boron-Doped Diamond Using X-Ray Photoelectron Spectroscopy,” *physica status solidi (a)* **214**, 1700233 (2017).
- [97] E. Neu, D. Steinmetz, J. Riedrich-Möller, S. Gsell, M. Fischer, M. Schreck, and C. Becher, “Single photon emission from silicon-vacancy colour centres in chemical vapour deposition nano-diamonds on iridium,” *New Journal of Physics* **13**, 025012 (2011).
- [98] E. Neu, M. Agio, and C. Becher, “Photophysics of single silicon vacancy centers in diamond: implications for single photon emission,” *Opt. Express* **20**, 19956–19971 (2012).
- [99] E. Neu, R. Albrecht, M. Fischer, S. Gsell, M. Schreck, and C. Becher, “Electronic transitions of single silicon vacancy centers in the near-infrared spectral region,” *Phys. Rev. B* **85**, 245207 (2012).
- [100] E. Gratton, S. Breusegem, J. D. B. Sutin, Q. Ruan, and N. P. Barry, “Fluorescence lifetime imaging for the two-photon microscope: time-domain and frequency-domain methods,” *Journal of Biomedical Optics* **8**, 381 – 390 – 10 (2003).
- [101] M. Schreck, S. Gsell, R. Brescia, and M. Fischer, “Ion bombardment induced buried lateral growth: the key mechanism for the synthesis of single crystal diamond wafers,” *Scientific reports* **7**, 44462 (2017).
- [102] S. Sangtawesin, B. L. Dwyer, S. Srinivasan, J. J. Allred, L. V. H. Rodgers, K. De Greve, A. Stacey, N. Dontschuk, K. M. O’Donnell, D. Hu, D. A. Evans, C. Jaye, D. A. Fischer, M. L. Markham, D. J. Twitchen, H. Park, M. D. Lukin, and N. P. de Leon, “Origins of Diamond Surface Noise Probed by Correlating Single-Spin Measurements with Surface Spectroscopy,” *Phys. Rev. X* **9**, 031052 (2019).
- [103] M. Toth and I. Aharonovich, “Single Photon Sources in Atomically Thin Materials,” *Annual Review of Physical Chemistry* **70**, 123–142 (2019). PMID: 30735459.

- [104] M. C. Niederländer, “Detektion des Ladungszustandes von NV Farbzentren in Diamant,” Bachelor thesis, Universität des Saarlandes (2019).
- [105] N. Aslam, G. Waldherr, P. Neumann, F. Jelezko, and J. Wrachtrup, “Photo-induced ionization dynamics of the nitrogen vacancy defect in diamond investigated by single-shot charge state detection,” *New Journal of Physics* **15**, 013064 (2013).
- [106] D. Bluvstein, Z. Zhang, and A. C. B. Jayich, “Identifying and Mitigating Charge Instabilities in Shallow Diamond Nitrogen-Vacancy Centers,” *Phys. Rev. Lett.* **122**, 076101 (2019).
- [107] B. J. Shields, Q. P. Unterreithmeier, N. P. de Leon, H. Park, and M. D. Lukin, “Efficient Readout of a Single Spin State in Diamond via Spin-to-Charge Conversion,” *Phys. Rev. Lett.* **114**, 136402 (2015).
- [108] J.-C. Jaskula, B. Shields, E. Bauch, M. Lukin, A. Trifonov, and R. Walsworth, “Improved Quantum Sensing with a Single Solid-State Spin via Spin-to-Charge Conversion,” *Phys. Rev. Applied* **11**, 064003 (2019).
- [109] A. Ariyaratne, D. Bluvstein, B. A. Myers, and A. C. B. Jayich, “Nanoscale electrical conductivity imaging using a nitrogen-vacancy center in diamond,” *Nature communications* **9**, 2406 (2018).
- [110] D. R. Glenn, R. R. Fu, P. Kehayias, D. Le Sage, E. A. Lima, B. P. Weiss, and R. L. Walsworth, “Micrometer-scale magnetic imaging of geological samples using a quantum diamond microscope,” *Geochemistry, Geophysics, Geosystems* **18**, 3254–3267 (2017).
- [111] M. Challier, R. Nelz, B. Kiendl, A. Slablab, M. Radtke, A. Krueger, and E. Neu, “Wet chemical fluorine treatment of diamond: towards hydrophobic diamond nano-devices for single NV sensing,” manuscript in preparation (2019).
- [112] L. M. Pham, S. J. DeVience, F. Casola, I. Lovchinsky, A. O. Sushkov, E. Bersin, J. Lee, E. Urbach, P. Cappellaro, H. Park, A. Yacoby, M. Lukin, and R. L. Walsworth, “NMR technique for determining the depth of shallow nitrogen-vacancy centers in diamond,” *Phys. Rev. B* **93**, 045425 (2016).
- [113] Y. Dovzhenko, F. Casola, S. Schlotter, T. Zhou, F. Büttner, R. Walsworth, G. Beach, and A. Yacoby, “Magnetostatic twists in room-temperature skyrmions explored by nitrogen-vacancy center spin texture reconstruction,” *Nature communications* **9**, 2712 (2018).
- [114] Photonikforschung Deutschland, “BrainQSens,” <https://www.photonikforschung.de/projekte/quantentechnologien/projekt/brainqsens.html>. Accessed: 2019-12-11.

- [115] C. Foy, L. Zhang, M. E. Trusheim, K. R. Bagnall, M. Walsh, E. N. Wang, and D. R. Englund, “Wide-field Magnetic Field and Temperature Imaging using Nanoscale Quantum Sensors,” arXiv preprint arXiv:1903.05717 (2019).

List of publications

Refereed journal publications

- *Color center fluorescence and spin manipulation in single crystal, pyramidal diamond tips*
Richard Nelz, Philipp Fuchs, Oliver Opaluch, Selda Sonusen, Natalia Savenko, Vitali Podgursky, and Elke Neu
Applied Physics Letters **109**, 193105 (2016); doi: 10.1063/1.4967189
- *Nanoscale Sensing Using Point Defects in Single-Crystal Diamond: Recent Progress on Nitrogen Vacancy Center-Based Sensors*
Ettore Bernardi, Richard Nelz, Selda Sonusen, and Elke Neu
Crystals **7(5)**, 124 (2017); doi: 10.3390/cryst7050124
- *Toward wafer-scale diamond nano- and quantum technologies¹*
Richard Nelz, Johannes Görlitz, Dennis Herrmann, Abdallah Slablab, Michel Chailier, Mariusz Radtke, Martin Fischer, Stefan Gsell, Matthias Schreck, Christoph Becher, and Elke Neu
APL Materials **7**, 011108 (2019); doi:10.1063/1.5067267
- *Spin Measurement of NV Centers Coupled to a Photonic Crystal Cavity*
Thomas Jung, Johannes Görlitz, Benjamin Kambs, Christoph Pauly, Nicole Raatz, Richard Nelz, Elke Neu, Andrew M. Edmonds, Matthew Markham, Frank Mücklich, Jan Meijer, and Christoph Becher
accepter for publication in APL Photonics (2019)
- *Reliable Nanofabrication of single-crystal diamond photonic nanostructures for nanoscale sensing*
Mariusz Radtke, Richard Nelz, Abdallah Slablab, and Elke Neu
Micromachines **10**, 718 (2019); doi: 10.3390/mi10110718
- *Nanoscale sensing based on nitrogen vacancy centers in single crystal diamond and nanodiamonds: achievements and challenges*
Mariusz Radtke, Ettore Bernardi, Abdallah Slablab, Richard Nelz, and Elke Neu
Nano Futures, in press (2019); doi: 10.1088/2399-1984/ab5f9b
- *Near-field energy transfer between a luminescent 2D material and color centers in diamond*
Richard Nelz, Mariusz Radtke, Abdallah Slablab, Zai-Quan Xu, Mehran Kianinia, Chi Li, Carlo Bradac, Igor Aharonovich, and Elke Neu
Adv. Quantum Technol. **1900088** (2019); doi: 10.1002/qute.201900088

¹This paper was selected as an Editor's Pick

- *Plasma treatments and photonic nanostructures for shallow nitrogen vacancy centers in diamond*
Mariusz Radtke, Lara Render, Richard Nelz, and Elke Neu
Opt. Mater. Express **9**, 4716-4733 (2019); doi: 10.1364/OME.9.004716

Refereed conference proceedings

The proceedings marked with * were presented by the author of this thesis.

- *Optimized nano-fabrication of diamond scanning probes for novel imaging techniques*
Selda Sonusen, Amandeep Kaur, Richard Nelz, Ettore Bernardi, and Elke Neu
Hasselt Diamond Workshop 2016, Hasselt (Belgium), March 2016
- *Single crystal, pyramidal diamond tips as sensors for scanning probe magnetometry*
Richard Nelz, Philipp Fuchs, Oliver Opaluch, Selda Sonusen, Natalia Savenko, Vitali Podgursky, and Elke Neu
Hasselt Diamond Workshop 2017, Hasselt (Belgium), March 2017
- *Toward Nitrogen Vacancy Center based Scanning Near Field Microscopy*
Ettore Bernardi, Richard Nelz, Alexander Meyer, Selda Sonusen, Michel Challier, and Elke Neu
Quantum 2017, Torino (Italy), May 2017
- *Fluorescent single crystal, pyramidal diamond tips as photonic structures for scanning probe magnetometry**
Richard Nelz, Philipp Fuchs, Oliver Opaluch, Selda Sonusen, Natalia Savenko, Vitali Podgursky, and Elke Neu
CLEO Europe, Munich (Germany), June 2017
- *Optimizing nanoscale sensing using color centers in diamond*
Richard Nelz, Alexander Meyer, Ettore Bernardi, Philipp Fuchs, Oliver Opaluch, Selda Sonusen, Michel Challier, Natalia Savenko, Vitali Podgursky and Elke Neu
COST Action MP1403 Nanoscale Quantum Optics, Single Photons Single Spins conference II, Troyes (France), August 2017
- *Lifetime study of single nitrogen vacancy (NV) centers in nanostructures: toward NV-based scanning near field microscopy*
Ettore Bernardi, Richard Nelz, Alexander Meyer, Michel Challier, Selda Sonusen, and Elke Neu
DIADEMS and SIRTEQ Quantum Technologies Workshop 14-15 September 2017
- *Towards Energy Transfer-Based Sensing and Imaging with Color Centers in Single-Crystal Diamond**
Richard Nelz, Alexander Meyer, Michel Challier, Selda Sonusen, Ettore Bernardi, and Elke Neu
MRS Fall Meeting 2018, Boston (USA), November 2017

- *Color Centers as Atomic-sized Sensors for Nanoscale Fields*
Mariusz Radtke, Abdallah Slablab, Richard Nelz, Michel Challier, Philipp Fuchs, Selda Sonusen, Ettore Bernardi and Elke Neu
COST Action MP1403 Nanoscale Quantum Optics Workshop, Prague (Czech Republic), February 2018
- *Towards Energy Transfer-based Sensing and Imaging with Color Centers in Single-Crystal Diamond**
Richard Nelz, Michel Challier, Ettore Bernardi, and Elke Neu
Groupreport at DPG Spring Meeting 2018, Erlangen (Germany), March 2018
- *Towards optimized scanning probe sensors with shallow nitrogen vacancy color centers*
Michel Challier, Richard Nelz, Philipp Fuchs, Benjamin Kiendl, Frank Müller, Samuel Grandthyll, Anke Krueger and Elke Neu
Hasselt Diamond Workshop 2018, Hasselt (Belgium), March 2018
- *Optical near-field probe based on individual NV color centers*
Abdallah Slablab, Richard Nelz, Mariusz Radtke, Michel Challier, and Elke Neu
International CECAM Workshop: Crystal defects for qubits, single photon emitters and nanosensors, Bremen (Germany), July 2018
- *Color centers in diamond: single spin quantum sensors for nanoscale imaging*
Abdallah Slablab, Richard Nelz, Mariusz Radtke, Michel Challier, and Elke Neu
Joint European Magnetic Symposia Conference, Mainz (Germany), September 2018
- *Diamond as sensing tool:surface treatments for controlling the charge state of nitrogen vacancies in nanophotonic devices*
Mariusz Radtke, Abdallah Slablab, Richard Nelz, Michel Challier, Benjamin Kiendl, Frank Müller, Anke Krueger and Elke Neu
Hasselt Diamond Workshop 2019, Hasselt (Belgium), March 2019
- *Toward coupling color centers in single crystal diamond to two-dimensional materials*
Oliver Opaluch, Richard Nelz, Michel Challier, Mariusz Radtke, Abdallah Slablab, Zaiquan Xu, Igor Aharonovich, and Elke Neu
CLEO Europe, Munich (Germany), June 2019
- *Diamond as Sensing Tool: NV⁻ Color Centers in Ultrasensitive Devices**
Mariusz Radtke, Abdallah Slablab, Richard Nelz, Michel Challier, Nimba Oshnik, and Elke Neu
ICMAT 2019, Singapore (Singapore), June 2019

Workshops and schools

During the work on this thesis, the author participated at the following schools and workshops:

- DIADEMS Diamond and Spins School, Cargèse (France), May 2016
- International School of Physics „Enrico Fermi“–Course on Nanoscale Quantum Optics, Varenna (Italy), July 2018
- WE-Heraeus Seminar on Diamond Quantum Technologies, Bonn (Germany), March 2019

Danke!

An dieser Stelle möchte ich mich bei den vielen Menschen bedanken, die das Gelingen dieser Arbeit ermöglicht haben.

An erster Stelle möchte ich mich bei meiner Betreuerin Elke Neu-Ruffing für die Möglichkeit zur Promotion bedanken. Ich möchte mich insbesondere für das mir entgegengebrachte Vertrauen und für die bereichernden Beiträge zu meiner Arbeit bedanken. Ebenfalls möchte ich mich für das Korrekturlesen meiner Publikationen und dieser Dissertation bedanken. Ebenso bin ich dankbar für die Möglichkeit, meine Arbeit auf vielen Konferenzen an interessanten Orten vorstellen zu dürfen. Ich muss mich ebenfalls dafür bedanken, dass sie mir bei der Entwicklung der experimentellen Aufbauten sowie der Verwirklichung geplanter Projekte und Messungen weitestgehend freie Hand gelassen hat, sodass ich mir meine eigene Expertise auf dem Gebiet der quantenbasierten Sensoren erarbeiten konnte. Uwe Hartmann danke ich ganz herzlich für die Bereitschaft, diese Arbeit als Zweitgutachter zu lesen.

Ein großes Dankeschön gilt natürlich auch den aktuellen aber auch allen ehemaligen Kollegen unserer Arbeitsgruppe. Ohne die vielen ergiebigen Diskussionen während meiner Zeit als Doktorand wären viele Ideen zu der Weiterentwicklung der Setups und zur Verwirklichung neuer Experimente nie entstanden. Ebenfalls konnte ich durch die Interdisziplinarität unserer Gruppe auch einmal über den Tellerrand hinaus schauen.

In diesem Zusammenhang muss ich auch den Studenten danken, denen ich während meiner Promotion helfen durfte, ihren eigenen Weg zu finden. Durch die vielen interessierten Nachfragen und Kommentare haben sie mir geholfen, neue Impulse für unsere Experimente zu finden. Alexander Meyer danke ich bei der großen Unterstützung beim Aufbau des AFM-Confocals. Lara Render danke ich für die Unterstützung bei der Arbeit an der Plasmabehandlung von Diamant. Ein großer Dank gilt Marie Niederländer für die Hilfe bei der Realisierung der Charge-State-Detection, aber auch für die Abende, die wir zum Entspannen in der Boulderhalle verbracht haben. Ebenfalls ein großer Dank gilt Oliver Opaluch, dessen Weg ich vom Studienanfänger über Bachelor- und Masterstudent bis hin zum Promotionsstudenten begleiten durfte. Ebenfalls würde ich die vielen Sitzungen an den Wochenenden, bei denen wir stundenlang gezoockt, haben nicht missen wollen.

Natürlich gilt auch ein Dank den Kooperationspartnern, ohne die eine Vielzahl von Experimenten in dieser Arbeit nicht möglich gewesen wären. Matthias Schreck und AuDiaTec danke ich dabei für die Stücke des wirklich außergewöhnlichen Diamantwafers. I would like to thank Vitali Podgursky and Artech Carbon for the pyramidal diamond scanning probes. In addition, I want to thank Igor Aharonovich and his group for the excellent collaboration on FRET with WSe₂.

Ein weiterer Dank gilt auch Christoph Becher, dessen Betreuung meiner Bachelor- und Masterarbeit geholfen hat, meinen Weg in die Wissenschaft zu finden. Seiner Gruppe möchte ich für die vielen Diskussionen während meiner Abschlussarbeiten und meiner Promotion danken. Insbesondere muss ich hierbei Andreas Lenhard, Christian Hepp, Benjamin Kambs und Matthias Bock dafür danken, dass sie mich in die Kunst der Justage von optischen Systemen eingeführt haben. Der Aussage von Andreas „Wer einen cw-OPO justieren kann, kann alles justieren“, kann ich rückblickend nur zustimmen. Ebenfalls möchte ich Johannes Görlitz und Alexander Bommer für die vielen nützlichen, aber auch für die weniger seriösen Diskussionen danken. Ein besonderer Dank gilt Philipp Fuchs und Anna Breunig für die vielen netten Abende außerhalb der Uni.

Außerhalb des Labors ist die forderndste und komplexeste Aufgabe während der Promotion den Umgang mit der Bürokratie zu meistern. Bei der Unterstützung dabei und für die stets freundliche Auskunft bei bürokratischen Fragen möchte ich Elke Huschens danken. Ebenfalls möchte ich der mechanischen Werkstatt danken, ohne die unsere optischen Tische wahrscheinlich noch recht leer wären. Bei Stefan Loew möchte ich mich für das Anfertigen einer Vielzahl an Netzteilen etc. bedanken.

Meinen ehemaligen Lehrern Julia Christians und Burkhard Wolf möchte ich danken, dass sie mein Interesse an den Naturwissenschaften gefördert haben, ohne das ich wohl nie begonnen hätte zu studieren.

Aber der allergrößte Dank gilt meiner Familie und meiner besseren Hälfte Kerstin. Ohne eure Unterstützung während meines bisherigen Lebens hätte ich nie den Weg bis hierhin geschafft. Ich danke euch dafür, dass ihr immer für mich da seid, mir Kraft gibt und es immer schafft, mich von der Uni abzulenken.

Ohne euch wäre mein Leben nicht annähernd so schön, wie es ist.